

**Laser spectroscopy of some transition-metal-containing
diatomic molecules: NbN, TaN, ScH, ScN, ScO and NiC**

By

SHEO MUKUND

PHYS01201104001

Bhabha Atomic Research Centre, Mumbai

A thesis submitted to the

Board of Studies in Physical Sciences

In partial fulfillment of requirements

for the Degree of

DOCTOR OF PHILOSOPHY

of

HOMI BHABHA NATIONAL INSTITUTE



January, 2018

Homi Bhabha National Institute

Recommendations of the Viva Voce Committee

As members of the Viva Voce committee, we certify that we have read the dissertation prepared by **Mr. Sheo Mukund** entitled “**Laser spectroscopy of some transition-metal-containing diatomic molecules: NbN, TaN, ScH, ScN, ScO and NiC**” and recommend that it may be accepted as fulfilling the thesis requirement for award of Degree of Doctor of Philosophy.


Chairman - Prof. B.N. Jagatap

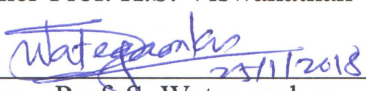
Date: 25/01/2018


Guide / Convener – Prof. S.G. Nakhate

Date: 25/01/2018


Examiner-Prof. K.S. Viswanathan


Date: 25/01/2018


Member – Prof. S. Wategaonkar

Date: 25/01/2018

Member – Prof. K.G. Manohar

Date: 25/01/2018



Prof. B.K. Nayak

Final approval and acceptance of this thesis is contingent upon the candidate's submission of the final copies of the thesis to HBNI.

I hereby certify that I have read this thesis prepared under my direction and recommend that it may be accepted as fulfilling the thesis requirement.

Date: January 25, 2018

Place: Mumbai


Prof. S. G. Nakhate

STATEMENT BY AUTHOR

This dissertation has been submitted in partial fulfillment of requirements for an advanced degree at Homi Bhabha National Institute (HBNI) and is deposited in the Library to be made available to borrowers under rules of the HBNI.

Brief quotations from this dissertation are allowable without special permission, provided that accurate acknowledgement of source is made. Requests for permission for extended quotation from or reproduction of this manuscript in whole or in part may be granted by the Competent Authority of HBNI when in his or her judgment the proposed use of the material is in the interests of scholarship. In all other instances, however, permission must be obtained from the author.

Sheo Mukund

DECLARATION

I, hereby declare that the investigation presented in the thesis has been carried out by me. The work is original and has not been submitted earlier as a whole or in part for a degree/diploma at this or any other Institution/University.

Sheo Mukund

Dedicated to

My Parents

List of Publications arising from the thesis

Publications in Refereed Journal: 9

1. Laser-induced fluorescence spectroscopy of TaN in free-jet: Observation of high-lying excited electronic states.
S.G. Nakhate, **Sheo Mukund** and Soumen Bhattacharyya
Chemical Physics Letters, **669**, 38 (2017).
2. The NbN $C^3\Pi-X^3\Delta$ (1-0) band: Experimental and Theoretical Study of the Spin-orbit interaction between the $C^3\Pi$ and $e^1\Pi$ states
Soumen Bhattacharyya, **Sheo Mukund**, J. F. Harrison and S.G. Nakhate
Chemical Physics Letters, **663**, 133 (2016).
3. Jet-cooled laser-induced dispersed fluorescence spectroscopy of TaN: Observation of $a^3\Delta$ and $A^1\Delta$ states
Sheo Mukund, Soumen Bhattacharyya, S.G. Nakhate
Chemical Physics Letters, **655-656**, 51 (2016).
4. LIF spectroscopy of NbN in free-jet: New bands in the 19000-21000 cm^{-1} region
Soumen Bhattacharyya, **Sheo Mukund** and Sanjay G. Nakhate
Molecular Physics, **114**, 592 (2016).
5. Free-jet laser-induced fluorescence spectroscopy of NbN: Observation of a new $^3\Pi$ state
Sheo Mukund, Soumen Bhattacharyya, S.G. Nakhate
Journal of Quantitative Spectroscopy & Radiative Transfer, **166**, 30 (2015).
6. Jet-cooled laser-induced dispersed fluorescence spectroscopy of NiC: Observation of low-lying $\Omega=0^+$ state
Sheo Mukund, Suresh Yarlagadda, Soumen Bhattacharyya, S.G. Nakhate
Chemical Physics Letters, **591**, 43 (2014).
7. Jet-cooled laser-induced fluorescence spectroscopy of ScH: Observation of an $\Omega'=2 - \Omega''=1$ transition
Sheo Mukund, Soumen Bhattacharyya, S.G. Nakhate
Journal of Quantitative Spectroscopy & Radiative Transfer, **147**, 274 (2014).
8. Jet-cooled laser-induced fluorescence spectroscopy of $B^2\Sigma^+-X^2\Sigma^+$ system of scandium monoxide: Improved molecular constants at equilibrium
Sheo Mukund, Suresh Yarlagadda, Soumen Bhattacharyya, S.G. Nakhate
Journal of Quantitative Spectroscopy & Radiative Transfer, **113**, 2004 (2012).

9. Jet-cooled laser-induced dispersed fluorescence spectroscopy of ScN: Observation of $a^3\Sigma^+$ state
Sheo Mukund, S.G. Nakhate
Chemical Physics Letters, **501**, 221 (2011).

Publication prior to the Ph.D. enrolment date:

10. Electronic structure of ScN: Jet-cooled laser-induced fluorescence spectroscopy
S.G. Nakhate, **Sheo Mukund**,
Chemical Physics Letters, **496**, 243 (2010).

Publications in Conferences/Symposia: 2

1. Observation of the low-lying $a^3\Delta$ and $A^1\Delta$ states in jet-cooled tantalum mononitride,
Sheo Mukund, Soumen Bhattacharyya, S.G. Nakhate, 71th International Symposium
on Molecular Spectroscopy, Venue: University of Illinois at Urbana-Champaign,
USA, June 20-24, (2016).
2. Laser-induced fluorescence spectroscopy of TaN molecule in free-jet, **Sheo Mukund**,
Soumen Bhattacharyya, S.G. Nakhate, DAE-BRNS National Laser Symposium,
Venue: KIIT University, Bhubaneswar, Odisha, Dec 20-23, (2016).

ACKNOWLEDGEMENTS

First and foremost, I would like to express my heartiest gratitude to my thesis advisor and doctoral committee convener Prof. S.G. Nakhate for his continuous support, invaluable guidance and constant encouragement throughout the course of this research work. I am extremely indebted to him for providing me enormous learning opportunities. I persuaded my research interests using the facility – ‘Supersonic Molecular Beam Setup’ indigenously developed by him. His wide knowledge and his logical way of thinking on critical scientific problems have been of great value for me. I am also grateful to him for being patient while critically reviewing this thesis. His suggestions have helped me to significantly improve the quality of the work presented in the thesis.

It gives me immense pleasure to express my sincere thanks to my doctoral committee chairman, Prof. B.N. Jagatap and members, Prof. S. Wategaonkar and Prof. K.G. Manohar for their critical reviews and suggestions during the annual reviews and pre-synopsis presentations.

I am deeply grateful to my senior colleague Dr. Soumen Bhattacharyya for his innumerable help during the experiments and data analysis. He has been truly invaluable to me both on an academic and a personal level, for which I am extremely grateful. I am also very thankful to former Ph.D. student, Dr. Suresh Yarlagadda from this laboratory.

I would like to express my sincere thank to Dr. N.K. Sahoo, Head, Atomic and Molecular Physics Division, Bhabha Atomic Research Centre, Mumbai for his constant support and encouragement. I also gratefully acknowledge the help and support rendered by all the members of my division including the technical staff members of general workshop and electronics workshop.

I would like to express my sincere thank to Prof. Saibal Basu, Dean-Academic, Physical & Mathematical Sciences, Homi Bhabha National Institute, Mumbai for his suggestions and help.

I owe my heartfelt gratitude and indebtedness to my parents for their love. They always encouraged me to follow my heart. I take this opportunity to express my heartiest gratitude to all my family members including my elder sister and brother for their support and encouragement in every stage of my life.

Finally, I express my sincere thanks to all my friends for their numerous help, criticism and support.

CONTENTS

Synopsis.....	xxi
List of Tables	xxxix
List of Figures.....	xli
Chapter 1: Introduction: Theoretical Background	1-28
1.1 Introduction	1
1.2 Diatomic Molecular Hamiltonian	4
1.2.1 Born-Oppenheimer Approximation	4
1.2.2 Nuclear Part of Hamiltonian	5
1.2.2.a Vibrational Structure	6
1.2.2.b Rotational Structure	7
1.2.3 Electronic Structure	9
1.2.3.a Orbital Angular Momentum.....	9
1.2.3.b Fine-Structure	10
1.2.3.b(i) Spin-Orbit Interaction	10
1.2.3.b(ii) Spin-Rotation Interaction.....	11
1.2.3.b(iii) Spin-Spin Interaction	11
1.2.4 Coupling of Rotation and Electronic Motion: Hund'S Coupling Cases	12
1.2.4.a Hund's Case (<i>a</i>).....	12
1.2.4.b Hund's Case (<i>b</i>).....	14
1.2.4.c Hund's Case (<i>c</i>)	15
1.2.4.d Hund's Case (<i>d</i>).....	16
1.2.4.e Hund's Case (<i>e</i>)	17
1.2.4.f Nuclear Spin Coupling: Extension of Hund's Coupling Cases	18

1.3 Symmetry, Parity and Selection Rules	20
1.4 Perturbation	22
1.5 Data Reduction and Evaluation of Molecular Parameters	23
1.5.1 Combination Difference Method	23
1.5.2 Least Square Fitting Procedure	23
1.5.3 PGOPHER Simulation Program	24
1.6 Rydberg, Klein and Rees Potential Energy Curve and Franck-Condon Factors.....	24
1.7 References	25
Chapter 2: Experimental Setup and Techniques	29-46
2.1 Introduction	29
2.2 Supersonic Molecular Beam Apparatus	29
2.2.1 Vacuum Chambers.....	30
2.2.2 Gas Pulsed Valve and Laser Vaporization Source	31
2.2.3 Laser Systems	33
2.2.3.a Ablation Laser.....	33
2.2.3.b Pulsed Dye Laser	34
2.2.3.c Photoionization Laser	34
2.2.4 Fluorescence Detection and Data Acquisition System	34
2.2.5 Time of Flight Mass Spectrometer (TOFMS)	36
2.2.6 Gas-Manifold System	37
2.3 Preparation of Molecules and Time Synchronization of Events	38
2.4 Experimental Techniques	41
2.4.1 Fluorescence Based Experiments	41
2.4.1.a Laser-Induced Fluorescence (LIF) Excitation Spectroscopy.....	41
2.4.1.b Wavelength-Resolved Dispersed Fluorescence (DF) Study.....	42

2.4.1.c Measurement of Radiative Lifetime	43
2.4.2 Mass-Selected Photoionization Experiment	44
2.5 Wavelength Calibration of LIF Excitation Spectra	45
2.6 References	46
Chapter 3: Laser-Induced Fluorescence Spectroscopy of Group 5, Niobium and Tantalum Mononitride Molecules (NbN, TaN).....	47-108
3.1 Introduction	47
3.2 Experiment	50
3.3 Spectroscopic Investigation of NbN in the Visible Region.....	51
3.3.1 Literature Survey	51
3.3.2 LIF Spectroscopy of High-energy Excited Electronic States of NbN.....	55
3.3.2.a Experimental and Theoretical Study of the Second-order Spin-orbit Interaction between the $C^3\Pi$ and $e^1\Pi$ States of NbN at $v = 1$ Vibrational Level	58
3.3.2.a(i) Description and Analysis of the Observed Bands	58
3.3.2.a(ii) Method of Calculation: Spin-orbit Interaction.....	62
3.3.2.b Bands Originating From the $v'' = 0$ of the $X^3\Delta$ State	64
3.3.2.b(i) $^3\Pi$ states with $^3\Pi_{0\pm}$, $^3\Pi_1$ and $^3\Pi_2$ spin-orbit components, respectively, at term energies 20,756.32, 20,900.1 and 21,240.3 cm^{-1}	64
3.3.2.b(ii) (0–0) band of $^3\Pi_{0\pm} - X^3\Delta_1$ and $^3\Pi_1 - X^3\Delta_2$ transitions with band origin at 19,841.5 and 19,716.1 cm^{-1}	68
3.3.2.c Hot Bands: Bands Originating From the $v'' = 1$ of the $X^3\Delta$ State	70
3.3.2.c(i) Band origin 19,980.7 cm^{-1} , $\tau = 207(8)$ ns, [0–1 of $\Omega = 2 - X^3\Delta_3$]	70
3.3.2.c(ii) Band origin 20,006.2 cm^{-1} , $\tau = 225(10)$ ns, [0–1 of $\Omega = 0 - X^3\Delta_1$]	71
3.3.2.c(iii) Band origin 20,063.0 cm^{-1} , $\tau = 95(4)$ ns, [0–1 of $\Omega = 1 - X^3\Delta_2$]	71
3.3.2.c(iv) Band origin 20,143.6 cm^{-1} , $\tau = 54(3)$ ns, [0–1 of $\Omega = 2 - X^3\Delta_3$]	72

3.3.2.c(v) Band origin 20,243.3 cm ⁻¹ , $\tau = 130(4)$ ns, [0–1 of $\Omega=1 - X^3\Delta_2$]	72
3.3.2.c(vi) Band origin 20,257.8 cm ⁻¹ , $\tau = 257(15)$ ns, [0–1 of $\Omega=1 - X^3\Delta_2$]	74
3.3.2.c(vii) Band origins 20,586.7 and 20,605.3 cm ⁻¹ , $\tau = 80(4)$ ns, [0–1 of $\Omega=0^+ - X^3\Delta_1$].....	74
3.3.3 Dispersed Fluorescence Studies on NbN and Observation of Vibrational Progression in the Low-lying States	74
3.3.4 Results and Discussions	77
3.4 Study of Electronic Structure of TaN	84
3.4.1 Literature Survey	84
3.4.2 Excitation Spectra: High-Energy States	86
3.4.2.a Rotational Analysis and Assignments of the Observed Bands	86
3.4.2.b Rotational Constants	91
3.4.3 Dispersed Fluorescence Spectra: Ground and Low-energy States	91
3.4.3.a Equilibrium Vibrational Constants of the $X^1\Sigma^+$ Ground State	94
3.4.3.b Observation of the $a^3\Delta_{1,2}$ and $A^1\Delta$ Low-lying Excited Electronic States	94
3.4.4 Results and Discussions	96
3.5 Conclusion	101
3.6 References	103
Chapter 4: Study of Electronic Structure of Scandium Monohydride (ScH), Scandium Mononitride (ScN) and Scandium Monoxide (ScO) Molecules	109-154
4.1 Introduction	109
4.2 Experiment	110
4.3 Laser-Induced Fluorescence (LIF) Study of ScH.....	111
4.3.1 Appearance of the Spectra	112
4.3.2 Assignments of Bands and Molecular Constants	113

4.3.3 Discussion.....	115
4.4 Spectroscopic Investigation of the Electronic Structure of ScN	117
4.4.1 Study of High-Energy States	119
4.4.1.a Description of the Observed Bands	119
4.4.1.b Quantum Number Assignment and Molecular Constants	121
4.4.2 Study of Low-lying States	127
4.4.2.a Dispersed Fluorescence Spectra and Assignments of the States	127
4.4.2.b Vibrational Constants and Potential Energy Curves.....	132
4.4.3 Discussion.....	134
4.5 LIF Spectroscopy of ScO in the Visible Region	139
4.5.1 Excitation and Dispersed Fluorescence Spectra of $B^2\Sigma^+ - X^2\Sigma^+$ System and Equilibrium Molecular Constants	141
4.5.2 Potential Energy Curves and Franck-Condon Factors for $B^2\Sigma^+ - X^2\Sigma^+$ Transition	148
4.6 Conclusion.....	149
4.7 References	151
Chapter 5: Wavelength-Resolved Laser-Induced Fluorescence Spectroscopy of the Jet-cooled Nickel Monocarbide (NiC) Molecule	155-168
5.1 Introduction	155
5.1.1 Motivation.....	155
5.2 Experiment	157
5.3 Observations and Analysis	157
5.3.1 Vibrational Constants of the $X^1\Sigma^+$ Ground State	158
5.3.2 Observation of the Low-lying $\Omega = 0^+$ Excited Electronic State	159
5.4 Discussion.....	161

5.4.1 Comparison of NiC with Isovalent Monocarbides in their Ground and Low-lying Electronic States	164
5.5 Conclusion.....	165
5.6 References	166
 Appendix 1: Supplementary information for rotational line positions and assignments of observed bands of NbN	169
Appendix 2: Supplementary information for rotational line positions and assignments of observed bands of TaN.....	179
Appendix 3: Supplementary information for rotational line positions and assignments of observed bands of ScH	194
Appendix 4: Supplementary information for rotational line positions and assignments of observed bands of ScN	195
Appendix 5: Supplementary information for rotational line positions and assignments of observed bands of ScO	200

SYNOPSIS

The chemical bond between transition metals and main group elements is of general interest because of their importance in catalysis [1], astrophysics [2], surface science [3], organometallic chemistry [4] and also in theoretical understanding of the simple metal-containing systems [5]. Due to the presence of partially filled *d*-shell in transition metals, the electronic structures of these molecules are complex and difficult to treat theoretically than the molecules containing main group elements [5]. The theoretical calculations necessitate including the large correlation energy of electrons and relativistic corrections, for even qualitatively correct results. A quite small change in the model can lead to very different predictions for the energy order and properties of the low-lying electronic states. For this reason, experimental results of these systems are of great importance as they provide a critical test of adequacy of selected methods and level of the theoretical treatment. In addition, the presence of open *d*-shells gives rise to states with high spin and large orbital angular momenta, which are split by substantial spin-orbit interactions in these molecular systems. Due to the presence of a large number of excited electronic states, which are derived from several close lying configurations, the spectra of these molecules are usually complex. Strong spin-orbit interactions especially in the excited states limit the validity of the usual Hund's case (a) coupling in these molecules. Also, under the Hund's case (a) coupling scheme, the subbands of a given electronic transition can be far apart and often lead to the misinterpretation of the spectroscopic data. The problems that plague theoretical calculations also apply to experimental side. Transition-metal-containing molecules are highly refractory materials and their high-temperature spectra are often complex, congested and difficult to interpret. The widespread hyperfine structure due to odd atomic mass number nuclei with large nuclear spin and magnetic moments add another dimension of complexity. The extensive perturbations make the understanding of the spectra further difficult. This problem

has held back progress with their spectra in the past. However, the advent of laser-vaporization supersonic expansion source [6] gave a tool to create these species in the gas phase under the non-equilibrium low temperature conditions. This simplified the spectra to a great extent and received a strong boost in the systematic experimental study of transition-metal-containing molecules.

This thesis presents the experimental study of electronic structure of laser-vaporization jet-cooled transition-metal-containing diatomic molecules in the gas phase using laser-induced fluorescence (LIF) spectroscopy. The investigated molecules are divided into three categories. (I). Group 5, *d*-block transition metal mononitrides viz. NbN and TaN molecules: Usually the electronic structure of isovalent molecules is similar. However, the difference in the electronic structure of these isovalent molecules motivated us to take up this study. Moreover, recently there has been interest in heavy, polar diatomic molecules [7] and molecular ions [8] in search of permanent electron electric dipole moment (eEDM), which provides a direct test of parity- and time-reversal symmetry violation. It was recently pointed out that the heavy polar diatomic molecules in paramagnetic $^3\Delta_1$ electronic state could be exploited to increase the current eEDM limit [9] and TaN could be a better candidate because of longer lifetime of its metastable $^3\Delta_1$ state [10]. Detailed spectroscopic information and electronic structure of the promising molecular candidates are of paramount importance for EDM experiments [10,11]. In view of this, we explored the spectroscopic parameters of the ground, low- and high-energy excited electronic states [12,13] of TaN molecule including $a^3\Delta$ state. A comparative study of electronic structure of group 5, *d*-block transition metal mononitrides is presented. (II). Scandium containing diatomic ScH, ScN, and ScO molecules: The spectroscopic investigation of a particular transition metal atom with a main group element throws light on the electronic structure and bonding of these diatomics, which serve as a model to understand the more complex systems. We investigated the earlier unobserved

transitions involving triplet manifolds in ScH, which otherwise are well characterized in its isovalent YH and LaH molecules. The determination of ground state symmetry in ScN was indirect and theoretically predicted low- and high-lying excited electronic states were not observed in the earlier experimental studies. We investigated this area in the present work. Due to the considerable astrophysical interest, the $B-X$ system of ScO molecule was extended to the higher vibrational levels and better molecular constants at equilibrium were determined in our study. Recently, Ziurys group [14] investigated the pure rotational spectrum of ScO in the $v=0$ and 1 vibrational levels of the ground state, in view of its importance for astronomical searches in the circumstellar environments. (III). NiC molecule: The uncertainty among theoretical studies over the energy ordering of the low-lying $a^3\Pi$ and $A^1\Pi$ excited electronic states was resolved in our present study. An overview of the thesis contents, grouped under five chapters is as follows:

Chapter 1. Introduction

This chapter gives brief theoretical account of electronic structure of diatomic molecules [15,16,17,18], in the context of the present study. The solution of the Schrodinger equation for the molecular Hamiltonian is described under Born-Oppenheimer approximation, in which the coupling between the nuclear and electronic motions is ignored. Nuclear part of the Hamiltonian is further solved for rotation and vibration of the molecules. Further, rotational and vibrational structure along with the symmetry properties of the diatomic energy levels are discussed in detail. Electronic states are designated by the term symbols which provide information about symmetry of the states, orbital angular momentum, spin-orbit coupling and coupling of rotation and electronic motion, i.e., Hund's coupling cases are explained. Selection rules for the dipole transitions in the different electronic states and perturbations in the spectra of diatomic molecules are also briefly discussed.

Chapter 2. Experimental Setup and Techniques

This chapter describes the Supersonic molecular beam setup, being utilized to explore the electronic structure of diatomic molecules in the present thesis. The setup essentially consists of a ‘Smalley source’ which utilises laser-vaporization with the pulsed supersonic expansion [6] to produce exotic molecular species containing various metal atoms of refractory nature. Supersonic molecular beam is a well known technique which offers collisionless atmosphere after expansion from the nozzle and thus stabilizes the reactive/exotic species in the beam. It also offers an excellent translational and rotational cooling, thereby simplifying the excitation spectrum which otherwise poses problems at high temperature.

The detailed description of the setup which include generation of cold molecules in the beam using gas pulsed valve and laser-vaporization source; laser-induced fluorescence (LIF) imaging, dispersing and detection techniques and related instrumentation; and also control/synchronization and data acquisition systems are given. In brief, a focused beam of a third harmonic Nd:YAG laser was employed to produce laser-induced plasma of a desired metal target. The resulting metal plasma reacted with a seed gas in helium emerging from a pulsed valve under a backing pressure of few atmospheres. The different seed gases with the optimized concentration in helium were used to generate different molecules; for example, ammonia was used to produce hydride/nitride species in the beam. The products of the reaction were expanded into vacuum and probed at right angle to the supersonic expansion axis by a narrow band tunable pulsed dye laser. The resulting fluorescence was collected orthogonal to both expansion and dye laser beam axes, dispersed by a monochromator and subsequently detected by a Peltier cooled photomultiplier tube (PMT). An output signal from the PMT was integrated by a gated integrator, and stored on a computer. The spectra were recorded in two modes; viz. LIF excitation and wavelength resolved or dispersed

fluorescence (DF). Excitation spectra were obtained by scanning the pulsed dye laser frequency and recording the LIF signal through the monochromator set at a fixed wavelength corresponding to the strongest fluorescence terminating either to a ground or low-lying excited electronic state. In this scheme, the monochromator was used as a broadband filter. The resolution of the obtained excitation spectra was typical spectral line width of the scanning dye laser, which is $\sim 0.1 \text{ cm}^{-1}$. In the other scheme, the DF spectra were investigated to get information on the ground and low-lying electronic states and their vibrational structure. The DF spectra were recorded by exciting the isolated rovibrational levels of the excited electronic states and monitoring the fluorescence by scanning the monochromator in the 300–925 nm wavelength region, offered by the sensitivity of the PMT. In general, the DF spectra were first recorded with monochromator entrance/exit slit width of 1/1 mm, corresponding to a moderate spectral resolution with FWHM $\sim 50\text{--}100 \text{ cm}^{-1}$, to get coarse information about the ground and the low-lying vibronic levels. Since the vibrational spacings are of the order of 1000 cm^{-1} , they are well separated under this resolution. To determine the identity of the low-lying states, the coarse DF spectra were then examined, wherever possible, under relatively higher resolution to resolve their rotational levels. For this experiment, the monochromator entrance/exit slit width was reduced to 0.1/0.1 mm, which corresponds to spectral resolution of FWHM $\sim 5 \text{ cm}^{-1}$. The observed number of rotational lines and their intensity pattern were used to determine the identity of the low-lying electronic states.

Chapter 3. Laser-induced fluorescence spectroscopy of group 5, Niobium & Tantalum Mononitride molecules (NbN, TaN)

This chapter presents LIF spectroscopic investigation of group 5, *d*-block transition metal mononitrides, NbN and TaN molecules in the free-jet. The isovalent molecules usually exhibit the same ground state electronic configuration and term symmetry. The group 5

transition metal mononitrides VN, NbN and TaN molecules are isovalent, however, while the $^3\Delta$ state is the ground state for VN and NbN, the $^1\Sigma^+$ state is the ground state for TaN. The ground state of VN and NbN has a triple bond with two metal-localized high-spin d -electrons, to give $^3\Delta$ term symmetry [19], which arise from the electron configuration $\pi^4 ns\sigma^1(n-1)d\delta^1$ ($n=4$ for VN and $n=5$ for NbN). However, for TaN molecule, *ab initio* calculations [20] predicted the ground state as $^1\Sigma^+$, arising from the electronic configuration $\pi^4 3\sigma^2$ while the low-lying $^3\Delta$ and $^1\Delta$ states arising from the $\pi^4 3\sigma^1 1\delta^1$ electronic configuration. The difference in the ground state of TaN molecules is due to the net relativistic stabilization of the $(n+1)s$ electron compared to the nd electron in Ta atom [21]. This difference in the electronic structure of these isovalent molecules prompted us to take up this study. The VN [22] and NbN [23,24] molecules also exhibit isoconfigurational spin-orbit interactions which is revealed in the asymmetric spin-orbit splitting of the $^3\Pi$ and $^3\Delta$ states. The details of the investigations on the electronic structure of individual molecules are described in the subsequent sections.

NbN

The spectra of NbN molecule have been studied in the past by employing various experimental techniques. A few high quality *ab initio* calculations are also available. The first electronic spectrum of a $B^3\Phi-X^3\Delta$ transition was recorded in 1969 [25], however due to large hyperfine splitting observed in the outer two spin components prevented the rotational analysis of the spectrum, except for the central spin component, $B^3\Phi_3-X^3\Delta_2$. The large hyperfine splitting were observed in the gas phase optical spectra of NbN, as the $^{93}_{41}\text{Nb}$ nucleus has the largest nuclear magnetic moment, 6.1436 nuclear magneton, among the stable nuclei. The hyperfine resolved spectrum was studied by Féménias *et al.* at higher resolution [26]. The rotational analyses of the 0-0 of $B^3\Phi-X^3\Delta$ band were published by Pazyuk *et al.* [27] and Féménias *et al.* [28]. Later, a detailed analysis of the rotational and hyperfine

structure of the 0-0 band of $B^3\Phi-X^3\Delta$ transition was published by Azuma *et al.* [23]. They determined the spin-orbit structure of the $X^3\Delta$ state, which was found to be asymmetric due to isoconfiguration interaction between the $X^3\Delta_2$ and $a^1\Delta_2$. Subsequently, Azuma *et al.* [24] also carried out the rotational and hyperfine analyses of the 0-0 bands of the $C^3\Pi-X^3\Delta$, $e^1\Pi-X^3\Delta$ and $f^1\Pi-X^3\Delta$ transitions. They also discovered three low-lying states $c^1\Gamma$, $A^3\Sigma^-$ and $b^1\Sigma^+$ in the wavelength resolved DF spectra. Azuma *et al.* observed all the low-lying electronic states predicted in *ab initio* calculation [29] except the $d^1\Sigma^+$ state, which Ram and Bernath [30] have observed subsequently. Recently, Ram and Bernath [31] reported a new $^3\Pi$ and probably $^3\Delta$ state, unaccounted in the present theory, by emission spectroscopy in the 8000–35,000 cm^{-1} region. In spite of these studies, we observed many more excited electronic states from our jet-cooled LIF spectroscopy of NbN molecule. The findings of laser spectroscopy of NbN molecule under the present study are categorised in the three parts: (I). The spin-orbit interaction and deperturbation analysis in the $v=1$ of $C^3\Pi_1/e^1\Pi$ electronic states. A strong second-order spin-orbit mixing was observed between these isoconfigurational states, which lifted the normal symmetric spin splitting in the $C^3\Pi$ and pushed the $^3\Pi_1$ substate below the other spin components of the $C^3\Pi$ state. The *ab initio* calculation on the NbN spin-orbit levels was also performed in collaboration with Prof. J. F. Harrison. The spin-orbit splitting of the $X^3\Delta$ and $C^3\Pi$, and isoconfiguration interaction in the $X^3\Delta/a^1\Delta$ and $C^3\Pi/e^1\Pi$ states were examined. The theoretical results were in reasonable agreement with the energy level separation $\Delta E(\Omega=2-\Omega=0)$, but underestimate the $\Delta E(\Omega=1-\Omega=0)$ separation of the $^3\Pi_\Omega$ state. This error is traced to our overestimate of the unperturbed singlet-triplet energy separation. However, the second order splitting mixes the $\Omega=2$ levels of the isoconfigurational ground $^3\Delta$ and low-lying $^1\Delta$ states is in excellent agreement with the experimental value. (II). The observation of two new $^3\Pi$ state and seven hot bands originating from the $v''=1$ level of the

ground state, in the 19,000–21,000 cm^{-1} region. The absence of regular energy spacing and a widely varying lifetime values among these hot bands did not permit to group them into subbands. The presently observed $^3\Pi$ states and other high-lying electronic states were not predicted by earlier theoretical studies, and await further *ab initio* calculation for elucidation.

(III). Determination of equilibrium vibrational constants of the ground $X^3\Delta$ and low-lying $A^3\Sigma_1^-$ state from wavelength resolved DF study.

TaN

Our studies on NbN molecule suggested that the electronic structure of excited states is quite complex than that suggested by existing *ab initio* studies and inclusion of more electronic configurations are required to elucidate new observations. Isoconfiguration second-order spin-orbit interactions disturb normal spin-orbit structure and poses difficulty in identifying the spin components, even in the low energy range. The spin-orbit effects are expected to be even stronger in Ta ($\zeta_{5d}=1699 \text{ cm}^{-1}$) than Nb ($\zeta_{4d}=524 \text{ cm}^{-1}$) and thus electronic structure of TaN is expected to be much more complex. The strong spin-orbit coupling in TaN molecule may heavily mix many of the terms and only Ω remains a good quantum number, thus exhibit Hund's case (c), especially for high-energy electronic states. We tried to address some of these issues in the present work.

Previous studies on TaN molecule in gas phase [32] identified several bands in electronic emission spectra, using a microwave discharge source. The bands were classified into singlet and triplet systems; however, symmetry of the ground state of TaN was not clear in their study. The studies in Ar matrix [33,34] determined the fundamental vibration. In the recent past, Ram *et al.* [20] investigated high-resolution emission spectra of TaN in the 3000–35,000 cm^{-1} region using a Fourier transform spectrometer. They observed a number of new bands involving $^1\Sigma^+$ and $^3\Delta$ as a lower state. The observation of intercombination transition suggested that the $^1\Sigma^+$ symmetry of the ground state, which was supported by their *ab initio*

calculation. The $\Omega=1$ and 2 spin components of the first excited state, $a^3\Delta$ were observed with determination of the term energy only for $a^3\Delta_1$. Thus, the spin-orbit splitting in the $a^3\Delta$ state was not known. In the absence of observation of off-diagonal transitions, the gas-phase vibration frequencies of the ground and low-lying electronic states were not known. They also reported several excited electronic states from ground and low-lying $a^3\Delta$ states.

In this thesis, we report the observation of the $\Omega=1$ and 2 spin components of the $a^3\Delta$ state and the $A^1\Delta$ state. The equilibrium term energies and vibrational constants of the $X^1\Sigma^+$, $a^3\Delta_{1,2}$ and $A^1\Delta$ states were measured from the observation of the extensive vibrational progressions in the DF spectra obtained from the excitation of the newly observed excited electronic states. With the determination of the term energies of the vibrational levels of the ground and low-lying states, the term energies of the several high-energy excited states observed in previous study of Ram *et al.* [20] were determined. We report the observation and assignment of the several new excited electronic states in the 23,500–30,000 cm^{-1} region. In the view of known term energy spacing, molecular constants, and radiative lifetime data, many states were grouped as a vibrational member of the electronic states. In the absence of term energy regularity and molecular constants, the observed states could not be clubbed as spin-components of the predicted terms. The assignment of the low- and high-lying excited electronic states in TaN indicate that the molecule follow Hund's case (a) coupling in the low-energy region, however, it tends towards case (c) at high-energy. The present observation of many more excited electronic states than those expected in the existing *ab initio* calculations warrant high-level *ab initio* studies with inclusion of newer electronic configurations, to elucidate the current results.

Chapter 4. Study of electronic structure of Scandium Monohydride (ScH), Scandium Mononitride (ScN) and Scandium Monoxide (ScO) molecules

Scandium, being the first and simplest among the transition metals, the LIF study on electronic structure of its diatomics with main group elements (H,N,O) has been addressed in this chapter. Determination of the ground state symmetry in transition-metal-containing molecules is very crucial both from theoretical and experimental points of view. In addition, experimental determination of excited electronic states, their energy level ordering and gas-phase vibrational frequency are important to validate the theoretical calculations. In the present experimental study, ground state symmetry in ScN has been confirmed. The electronic structure of ScN, predicted by *ab initio* studies, suggested few strongly bound low-energy excited electronic states that correlate to excited atomic asymptote and also shallow high-energy excited electronic states that correlate to the lowest atomic asymptote, were unobserved experimentally. Our experimental study revealed new low- and high-lying excited electronic states in ScN. In the study of ScH molecule, the first observation of transition in the triplet manifold was reported. The spectra of ScO molecule are of considerable astrophysical interest and in view of this, the $B^2\Sigma^+ - X^2\Sigma^+$ system, which falls in the visible region of the electromagnetic spectra was studied. Our observation of higher vibrational levels of this system resulted in precise knowledge on equilibrium rotational and vibrational constants. The details of the investigations on the electronic structure of individual molecules are described in the following sections.

ScH

The ground state of ScH molecule is $^1\Sigma^+$ and a number of transitions are observed only in the singlet manifold in earlier experimental studies. However, transitions involving the triplet manifold in ScH have never been observed, which otherwise are well characterized in its isovalent YH and LaH molecules. This study is important in order to understand the

bonding and validating the theoretical treatment in this simple metal hydride system. Being the simplest among transition-metal-containing molecules, there have been large number of theoretical studies on the electronic structure and spectroscopic properties of ScH molecule. The early theoretical calculation [35] on ScH, where electron correlation in $4s^2$ pair was not included, predicted the ground state to be $^3\Delta$. When the proper correlation was included [36], the $[6\sigma^2 7\sigma^2] ^1\Sigma^+$ becomes the ground state and $[1\delta 6\sigma 7\sigma^2] ^3\Delta$ the first low-lying state. Ram and Bernath [37,38] studied the emission spectra of ScH and ScD in the $3500\text{--}26,000\text{cm}^{-1}$ range by Fourier transform spectroscopy and observed several transitions involving only singlet manifolds. The observed bands were classified into electronic transitions between the ground $X^1\Sigma^+$, low-energy $A^1\Delta$ and $B^1\Pi$ and high-energy $C^1\Sigma^+$, $D^1\Pi$, $E^1\Delta$, $F^1\Sigma^-$, and $G^1\Pi$ states. We, in the present work identified the $g^3\Phi_2 - a^3\Delta_1$ transition among the triplet manifold and presented molecular constants for the first excited $a^3\Delta_1$ and $g^3\Phi_2$ states in $v=0$ and 1 vibrational levels. Although the observed bands had rotational line spacing typical to ScH, further confirmation of the carrier of the bands was done by mass-selected resonance two-photon ionization (R2PI) spectroscopy.

ScN

This section presents the experimental study of the ground, low- and high-lying excited electronic states in ScN molecule. The $^1\Sigma^+$ ground state symmetry, predicted theoretically [39,40] is confirmed in the present study. The *ab initio* calculation [40] predicted that the $^1\Sigma^+$ ground state correlates with the excited Sc atomic state asymptote $^4F(4s3d^2)$ and N ground $^4S(2p^3)$ state asymptote having mixed configuration with the major contribution from $1\sigma^2 1\pi^4 2\sigma^1 3\sigma^1$. Earlier experimental studies on the spectroscopic properties of ScN were limited, which include Fourier transform emission spectroscopy in the near-infrared region by Ram and Bernath [41] and the matrix isolation spectroscopy [42]. Ram and Bernath reported (0,0), (1,1), and (2,2) band of $A^1\Sigma^+ - X^1\Sigma^+$ transition in infrared

region. Their assignment of the ground state symmetry $^1\Sigma^+$ of ScN, was rather indirect and based on the comparison with the analogous transition in the isoelectronic CaO molecule [43] and the *ab initio* predictions [39]. Vibrational frequencies for both the states could not be determined due to lack of observation of off-diagonal bands in their study. In the present study, ground, low- and high-lying electronic states of jet-cooled ScN molecules have been studied. The excitation spectra of ScN molecules observed in the energy range 19,300–21,800 cm^{-1} , showed nine vibronic bands belonging to three new systems of the electronic transitions. Rotational analysis confirmed $^1\Sigma^+$ symmetry for the ground state and identified three excited electronic states *B*1, *C*1, and *D*1, respectively, at 20150.3(1), 20184.4(1) and 21774.6(1) cm^{-1} . The identity of the newly observed excited electronic states cannot be corroborated with existing *ab initio* results and demand more rigorous calculations taking in to account excited asymptotes, in particular $\text{Sc}(3d^1 4s^2 \ ^2D) + \text{N}(^2D)$. The low-energy first excited electronic state, $a^3\Sigma^+$ predicted by *ab initio* calculations [39,40], has been observed for the first time in wavelength resolved DF spectra from the newly observed state. The term energies of the vibrational levels of the ground $X^1\Sigma^+$, $a^3\Sigma^+$, and $A^1\Sigma^+$ states have been determined. The RKR potential energy curves of the $X^1\Sigma^+$ ground as well as $a^3\Sigma^+$, and $A^1\Sigma^+$ low-energy excited states have been constructed. Close resemblance between the electronic structure of ScN and its isovalent YN has been observed.

ScO

The ScO molecule has two known *A – X* and *B – X* band systems in the visible region. Spectroscopy of rotationally resolved *B – X* system of ScO was first carried out by Akerlind [44]. They assigned this transition as $^2\Sigma-^4\Sigma$ because of a group of four line structure. Later, Adams *et al.* [45] reanalyzed the (0,0) band at higher resolution and assigned it as $^2\Sigma-^2\Sigma$ transition. The wrong assignment of the ground state of ScO was due to the applicability of different angular momentum coupling scheme, which was not recognized

initially because of the presence of strong coupling of the nuclear spin with electron spin. The ground state electronic configuration of ScO is $8\sigma^2 3\pi^4 9\sigma^1$, where, 9σ orbital is $4s\sigma$ of Sc. This configuration results the ground state as $X^2\Sigma^+$. The ground state belongs to the unusual hyperfine coupling case $b_{\beta S}$, where the Fermi contact operator $b\mathbf{I}\cdot\mathbf{S}$, couples the electron spin \mathbf{S} with the nuclear spin \mathbf{I} . The only stable isotope, ^{45}Sc , has a nuclear spin $I=7/2$ and a very large magnetic moment such that the Fermi contact interaction for an unpaired electron in the 9σ ($4s\sigma$ of Sc) molecular orbital of the ground state $X^2\Sigma^+$ in ScO is large. The fine doubling of $4b \sim 0.25\text{cm}^{-1}$ observed in the spectrum was attributed to nuclear hyperfine structure. Due to the presence of fine doubling, there appear to be twice of the electron spin components in the excitation spectrum as there actually are, and therefore, the first rotational analyses [44] assigned the ground state of ScO as $^4\Sigma^+$. However, the excited electronic state $B^2\Sigma^+$ arises by promotion of 9σ electron to the 10σ ($3d\sigma$ of Sc), results in $8\sigma^2 3\pi^4 10\sigma^1$ configuration. The 10σ electron does not couple with the nuclear spin of the Sc. Thus, the excited state $B^2\Sigma^+$ follows the more usual coupling case $b_{\beta N}$, where the electron spin \mathbf{S} is more strongly coupled to rotation \mathbf{N} than to \mathbf{I} .

In the present study, LIF excitation spectroscopy on $B^2\Sigma^+ - X^2\Sigma^+$ system of ScO was extended to higher vibrational levels up to $v'=4$ of the $B^2\Sigma^+$ state and $v''=2$ of the $X^2\Sigma^+$ state. In addition, the vibrational progression up to $v''=8$ of the ground $X^2\Sigma^+$ state were observed from the DF wavenumbers from the excitation of various rovibronic levels of $B^2\Sigma^+$ state. Analyses of these excitation and DF spectra resulted in the determination of improved molecular constants at equilibrium for the B and X states. These data were used to construct the RKR potential energy curves and subsequently to determine the the Franck-Condon factors.

Chapter 5. Wavelength-resolved laser-induced fluorescence spectroscopy of jet-cooled Nickel Monocarbide (NiC) molecule

In this chapter, the first observation of lowest-lying excited electronic state $a^3\Pi_{0+}$ of NiC molecule is presented. The first spectroscopic observation of NiC in the gas phase has been reported by Brewster and Ziurys [46] in the millimetre region which provided the ground state ($X^1\Sigma^+$) rotational constants to high accuracy. Later, Brugh and Morse [47] studied the jet-cooled NiC molecule by resonant two-photon ionization (R2PI) in the optical region and observed numerous transitions originating from the ground $X^1\Sigma^+$ state to the excited electronic states, all having $\Omega=0^+$. In contrast to the experimental studies, NiC has been theoretically studied extensively; however, there has been uncertainty among theoretical investigations [48,49,50,51] over the energy ordering of the low-lying $a^3\Pi$ and $A^1\Pi$ excited electronic states. In order to resolve this ambiguity, the experimental study of low-energy states becomes important, as it can provide a validation of the level of theoretical calculations.

The DF spectra are investigated in the 400–925 nm wavelength range by exciting a single rotational level belonging to $^{58}\text{Ni}^{12}\text{C}$ isotopomer of the several $\Omega=0^+$ excited states observed by Brugh and Morse [47]. We have observed a vibrational progression up to $v=3$ terminating on a first excited electronic state at $T_e=5178(6)\text{ cm}^{-1}$ with $\omega_e=833(4)\text{ cm}^{-1}$. The doublet splitting observed under higher resolution (FWHM $\sim 5\text{ cm}^{-1}$) DF spectra for this new low-lying state confirmed $\Omega=0^+$ assignment and thus the first excited state is confirmed as $^3\Pi_{0+}$. In addition to this, a vibrational progression up to $v=10$ for the ground state $X^1\Sigma^+$ are observed. This data provided equilibrium vibrational constants for the ground and first excited electronic state of NiC, which are in good agreement with the theory.

In summary, this thesis is about the investigation of electronic structures of diatomic molecules in gas phase, involving an atom from transition metal and a main group element.

The inherent complex electronic spectra, associated with this class of molecules are simplified to the considerable extent by employing the experimental methodology adapted in this work. This is achieved by cooling these molecules of refractory nature, under the non-equilibrium low temperature conditions, by utilizing laser-vaporization supersonic expansion source. The spectroscopic informations obtained in this work lead to the understanding of electronic structure of these molecules in ground, low- and high-energy regions. The information of electronic structure is important in understanding the nature of the bond between transition metals and main group elements. This understanding is important from application point of view, like heterogeneous catalysis and also from fundamental point of view, like validating the adapted level/model of theoretical calculations and thus may provide guide line for benchmark calculation for these complex systems.

References:

-
- [1] M. Grunze, Synthesis and decomposition of ammonia, in: D.A. King, D.P. Woodruff (Eds.), *The Chemical Physics of Solid Surfaces and Heterogeneous Catalysis*, vol. **4**, Elsevier, New York, 1982, p. 143.
 - [2] A.J. Sauval, *Astron. Astrophys.* **62**,295 (1978).
 - [3] W. A. Brown, R. Kose and D. A. King, *J. Mol. Catal. A* **141**, 21 (1999).
 - [4] F.A. Cotton, G. Wilkinson, *Advanced Inorganic Chemistry, A Comprehensive Text*, fifth edn., Wiley, New York, 1988.
 - [5] J.F. Harrison, *Chem. Rev.* **100**, 679 (2000).
 - [6] T. G. Dietz, M. A. Duncan, D. E. Powers, and R. E. Smalley, *J. Chem. Phys.* **74**, 6511 (1981).
 - [7] V.V. Flambaum, D. DeMille, M.G. Kozlov, *Phys. Rev. Lett.* **113**, 103003 (2014).
 - [8] B.J. Barker, I.O. Antonov, V.E. Bondybey, M.C. Heaven, *J. Chem. Phys.* **144**, 201102 (2011).

-
- [9] J. Baron, W.C. Campbell, D. DeMille, J.M. Doyle, G. Gabrielse, Y.V. Gurevich, P.W. Hess, N.R. Hutzler, E. Kirilov, I. Kozyryev, B.R. O’Leary, C.D. Panda, M.F. Parsons, E.S. Petrik, B. Spaun, A.C. Vutha, A.D. West, *Science* **343**, 269 (2014).
- [10] A.E. Leanhardt, J.L. Bohn, H. Loh, P. Maletinsky, E.R. Meyer, L.C. Sinclair, R.P. Stutz, E.A. Cornell, *J. Mol. Spectrosc.* **270**, 1 (2016).
- [11] D.N. Gresh, K.C. Cossel, Y. Zhou, J. Ye, E.A. Cornell, *J. Mol. Spectrosc.* **319**, 1 (2016).
- [12] S. Mukund, S. Bhattacharyya, S.G. Nakhate, *Chem. Phys. Lett.* **655-656**, 51 (2016).
- [13] S.G. Nakhate, S. Mukund, S. Bhattacharyya, *Chem. Phys. Lett.* (2016) Communicated.
- [14] D.T. Halfen, J. Min, L.M. Ziurys, *J. Mol. Spectrosc.* **331**, 1 (2017).
- [15] G. Herzberg, *Molecular Spectra and Molecular Structure, I. Spectra of Diatomic Molecules*, 2nd Edition, D. Van Nostrand, New York, 1950.
- [16] H. Lefebvre-Brion, R.W. Field, *The spectra and Dynamics of Diatomic Molecules*, revised and enlarged edition, Elsevier Academic Press, New York, 2004. β
- [17] I. Kovacs, *Rotational Spectroscopy in the spectra of Diatomic Molecules* Elsevier Publishing, New York, 1969.
- [18] P. F. Bernath, *Spectra of Atoms and Molecules*, Oxford University Press, New York, 2nd edition, 2005.
- [19] James F. Harrison. *J. Phys. Chem.* **100**, 3513-3519 (1996).
- [20] R.S. Ram, J. Liévin, P.F. Bernath, *J. Mol. Spectrosc.* **215**, 275 (2002).
- [21] O. Krechkivska, M.D. Morse, *J. Phys. Chem. A* **117**, 13284 (2013).
- [22] W.J. Balfour, A.J. Merer, H. Niki, B. Simard, P.A. Hackett, *J. Chem. Phys.* **99**, 3288 (1993).
- [23] Y. Azuma, J.A. Barry, M.P.J. Lyne, A.J. Merer, J.O. Schröder, J.L. Féménias, *J. Chem. Phys.* **91**, 1 (1989).

-
- [24] Y. Azuma, G. Huang, M.P.J. Lyne, A.J. Merer, V.I. Srdanov, *J. Chem. Phys.* **100**, 4133 (1994).
- [25] T.M. Dunn and K.M. Rao, *Nature*. **222**, 266 (1969).
- [26] J.L. Féménias, C. Athenour, and T.M. Dunn, *J. Chem. Phys.* **63**, 2861 (1975).
- [27] E.A. Pazyuk, E.N. Moskvitina, and Yu.Ya. Kuzyakov, *Spectrosc. Lett.* **19**, 627 (1986).
- [28] J.L. Féménias, C. Athenour, K.M. Rao, and T.M. Dunn, *J. Mol. Spectrosc.* **130**, 269 (1988).
- [29] S.R. Langhoff and C.W. Bauschlicher Jr., *J.Mol. Spectrosc.* **143**, 169 (1990).
- [30] R.S. Ram and P.F. Bernath, *J. Mol. Spectrosc.* **201**, 267 (2000).
- [31] R.S. Ram and P.F. Bernath, *J. Mol. Spectrosc.* **243**, 62 (2007).
- [32] J.K. Bates, Optical Emission Spectra of Diatomic Metal Nitrides Ph.D. thesis, University of Michigan, (1975).
- [33] J.K. Bates, D.M. Gruen, *J. Chem. Phys.* **70**, 4428 (1979).
- [34] M. Zhou, L. Andrews, *J. Phys. Chem. A*. **102**, 9061 (1998).
- [35] A.B. Kunz, M.P. Guse, R.J. Blint, *J. Phys. B: At. Mol. Phys.* **8**, L358 (1975).
- [36] C.W. Bauschlicher Jr., S.P. Walch, *J. Chem. Phys.* **76**, 4560 (1982).
- [37] R.S. Ram, P.F. Bernath, *J. Chem. Phys.* **105**, 2668 (1996).
- [38] R.S. Ram, P.F. Bernath, *J. Mol. Spectrosc.* **183**, 263 (1997).
- [39] K.L. Kunze, J.F. Harrison, *J. Am. Chem. Soc.* **112**, 3812 (1990).
- [40] A. Daoudi, S. Elkhatabi, G. Berthier, J.P. Flament, *Chem. Phys.* **230**, 31 (1998).
- [41] R.S. Ram, P.F. Bernath, *J. Chem. Phys.* **96**, 6344 (1992).
- [42] G.V. Chertihin, L. Andrews, C.W. Bauschlicher, *J. Am. Chem. Soc.* **120**, 3205 (1998).
- [43] J.B. Norman, K.J. Cross, H.S. Schweda, M. Polak, R.W. Field, *Mol. Phys.* **66**, 235 (1989).
- [44] L. Akerlind, *Ark Fys.* **22**, 41 (1962).

-
- [45] A. Adams, W. Klemperer, T.M. Dunn, *Can J Phys.* **46**, 2213 (1968).
- [46] M.A. Brewster, L.M. Ziurys, *Astrophys.J.* **559**, L163 (2001).
- [47] D.J. Brugh, M.D. Morse, *J. Chem. Phys.* **117**, 10703 (2002).
- [48] I. Shim, K.A. Gingerich, *Z. Phys. D: At. Mol. Clusters.* **12**, 373 (1989).
- [49] I. Shim, K.A. Gingerich, *Chem. Phys. Lett.* **303**, 87 (1999).
- [50] A.C. Borin, L.G.M. de Macedo, *Chem. Phys. Lett.* **383**, 53 (2004).
- [51] D. Tzeli, A. Mavridis, *J. Chem. Phys.* **126**, 194304 (2007).

LIST OF TABLES

Table 1.1 Angular momenta in diatomic molecules	9
Table 3.1 Comparison among the ground state electronic configuration of group 5 transition metal monocarbides, mononitride and monoxides.	48
Table 3.2 Molecular constants (in cm^{-1}) and radiative lifetimes for the excited electronic states of NbN.....	60
Table 3.3 Rotational molecular constants for the deperturbed $\text{C}^3\Pi$ ($v = 1$) and $\text{e}^1\Pi$ ($v = 1$) states of NbN along with the interaction parameter. Values in cm^{-1} . T is the term energy, B , D , A and o are respectively rotational, rotational centrifugal distortion, spin-orbit and lambda doubling constants. $A^{(2)}$ and $A_D^{(2)}$ are respectively the second-order spin-orbit and its centrifugal distortion constants.....	62
Table 3.4 Vibrational term energies and equilibrium constants (in cm^{-1}) for the ground and low-lying states of NbN.....	76
Table 3.5 Basis set dependence for energy separation in $^3\Pi/{}^1\Pi$ states; all entries are in cm^{-1}	80
Table 3.6 Observed bands with their assignments, molecular constants (in cm^{-1}) and radiative lifetimes (in ns) of the excited electronic states of the TaN molecule.....	89
Table 3.7 Vibrational levels observed in the dispersed fluorescence spectra recorded by excitation of various relevant excited electronic states.....	93
Table 3.8 Vibrational term values T_v (in cm^{-1}) of the ground & low-lying electronic states of TaN molecule.....	94
Table 3.9 Equilibrium molecular constants (in cm^{-1}) for the ground and low-lying $a^3\Delta$ and $A^1\Delta$ states of TaN molecule and their comparison with the <i>ab initio</i> values.....	95
Table 3.10 The high-lying excited electronic states of TaN observed in the present and earlier work with their term energy, molecular constants (cm^{-1}) and radiative life-times (ns). The lower state from which the state is observed is also listed.	99

Table 4.1 Molecular constants (cm^{-1}) for the $g^3\Phi_2 - a^3\Delta_1$ system and radiative lifetimes (ns) of ScH.	115
Table 4.2 Band origins, vibronic assignments and excited state radiative lifetimes of ScN molecule.	123
Table 4.3 Molecular constants (in cm^{-1}) of the $X^1\Sigma^+$ ground state and $B1$, $C1$, $D1$ excited states.	124
Table 4.4 Term values (cm^{-1}) of the vibrational levels of the $X^1\Sigma^+$, $a^3\Sigma^+$, and $A^1\Sigma^+$ states of ScN.	129
Table 4.5 Spectroscopic constants of the $X^1\Sigma^+$, $a^3\Sigma^+$, and $A^1\Sigma^+$ states of ScN.	133
Table 4.6 Molecular constants (in cm^{-1}) for the $X^2\Sigma^+$ and $B^2\Sigma^+$ states of ScO. The T_v values are accurate to 0.1 cm^{-1}	145
Table 4.7 $\Delta G_{v+1/2}$ values and vibrational term values T_v for the ground $X^2\Sigma^+$ state. Experimental error in $\Delta G_{v+1/2}$ is $\sim 4 \text{ cm}^{-1}$	147
Table 4.8 Equilibrium molecular constants for the $X^2\Sigma^+$ and $B^2\Sigma^+$ states of ScO.	147
Table 4.9 The classical turning points (in Å) and corresponding calculated term values (in cm^{-1}) of RKR potential energy curves of the $X^2\Sigma^+$ and $B^2\Sigma^+$ states of ScO.	148
Table 4.10 Franck-Condon factors for the $B^2\Sigma^+ - X^2\Sigma^+$ transition of ScO.	149
Table 5.1 Term values (in cm^{-1}) of the vibrational levels of the $X^1\Sigma^+$ and $\Omega = 0^+$ states of $^{58}\text{Ni}^{12}\text{C}$	159
Table 5.2 Spectroscopic constants of the experimentally observed $X^1\Sigma^+$ and $\Omega = 0^+$ states of $^{58}\text{Ni}^{12}\text{C}$ and their comparison with <i>ab initio</i> values.	162
Table 5.3 Comparison of symmetry, term energy and vibrational frequency (in cm^{-1}) of the ground and first low-lying state of group 10 transition-metal-containing monocarbides	165

LIST OF FIGURES

Figure 1.1 Vector diagram for Hund's Case (a).....	12
Figure 1.2 Vector diagram for Hund's Case (b).....	15
Figure 1.3 Vector diagram for Hund's Case (c).....	16
Figure 1.4 Vector diagram for Hund's Case (d).....	17
Figure 1.5 Vector diagram for Hund's Case (e).....	18
Figure 2.1 Schematic of supersonic molecular beam apparatus	30
Figure 2.2 Schematic of homemade gas pulsed valve and laser vaporization source	32
Figure 2.3 A typical voltage pulse given to the PZT	32
Figure 2.4 Schematic of ion extraction optics of TOFMS	36
Figure 2.5 Schematic of the gas-manifold system	37
Figure 2.6 Trigger signal from a digital delay generator to various equipments.....	39
Figure 2.7 Block diagram of control electronics and various equipments of the supersonic molecular beam setup.	40
Figure 2.8 Diagram of electronic transition in a diatomic molecule. For recording of excitation spectrum, monochromator is set at the fixed wavelength corresponding to the strongest fluorescence and the dye laser frequency is scanned, while in DF study, excitation frequency is fixed and the monochromator is used in scanning mode to probe the ground and low-lying vibronic states.....	42
Figure 2.9 Reaction products of scandium metal plasma and ammonia in the molecular beam.....	45
Figure 3.1 Change in the atomic orbital energy due to relativistic effects in the group 5 transition metals.	48
Figure 3.2 A schematic of the electronic states and observed transitions of NbN, reported prior to the present work.	54

- Figure 3.3** Laser-induced excitation survey spectrum of jet-cooled NbN molecule is shown in two parts. The band marked by ‘†’ is reported in reference [23] and the bands marked by ‘*’ are reported in reference [39]. Many atomic niobium (Nb I) lines are also appeared in the spectrum.....55
- Figure 3.4** The experimental and simulated spectrum of the $(1-0)$ $C^3\Pi_1 - X^3\Delta_2$ subband.62
- Figure 3.5** Rotational structure of the $^3\Pi_{0^\pm} - X^3\Delta_1$ ($\nu',0$) band of the jet-cooled NbN molecule.....65
- Figure 3.6** A compressed portion of the spectrum showing 0–0 bands of the two subbands of $^3\Pi - X^3\Delta$ transition and 0–0 of $^3\Pi_{0^\pm} - X^3\Delta_1$ subband at 19750 cm^{-1} reported in reference [39].69
- Figure 3.7** Schematic energy level diagram of the presently known observed electronic states of NbN in the energy region relevant to excitation study of this work. The dashed dotted lines ($-\cdot-\cdot-$) represent the states observed by Azuma *et al.* [23] and the states observed by Ram and Bernath [38] are marked by dashed lines ($- - -$). The solid lines ($—$) are the states from this work.....73
- Figure 3.8** The DF spectrum obtained by exciting the isolated $P_{ff}(3)$ line of the $^3\Pi_{0^\pm} - X^3\Delta_1$ (0,0) band.75
- Figure 3.9** The DF spectrum obtained by exciting the isolated $Q(6)$ line of the $\Omega=1 - X^3\Delta_2$ (0,1) band.75
- Figure 3.10** Comparison of experimental and theoretical study of the spin-orbit interaction between (a) the ground $X^3\Delta$ and $a^1\Delta$ states and (b) the $C^3\Pi$ and $e^1\Pi$ states of NbN at $\nu = 1$ vibrational level. Horizontal dashed lines ($- - -$) are expected unperturbed positions and solid lines ($—$) are experimentally observed/calculated positions of the states. Experimental values in Figure 3.10(a) are taken from Ref. [22].79

Figure 3.11 Laser-induced excitation survey spectrum of jet-cooled TaN is shown in two parts. Many atomic tantalum (Ta I) lines and TaO bands are also appeared in the spectrum. 86

Figure 3.12 The observed jet-cooled and simulated spectrum of the $[23.58]1 - X^1\Sigma^+$ band of TaN.88

Figure 3.13 Rotational structure of the (0,0) band of the $\Omega = 0^+ - X^1\Sigma^+$ transition of TaN. The line marked as * is the additional peak and perturbed region is shown inside box.88

Figure 3.14 (a) Reduced term value plot for the $[26.35]0^+$ state of TaN. Square and circle symbols respectively represent rotational levels of $[26.35]0^+$ and perturber states. (b) The J -dependent radiative lifetime of $[26.35]0^+$ and a perturber state.....90

Figure 3.15 The dispersed fluorescence spectra of TaN following excitation of the $Q(8)$ line of the $\Omega' = 1 - X^1\Sigma^+$ (0,0) band at 19217 cm^{-1} ; the x-axis shows the displacement in cm^{-1} from the excitation line. The inset shows the DF spectra at high-resolution where the R -, Q - and P -lines are well resolved.92

Figure 3.16 The dispersed fluorescence spectra of TaN, observed from the $J = 4$ level of the $\Omega = 1$ state at 23582 cm^{-1} . The observed vibrational progressions for the $X^1\Sigma^+$, $\Omega = 1-2$ spin components of the $a^3\Delta$ and the $A^1\Delta$ state are shown. The peak marked with '*' is the laser excitation line in second order of the grating.....93

Figure 4.1 Rotational structure of the $g^3\Phi_2 - a^3\Delta_1$ band of jet-cooled ScH molecule. The PQR and $P'Q'R'$ represent (0,0) and (1,1) ScH bands respectively.....112

Figure 4.2 Laser-induced excitation survey spectrum of jet-cooled ScN molecule.120

Figure 4.3 Rotational structure of the (0,0) $D1 - X^1\Sigma^+$ excitation band of jet-cooled ScN molecule.....121

Figure 4.4 Laser-induced dispersed fluorescence spectra of ScN observed from $\nu = 0$ level of $B1$, $C1$, and $D1$ states; the x-axis shows the displacement in cm^{-1} from the excitation line. 128

- Figure 4.5** High-resolution dispersed fluorescence patterns from e - and f - symmetry levels of an $\Omega = 1$ state to (a) $^1\Sigma^+$ and (b) $a^3\Sigma^+$ state. The relevant energy levels of the upper and the lower states involved in the transitions are also shown. 130
- Figure 4.6** RKR potential energy curves for the $X^1\Sigma^+$, $a^3\Sigma^+$, and $A^1\Sigma^+$ states of ScN. Observed vibrational levels are shown by solid lines. 134
- Figure 4.7** Vector diagram of (a) Case ($b_{\beta S}$) and (b) Case ($b_{\beta J}$) coupling scheme for the Σ states. 140
- Figure 4.8** Rotational structure in the (4,0) $B^2\Sigma^+ - X^2\Sigma^+$ excitation band of jet-cooled ScO molecule. 142
- Figure 4.9** Energy level diagram of the $X^2\Sigma^+ - X^2\Sigma^+$ transition of ScO 143
- Figure 4.10** Dispersed fluorescence (DF) spectra of ScO observed from $\nu' = 2$, $N' = 10$ of $B^2\Sigma^+$ state; the x-axis shows the displacement (in cm^{-1}) from the excitation line. The inset shows the DF spectra at high-resolution where the $P(11)$ and $R(9)$ lines are well resolved. 146
- Figure 4.11** RKR potential energy curves for the $X^2\Sigma^+$ and $B^2\Sigma^+$ states of ScO. 149
- Figure 5.1** Dispersed fluorescence (DF) spectrum of $^{58}\text{Ni}^{12}\text{C}$ observed from $\nu' = 0$, $J' = 7$ of [24.6] $\Omega=0^+$ state; the x-axis shows the displacement in cm^{-1} from the excitation line. The inset shows the DF spectra at high-resolution where the $P(8)$ and $R(6)$ lines are well resolved. 158
- Figure 5.2** RKR potential energy curves for the $X^1\Sigma^+$, and $a^3\Pi_{0+}$ states of $^{58}\text{Ni}^{12}\text{C}$. Observed vibrational levels are shown by solid lines. 161

Chapter 1

Introduction: Theoretical Background

1.1 Introduction

The understanding of simple diatomic molecular system is an important step towards insight for a higher and more complex level of the structure of matter. Instead of simply adding atomic properties, molecules composed of atoms have many internal degrees of freedom to carry out their motion and store discrete amount of energy. The orbital motion of electrons gives rise the electronic states in the molecular system. Nuclei carry out vibrations along the line joining the nuclei and have discrete vibrational energy in each electronic state. Further each vibrational level has a set of discrete rotational energy levels resulting from the rotation of the molecule. The detailed treatment for the diatomic molecular structure can be found in various standard reference books [1,2,3,4,5,6].

A wide range of methods are applied in different spectral range to gather detailed information about the electronic structure of molecules. However, study of electronic structure transition-metal-containing molecules presents additional challenges on both theoretical as well as experimental side. Due to the presence of partially filled *d*-shell in the transition metals, electronic structure of these molecules are complex and difficult to treat theoretically than the molecules containing main group elements [7]. The theoretical calculations necessitate including the large correlation energy of electrons and relativistic corrections, for even qualitatively correct results. A quite small change in the model can lead to very different predictions for the energy order and properties of the low-lying electronic states. For this reason, experimental results of these systems are of great importance as they provide a critical test of adequacy of selected methods and level of the theoretical treatment.

In past, production as well as spectroscopic study of transition-metal-containing molecules was very difficult due to their highly refractory nature. These molecules were

formed in gaseous phase using high temperature sources. Under such condition, their spectra are often complex, congested and difficult to interpret, due to their thermal distribution in electronic and vibrationally excited states and enough population in high J rotational levels. Lowest rotational levels, which carry information about the symmetries of the states are insufficiently populated and invariably absent from the spectra. For example, the electronic structure of one of the simplest transition-metal monohydride, YH molecule was investigated by Simard's group and resolved the ambiguity in the ground state symmetry using jet-cooled laser spectroscopy in their preliminary report [8] and subsequent detailed studies [9,10]. Prior to their study, the first experimental study in the hollow cathode emission source [11] assumed the ground state of YH to be a $^3\Delta$ state based on the observation of a number of systems within singlet and triplet manifold, and absence of observation of singlet-triplet intercombination transition. Their assumption was based on the analogy with the spectra of isovalent ScH [12] and LaH [13] molecules, for which the $^3\Delta$ state was believed to be the ground state based on similar experimental observations and a rudimentary theoretical calculation [14] on ScH which did not account for electron correlation effects, important in d -block elements. However, later this assignment was questioned by advanced theoretical treatments [15,16], which indicated that the YH ground state is $^1\Sigma^+$. Simard's group [9,11] have observed several transitions originating from a $^1\Sigma^+$ but none from a $^3\Delta$ lower state in the jet-cooled spectra. Further, the ground states of ScH [17] and LaH [18] was also revised by Ram and Bernath to be $^1\Sigma^+$.

In addition, the presence of open d -shells in the transition metals, which is responsible for its catalytic behavior, gives rise to states with high-spin and large orbital angular momenta, which are split by substantial spin-orbit interactions in these molecular systems. Due to the presence of a large number of low- and high-lying excited electronic states, which are derived from several close lying configurations, the excitation spectra of these molecules

are usually complex. Strong spin-orbit interactions especially in the excited states limit the validity of the usual Hund's case (*a*) (see Section 1.2.4.a) coupling in these molecules. Also, under the Hund's case (*a*) coupling scheme, the subbands of a given electronic transition can be far apart and often lead to the misinterpretation of the spectroscopic data. The widespread hyperfine structure due to odd atomic mass number nuclei with large nuclear spin and magnetic moments add another dimension of complexity. The extensive perturbations make the understanding of the spectra further difficult. This problem has held back progress with the spectra of transition metal bearing molecules in the past.

Advances in the experimental techniques for production of such high temperature molecules at non-equilibrium low temperature with their vibrational and rotational degrees of freedom frozen mostly in their ground state, brought success to this field. The technique of laser vaporization in conjunction with supersonic free-jet expansion (see Chapter 2), simplified the spectra to a great extent and received a strong boost in the systematic experimental study of transition-metal-containing molecules.

This thesis presents experimental study of the electronic structure of transition-metal-containing diatomic molecules produced in the free-jet by laser vaporization technique and probed by laser-induced fluorescence (LIF) and two-photon resonance ionization mass spectroscopy. This thesis is organized in five chapters. The present Chapter describes the basic theoretical background of diatomic molecules, necessary to analyze and interpret the molecular spectra presented in the Chapters 3-5. The Chapter 2 discusses the experimental set up and techniques to record the jet-cooled molecular spectra. Electronic structure of group 5, *d*-block transition metal mononitrides, NbN and TaN molecules are presented in the Chapter 3. Laser spectroscopic investigation of Scandium containing diatomic ScH, ScN, and ScO molecules are presented in the Chapter 4. The Chapter 5 discusses electronic structure of the ground and low-lying states of NiC molecule.

1.2 Diatomic Molecular Hamiltonian

The time independent Schrödinger equation of a diatomic molecule is written as

$$\mathbf{H}\Psi = [\mathbf{T}_N + \mathbf{T}_e + \mathbf{V}_N + \mathbf{V}_{eN} + \mathbf{V}_e]\Psi = E\Psi \quad (1.1)$$

where, \mathbf{H} is the Hamiltonian and Ψ is the eigenfunction excluding contributions of the

electron and nuclear spin. $\mathbf{T}_N = \frac{-\hbar^2}{2} \sum_{i=1}^2 \frac{\nabla_{Ni}^2}{M_i}$ and $\mathbf{T}_e = \frac{-\hbar^2}{2m_e} \sum_i \nabla_{ei}^2$ are the kinetic energy

operators for the nuclei and electrons respectively. M and m_e are the mass of the nucleus and

electrons respectively in the above expression. Further, $\mathbf{V}_N = \frac{Z_1 Z_2 e^2}{4\pi\epsilon_0 r_{AB}}$, $\mathbf{V}_{eN} = -\sum_i \frac{Z_1 e^2}{4\pi\epsilon_0 r_{Ai}} -$

$\sum_i \frac{Z_2 e^2}{4\pi\epsilon_0 r_{Bi}}$ and $\mathbf{V}_e = \sum_i \sum_{j>i} \frac{e^2}{4\pi\epsilon_0 r_{ij}}$ are the self-explanatory expression for the nuclear-nuclear

repulsion, electron-nuclear attraction and electron-electron repulsion potential energies

respectively. r_{AB} represents the separation of the nuclei A and B, and r_{Ai} and r_{Bi} represents the

coordinate of the electrons from these nuclei. E represents the quantized energy levels or

eigenvalues of the molecular system. Born-Oppenheimer approximation is introduced to

solve the Schrödinger equation (1.1), because it cannot be solved analytically. Under this

approximation, the coupling between the nuclear and electronic motions is ignored.

1.2.1 Born-Oppenheimer Approximation

Due to smallness of the mass of electrons compared to that of the nuclei, they move

much more rapidly than the nuclei within the molecule. Thus, the electronic energy, when

the nuclei are no longer fixed, takes up the value corresponding to the momentary positions

of the nuclei, and so, the electronic and nuclear motion can be treated independently. In other

words, the Schrödinger equation (1.1) can be solved for the fixed positions of the nuclei (r_α).

This was first proposed by Born and Oppenheimer [19]. Now, the total eigenfunction Ψ can

be written as product of electronic $\Psi_{el}(r_i, r_\alpha)$ and nuclear $\chi(r_\alpha)$ eigenfunctions as,

$$\Psi(r_i, r_\alpha) \approx \Psi_{el}(r_i, r_\alpha) \chi(r_\alpha) \quad (1.2)$$

where, r_i denotes the coordinates of the electrons. For the fixed position of the nuclei (r_α) the electronic part of the Schrödinger equation is given by,

$$\mathbf{H}_{\text{el}}\Psi_{\text{el}}(r_i, r_\alpha) = [\mathbf{T}_e + \mathbf{V}_{eN} + \mathbf{V}_e] \Psi_{\text{el}}(r_i, r_\alpha) = E_{\text{el}}(r_\alpha)\Psi_{\text{el}}(r_i, r_\alpha) \quad (1.3)$$

This equation can be solved parametrically for a given fixed geometry of the nuclei (r_α), as there is no general analytic function for it. The total electronic energy $E_{\text{el}}(r_\alpha)$, together with Coulomb potential energy of the nuclei $\mathbf{V}_N(r_\alpha)$ acts as the total potential energy $\mathbf{U}(r_\alpha)$ under whose influence the nuclei carry out their motion, i.e.,

$$\mathbf{U}(r_\alpha) = E_{\text{el}}(r_\alpha) + \mathbf{V}_N(r_\alpha) \quad (1.4)$$

Hence the nuclear part of the Schrödinger equation can be written as,

$$\mathbf{H}_N\chi(r_\alpha) = [\mathbf{T}_N + \mathbf{U}(r_\alpha)] \chi(r_\alpha) = E\chi(r_\alpha) \quad (1.5)$$

If the expression (1.2) is substituted into the original Schrödinger equation (1.1) and account is taken of the equations (1.3) and (1.5), it is readily seen that (1.1) is satisfied only if the term

$$\sum_i \frac{1}{2M_i} (2\nabla_N \Psi_{\text{el}} \nabla_N \chi + \chi \nabla_N^2 \Psi_{\text{el}}) \approx 0 \quad (1.6)$$

that is, the variation of Ψ_{el} with the internuclear distance is sufficiently slow so that its first and second order derivatives can be neglected, which is the mathematical representation of the Born-Oppenheimer approximation.

1.2.2 Nuclear Part of Hamiltonian

Nuclear part of the Schrödinger equation (1.5), can be further solved for vibration and rotation of the nuclei and their eigenfunction for rotating oscillator in a first approximation is given by,

$$\chi_N = \frac{1}{r} \psi_v(r - r_e) \psi_r(\vartheta, \varphi) \quad (1.7)$$

where, $\psi_v(r - r_e)$ and $\psi_r(\vartheta, \varphi)$ are the vibrational and rotational eigenfunctions.

1.2.2.a Vibrational Structure

Schrödinger equation (1.5) with (1.7) can be solved for ψ_v for the vibration of the nuclei. The form of potential $U(r_\alpha)$ under which the nuclei carry out their vibration, is first introduced by Dunham [20], and is given by a Taylor series expansion about the equilibrium internuclear distance (r_e), at which the potential $U(r)$ has minimum,

$$U(r) = \frac{1}{2!}k_2(r - r_e)^2 + \frac{1}{3!}k_3(r - r_e)^3 + \frac{1}{4!}k_4(r - r_e)^4 + \dots \quad (1.8)$$

where, $k_i = \frac{\partial^i U(r)}{\partial r^i} |_{r=r_e}$. The term $k_1 = \frac{\partial U(r)}{\partial r} |_{r=r_e}$ is zero in the above expression. The first term in the expression (1.8) is the potential energy function of the non-rotating harmonic oscillator, whose quantized energy values is given by solving Schrödinger equation,

$$E(v) = hcG(v) = hc\omega_e \left(v + \frac{1}{2} \right) \quad (1.9)$$

where,

$$\omega_e = \frac{1}{c} \sqrt{\frac{k_2}{\mu}} \quad (1.10)$$

Further, eigenfunction for harmonic oscillator is given by

$$\psi_v(x) = N_v \exp\left(-\frac{1}{2}\alpha x^2\right) H_v(\sqrt{\alpha}x) \quad (1.11)$$

where, $x = \sqrt{\mu}(r - r_e)$ is the mass-weighted change in bond length from its equilibrium value and $\alpha = \frac{c\omega_e}{\hbar}$. Normalization factor is given by $N_v = \left(\frac{\alpha}{\pi}\right)^{1/4} / \sqrt{2^v v!}$. $H_v(\sqrt{\alpha}x)$ is the v degree Hermite polynomial. However, for actual molecule, the potential energy curve of a diatomic molecule is always anharmonic and represented by non-vanishing higher order terms in equation (1.8). Perturbation calculation, using harmonic oscillator as a zero order approximation must be carried out with

$$W = \frac{1}{3!}k_3(r - r_e)^3 + \frac{1}{4!}k_4(r - r_e)^4 + \dots \text{ as the perturbation function.}$$

The term value of the anharmonic oscillator is given by,

$$G(v) = \omega_e \left(v + \frac{1}{2}\right) - \omega_e x_e \left(v + \frac{1}{2}\right)^2 + \omega_e y_e \left(v + \frac{1}{2}\right)^3 + \dots \quad (1.12)$$

where, $\omega_e x_e$, $\omega_e y_e, \dots$ are the anharmonic constants and are generally much smaller than ω_e .

To represent a potential energy function $U(r)$, even for a large value of r Morse proposed the following expression [21]:

$$U(r) = D_e (1 - e^{-\beta(r-r_e)})^2 \quad (1.13)$$

where, D_e is the dissociation energy from the potential minimum and β is a constant.

Analytical solution using Morse potential results in the following expression for non-rotating molecule,

$$G(v) = \omega_e \left(v + \frac{1}{2}\right) - \omega_e x_e \left(v + \frac{1}{2}\right)^2 \quad (1.14)$$

1.2.2.b Rotational Structure

On substitution of (1.7) into Schrödinger equation (1.5), since there is no potential energy associated to the rotation of the nuclei, it can be shown that the quantized energy of the rotational levels under the rigid rotator approximation as,

$$E(J) = hcF(J) = hcBJ(J+1), J = 0, 1, 2, \dots \quad (1.15)$$

where, $B = \frac{h}{4\pi c\mu r^2}$ is called the rotational constant. Here, h , c , μ and r are the Planck's constant, speed of light, reduced mass of the nuclei and internuclear distance of the rigid rotator respectively.

Expression of μ in terms of nuclear mass is given by,

$$\mu = \frac{M_A M_B}{M_A + M_B} \quad (1.16)$$

Since, the rotation of the nuclei cannot be rigid as it can carry out vibrations in the direction of the line joining to the two nuclei. In this case, as a result of the action of the centrifugal force, the internuclear distance increases with increasing rotation. Hence, the rotational term in the expression (1.15) can be extended, to a very good approximation, for a nonrigid rotator model as,

$$F(J) = BJ(J+1) - D[J(J+1)]^2 + H[J(J+1)]^3 + L[J(J+1)]^4 + \dots \quad (1.17)$$

where, D is called the centrifugal distortion constant and H, L, \dots are the higher order corrections. The centrifugal distortion constant D depends on the vibrational frequency ω , and under the harmonic oscillator model, this dependency is given by,

$$D = \frac{4B^3}{\omega^2} \quad (1.18)$$

Now we have to consider the situation of simultaneous rotation and vibration of the molecule. Under rotating oscillator model, since the period of vibration is very small compared to the period of rotation, the mean rotational constant is given as,

$$B_v = \frac{\hbar}{4\pi c \mu} \left[\overline{\frac{1}{r^2}} \right] \quad (1.19)$$

where $\left[\overline{\frac{1}{r^2}} \right]$ is the mean value of $\frac{1}{r^2}$ and to a good approximation, B_v in the v^{th} vibrational state is given by,

$$B_v = B_e - \alpha_e \left(v + \frac{1}{2} \right) + \dots \quad (1.20)$$

where, $B_e = \frac{\hbar}{4\pi c \mu r_e^2}$. For theoretical value of α_e , if calculated using Morse function (1.13), Pekeris [22] has shown,

$$\alpha_e = \frac{6 \sqrt{\omega_e x_e B_e^3}}{\omega_e} - \frac{6B_e^2}{\omega_e} \quad (1.21)$$

Similar expression for centrifugal distortion constant D_v is given by,

$$D_v = D_e + \beta_e \left(v + \frac{1}{2} \right) + \dots \quad (1.22)$$

Thus, the term value of a rotating oscillator is given by,

$$\begin{aligned} T = G(v) + F_v(J) = & \omega_e \left(v + \frac{1}{2} \right) - \omega_e x_e \left(v + \frac{1}{2} \right)^2 + \dots \\ & + B_v J(J+1) - D_v [J(J+1)]^2 + \dots \end{aligned} \quad (1.23)$$

1.2.3 Electronic Structure

Electronic structure of diatomic molecules can be derived by considering different angular momenta and their interaction within the molecule. The electronic orbital momentum L , the resultant electron spin S together with nuclear rotation R form total angular momentum J excluding the nuclear spin and is given by,

$$\mathbf{J} = \mathbf{R} + \mathbf{L} + \mathbf{S} \quad (1.24)$$

The different angular momenta and their projections on the internuclear axis are given in Table 1.1 [5].

Table 1.1 Angular momenta in diatomic molecules

Angular Momentum	Projection on molecular axis (units of \hbar)
J	$\Omega = \Lambda + \Sigma$
L	Λ
S	Σ
R	—
$N = R + L$	Λ

1.2.3.a Orbital Angular Momentum

There is only axial symmetry about the internuclear axis in a diatomic molecule due to strong electric field of the nuclei. A precession of total electronic orbital momentum L takes place about the field direction and its constant component M_L with magnitude $M_L\hbar$, can take the values,

$$M_L = L, L - 1, \dots, -L \quad (1.25)$$

Further we define,

$$\Lambda = |M_L| = 0, 1, 2, \dots, L \quad (1.26)$$

Thus, for a given value of L , there are $L + 1$ distinct state with different energy. Molecular state is designated by a $\Sigma, \Pi, \Delta, \Phi, \dots$ for the corresponding values of $\Lambda = 0, 1, 2, 3, \dots$. The Π, Δ, Φ, \dots states are doubly degenerate due to $M_L = \pm\Lambda$. The Λ can be written as the sum of individual orbital angular momenta λ_i of electrons in the molecule,

$$\Lambda = \sum \lambda_i \quad (1.27)$$

1.2.3.b Fine-Structure

The contribution of electron spin arise from its intrinsic angular momentum and resultant electron spin is given as sum of the individual spins,

$$S = \sum s_i \quad (1.28)$$

Due to orbital motion of the electrons, if internal magnetic field in the direction of internuclear axis is present, a precession of S takes place about the field direction with a constant magnitude $M_S \hbar$. M_S is denoted by Σ (not to be confused with a Σ molecular state as defined in the previous section) and it can take values,

$$\Sigma = S, S - 1, \dots, -S \quad (1.29)$$

Thus, for a given value of S , there are $2S + 1$ different values are possible. Effects of non-zero electronic spin results in various interactions in the molecule and are discussed in the following section.

1.2.3.b(i) Spin-Orbit Interaction

Spin-orbit interaction Hamiltonian is given by,

$$H_{So} = \sum_i a_i \mathbf{l}_i \cdot \mathbf{s}_i = \sum_i a_i \left[l_{iz} s_{iz} + \frac{1}{2} (l_i^+ s_i^- + l_i^- s_i^+) \right] \quad (1.30)$$

where a is an operator that acts only on the radial part of the wave function. Macroscopic form of equation (1.30) is approximately given by,

$$H_{So} = AL \cdot S \quad (1.31)$$

where, A is the macroscopic spin-orbit coupling constant and $\mathbf{L} = \sum \mathbf{L}_i$, $\mathbf{S} = \sum \mathbf{S}_i$. Isolated, unperturbed multiplet electronic structure is well described by equation (1.31), however, equation (1.30) can be used to model interactions between electronic states with different S or A . To describe the second-order spin orbit interaction for the states with $\Delta A = \Delta \Sigma = 0$ but $\Delta S = 1$ in NbN molecule, the expression (1.30) is used in the present thesis.

1.2.3.b(ii) Spin-Rotation Interaction

The spin-rotation interaction is given as,

$$H_{SR} = \sum_i b_i \mathbf{R} \cdot \mathbf{s}_i \quad (1.32)$$

Macroscopic form of the equation (1.32) is,

$$H_{SR} = \gamma \mathbf{R} \cdot \mathbf{S} \quad (1.33)$$

where, γ is coupling constant for spin and rotation, and \mathbf{S} is given in equation (1.28). This direct spin-rotation constant, say γ^{SR} is often dominated by a larger indirect spin-rotation coupling that arises from off-diagonal matrix element of the spin-orbit Hamiltonian H_{SO} , say γ^{SO} . Thus, experimentally determined γ is the inseparable sum of γ^{SR} and γ^{SO} , and is given by,

$$\gamma = \gamma^{SR} + \gamma^{SO} \quad (1.34)$$

1.2.3.b(iii) Spin-Spin Interaction

Macroscopic form spin-spin interaction is given by,

$$H_{SS} = \frac{2}{3} \lambda (3S_z^2 - \mathbf{S}^2) \quad (1.35)$$

where, λ is spin-spin interaction parameter. This interaction comes from the interaction of spin magnetic moment of each electron with the magnetic field produced by the remaining electron spin. Similar to equation (1.34) for γ , on taking account of off-diagonal matrix element of the spin-orbit Hamiltonian, there is indirect contribution of spin-spin interaction constant λ arise and experimentally determined λ is the sum of λ^{SS} and λ^{SO} , and is given by,

$$\lambda = \lambda^{SS} + \lambda^{SO} \quad (1.36)$$

1.2.4 Coupling of Rotation and Electronic Motion: Hund'S Coupling Cases

In this section, influence of rotational and electronic motions on each other is considered. The electronic angular momenta (orbital and spin) as discussed in the Section 1.2.3, together with angular momentum of the nuclear rotation N from a resultant which is always designated by J (disregarding the nuclear spin). Different modes of coupling of the angular momenta are first given by Hund [23]. Only Hund's case (a), (b), (c) and extended case ($b_{\beta S}$) are observed in the present thesis, however, all the cases are discussed in the following subsections for completeness.

1.2.4.a Hund's Case (a)

This coupling scheme is illustrated in Figure 1.1. In this case, it is assumed that the coupling between the nuclear rotation with the electronic motion (electronic orbital angular momentum L as well as spin S) is very weak. However, the coupling of the electronic motion to the internuclear axis is very strong [1].

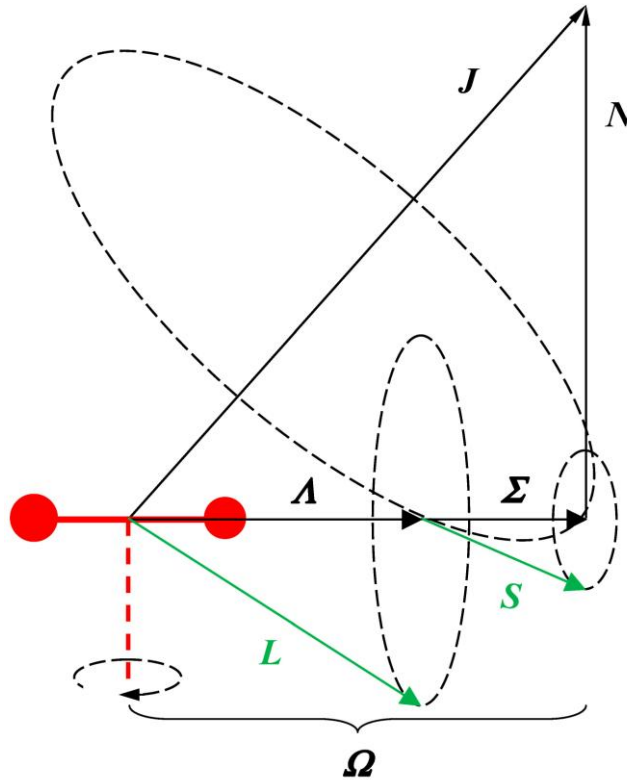


Figure 1.1 Vector diagram for Hund's Case (a)

Due to axial symmetry of the diatomic molecule, component of the orbital angular momentum L of the electrons about the internuclear axis is a constant of motion and is defined by A as described in Section 1.2.3.a. For, $A = 0$, the resultant spin S , since it is unaffected by an electric field is fixed in space as long as molecule does not rotate and if there is no magnetic field. However, if $A \neq 0$, there is an internal magnetic field in the direction of the internuclear axis resulting from the orbital motions of the electrons. This causes a constant component Σ of S along the internuclear axis. Thus, for the non-rotating molecule the resultant electronic angular momentum about the internuclear axis we have,

$$\Omega = A + \Sigma \quad (1.37)$$

where, $A = 0, 1, 2, 3, \dots$ and $\Sigma = -S, -S+1, \dots, S-1, S$.

The molecular term symbol is designated as $^{2S+1}\Lambda_{\Omega}$. An electronic term with $A \neq 0$ splits into a multiplet of $2S+1$ component, where the quantity $2S+1$ is called the multiplicity of a molecular state. The electronic energy of a multiplet term T_e is given by to a first approximation,

$$T_e = T_0 + AA\Sigma \quad (1.38)$$

where, T_0 is the term value when the spin is neglected and A is a constant for a given multiplet term. Also, Π, Δ, Φ, \dots states (i.e. $A \neq 0$) are doubly degenerate as component of the orbital angular momentum L about the internuclear axis can take two values $+A$ and $-A$. Σ states (not to be confused with Σ quantum number) are non-degenerate and a superscript $+$ or $-$ sign in the term symbol ($^{2S+1}\Sigma^{+/-}$) is added corresponding to whether electronic part of the wave function is remains unchanged or changes sign upon reflection in any plane through the line joining the nuclei. Also for Σ states, Hund's case (a) coupling is rare, since there is no contribution by the diagonal spin-orbit term to the energy levels [5]. Although $A = 0$ for Σ states, in case of $A = 0$ formed by $\lambda_i \neq 0$; second order off-diagonal spin-orbit coupling can

split a $^{2S+1}\Sigma$ state into $S+1$ spin components [5] and is referred as Hund's coupling case (a') [24].

The angular momentum $\mathbf{\Omega}$, which is well defined even in the rotating molecule, together with the nuclear rotation \mathbf{N} forms the resultant \mathbf{J} excluding the nuclear spin,

$$\mathbf{J} = \mathbf{\Omega} + \mathbf{N} \quad (1.39)$$

Each \mathbf{J} is doubly degenerate (for $\Lambda > 0$), corresponding to e and f parities (section 1.3). However, this degeneracy is lifted with increasing rotation and is called Λ -doubling. The rotational energy in this case is given by,

$$F_v(J) = B_{\Omega_{eff}} J(J+1) \quad (1.40)$$

here, values of $J < |\Omega|$ are not possible and $J = |\Omega|, |\Omega| + 1, |\Omega| + 2, \dots$ (1.41)

1.2.4.b Hund's Case (b)

As we have seen in Hund's Case (a), states with $\Lambda = 0$ ($^{2S+1}\Sigma$ states), the spin vector \mathbf{S} is not coupled to the internuclear axis at all. Particularly for light molecules, the electron spin sometimes very weakly coupled to the orbit ($\Lambda \neq 0$) and there is no coupling of the spin \mathbf{S} to the internuclear axis. The vector diagram of case (b) is shown in Figure 1.2.

For $\Lambda \neq 0$, Λ and nuclear rotation \mathbf{R} is coupled to form resultant \mathbf{N} without spin \mathbf{S} .

$$\mathbf{N} = \mathbf{R} + \Lambda \quad (1.42)$$

If $\Lambda = 0$, angular momentum \mathbf{N} is identical to \mathbf{R} and perpendicular to internuclear axis. In this case ($\Lambda = 0$), \mathbf{N} is quantized and has all integral values ($N = 0, 1, 2, \dots$). Finally angular momenta \mathbf{N} and \mathbf{S} form a total angular momentum \mathbf{J} (without nuclear spin),

$$\mathbf{J} = \mathbf{N} + \mathbf{S} \quad (1.43)$$

The molecular term symbol is designated similar to case (a) as $^{2S+1}\Lambda$, dropping the subscript $\mathbf{\Omega}$, which is not relevant here. The energy level expression is given by

$$F_v(N) = B_v N(N+1) \quad (1.44)$$

and each N -level (except for $N < S$) is split into $2(2S+1)$ for $\Lambda \neq 0$ (due to Λ -type doubling) and $(2S+1)$ for $\Lambda = 0$. It is obvious that for singlet states ($S = 0$) and $\Lambda \neq 0$, the distinction between case (a) and case (b) disappears as $\Lambda = \Omega$ and $N = J$. Hund's cases (a) and (b) are idealized limiting cases, while $^{2S+1}\Sigma$ states always belongs strictly to case (b), however, multiplet Π, Δ, \dots states belong to cases sometimes intermediate between (a) and (b) as do not obey either coupling cases closely.

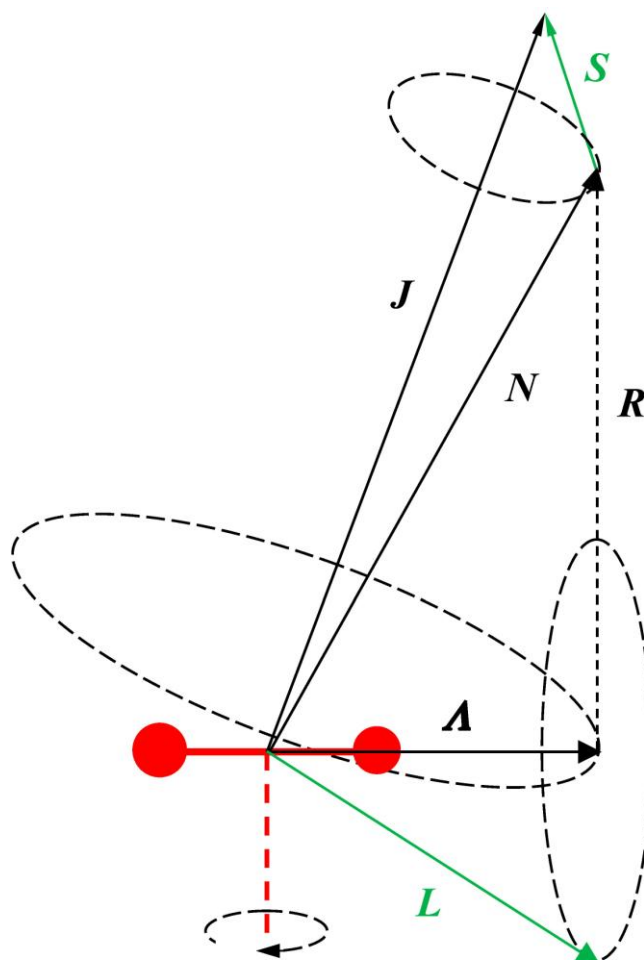


Figure 1.2 Vector diagram for Hund's Case (b)

1.2.4.c Hund's Case (c)

In case of particularly heavy molecules, the interaction between L and S is stronger than the interaction with the internuclear axis, which is described by this coupling scheme. Here, L and S together formed an electronic total angular momentum J_a whose component Ω

along the internuclear axis, as in Case (a) is well defined, however, Λ and Σ quantum numbers are not defined. The vector diagram of this scheme is shown in Figure 1.3. The electronic total angular momentum Ω together with nuclear rotation N form the resultant angular momentum J similar to case (a). The rotational energy levels are described by formula (1.40) as in case (a) and each J levels are doubly degenerate in absence of Ω -type doubling. Each electronic state is recognized by their Ω quantum number and usually represented by $[T_0]\Omega$ following to Linton et al. [25], where T_0 is the term energy of the excited electronic state from $v = 0$ of the ground state and its value is given in thousands of wavenumbers.

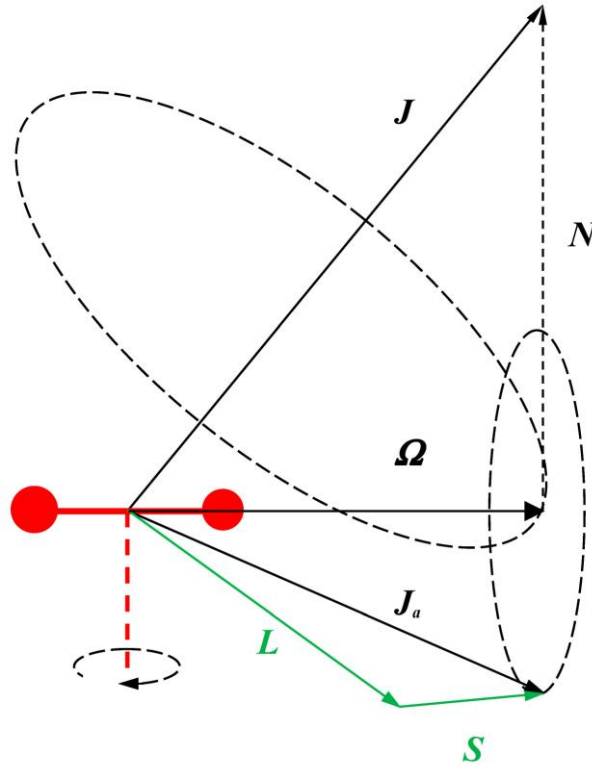


Figure 1.3 Vector diagram for Hund's Case (c)

1.2.4.d Hund's Case (d)

This coupling scheme is referred for a weakly coupled L to the internuclear axis, while the coupling between L and the axis of rotation R is strong. This coupling case is shown in Figure 1.4.

Here, nuclear rotation R is quantized with magnitude $[R(R+1)]^{1/2}\hbar$. The angular momentum L , together with the nuclear rotation R forms the resultant K . The rotational energy in this case is given by,

$$F(R) = B_v R(R + 1) \quad (1.45)$$

There are $(2L + 1)$ values of K for each value of R , i.e., each term given by this formula is split into $(2L + 1)$ components.

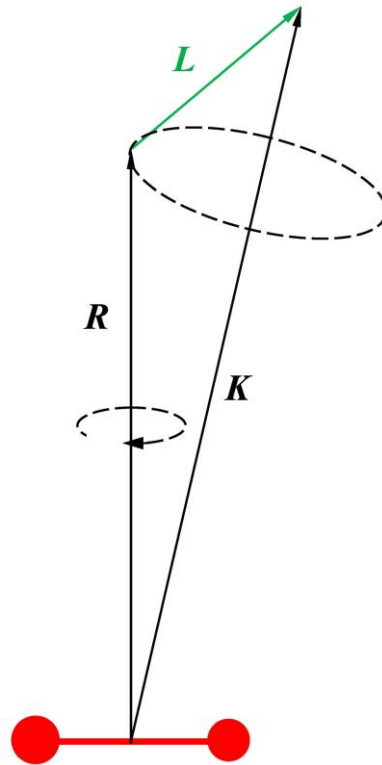


Figure 1.4 Vector diagram for Hund's Case (d)

1.2.4.e Hund's Case (e)

This coupling case is realized as similar to case (d) in which, L and S are strongly coupled to form a total electronic angular momentum J_a , which is weakly coupled to the internuclear axis [1]. This case is shown in Figure 1.5. Splitting of the rotational levels in this case would be $(2J_a + 1)$ fold.

Earlier, no practical examples of this case (e) were observed [1]. However recently, this coupling scheme has been detected in the case of high lying Rydberg states of diatomic

molecules HI and O₂. For HI molecule, the Rydberg states has been described in terms of a transition in angular momentum coupling cases, going from Hund's case (c) to case (e) [26]. For of O₂ molecule, the *ns* and *nd* Rydberg states have been described by this coupling scheme [27]. In another example of case (e) reported for the interaction potential of the long-range He•••Kr⁺ ion [28].

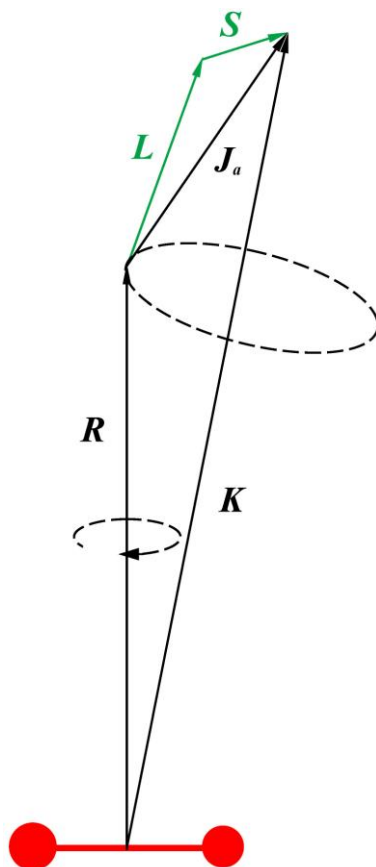


Figure 1.5 Vector diagram for Hund's Case (e)

1.2.4.f Nuclear Spin Coupling: Extension of Hund's Coupling Cases

So far in the discussion of Hund's coupling cases, nuclear spin effects are not considered. In this section, nuclear spin effects are described only to Hund's cases (a), (b) and (c). The nuclear spin angular momentum I can couple either to the internuclear axis or to another angular momenta within the molecule. The coupling case in which I couple to the internuclear axis, the applicable Hund's case is modified by putting a subscript α and for all the other cases, a subscript β is used. The former possibility is expected to arises very rarely

due to interaction of the nuclear spin to the internuclear axis is very weak, hence, we will discuss only later cases.

In the Hund's case (a_β), the nuclear spin angular momentum I is coupled to the total angular momentum exclusive of nuclear spin J to form total angular momentum F . Thus,

$$F = J + I \quad (1.46)$$

and the quantum number F can take values,

$$F = J + I, (J + I) - 1, \dots, |J - I| \quad (1.47)$$

An example of this coupling case can be found in NbN [29].

The nuclear spin can be coupled in three ways in Hund's case (b) depending on the strong interaction of I with either of N , J or S and is represented by putting corresponding additional subscript N , J or S . In Hund's case ($b_{\beta N}$) the nuclear spin I couple to N to form intermediate coupling $F1$ which further couples to S to form resultant J , however, it is unlikely because coupling of S to N is invariably much stronger than that between I and N [4] and no example of this case ($b_{\beta N}$) has been reported. Further, in the coupling case ($b_{\beta J}$), the nuclear spin I is coupled to the J to form total angular momentum F , similar to case (a_β). The third case ($b_{\beta S}$) is encountered if the nuclear spin I is coupled to the total electron spin S to form an intermediate G , sometimes called pseudo-spin and this interaction is referred as Fermi contact interaction. Thus,

$$G = I + S \quad (1.48)$$

and the quantum number G can take values,

$$G = I + S, (I + S) - 1, \dots, |I - S| \quad (1.49)$$

Further G couples to couples to N to form resultant F , i.e.

$$F = N + G \quad (1.50)$$

with

$$F = N + G, (N + G) - 1, \dots, |N - G| \quad (1.51)$$

This coupling scheme is observed in the ground $X^2\Sigma^+$ state of ScO molecule and is discussed in the Chapter 4. However, the excited $B^2\Sigma^+$ state in ScO is described by Hund's case ($b_{\beta J}$).

In the Hund's case (c_{β}), the nuclear spin I is coupled to the J to form total angular momentum, F , similar to case (a_{β}).

1.3 Symmetry, Parity and Selection Rules

Only heteronuclear diatomic molecules are investigated in this thesis and we will limit our discussion to only this class of molecules. The total parity of a molecular state can be obtained by symmetry operation E^* , which inverts all the coordinate of the particles (nuclei and electrons) in the laboratory frame with the origin at the centre of mass of the molecule. Thus,

$$E^*\psi = E^*(\psi_{el}\psi_{vib}\psi_r) = \pm\psi \quad (1.52)$$

excluding the nuclear spin part.

The problem of electronic part of eigenfunction ψ_{el} for the inversion operation is most difficult, because ψ_{el} is known in the molecular frame. However, it is shown that the inversion operation E^* in the laboratory frame is equivalent to the symmetry operation of reflection by any plane through the internuclear axis in the molecular frame. Hence, any plane through the internuclear axis is a plane of symmetry in the diatomic molecules. Let us consider first the non-degenerate states ($^{2S+1}\Sigma$ states). For a $^{2S+1}\Sigma$ state, electronic eigenfunction (excluding vibration, rotation and nuclear spin) upon reflection through such a plane of symmetry remains unchanged or changes sign. In former case a $^{2S+1}\Sigma^+$ and in the latter a $^{2S+1}\Sigma^-$ state arises. For degenerates state with $\Omega = 0$, but $A \neq 0$, a slight splitting exists even for disregarding rotation, and electronic eigenfunctions of one of the component upon reflection from any plane through the two nuclei remains unchanged, while the other component changes sign. For example a $^3\Pi_0$ state is split into two component and is distinguished by $^3\Pi_{0+}$ and $^3\Pi_{0-}$.

Further for degenerate states with $\Omega, A \neq 0$, the additional superscript \pm is not necessary as the rotational levels always occur with \pm pair because of two-fold orbital degeneracy without rotation. However, on taking account of interaction of rotation of nuclei with L , produce a splitting into two components for each rotational level. This effect increases with increasing rotation and is present for all states with $A \neq 0$ and is called A -type doubling.

Since, inversion operation leaves internuclear distance r_{AB} unchanged thus, $E^*\psi_{\text{vib}}(r_{AB}) = \psi_{\text{vib}}(r_{AB})$. Finally total parity is changed with alternate rotational levels J in Hund's case (a) and (c) while with N in case (b). Hence it is useful to define rotationless e/f parity as follows:

$$E^*\psi = +(-1)^{J-\sigma}\psi \text{ for } e \quad (1.53)$$

$$E^*\psi = -(-1)^{J-\sigma}\psi \text{ for } f \quad (1.54)$$

where, ψ is total eigenfunction excluding nuclear spin and $\sigma = 0$ for integral J and $1/2$ for half-integral J .

Selection rules for electric dipole one-photon transitions among different electronic states are summarized [1] as follows.

(i) General selection rules:

For the total angular momentum: $\Delta J = 0, \pm 1$ but $J = 0 \nrightarrow J = 0$

Positive rotational levels combines $+ \longleftrightarrow -, + \leftrightarrow +, - \leftrightarrow -$

only with negative, and vice versa:

In terms of e/f parity the above selection rules becomes

$$e \leftrightarrow e \text{ and } f \leftrightarrow f \text{ for } R \text{ and } P \text{ branches } (\Delta J = \pm 1),$$

$$e \leftrightarrow f \text{ for } Q \text{ branch } (\Delta J = 0)$$

(ii) Hund's case (a): $\Delta S = 0, \Delta \Sigma = 0$

$$\Delta\Omega = 0, \pm 1, \Delta\Lambda = 0, \pm 1; \Delta\Lambda = 0$$

$$\Delta J = 0 \text{ is forbidden for } \Omega = 0 \longrightarrow \Omega = 0$$

(iii) Hund's case (b):

$$\Delta S = 0$$

$$\Delta\Lambda = 0, \pm 1$$

$$\Delta K = 0, \pm 1, \Delta K = 0 \text{ is forbidden for } \Sigma-\Sigma \text{ transitions}$$

$$\Sigma^+ \longleftrightarrow \Sigma^+, \Sigma^- \longleftrightarrow \Sigma^-, \Sigma^+ \leftrightarrow \Sigma^-$$

(iv) Hund's case (c):

$$\Delta\Omega = 0, \pm 1$$

$$\Delta J = 0 \text{ is forbidden for } \Omega = 0 \longrightarrow \Omega = 0$$

$$0^+ \longleftrightarrow 0^+, 0^- \longleftrightarrow 0^-, 0^+ \leftrightarrow 0^-$$

(v) Hund's case (d):

$$\Delta L = 0, \pm 1$$

$$\Delta R = 0$$

1.4 Perturbation

Perturbations in the spectra of molecules may be referred as irregular behavior among observed spectral lines [30]. The irregular behavior is reflected as deviation of rotational lines from the regular course, intensity variation and also appearance of extra lines. Sometimes radiative lifetimes of the perturbed rotational levels also shows systematic variations [10,31]. The deviations in the rotational line positions cannot be explained by simply introducing non-physical higher order polynomial terms in the fittings. In such cases the interaction between perturbing states must be considered. This consideration can be simple in the case of a single interacting state [32] however in some cases it is complex due to several interacting states either observed or unobserved. On introduction of off-diagonal term in the rotational Hamiltonian of two interacting electronic states, a perturbation analysis can be performed [32]. However, the form of the interaction term is not straightforward if the nature of the perturbing state is unknown. Selection rules for perturbing states derived by Kronig [33] are described below:

(i) $\Delta J = 0$; both states must have the same total angular momentum J ($\Delta K = 0$ for Hund's case (b)).

(ii) $\Delta S = 0$; both states must have the same multiplicity S , however, this rule is non-rigorous.

(iii) $\Delta A = 0, \pm 1$; ($\Delta \Omega = 0, \pm 1$ for Hund's case (c)). Perturbation among $\Delta A = 0$ states is called homogeneous while for $\Delta A = \pm 1$ states is heterogeneous.

(iv) $+$ \leftrightarrow $-$; both states must be positive or both negative.

1.5 Data Reduction and Evaluation of Molecular Parameters

The assignment of the observed bands and fitting methods of the rotational lines are described in this section. Due to uncongested and intense nature of the jet-cooled spectra, the lowest rotational levels are well populated and invariably observed. Symmetries of the states involved in a transition are unequivocally established by observing number of rotation branches and assignment of first rotational line.

1.5.1 Combination Difference Method

This method utilizes the transitions with common upper (/lower) rotational level to determine the separation of rotational levels of the lower (/upper) electronic state. In this way, a set of difference of rotational levels data is obtained and fitted to determine the rotational constants. However, we used this method for rotational quantum number J assignment. In case of perturbations are present in the excited state rotational levels, this method is used as the lower state combination difference. The following two data fitting method are extensively used in this thesis.

1.5.2 Least Square Fitting Procedure

A program written in FORTRAN, which utilizes weighted nonlinear least-squares iterative procedure is used to determine molecular parameters by fitting given Hamiltonian matrix with the input provided as a set of all the observed spectral lines along with their J assignments in a band system. This program uses the Hellmann-Feynman theorem to

calculate derivatives of the Hamiltonian as a function of molecular constants. An initial guess of molecular parameter is included and the program computes the correction which is added to these initial guess values. Further, standard deviation of the total fit is calculated and if convergence criteria are satisfied the Hamiltonian matrix elements are evaluated.

1.5.3 PGOPHER Simulation Program

PGOPHER simulation program by C.M. Western simulates rotational, vibrational and electronic structure of molecular spectra [34]. The experimental spectra are simulated and molecular constant are derived using this program.

1.6 Rydberg, Klein and Rees Potential Energy Curve and Franck-Condon Factors

The method developed by Rydberg, Klein and Rees [35,36,37] is used to determine potential energy curves directly from the spectroscopic constants. The program RKR1, written in FORTRAN uses experimentally determined rotational and vibrational constants as input [38] to construct the potential energy curve. Further, the classical turning points $R_{\max}(v)$, $R_{\min}(v)$ are calculated by solving the equations (1.55-1.58) The Klein integrals on which the RKR method is based are given as,

$$R_{\max}(v) - R_{\min}(v) = \frac{2}{\beta} \int_{v_{\min}}^v \frac{dv'}{[G(v) - G(v')]^{\frac{1}{2}}} \equiv 2f \quad (1.55)$$

$$\frac{1}{R_{\min}(v)} - \frac{1}{R_{\max}(v)} = \frac{1}{2\pi\beta} \int_{v_{\min}}^v \frac{B_v dv'}{[G(v) - G(v')]^{\frac{1}{2}}} \equiv 2g \quad (1.56)$$

where $\beta^2 = 2\mu/\hbar^2$, R_{\min} and R_{\max} are the inner and outer classical turning points of the potential at the energy $G(v)$ associated with vibrational level v . B_v is the rotational constant for vibrational level v . Equation (1.55) and (1.56) are further solved for classical turning points,

$$R_{\min}(v) = \sqrt{f^2 + f/g} - f \quad (1.57)$$

$$R_{\max}(v) = \sqrt{f^2 + f/g} + f \quad (1.58)$$

Another program is used to calculate Franck-Condon factors, which accepts potential

energy curves, generated in RKR1 program as input, and solves the Schrödinger equation for the vibronic eigenfunctions and eigenvalues. Franck-Condon factors are determined from the overlap integral of these eigenfunctions.

1.7 References

-
- [1] G. Herzberg, *Molecular Spectra and Molecular Structure, I. Spectra of Diatomic Molecules*, Second Edition, D. Van Nostrand, New York (1950).
 - [2] I. Kovacs, *Rotational Spectroscopy in the spectra of Diatomic Molecules* Elsevier Publishing, New York (1969).
 - [3] H. Lefebvre-Brion, R.W. Field, *The spectra and Dynamics of Diatomic Molecules*, revised and enlarged edition, Elsevier Academic Press, New York (2004).
 - [4] J.M. Brown, A. Carrington, *Rotational Spectroscopy of Diatomic Molecules*, Cambridge University Press, Cambridge (2003).
 - [5] P. F. Bernath, *Spectra of Atoms and Molecules*, Oxford University Press, New York, second edition (2005).
 - [6] I.V. Hertel, C.-P. Schulz, *Atoms, Molecules and Optical Physics 2: Molecules and Photons – Spectroscopy and Collisions*, Springer-Verlag Berlin Heidelberg (2015).
 - [7] J.F. Harrison, *Chem. Rev.* **100**, 679 (2000).
 - [8] B. Simard, W. J. Balfour, H. Niki, and P. A. Hackett, in “45th Ohio State University International Symposium on Molecular Spectroscopy,” Columbus, Ohio (1990), Abstracts RC11 and RC12.
 - [9] R. S. Ram and P. F. Bernath, *J. Chem. Phys.* **101**, 9283 (1994).
 - [10] Z.J. Jakubek, S.G. Nakhate, B. Simard, W.J. Balfour, *J. Mol. Spectrosc.* **211**, 135 (2002).
 - [11] A. Bernard, R. Bacis, *Can. J. Phys.* **55**, 1322 (1977).
 - [12] A. B. Kunz, M. P. Guse, and R. J. Blint, *J. Phys. B* **8**, L358 (1975).
 - [13] R. Bacis, A. Bernard, and A. Zgainsky, *C. R. Acad. Sci. Ser. B* **280**, 77 (1975).

-
- [14] P R Scott and W G Richards, *J. Phys. B: Atom. Molec. Phys.*, Vol. 7. No. 13. 1974
- [15] S. R. Langhoff, L. G. M. Pettersson, C. W. Bauschlicher, H. Partridge, *J. Chem. Phys.* **86**, 268 (1987).
- [16] K. Balasubramanian, J. Z. Wang, *J. Mol. Spectrosc.* **133**, 82 (1989).
- [17] R. S. Ram, P. F. Bernath, *J. Chem. Phys.* **105**, 2668 (1996).
- [18] R. S. Ram, P. F. Bernath, *J. Chem. Phys.* **104**, 6444 (1996).
- [19] M. Born and R. Oppenheimer, *Ann. Physik.* **84**, 457 (1927).
- [20] J.L. Dunham, *Phys. Rev.* **41**, 721 (1932).
- [21] P.M. Morse, *Physic. Rev.* **34**, 57 (1929)
- [22] C.L. Pekeris, *Physic. Rev.* **45**, 98 (1934).
- [23] F. Hund, *Handbuch der Physik* **24**, 561 (1933).
- [24] I. Kopp and J. T. Hougen, *Can. J. Phys.* **45**, 2581 (1967).
- [25] C. Linton, M. Dulick, R.W. Field and P. Caratte, *J. Mol. Spectrosc.* **102**, 441 (1983).
- [26] A. Mank, M. Drescher, T. Huth-Fehre, N. Böwering, and U. Heinzmann, H. Lefebvre-Brion, *J. Chem. Phys.* **95**, 1676 (1991).
- [27] H. Lefebvre-Brion, T. Ridley, *J. Chem. Phys.* **123**, 144306 (2005).
- [28] A. Carrington, C.H. Pyne, A.M. Shaw, S.M. Taylor, J.M. Hutson, M.M. Law, *J. Chem. Phys.* **105**, 8602 (1996).
- [29] J.L. Féménias, C. Athenour, and T.M. Dunn, *J. Chem. Phys.* **63**, 2861 (1975).
- [30] H. Lefebvre-Brion, R.W. Field, *Perturbations in the spectra of diatomic molecules*, Academic Press, San Diego (1986).
- [31] S.G. Nakhate, S. Mukund, S. Bhattacharyya, *Chem. Phys. Lett.* **669**, 38 (2017).
- [32] R.S. Ram, G. Li, and P.F. Bernath, *J. Chem. Phys.* **135**, 194308 (2011).
- [33] R. de L. Kronig, *Z. Physik* **50**, 347 (1928).

-
- [34] C.M. Western, PGOPHER, a program for simulating rotational structure, University of Bristol, Bristol (2010). <<http://pgopher.chm.bris.ac.uk>>.
- [35] R. Rydberg, *Z. Phys.***73**, 376 (1931).
- [36] O. Klein, *Z. Phys.***76**, 226 (1932).
- [37] A.L.G. Rees, *Proc. Phys. Soc.* **59**, 998 (1947).
- [38] R.J. LeRoy, RKR1 2.0, A computer program implementing the first-order RKR method for determining diatomic molecule potential energy curves. University of Waterloo, Chemical Physics Research Report CP-657R (2004). <<http://scienide2.uwaterloo.ca/~rleroy/rkr/>>.

Chapter 2

Experimental Setup and Techniques

2.1 Introduction

Supersonic molecular beam method is a well-known technique to produce wide variety of refractory metal containing species in the gas phase, under the non-equilibrium low-temperature conditions by cooling the internal degrees of freedom. The development of laser vaporization in supersonic pulsed nozzle source by group of Professor R.E. Smalley [1] has made possible to study a wide variety of refractory metal atoms, diatomic and polyatomic metal-containing-molecules, and clusters in both neutral and ionized forms. This source utilizes a pulsed laser to vaporize refractory elements in conjunction with supersonic expansion of a carrier gas (helium/argon). The laser-produced metal plasma gets cooled and recombined and the reaction products undergo several collisions with helium in the gas-flow channel and finally undergo supersonic expansion in vacuum to cool their internal degrees of freedom to a low temperature in their ground state. A wide range of studies have been performed by using many variation of the original idea of the laser vaporization source. A detailed review on the laser vaporization cluster sources is recently published by Professor Duncan [2]. This chapter provides an overview of the supersonic molecular beam setup being utilized in our research group and the description of experimental techniques are limited to the laser-induced fluorescence (LIF) and mass spectroscopic studies on the transition metal-containing diatomic molecules.

2.2 Supersonic Molecular Beam Apparatus

Figure 2.1 shows a representative schematic of the experimental setup and essential parts of the setup are described in the following subsections.

2.2.1 Vacuum Chambers

The free-jet expansion takes place in a vacuum chamber is called as source chamber. This chamber is a six-port double cross built with 250 CF-F flanges. It has additional four 35 CF ports on a side-port 250 CF-F flange to insert vacuum gauges and high voltage ceramic vacuum feedthroughs. One of the 250 CF port is used to mount an indigenously built gas pulsed valve which is described in detail in Section 2.2.2. The side ports are used to deliver the ablation and probe laser beams. A high pumping speed turbomolecular pump (Pfeiffer vacuum TPU 2301, 1900 l/s) backed by a rotary vane pump (Pfeiffer vacuum DUO 65) is attached to the bottom port of the chamber and is separated from the chamber through a pneumatically operated gate valve (VAT).

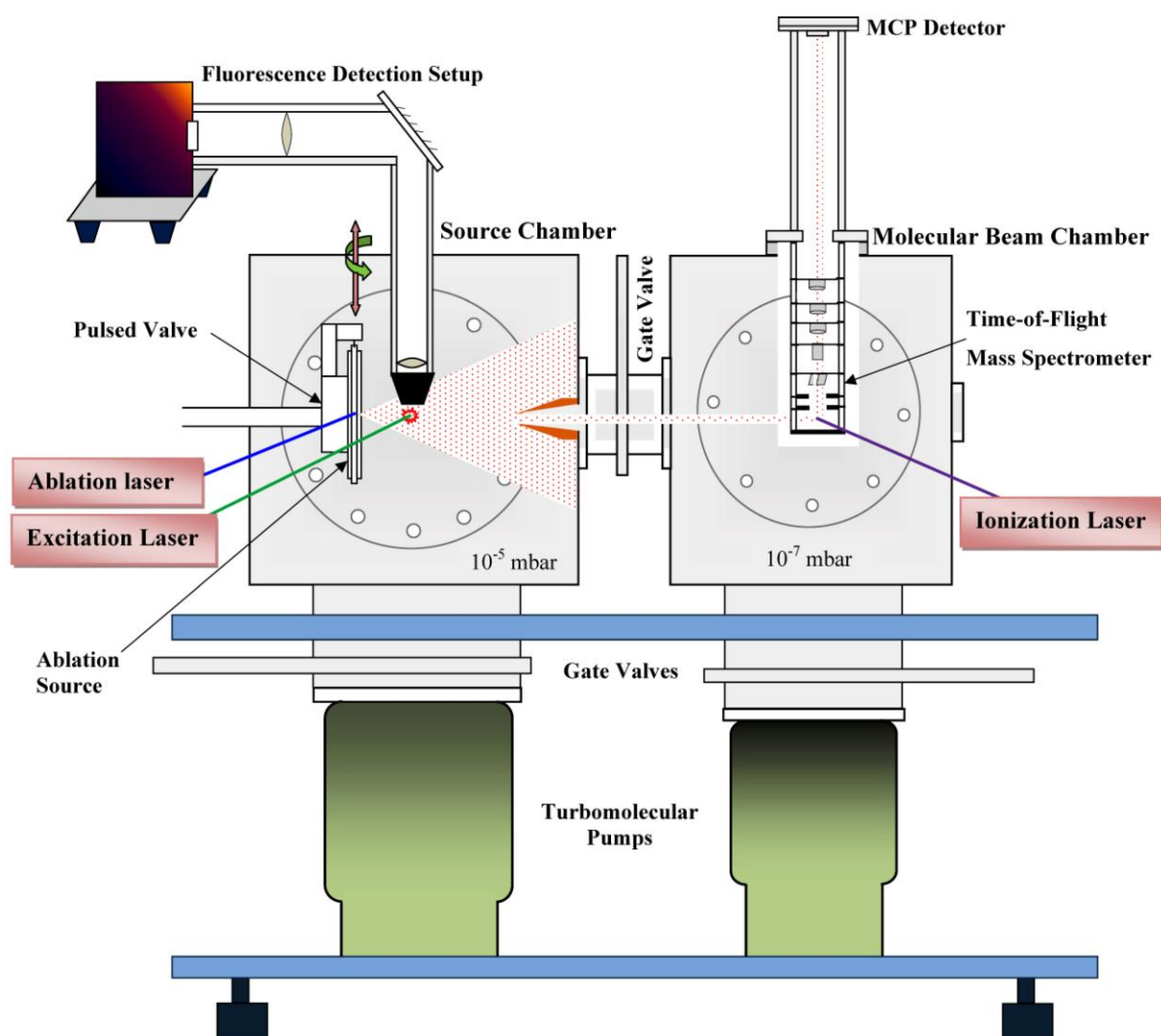


Figure 2.1 Schematic of supersonic molecular beam apparatus

Laser-induced fluorescence collection optics is mounted on the top port of the source chamber. A skimmer of diameter 5 mm is fixed on the opposite port of the pulsed valve at a distance of 200 mm from nozzle of the pulsed valve. This allows central portion of the free-jet to flow into the second vacuum chamber. The free-jet is skimmed into a molecular beam, enters into the second vacuum chamber separated from the source chamber by a gate valve (VAT) and differentially pumped by a turbomolecular pump (Pfeiffer vacuum TPU 1201 1250 l/s) backed by a rotary vane pump (Pfeiffer vacuum DUO 35). This chamber is also a six-port double cross built with 200 CF-F flanges. An indigenously built linear time of flight mass spectrometer (TOFMS) with Wiley-McLaren ion extraction optics is mounted in the orthogonal geometry to the molecular beam on the top port of this chamber. Two side ports of this chamber are used for delivering the excitation/ionization laser beam perpendicular to the molecular beam axis. The background pressure $\sim 1 \times 10^{-8}$ mbar is obtained in both the vacuum chambers in absence of gas load.

2.2.2 Gas Pulsed Valve and Laser Vaporization Source

The schematic of gas pulsed valve and laser vaporization source is shown in Figure 2.2. We followed the design of Proch and Trickl [3] for the gas pulsed valve, which generate high-intensity supersonic free-jet of helium gas. The pulsed valve consists of a piezoelectric disc translator (PZT) (Physik-Instrumente P286.20). This disk flexes $\sim 100 \mu\text{m}$ at a voltage of -1000V. An adjustable sealing plunger, which opens and closes the nozzle, is mounted on the orifice in the center of the PZT with lock nuts. The nozzle has diameter $400 \mu\text{m}$. The plunger seals the nozzle with a Viton O-ring mounted on the tip. A typical backing pressure about 210 kPa is applied before the nozzle. The pulsed valve is operated with a voltage pulse of $\sim 250 \text{ V}$ and pulse duration $\sim 250 \mu\text{s}$ (Figure 2.3) to the PZT by a homemade voltage pulse generator. The temporal profile of the gas pulse is expected similar

to the applied voltage [3]. When the gas pulse valve/expansion source is operated at a repetition rate of 10 Hz, the pressure inside the chamber is increased to $\sim 10^{-5}$ mbar.

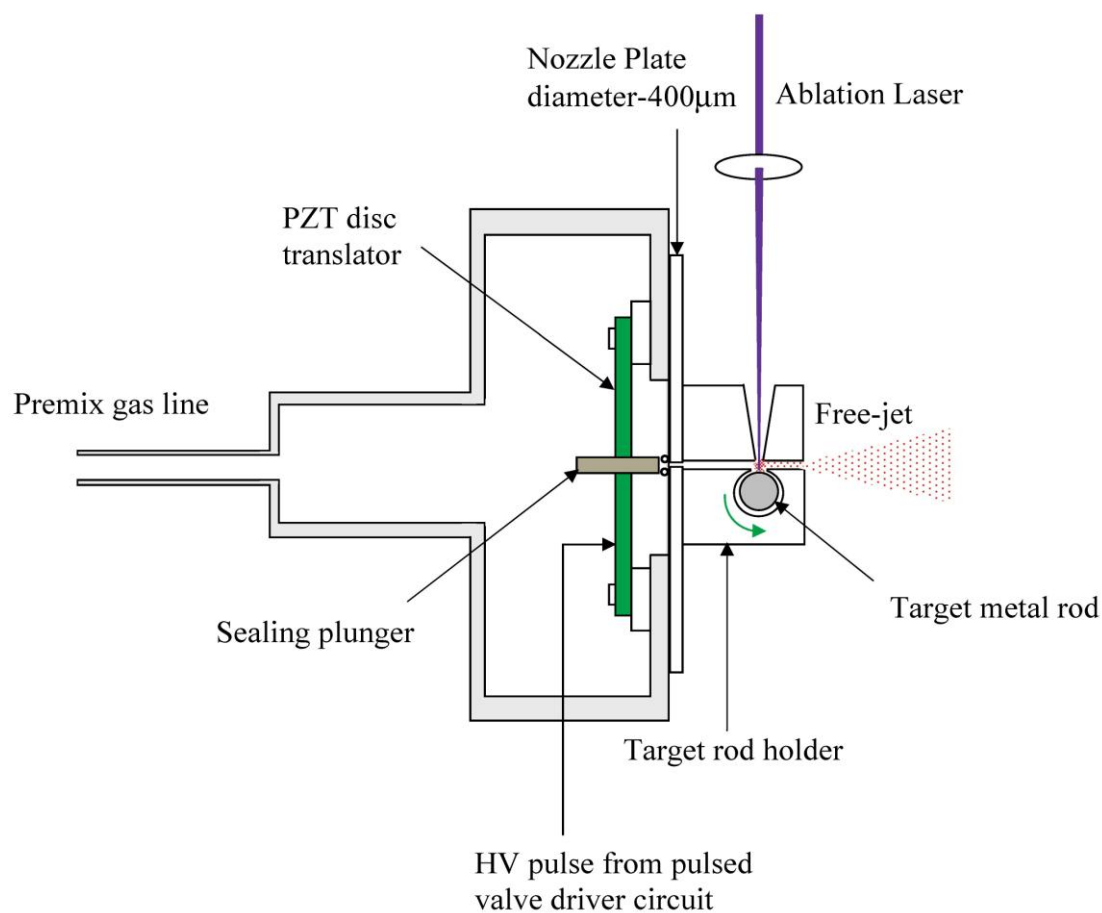


Figure 2.2 Schematic of homemade gas pulsed valve and laser vaporization source

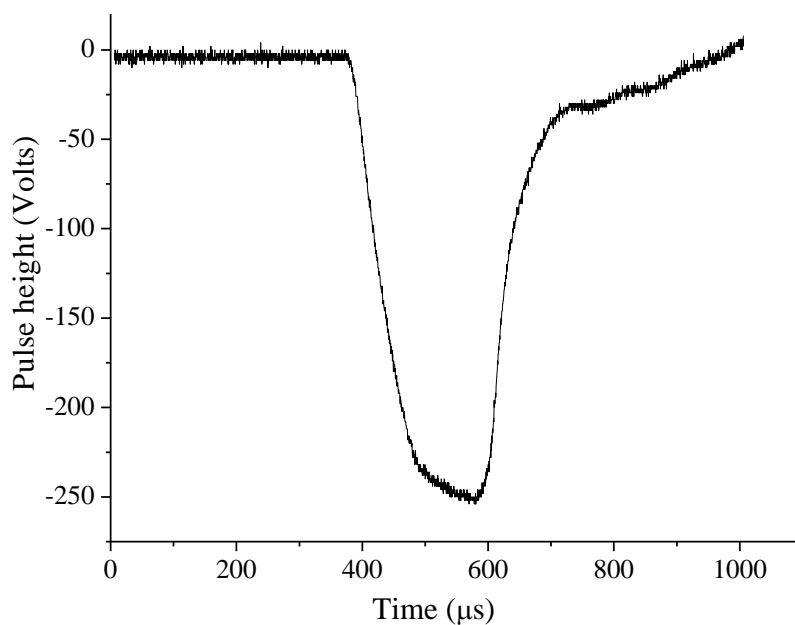


Figure 2.3 A typical voltage pulse given to the PZT

The design of the laser vaporization source is similar to the one used by Hopkins et al. [4] and is given in Figure 2.2. The sample of a refractory metal is used in the form of rod of $\frac{1}{4}$ inches in diameter and is located in a holder in-line with the gas flow from the pulsed valve. On opening of the pulsed valve, helium emerging from the nozzle into a channel of diameter 2 mm and flow along the surface of the metal rod. At a point of this gas flow and surface of the metal rod, the ablation laser is focused to generate metal plasma. The metal rod is rotated and translated up and down by a mechanical connection to a motor driven micrometer screw (Oriental Motor). This mechanism ensures fresh metal surface for ablation to the next ablation laser pulse and to effect uniform and stable plasma density. The generated hot metal plasma is cooled and recombined by the supersonic helium gas pulse emanating from the nozzle into a channel of diameter 2 mm and length 7 mm and expanded freely into the vacuum chamber. The details on the formation of the molecular species are given in Section 2.3.

2.2.3 Laser Systems

Three lasers are used for different functions in the experiments. Nd:YAG laser in third harmonic at 355 nm is used for ablation of target metal rod and a XeCl excimer pumped tunable pulsed dye laser is used for laser-excitation of molecular species. The same XeCl excimer laser is used to photoionize the beam content in mass spectroscopic studies. All these laser systems are described in the following subsections.

2.2.3.a Ablation Laser

Free metal atoms and ions are generated in a laser produced plasma by focusing the third harmonic, 355 nm radiation of a Nd:YAG laser (Quanta System SYL 203) having pulse duration ~ 8 ns and energy ~ 15 mJ. The Nd:YAG laser beam is passed through a 2 mm open channel in the vaporization source from a side-port of the chamber and is focused by a 25 cm focal length quartz lens on surface of the metal target. Optimum and stable production of

molecules in the free-jet is achieved by maintaining proper time delay between the laser pulse and opening of the pulsed valve (see Section 2.3), proper focusing and varying energy of the ablation laser beam.

2.2.3.b Pulsed Dye Laser

The cooled metal bearing molecules are excited by a tunable pulsed dye laser (Coherent ScanMatePro) pumped by a XeCl excimer laser (Coherent CompexPro 201) 50 mm downstream the nozzle. Typical temporal pulse width (FWHM) and line width of the dye laser are $\delta t \sim 10$ ns and $\delta \bar{\nu} \sim 0.08$ cm⁻¹, respectively. Several dyes are used to cover tunability in ~ 330 – 750 nm range for searching new excited electronic states of molecules as well recording wavelength resolved spectra and radiative lifetimes of the excited electronic states. Description of the time delay between ablation and pulsed dye lasers for optimum LIF signal of molecular species is given in Section 2.3.

2.2.3.c Photoionization Laser

The XeCl excimer laser (Coherent CompexPro 201) at 308 nm is used in the resonance two photon ionization (R2PI) studies. It is understood from the kind of experiment being performed, two color laser radiation are required: one for resonant excitation and other for non-resonant photoionization of the excited molecular species. Due to use of common XeCl excimer laser for pumping the dye laser, which excite particular molecular species in the beam and to further photoionize, the optical time delay is applied between excitation and photoionization laser radiation for optimum photoionization signal. We have recorded R2PI spectra for scandium monohydride (ScH) to validate the molecule carrier of the spectra presented in this thesis.

2.2.4 Fluorescence Detection and Data Acquisition System

The fluorescence detection setup is integrated to the top port of the source chamber. The free-jet is probed by a tunable dye laser at right angle to the beam expansion axis about

50 mm downstream from the nozzle as shown in Figure 1.1. The resulting fluorescence signal is collected orthogonal to both the free-jet and the dye laser beam axes by a lens system. A biconvex quartz lens of 50 mm focal length is used to image fluorescence spot, which lies at focal point of this lens. The parallel fluorescence beam is further folded to right angle by an aluminum coated mirror and focused on the entrance slit of 0.27 meter focal length monochromator (Spex 270M) by another biconvex lens of focal length 30 cm. The lens system of fluorescence collection optics images the intersecting spot of the laser and the free-jet with a magnification of 4 on the entrance slit of the monochromator. The lens system matches the *f/number* (entrance aperture ratio) of the monochromator. The fluorescence is detected by a wide spectral response 160–930 nm and fast rise time ~ 3 ns Peltier cooled photomultiplier tube (PMT) (Hamamatsu R943-02). A black anodized cone of aperture 3 mm diameter is attached in front of the collection lens to minimize the scattered light from excitation laser falling on the PMT. The output from the PMT is further amplified by a variable-gain 20-60 dB and 1.2 GHz voltage amplifier (Femto Messtechnik, DUPVA-1-60). This amplified signal is displayed on a 200 MHz digital storage oscilloscope (Tektronics TDS 2024) having sampling rate of 2 giga-samples/s and rise time < 2 ns. To record fluorescence spectrum, this signal is fed to a boxcar integrator (Stanford Research System, SR250), which is used to average the signal, appeared within employed adjustable time-gate. The output signal from the boxcar integrator is send to a data acquisition system provided by the tunable dye laser (ScanMatePro) for recording excitation spectrum. For wavelength resolved dispersed fluorescence experiments, where fluorescence signal is recorded by scanning the monochromator, output signal from the boxcar integrator is send to a controller system (Jobin Yvon Spex DataScan2) of the monochromator. The output from the controller system, which provides output signal with monochromator wavelength position is stored on a computer.

2.2.5 Time of Flight Mass Spectrometer (TOFMS)

An indigenously built linear TOFMS with Wiley-McLaren ion extraction optics is utilized in the mass spectroscopic studies. A schematic of TOFMS is given in Figure 2.4. The TOFMS has been integrated in perpendicular configuration to the molecular beam formed by skimming the free-jet in the second chamber separated from the source chamber by a gate valve (VAT).

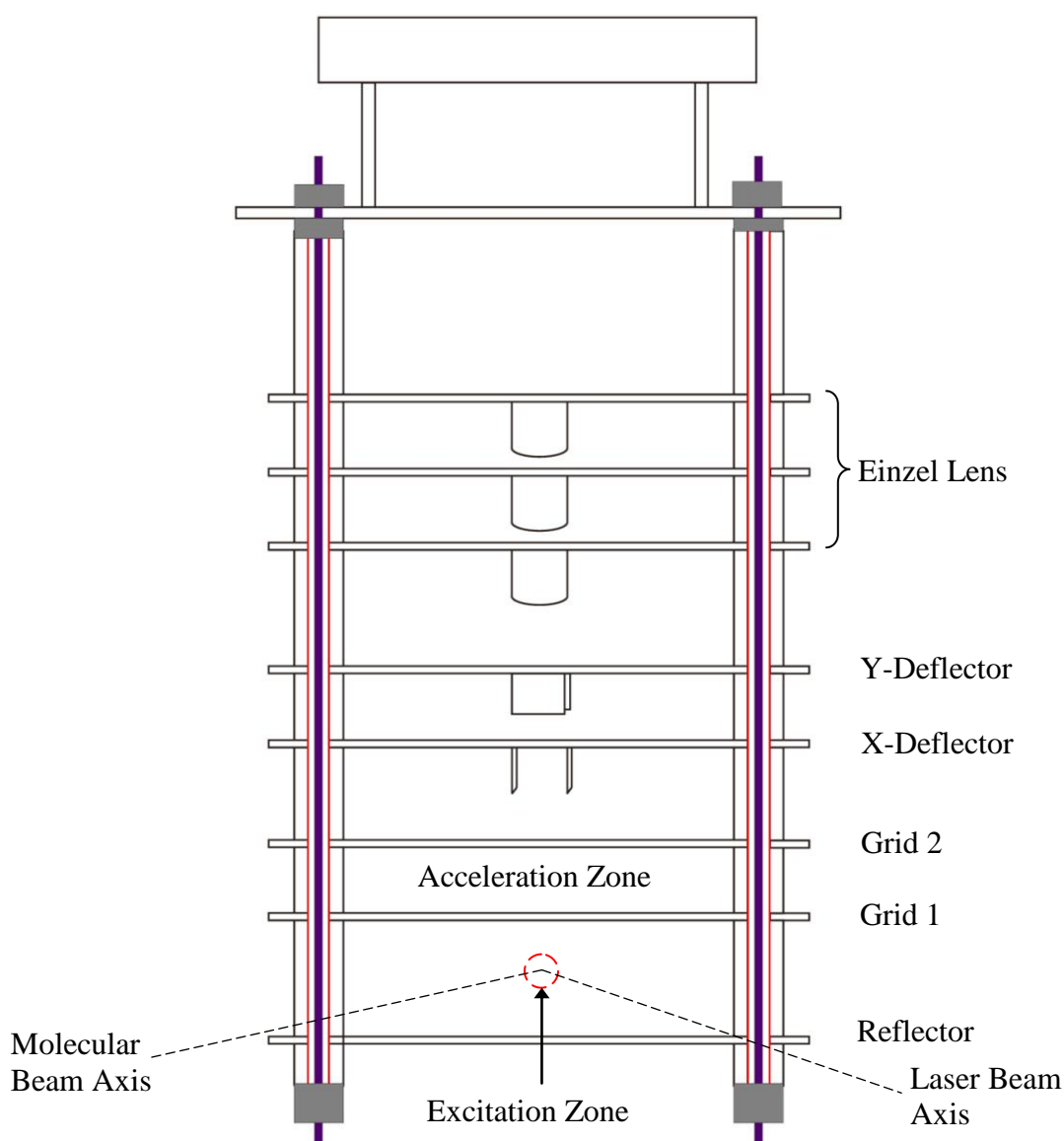


Figure 2.4 Schematic of ion extraction optics of TOFMS

Typical applied voltages at reflector, Grid 1, deflectors and Einzel lens are 1350 V, 1100 V, 120 V and 250 V, respectively while Grid 2 and end plates of Einzel lens are kept grounded. A field free drift tube of length 56 cm is used. The molecular beam content is

ionized in the extraction zone by the XeCl excimer laser at 308 nm. The generated photoions are detected by a microchannel plate (MCP) detector (Burle, APTOF 25). The output signal from the MCP detector is amplified by the voltage amplifier and displayed/recorded on the digital storage oscilloscope. Mass resolution of the TOFMS is estimated by measuring temporal position and width of a mass peak. A mass resolution ~ 400 is obtained for this setup. To record a mass-selected resonance two-photon ionization (R2PI) spectrum, the signal is fed to the boxcar integrator where required mass-peak is gated. The averaged output from the boxcar is sent to the data acquisition system of the tunable dye laser (ScanMatePro) for recording the excitation spectrum.

2.2.6 Gas-Manifold System

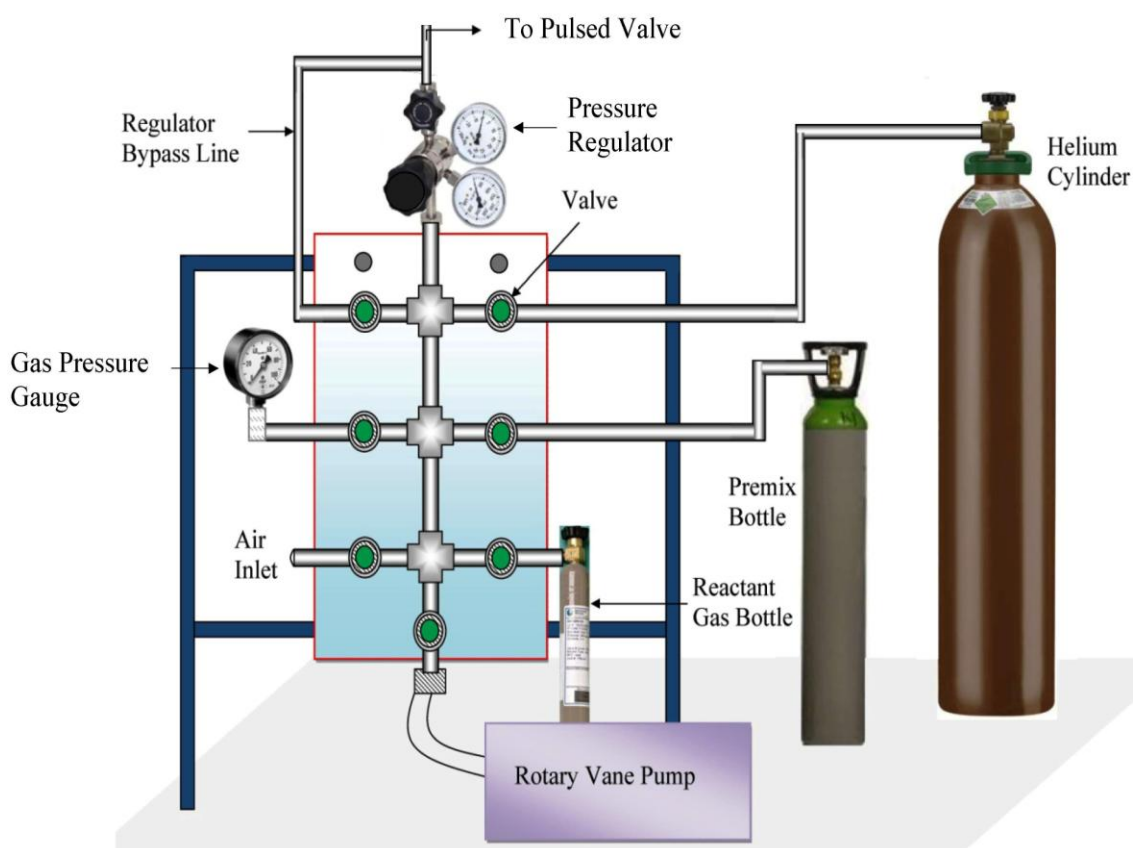


Figure 2.5 Schematic of the gas-manifold system

According to the species being studied, premix gas is prepared and flown into the free-jet chamber through a gas pulsed valve operated at 10 Hz repetition rate. A schematic of the gas-manifold system, used to prepare premix gas is shown in Figure 2.5. The gas-

manifold system is made from ¼" stainless steel tubing and several manually operated valves connected to the nozzle, gas cylinders and pressure regulators. The premix gas is prepared in a 10 liter premix cylinder connected through the gas manifold to a helium cylinder and a seed/reactant gas cylinder for example ammonia, methane or oxygen. The gas manifold system is also connected to a rotary pump (Hindhivac ED-12) to evacuate the whole system including the premix cylinder. A premix cylinder is first filled with predetermined concentration of a seed gas measured through a pressure gauge and then topped up the rest with helium up to 100 PSIG to the premix gas of required concentration by volume. A pressure regulator before the nozzle is used to maintain the desired premix gas pressure at the nozzle.

2.3 Preparation of Molecules and Time Synchronization of Events

The desired molecules are produced in the free-jet by the reaction of laser-produced metal plasma and seed gas in helium. For this purpose, time synchronization between opening of the pulsed valve which delivers premix gas pulse and firing the ablation laser which create metal plasma are important to make optimum and stable production of the molecular species of interest. Further, the molecular beam content, which is probed by a tunable pulsed dye laser or ionization laser should also be synchronized as it takes specific time to reach the probe region which further depends on the molecular beam velocity. For this purpose, a digital delay generator (Stanford Research Systems Inc. DG535) is used to send synchronous trigger signals at a 10 Hz repetition rate to the various equipments to get activated in different timings as shown in Figure 2.6 and 2.7.

At first, the pulsed valve is opened by sending a trigger pulse T_0 from the delay generator to activate a pulsed valve driver circuit, which sends a voltage pulse (~ 250 V, pulse width ~ 250 μ s) to the PZT actuator of the pulsed valve. The premix gas is entered into the vacuum chamber as the nozzle is opened for a short time ~ 250 μ s by the pulling of

sealing plunger attached with PZT onto the nozzle. After opening of the pulse valve, at a proper delay of $T_1 \sim 280 \mu\text{s}$, the delay generator sends a trigger signal to the ablation laser. In this way, the reaction between laser produced metal plasma and seed gas inside the vacuum chamber is achieved.

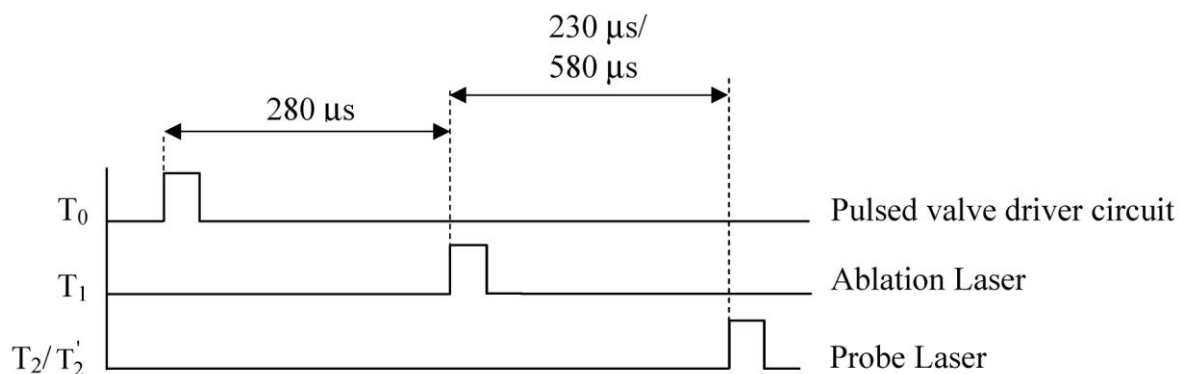


Figure 2.6 Trigger signal from a digital delay generator to various equipments

Fluorescence based experiments are performed in the free-jet due to higher density of molecules. The molecules are probed by a XeCl excimer pumped pulsed dye laser orthogonal to expansion axis at 50 mm downstream of the nozzle. For this, a time delayed trigger pulse T_2 is send to the excimer laser approximately $230 \mu\text{s}$ after the trigger signal to the ablation laser. This effectively delays the optical pulses of the excitation laser from the ablation laser by $\sim 25 \mu\text{s}$. From this delay time we have evaluated the typical beam velocity of $\sim 2 \times 10^3 \text{ m/s}$. Mass spectroscopy is performed into the second vacuum chamber. The probe (excitation/ionization) laser is triggered at $T_2' \sim 580 \mu\text{s}$ after the ablation laser in this experiment. The LIF/ion signal are optimized further by looking it on a oscilloscope and fine tuning various parameters like time delays by the digital delay generator, energy of the ablation laser, and alignment of the lasers (ablation/probe). Apart from this, seed gases are used in varied concentration and at different pressure to the nozzle to get optimized signal. Adjustment of these parameters play crucial role, especially in the low-yield signals. Molecular spectra are recorded in best signal to noise ratio (S/N) conditions and are described in the following section.

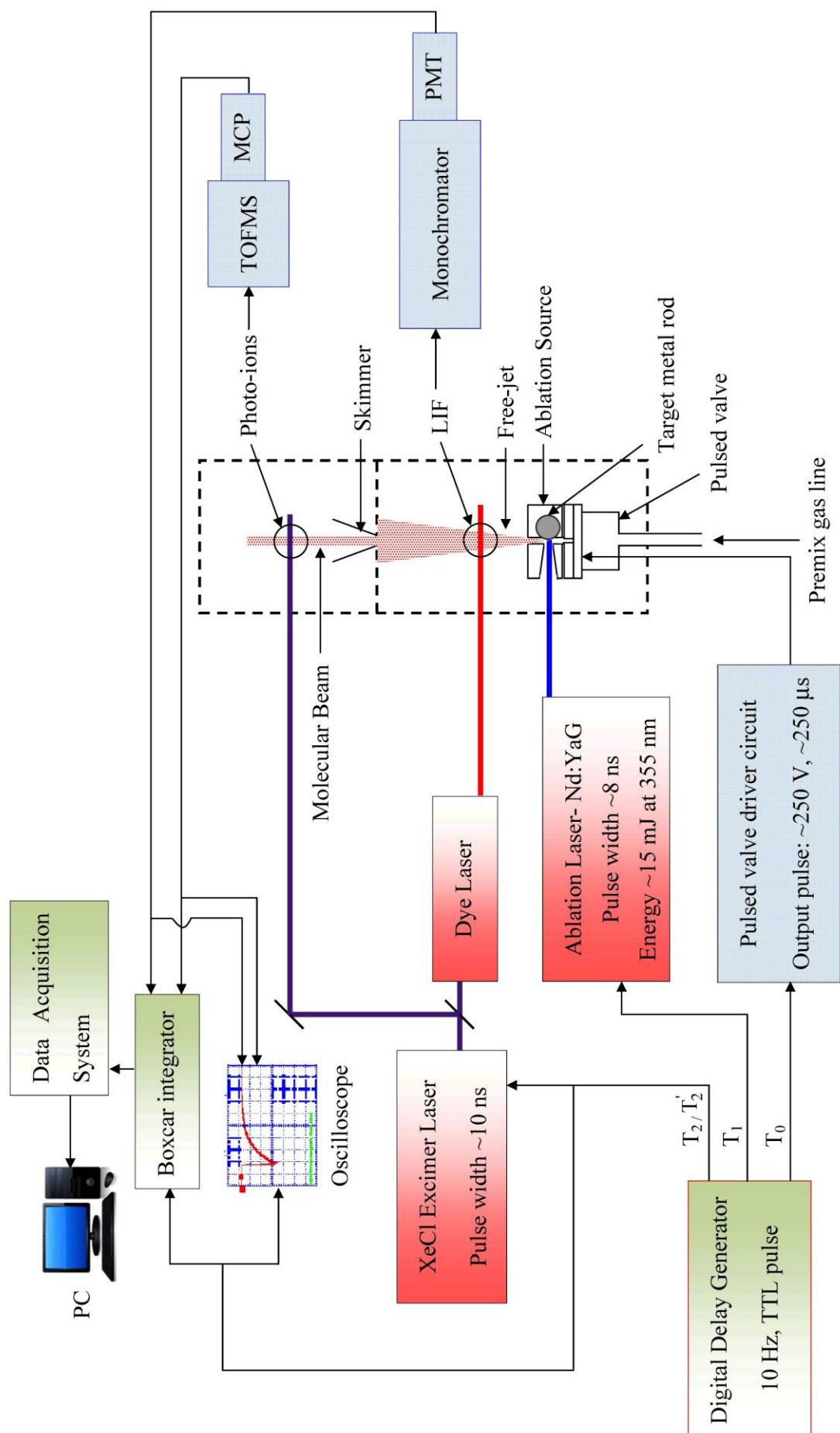


Figure 2.7 Block diagram of control electronics and various equipments of the supersonic molecular beam setup.

2.4 Experimental Techniques

In the following sections, Laser-induced fluorescence and photoionization based studies are discussed.

2.4.1 Fluorescence Based Experiments

2.4.1.a Laser-Induced Fluorescence (LIF) Excitation Spectroscopy

Laser excitation spectra are obtained by scanning the tunable pulsed dye laser frequency and recording the LIF signal through the monochromator set at a fixed wavelength corresponding to the strongest fluorescence terminating either to a ground or low-lying excited electronic states. In this scheme, the monochromator is used as a broadband filter by setting full width of the entrance and exit slits to 2.24 mm. The resolution of obtained excitation spectra is the typical spectral line width of the scanning dye laser, which is $\sim 0.08 \text{ cm}^{-1}$. In few cases, where two excitation bands are overlapped, wavelength-filtered laser-induced fluorescence technique [5] is used to separate these bands in specific favorable conditions. In this technique, spectra are recorded by collecting the fluorescence separately at the two different displaced wavelength positions of the monochromator where one band fluoresce but not other.

Supersonic expansion cools the internal degrees of freedom of molecules. Translation degree of freedom is cooled most effectively than the rotation and vibration. Similarly rotational degrees of freedom are cooled more effectively than vibrations [6]. We characterized our experimental setup by estimating the translational temperature on zirconium atom, and rotational and vibrational temperature of the generated molecular species. The laser-induced fluorescence spectroscopy of zirconium atoms with a single frequency ring dye laser (Tekhnoscan, DYE-SF-077) pumped by a diode pumped solid state (DPSS) laser (Tekhnoscan, MOZART) is revealed the Doppler width of approximately 150 MHz, which corresponds to a translational temperature of 15 K. Typical rotational and

vibrational temperatures of diatomic molecules are determined respectively as 50 K and 450 K in this setup.

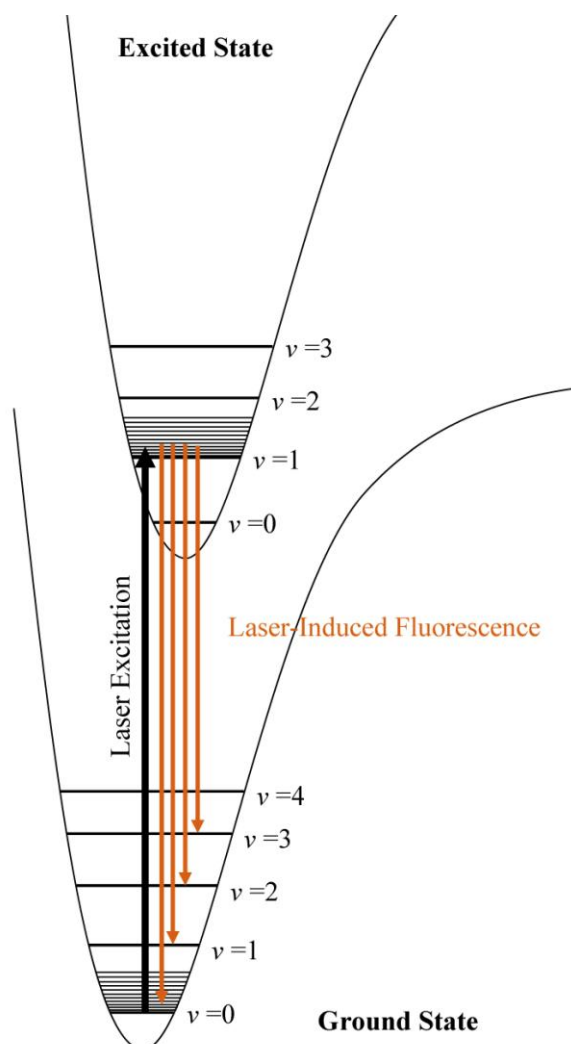


Figure 2.8 Diagram of electronic transition in a diatomic molecule. For recording of excitation spectrum, monochromator is set at the fixed wavelength corresponding to the strongest fluorescence and the dye laser frequency is scanned, while in DF study, excitation frequency is fixed and the monochromator is used in scanning mode to probe the ground and low-lying vibronic states.

2.4.1.b Wavelength-Resolved Dispersed Fluorescence (DF) Study

The DF spectra are recorded to get information on the ground and low-lying electronic states and their vibrational structure. The DF spectra are recorded by exciting the isolated rovibrational levels of the excited electronic states and monitoring the fluorescence by scanning the monochromator in the 300–925 nm wavelength region, offered by the sensitivity of the PMT. In general, the DF spectra are first recorded with the monochromator

entrance/exit slit width of 1/1 mm, corresponding to a moderate spectral resolution with FWHM $\sim 50\text{--}100\text{ cm}^{-1}$, to get coarse information about the ground and low-lying vibronic levels. Since vibrational spacing are of the order of 1000 cm^{-1} , they are well separated under this resolution. To determine the identity of the low-lying electronic states, the coarse DF spectra are then examined, wherever possible, under relatively higher resolution to resolve their rotational structure. In this experiment, the monochromator entrance/exit slit width is reduced to 0.1/0.1 mm, which corresponds to spectral resolution with FWHM $\sim 5\text{ cm}^{-1}$. The observed number of rotational lines and their intensity pattern are used to determine the symmetry of the low-lying electronic states. In the present work, in addition to the study of vibrational structures of the ground and low-lying states of various molecules, symmetry of low-lying states of ScN and NiC are established in the wavelength resolved DF Studies, where fluorescence pouring to the desired state is rotationally resolved and analyzed.

2.4.1.c Measurement of Radiative Lifetime

In radiative lifetime measurement experiments, intensity of fluorescence decay from the excited rovibronic level of molecules is recorded on the digital storage oscilloscope. The decay curve is averaged for 128 shots in order to obtain a good signal-to-noise ratio. The radiative lifetime is determined by fitting the recorded fluorescence decay curve to usual exponential decay function $\sim \exp(-t/\tau)$. However, short lifetimes (few tens of nanosecond) cannot be determined by simply fitting exponential decay function due to the convolution of laser pulse as a response function and the decay function. Short lifetime values are determined by fitting the observed fluorescence decay curve using a fitting program by deconvolution of the excitation laser pulse (assumed as Gaussian function) and an exponential decay function with adjustable parameters as given by,

laser excitation pulse:

$$y_{\text{Gauss}} = y_0 + \frac{A}{w\sqrt{\pi/2}} \exp - 2 \left(\frac{t' - t_c}{w} \right)^2 \quad (2.1)$$

and exponential decay function:

$$y_{\text{Exp}} = \exp - \left(\frac{t - t'}{\tau} \right) \quad (2.2)$$

Deconvolution program is used to fit the fluorescence decay curve to $y_{\text{Gauss}} * y_{\text{Exp}}$, where, $*$ stands for convolution operation. The lifetime values reported in this thesis is an average of about 10 values measured under different experimental conditions like excitation and ablation laser intensities, and different delay timings. This ensured no systematic effects like collisional depopulation, radiation trapping, saturation and flight-out-of view get reflected in our data. Collisional depopulation and radiation trapping effects are not present due to collision-free conditions and low-density of species in the free-jet. The effect of saturation is investigated by varying the excitation laser intensity. The flight-out-of view effect would be significant for longer lifetime values of the order of 1 μs in our set up, however, lifetime values (maximum value ~ 550 ns) reported in this thesis are free from this effect.

2.4.2 Mass-Selected Photoionization Experiment

As mentioned earlier, the TOFMS is integrated on the second vacuum chamber. Mass spectrometry is performed by non-resonantly ionizing the content of molecular beam by XeCl excimer laser. A typical mass spectrum is obtained by non-resonant photoionization with 308 nm (4.02 eV) of neutral species generated by the reaction of laser-produced scandium metal plasma and 2% ammonia seeded in helium and is shown in Figure 2.9. Due to surface oxidation of scandium metal rod, ScO and other oxygen containing species are also present in the beam. No photoion signal corresponding to ScH^+ is present in the mass spectrum, probably due to higher ionization energy of ScH than 4.02 eV provided by XeCl excimer

laser. However, a weak photoion signal corresponding to ScH^+ is observed only with mass-selected R2PI spectroscopy (see Chapter 4).

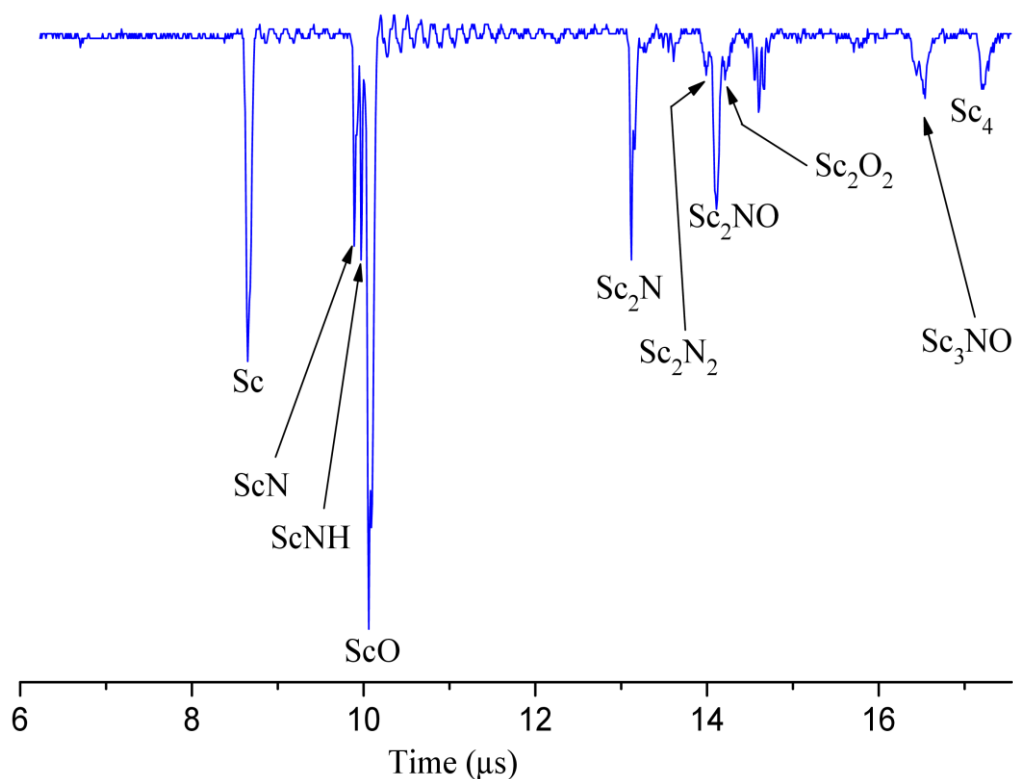


Figure 2.9 Reaction products of scandium metal plasma and ammonia in the molecular beam.

2.5 Wavelength Calibration of LIF Excitation Spectra

The LIF excitation spectra are obtained by scanning the wavelength of the pulsed dye laser having spectral bandwidth of $\sim 0.08 \text{ cm}^{-1}$. All the excitation spectra are calibrated by a commercial wavelength meter (HighFinesse WS-5). A small portion of laser radiation from the pulsed dye laser is sent to the wavelength meter, and frequency reading from the wavelength meter and fluorescence signal intensity is recorded simultaneously. Transition wavenumbers are also calibrated with an absolute precision of $\sim 0.1 \text{ cm}^{-1}$ by recording Ne optogalvanic spectral lines provided by laser wavelength calibration facility of the dye laser. In addition, wavelength calibration of the LIF spectra are also ensured by known atomic lines [7] appeared in the spectra.

2.6 References

-
- [1] T.G. Dietz, M.A. Duncan, D.E. Powers, and R.E. Smalley, *J. Chem. Phys.* **74**, 6511 (1981).
- [2] M.A. Duncan, *Rev. Sci. Instrum.* **83**, 041101 (2012).
- [3] D. Proch and T. Trickl, *Rev. Sci. Instrum.* **60**, 713 (1989).
- [4] J.B. Hopkins, P. R. R. Langridge-Smith, M. D. Morse, and R. E. Smalley, *J. Chem. Phys.* **78**, 1627 (1983).
- [5] S.G. Fougère, W.J. Balfour, J. Cao, C.X.W. Qian, *J. Mol. Spectrosc.* **199**, 18 (2000).
- [6] J.T. Yardley, *Introduction to Molecular Energy Transfer*, Academic, New York (1980).
- [7] W.F. Meggers, C.H. Corliss, B.F. Scribner. *Tables of spectral line intensities, Part I-arranged by elements*, NBS Monograph no.145. Washington, DC (1975).

Chapter 3

Laser-Induced Fluorescence Spectroscopy of Group 5, Niobium and Tantalum Mononitride Molecules (NbN, TaN)

3.1 Introduction

There has been considerable interest in new nitrides [1], and in particular, transition metal nitrides [2] due to their interesting properties [3,4] and applications [5,6] including catalysis [7], organometallic chemistry [8] and astrophysics [9]. This chapter presents laser-induced fluorescence (LIF) spectroscopic investigation on group 5, *d*-block transition metal mononitrides, NbN and TaN isovalent molecules in the free-jet. The isovalent molecules usually exhibit the same ground state electronic configuration and term symmetry. However, while the $^3\Delta$ state is the ground state for VN and NbN, the $^1\Sigma^+$ state is the ground state for TaN. The ground state of VN and NbN has a triple bond with two metal-localized, high-spin *d*-electrons, to give $^3\Delta$ term symmetry [10,11], which arise from the electron configuration $\pi^4(n+1)s\sigma^1nd\delta^1$ ($n = 3$ for VN and $n = 4$ for NbN). However, for TaN molecule, *ab initio* calculations [12] predicted the ground state as $^1\Sigma^+$, arising from the electronic configuration $1\pi^43\sigma^2$ while the low-lying $^3\Delta$ and $^1\Delta$ excited electronic states arising from the $1\pi^43\sigma^11\delta^1$ electronic configuration. The difference in the ground state of TaN molecules is due to the net relativistic stabilization of the $(n+1)s$ electron compared to the *nd* electron in Ta atom [13]. Using the data of relativistic and nonrelativistic orbital energies by Desclaux [14], Figure 3.1 illustrates the change in the orbital energies due to relativistic effects on the *nd* and $(n+1)s$ orbitals. Similar plot is given in Ref. [13]. It is clear from the Figure 3.1 that the relativistic effect stabilizes the 6s orbital in tantalum atom. The ratio of mean orbital radius $\langle r_{(n+1)s} \rangle / \langle r_{nd} \rangle$ at the numerical relativistic Dirac-Fock level [14] for the V, Nb and Ta are 2.63, 1.92 and 1.67. It is also evident from these values that the radial overlap for the *nd*

and $(n+1)s$ orbitals is larger for tantalum and this results in better s - d hybridization and greater d -orbital involvement in the bonding.

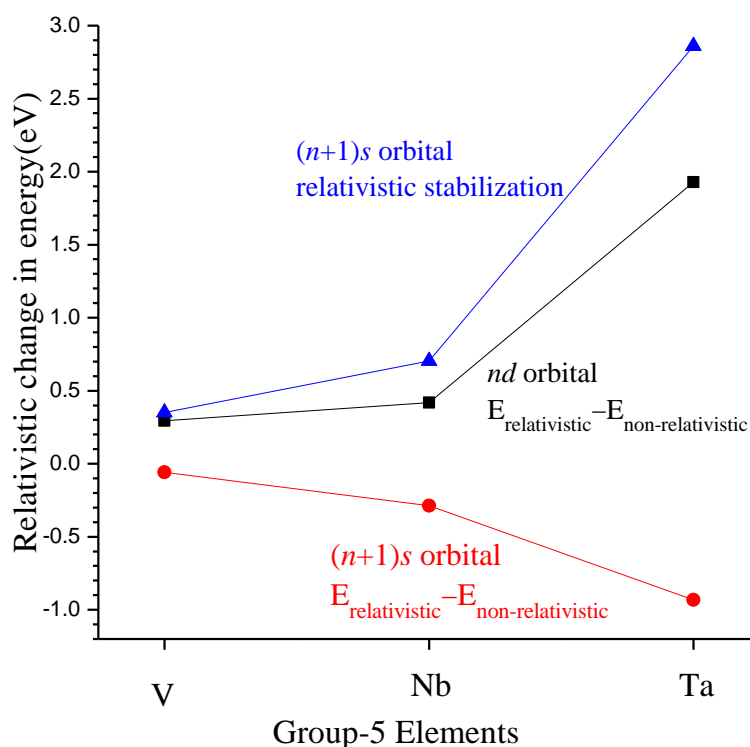


Figure 3.1 Change in the atomic orbital energy due to relativistic effects in the group 5 transition metals.

This trend in the ground state symmetry is obviously not particular to the group 5, d -block transition metal mononitride molecules; but similar trends are also observed in their isovalent carbide and oxide molecules (see Table 3.1).

Table 3.1 Comparison among the ground state electronic configuration of group 5 transition metal monocarbides, mononitride and monoxides.

Group 5d transition metal monocarbide, mononitride and monoxide molecules		
VC	VN	VO
$1\sigma^2 2\sigma^2 1\pi^4 1\delta^1$, $^2\Delta_{3/2}$ Ref. [15]	$1\sigma^2 2\sigma^2 1\pi^4 3\sigma^1 1\delta^1$, $^3\Delta_1$ Ref.[10]	$1\sigma^2 2\sigma^2 1\pi^4 3\sigma^1 1\delta^2$, $^4\Sigma^-$ Ref. [16]
NbC	NbN	NbO
$1\sigma^2 2\sigma^2 1\pi^4 1\delta^1$, $^2\Delta_{3/2}$ Ref. [17]	$1\sigma^2 2\sigma^2 1\pi^4 3\sigma^1 1\delta^1$, $^3\Delta_1$ Ref. [11]	$1\sigma^2 2\sigma^2 1\pi^4 3\sigma^1 1\delta^2$, $^4\Sigma^-$ Ref. [18]
TaC	TaN	TaO
$1\sigma^2 2\sigma^2 1\pi^4 3\sigma^1$, $^2\Sigma^+$ Ref. [19]	$1\sigma^2 2\sigma^2 1\pi^4 3\sigma^2$, $^1\Sigma^+$ Ref. [12]	$1\sigma^2 2\sigma^2 1\pi^4 3\sigma^2 1\delta^1$, $^2\Delta_{3/2}$ Ref. [20]

The difference in the electronic structure of these isovalent group 5 transition metal mononitride molecules prompted us to take up this study. The VN [21] and NbN [22,23] molecules also exhibit isoconfigurational second-order spin-orbit interactions which is

revealed in the asymmetric spin-orbit splitting of the $^3\Pi (nd\pi^1 nd\delta^1)$ and $^3\Delta ((n+1)s\sigma^1 nd\delta^1)$ states ($n = 3$ for VN and $n = 4$ for NbN). An isoconfiguration second-order spin-orbit interaction disturbs the symmetric spin-orbit structure and poses difficulty in identifying the spin components, even in the low energy range. The isoconfigurational spin-orbit interactions in the $^3\Pi$ and $^3\Delta$ states of NbN are investigated and discussed in this Chapter along with investigations on other low- and high-lying excited electronic states. The spin-orbit effects are expected to be even stronger in Ta ($\zeta_{5d} = 1699 \text{ cm}^{-1}$, where ζ is the spin-orbit constant in atom) than Nb ($\zeta_{4d} = 524 \text{ cm}^{-1}$) [24] and thus the electronic structure of TaN is expected to be much more complex. The strong spin-orbit coupling in TaN molecule may heavily mix many of the terms and only Ω remains a good quantum number, thus exhibit Hund's case (c), especially for high-energy electronic states and this hinders the identification of the term manifold of the electronic state.

Moreover, recently there has been interest in heavy polar diatomic molecules [25] and molecular ions [26] in search of the permanent electron electric dipole moment (eEDM), which provide a direct test of parity- and time-reversal symmetry violation. It was recently pointed out that the heavy polar diatomic molecules in paramagnetic $^3\Delta_1$ electronic states could be exploited to increase the current eEDM limit [27]. The nuclear magnetic quadrupole moment (MQM) can lead to a permanent atomic or molecular EDM, which can be exploited in an endeavor to measure MQM-induced EDMs. The TaN molecule being heavy and polar, identified as the prime candidate for measurement of MQM-induced EDM in its metastable $^3\Delta_1$ state with longer radiative lifetime [25]. The longer lifetime offers the larger coherence time which is important to enhance the sensitivity to an eEDM signal. The deformed ^{181}Ta ($I = 7/2$) nucleus is expected to have a strongly enhance MQM due to the collective effect [28] which is also the cause [29] of the large nuclear electric quadrupole moment (EQM = $+317 \text{ fm}^2$) of ^{181}Ta . Detailed spectroscopic information to prepare the molecule in

the EDM important molecular state, in particular $a^3\Delta_1$ state of TaN is required. Thus, spectroscopic information on the electronic structure of the promising molecular candidate are of paramount importance for EDM experiments [30,31]. In view of this, we explored the spectroscopic parameters of the ground, low-energy including $a^3\Delta$ state and high-energy excited electronic states of TaN molecule.

Section 3.2 of this Chapter provides a brief account of the experimental details employed in the study, while Section 3.3 and 3.4 describes the detailed analysis and results obtained in our study on the electronic structure of NbN and TaN molecules. Section 3.5 concludes the Chapter by summarizing the important results.

3.2 Experiment

The NbN and TaN molecules were produced in a pulsed free-jet apparatus, details of which are already discussed in Chapter 2. In brief, laser-produced target metal (Niobium/Tantalum) plasma was reacted with 2% ammonia seeded in helium in the throat of the pulse valve to produce metal mononitrides (NbN/TaN) molecules. The free-jet was probed by a tunable dye laser at right angles to the beam expansion axis about 50 mm downstream from the nozzle. The resulting LIF was collected orthogonal to both the free-jet and dye laser beam axes by a lens system. The fluorescence was dispersed by a monochromator and subsequently detected by a Peltier cooled photomultiplier tube. An output signal from the photomultiplier was amplified by a 1 GHz bandwidth amplifier, integrated by a gated integrator, and stored on a computer.

The excitation spectra were obtained by scanning the wavelength of the pulsed dye laser having spectral bandwidth of $\sim 0.08 \text{ cm}^{-1}$. The monochromator was used as a broadband filter and was parked at a fixed wavelength, where the fluorescence terminating either to the ground or an excited state was strongest. Transition wavenumbers were calibrated with an absolute precision of $\sim 0.1 \text{ cm}^{-1}$ using a commercial wavelength meter as well as the laser

wavelength calibration facility of the dye laser utilizing Ne optogalvanic spectral lines and also known atomic lines of Nb I/Ta I [32] appeared in the spectra. Dispersed fluorescence (DF) spectra were obtained by exciting the isolated rotational lines of the observed excitation bands. Typical spectral line widths, FWHM, were of the order $50\text{--}100\text{ cm}^{-1}$ in the DF spectra, depending on spectral region at the moderate resolution and the accuracy of the DF wavenumber measurement is $\sim 10\text{ cm}^{-1}$. The radiative lifetimes of the excited electronic states were also recorded by acquiring fluorescence decay curve for 128 pulses on a 200 MHz digital storage oscilloscope. We have used naturally abundant ammonia in our experiments. Niobium has single natural isotope ^{93}Nb , while natural isotopic abundance of Tantalum is ^{180}Ta (0.01%) and ^{181}Ta (99.99%). Thus, the spectra of only the $^{93}\text{Nb}^{14}\text{N}$ and $^{181}\text{Ta}^{14}\text{N}$ isotopologue were observed in our experiments.

3.3 Spectroscopic Investigation of NbN in the Visible Region

3.3.1 Literature Survey

The spectra of NbN molecule have been studied extensively over the years by employing various experimental techniques starting from the emission spectrum recorded on a photographic plate [33,34,35], the IR-spectrum of NbN isolated in an argon matrix [36], intracavity laser spectroscopy [37], laser spectroscopy at sub-Doppler resolution [22,23] to the emission spectrum recorded by a Fourier transform spectrometer [38,39]. Some high quality *ab initio* calculations were also performed [11,40,41,42], which predicted the internuclear distance, ionization potential, dissociation energy, dipole moment and spectroscopic properties of the ground and low-lying electronic states. The first electronic spectrum of a $^3\Phi - ^3\Delta$ transition in the red wavelength region was recorded by Dunn and Rao in 1969 [33]. The complex and widespread hyperfine structure were observed in the gas phase optical spectra of NbN, as the $^{93}_{41}\text{Nb}$ has nuclear spin $\mathbf{I} = 9/2$ and the largest nuclear magnetic moment, 6.1436 nuclear magneton, among the stable nuclei. The large hyperfine

splitting observed in the outer two spin components, i.e. ${}^3\Phi_4 - {}^3\Delta_3$, ${}^3\Phi_2 - {}^3\Delta_1$ subbands prevented the rotational analysis of the spectrum, except for the central spin component, ${}^3\Phi_3 - {}^3\Delta_2$. This was also in agreement with an a_β coupling case (see Chapter 1) in NbN. The hyperfine resolved spectrum was studied later by Féménias *et al.* [34] at higher resolution. They found that the high J lines had more hyperfine splitting than expected from the extrapolation of hyperfine effects from the low J lines. This was attributed to the spin uncoupling of one of the states causing further hyperfine effects. The rotational analyses of the 0–0 of ${}^3\Phi - {}^3\Delta$ bands were published by Pazyuk *et al.* [37] and Féménias *et al.* [35]. Féménias *et al.* [35] carried out a rotational analysis of this transition. They assigned this transition as $A^3\Phi - X^3\Delta$ and reported molecular constants for both the states. The asymmetry of energy separations of the three subbands indicated perturbation of these states by nearby states of the same electronic configuration. However, in the absence of observation of the satellite subbands, none of the groups could determine spin-orbit intervals of the $X^3\Delta$ state, which was necessary to interpret the hyperfine structure. Azuma *et al.* [22] investigated a ${}^3\Phi - {}^3\Delta$ transition, which they renamed as $B^3\Phi - X^3\Delta$, at sub-Doppler resolution and determined the molecular constants and hyperfine parameters of the 0–0 band of $B^3\Phi - X^3\Delta$ transition. They determined the spin-orbit structure of the $X^3\Delta$ state, which was found to be asymmetric and this was explained by the isoconfiguration second-order spin-orbit interaction between the $a^1\Delta$ and $X^3\Delta_2$ states arising from the same electron configuration, $\delta\sigma$. The permanent electric dipole moments of NbN for the $X^3\Delta$ and $B^3\Phi$ states were determined experimentally by Fletcher *et al.* and the measured dipole moment compared well with their *ab initio* value for the $X^3\Delta$ state [42]. Subsequently, Azuma *et al.* [23] also carried out the rotational and hyperfine analyses of the 0–0 bands of the $C^3\Pi - X^3\Delta$, $e^1\Pi - X^3\Delta$ and $f^1\Phi - a^1\Delta$ transitions. They also discovered three low-lying states $c^1\Gamma$, $A^3\Sigma^-$ and $b^1\Sigma^+$ in the wavelength resolved dispersed fluorescence (DF) spectra. The term energies

of the $a^1\Delta$, $b^1\Sigma^+$, $c^1\Gamma$, $e^1\Pi$, and $f^1\Phi$ singlet states and spin components of the $A^3\Sigma^-$, $B^3\Phi$ and $C^3\Pi$ states were determined. The order and the term energies of the electronic states observed by Azuma *et al.* [23] matched well with the theoretical predictions of Langhoff and Bauschlicher [11]. Azuma *et al.* observed all the low-lying electronic states predicted in [11] except the $d^1\Sigma^+$ state arising from a $4d\delta^2$ electronic configuration, which Ram and Bernath [38] have observed later. Ram and Bernath [38] observed numerous electronic transitions between the low-lying singlet and triplet states reported earlier by Azuma *et al.* [23] in their emission spectroscopy work on NbN in the red and near infrared regions. Recently, Ram and Bernath [39] reinvestigated the emission spectrum of NbN in the region 8000–35,000 cm^{-1} and reported two groups of new bands. The bands observed in the region 18,000–20,000 cm^{-1} were assigned to a new $^3\Pi - X^3\Delta$ transition. Two of the three spin-orbit components of the $^3\Pi$ state $^3\Pi_{0^\pm}$ and $^3\Pi_1$ were observed to be heavily perturbed. Three additional bands in the region 24,000–26,000 cm^{-1} were assigned as the $\Delta\Omega = 0$ transitions from the ground state. Two of these three bands are perhaps subbands of a new $^3\Delta - X^3\Delta$ transition. Most of the excited levels observed in this work are affected by perturbations. The $^3\Delta$ ground state of NbN is derived from the electron configuration $5s\sigma^1 4d\delta^1$, which also gives a low-lying $^1\Delta$ state. The excitation of an electron from the $5s\sigma$ or $4d\delta$ molecular orbital to the higher Nb-centered orbital results in the other low-lying excited electronic states viz. $^1\Sigma^+$ ($5s\sigma^2$), $^1\Sigma^+{}^3\Sigma^-{}^1\Gamma$ ($4d\delta^2$), $^3\Phi_r$ $^3\Pi_r$ $^1\Pi$ $^1\Phi$ ($4d\delta^1 4d\pi^1$), $^3\Pi_r$ $^1\Pi$ ($5s\sigma^1 4d\pi^1$) and $^3\Delta_r$ $^1\Delta$ ($4d\delta^1 4d\sigma^1$). Langhoff and Bauschlicher [11] predicted all these states below 20,000 cm^{-1} except the $^1\Phi$ state and their predicted energies agreed well with the experiments [22,23,38]. The $^3\Pi_r$ and $^3\Delta_r$ states reported in Ref. [39] belong to the $5s\sigma^1 4d\pi^1$ and $4d\delta^1 4d\sigma^1$ configurations respectively. A schematic of the electronic states in their $v = 0$ vibrational quantum number and transitions of NbN, reported prior to the present work is shown in Figure 3.2

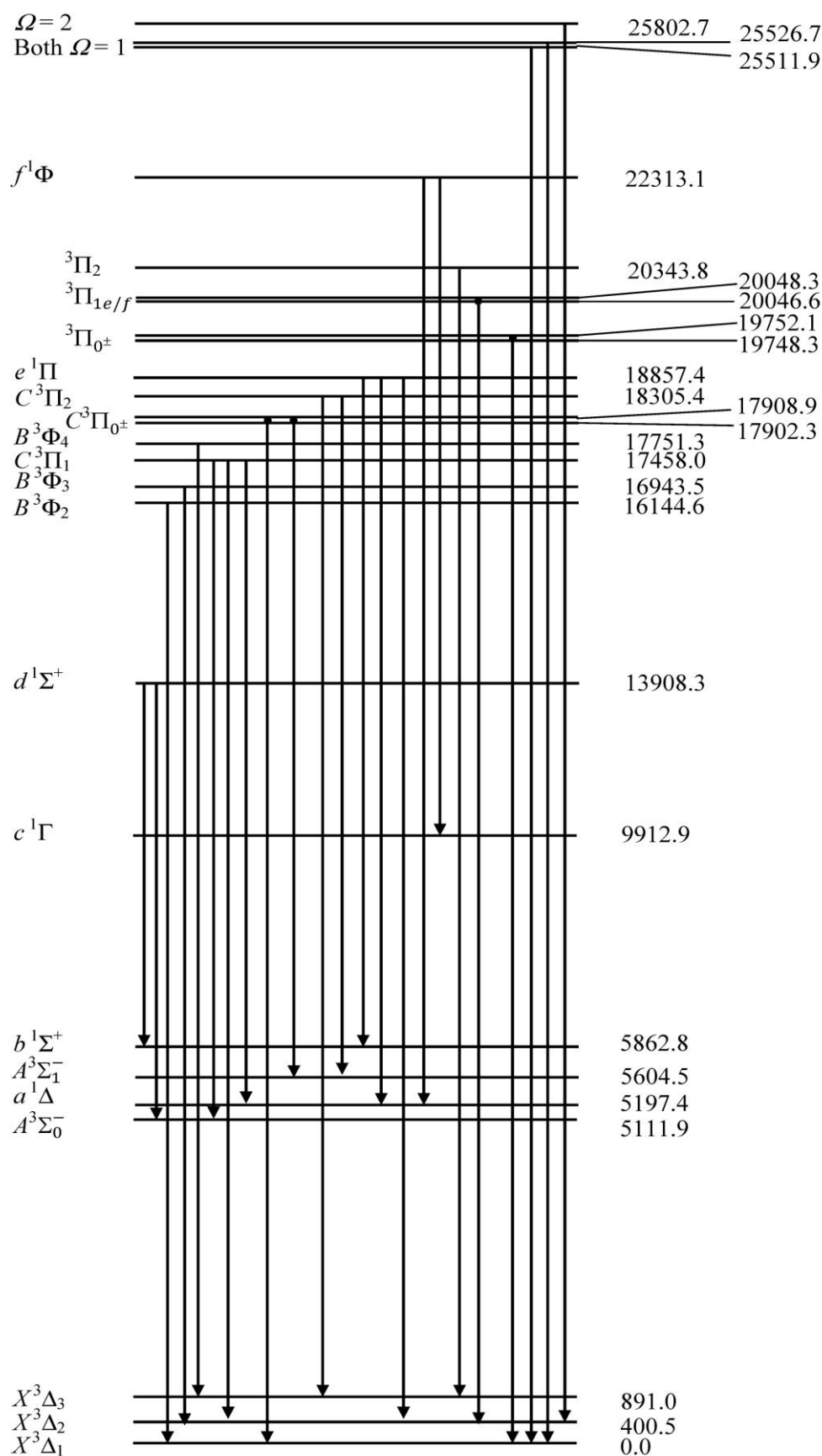


Figure 3.2 A schematic of the electronic states and observed transitions of NbN, reported prior to the present work.

3.3.2 LIF Spectroscopy of High-energy Excited Electronic States of NbN

Figure 3.3 shows a survey spectrum of NbN in the 18,000-21,000 cm^{-1} region.

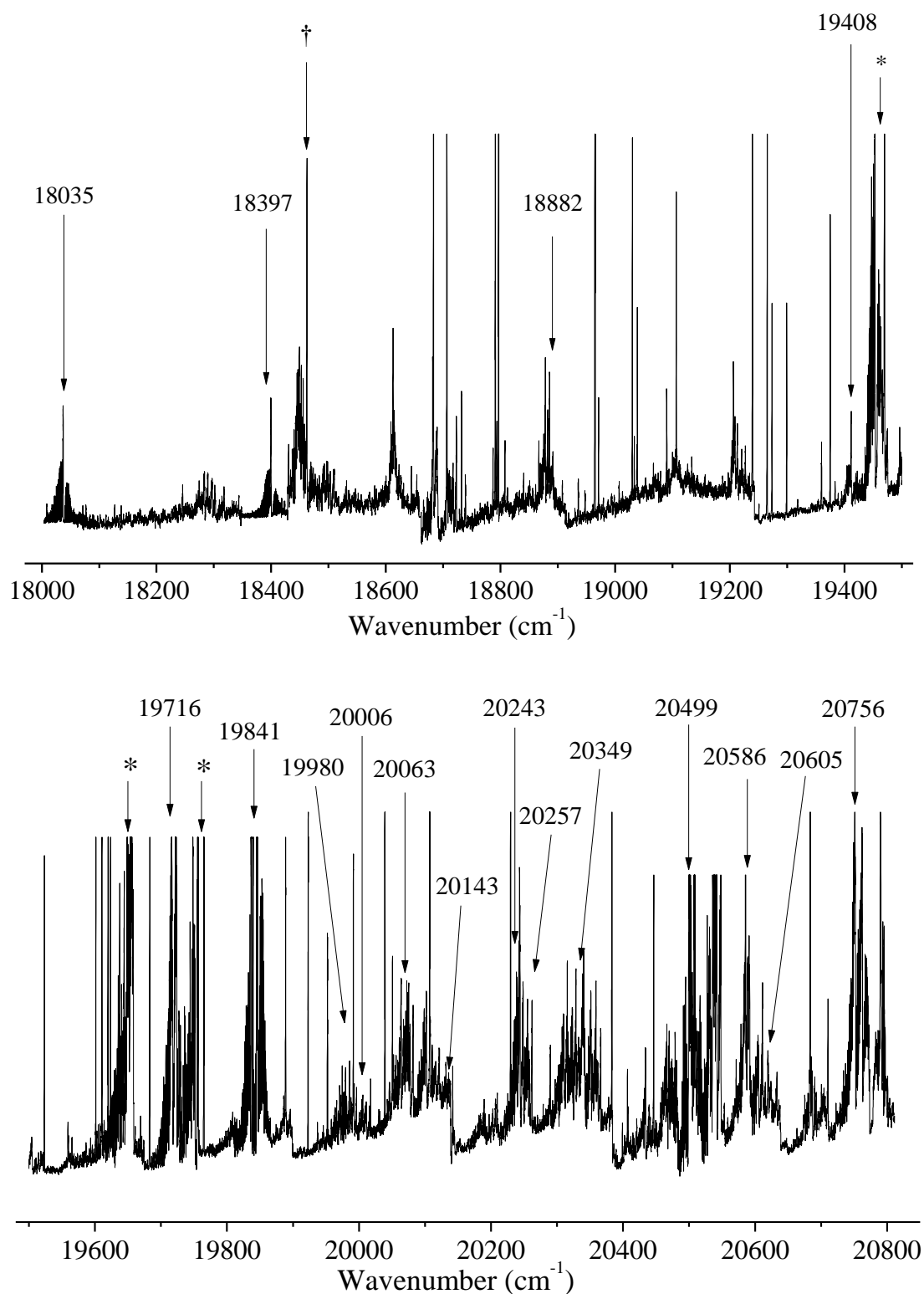


Figure 3.3 Laser-induced excitation survey spectrum of jet-cooled NbN molecule is shown in two parts. The band marked by '†' is reported in reference [23] and the bands marked by '*' are reported in reference [39]. Many atomic niobium (Nb I) lines are also appeared in the spectrum.

The details of findings of laser spectroscopy of NbN molecule under the present study are given in the two sections. The present section describes the account of the spin-orbit interaction and deperturbation analysis in the $\nu = 1$ of the $C^3\Pi_1/e^1\Pi$ electronic states along with the observation of two new $^3\Pi$ states and seven hot bands in the 18,000–21,000 cm^{-1} region. The rotationally resolved excitation spectra have been recorded, and the radiative lifetimes of the upper electronic states have been measured. While the next Section 3.3.3 describes determination of the equilibrium vibrational constants of the ground and low-lying electronic states from the DF studies.

We have observed all the bands originating from the ground $X^3\Delta$ state at the $\nu = 0$ or 1 vibrational levels, while the observed excited electronic state are either belong to a $^3\Pi$ state or designated by their Ω quantum number (in case(c)). The ground state, $X^3\Delta$, is well characterized from the previous studies and the molecular constants and spin-orbit splitting are accurately known [22,23,35,38,39]. The ground state has asymmetric spin-orbit splitting with a separation 400.5 and 491.0 cm^{-1} respectively between the $^3\Delta_1 - ^3\Delta_2$ and $^3\Delta_2 - ^3\Delta_3$ spin-orbit components. Thus we have treated these presently observed spin-orbit subbands separately. The laser excitation spectra have been reduced to a set of molecular constants using a nonlinear least-squares fitting procedure. The three spin-orbit components of the ground $X^3\Delta$ state are described by a Hamiltonian without spin-orbit constants of the following form [22]:

$$\text{For } X^3\Delta_1 \text{ substate: } H = T_1 + B_1Z - D_1(Z^2 + 2Z - 4) \quad (3.1)$$

$$\text{For } X^3\Delta_2 \text{ substate: } H = T_2 + B_2(Z - 2) - D_2(Z^2 - 12) \quad (3.2)$$

$$\text{For } X^3\Delta_3 \text{ substate: } H = T_3 + B_3(Z - 8) - D_3(Z^2 - 14Z + 52) \quad (3.3)$$

where T_i is the rotationless energy, B_i is the rotational constant, D_i is a higher order correction to B_i , $Z = J(J+1)$, and $i = 1, 2, 3$ indicates the Ω quantum number of the $^3\Delta_i$ substates i.e. $^3\Delta_1$,

$^3\Delta_2$, $^3\Delta_3$. The molecular constants of all the substates of the $X^3\Delta$ ground state have been constrained in the fits at the more accurate values reported by Ram and Bernath [39].

The excited state, $^3\Pi$ described in Section 3.3.2.b is represented by an effective Hamiltonian of the form [43],

$$\text{For } ^3\Pi_{0^\pm} \text{ substate: } H\left(\begin{smallmatrix} e \\ f \end{smallmatrix}\right) = T_0 \pm \frac{1}{2}x_0 + \left(B_0 \pm \frac{1}{2}b_0\right)(Z+1) - \left(D_0 \pm \frac{1}{2}d_0\right)(Z^2 + 4Z + 1) \quad (3.4)$$

$$\text{For } ^3\Pi_1 \text{ substate: } H\left(\begin{smallmatrix} e \\ f \end{smallmatrix}\right) = T_1 \pm \frac{1}{2}x_1 + \left(B_1 \pm \frac{1}{2}b_1\right)(Z+1) - \left(D_1 \pm \frac{1}{2}d_1\right)(Z^2 + 6Z - 3) \quad (3.5)$$

$$\text{For } ^3\Pi_2 \text{ substate: } H\left(\begin{smallmatrix} e \\ f \end{smallmatrix}\right) = T_2 + \left(B_2 \pm \frac{1}{2}b_2\right)(Z-3) - \left(D_2 \pm \frac{1}{2}d_2\right)(Z^2 - 4Z + 5) \quad (3.6)$$

where T_i is the rotationless energy; B_i and D_i are the rotational constant and its higher order correction respectively; x_i is the separation between the e and f levels at $J = 0$, as a result of J independent Λ -doubling and b_i and d_i are J dependent Λ -doubling splitting parameters. The $i = 0, 1, 2$ indicate the Ω quantum numbers of the $^3\Pi_i$ substates i.e. $^3\Pi_0$, $^3\Pi_1$, $^3\Pi_2$. The effective Hamiltonian matrix elements for the $^3\Pi$ state are similar to those recently used by Sbata and Schamps [43] in the analysis of the $a^3\Pi$ state of GaH. However, the Λ -doubling terms in our effective Hamiltonian matrix elements for the $^3\Pi_1$ substate have a slightly different form. Due to unusually large separation between the e and f parity levels in the few $^3\Pi_1$ upper state, it was necessary to add the x_1 , the J independent Λ -doubling parameter, not present in Hamiltonian of Ref. [43]. Without the x_1 parameter it was not possible to fit the $19,716 \text{ cm}^{-1}$ and $20,499 \text{ cm}^{-1}$ bands with e and f levels together.

The Hamiltonian for the excited states, described in Section 3.3.2.c, for which only Ω quantum number was determined, was represented by the following customary expression:

$$H\left(\begin{smallmatrix} e \\ f \end{smallmatrix}\right) = T + B(Z - \Omega^2) - D(Z - \Omega^2)^2 \pm \frac{1}{2}qZ \quad (3.7)$$

where q is the Ω -doubling parameter.

3.3.2.a Experimental and Theoretical Study of the Second-order Spin-orbit Interaction between the $C^3\Pi$ and $e^1\Pi$ States of NbN at $v = 1$ Vibrational Level

The NbN $C^3\Pi - X^3\Delta$ (1–0) band is recorded in the free-jet setup. While a slight asymmetry was observed in the spin-orbit interval of the ground state, the lower interval ($^3\Delta_2 - \Delta_1$) 46 cm^{-1} smaller than the upper one ($^3\Delta_3 - \Delta_2$), a huge spin-orbit asymmetry was observed in the $C^3\Pi$ $v = 0$ state [23]. The $C^3\Pi_1$ state was located 648 cm^{-1} below its unperturbed position. These irregularities in the $X^3\Delta$ ground and $C^3\Pi$ states were attributed to the isoconfigurational second-order spin-orbit interaction between the $\Omega = 2$ $X^3\Delta_2$ and $a^1\Delta$ states, and between the $\Omega = 1$ $C^3\Pi_1$ and $e^1\Pi$ states. The present work follows Azuma et al. [23] at the $v = 1$ level of these two singlet and triplet Π -states. The spin-orbit interaction between $v = 1$ of $C^3\Pi_1$ and $e^1\Pi$ states destroyed the symmetric splitting of $C^3\Pi$ substates. Unusually high 685 cm^{-1} spin-orbit interaction matrix element between them pushed the $^3\Pi_1$ substate below $^3\Pi_0$ component. Our *ab initio* calculations estimate $^3\Pi_2 - ^3\Pi_0$ separation 414 cm^{-1} , which is in an excellent agreement with the observed value 404 cm^{-1} , and places the $^3\Pi_1$ state 244 cm^{-1} below $^3\Pi_0$ state, in somewhat poor agreement with the experimental separation of 449 cm^{-1} . This error is primarily due to the error in our calculated unperturbed $^3\Pi - ^1\Pi$ energy separation. A global fit has been performed on the experimental data to determine the rotational constants for both the electronic states with their interaction parameters.

3.3.2.a(i) Description and Analysis of the Observed Bands

The $C^3\Pi - X^3\Delta$ (1–0) system lies at $18,000\text{--}19,500\text{ cm}^{-1}$ region with the $^3\Pi_{0^\pm} - X^3\Delta_1$ and $^3\Pi_2 - X^3\Delta_3$ subbands origins located respectively at 18882.4 (e/f parity averaged) and 18397.3 cm^{-1} (see Figure 3.3). The $^3\Pi_1 - X^3\Delta_2$ subband does not lie at the middle of the other two subbands and its band origin is located at 18035.8 cm^{-1} . The isolated R –, Q – and P – rotational branches were observed in all subbands with the same trend in intensity; $I_Q > I_P > I_R$.

Appearance of the rotational branches are consistent with the $\Delta A = -1$ transition. The Q -branch was observed mostly as a broad unresolved peak at low J in all the cases. They could not be traced at higher J except for a few high J lines in the ${}^3\Pi_{0^\pm} - X^3\Delta_1$ subband.

The Λ -doubling was observed in the ${}^3\Pi_{0^\pm} v = 1$ state, two Q -branches belonging to the e and f parity states, were located respectively at 18878.1 and 18885.7 cm^{-1} in the ${}^3\Pi_{0^\pm} - X^3\Delta_1$ subband. The f parity levels were chosen to lie at higher energy following the observation of Azuma *et al.* [23] in the $v=0$ $C^3\Pi_{0^\pm}$ state. The Λ -doubling was not observed in the other two spin components of the ${}^3\Pi$ state. The first rotational line in the R - and P -branches were observed isolated in the ${}^3\Pi_1 - X^3\Delta_2$ and ${}^3\Pi_2 - X^3\Delta_3$ subbands, which confirmed the assignment of the transition. In the ${}^3\Pi_{0^\pm} - X^3\Delta_1$ subband, only $R_{ff}(1)$ line was observed isolated. The J -assignments were confirmed from the lower state combination difference fit. Rotational lines up to $P(33)$ and $R(27)$ in both the e/f parities for the ${}^3\Pi_{0^\pm} - X^3\Delta_1$, $P(26)$ and $R(19)$ in the ${}^3\Pi_1 - X^3\Delta_2$, $P(23)$ and $R(20)$ in the ${}^3\Pi_2 - X^3\Delta_3$ subbands were observed. First few rotational lines of the R - and P -branches of the ${}^3\Pi_2 - X^3\Delta_3$ subband are broad because of large hyperfine structure in the ground state. All three bands are well behaved in the sense that there are no local rotational perturbations in the spectra except irregularity in the spin-orbit splitting. The $e^1\Pi - X^3\Delta_2$ band is located at 19408.5 cm^{-1} (see Figure 3.3). Single R -, Q - and P -branch rotational lines are present in the spectrum with the Q -branch most intense and then the P -branch. The J assignments of the rotational lines were carried out by identifying the first line in the R - and P -branches and the lower state combination differences. Rotational lines up to $R(13)$ and $P(14)$ were identified. Rotational lines in the Q -branch could be traced up to $J'' = 13$, $J'' = 2-4$ lines were observed as a broad peak and $J'' = 5-7$ lines were partially resolved.

Table 3.2 Molecular constants (in cm^{-1}) and radiative lifetimes for the excited electronic states of NbN.

Band Origin (cm^{-1}) ^a	Assignment	$v'-v''$	T_v	x	B	$D \times 10^5$	$b \times 10^2$	$d \times 10^5$	$q \times 10^2$	τ (ns)
18882.38(1) ^a	$C^3\Pi_{0^+} - X^3\Delta_1$	1-0	18882.38(1)	-6.07(1)	0.49284(12)	0.048(21)	-	-	-	122(4)
18035.83(1)	$C^3\Pi_1 - X^3\Delta_2$	1-0	18436.33(1)	-	0.49214(4)	0.031(6)	-	-	-	92(4)
18397.29(1)	$C^3\Pi_2 - X^3\Delta_3$	1-0	19288.29(1)	-	0.49277(6)	0.195(9)	-	-	-	92(4)
19408.47(1)	$e^1\Pi - X^3\Delta_2$	1-0	19808.97(1)	-	0.49083(31)	0.94(15)	-	-	-	107(4)
20756.32(1)	$^3\Pi_{0^+} - X^3\Delta_1$	0-0	20756.32(1)	-10.80(2)	0.47569(17)	0.104(49)	-0.130(12)	-	-	66(4)
20499.60(2)	$^3\Pi_1 - X^3\Delta_2$	0-0	20900.1(1)	-2.38 (3)	0.45586(43)	3.55 (23)	-1.464(86)	6.29 (45)	-	119(9)
20349.33(1)	$^3\Pi_2 - X^3\Delta_3$	0-0	21240.3(1)	-	0.48360(8)	0.146(13)	-	-	-	65(5)
19841.51(7)	$^3\Pi_{0^+} - X^3\Delta_1$	0-0	19841.51(7)	-9.13(1)	0.48796(4)	0.100(3)	-0.083(2)	-	-	95(4)
19716.08(1)	$^3\Pi_{1_{eff}} - X^3\Delta_2$	0-0	20116.6(1)	-1.31(2)	0.46932(26)	2.91(9)	1.31(2)	-	-	60(4)
19980.69(2)	$\Omega=2 - X^3\Delta_3$	0-1	21905.65(2)	-	0.42404(41)	-2.1(2)	-	-	-0.104(15)	207(8)
20006.16(2)	$\Omega=0 - X^3\Delta_1$	0-1	21039.91(2)	-	0.45006(34)	-2.35(9)	-	-	-	225(10)
20063.03(1)	$\Omega=1 - X^3\Delta_2$	0-1	21497.59(1)	-	0.48045(33)	3.08(14)	-	-	-	95(4)
20143.61(2)	$\Omega=2 - X^3\Delta_3$	0-1	22068.57(2)	-	0.47260(13)	0.19(2)	-	-	-	54(3)
20243.33(1)	$\Omega=1 - X^3\Delta_2$	0-1	21677.89(1)	-	0.44855(23)	-0.099(67)	-	-	-	130(4)
20257.81(2)	$\Omega=1 - X^3\Delta_2$	0-1	21692.37(2)	-	0.43597(97)	-1.25(87)	-	-	-	257(15)
20586.65(1)	$\Omega=0^+ - X^3\Delta_1$	0-1	21620.40(1)	-	0.44959(30)	0.41(12)	-	-	-	-
20605.27(2)	$\Omega=0^- - X^3\Delta_1$	0-1	21639.02(2)	-	0.45987(59)	1.44(40)	-	-	-	80(4)

^aNumbers in parentheses denote one standard deviation in the last quoted digits.

First we fitted all these bands individually using PGOPHER software [44]. The term energy, molecular constants and radiative lifetime values of these bands are listed in the Table 3.2. Further, global fit of the (1–0) bands of the $C - X$ and $e - X$ transitions together were performed using the Hamiltonian for a ${}^3\Pi - {}^3\Delta$ transition defined in the PGOPHER software [44]. The rotational Hamiltonian was chosen on the \mathbf{R}^2 form. A ${}^1\Pi$ and a ${}^3\Pi_1$ state, for which $\Delta M = \Delta \Sigma = 0$ but $\Delta S = 1$, can interact through the $l_{iz}s_{iz}$ part of the spin-orbit Hamiltonian [24] $\hat{H}_{SO} = \sum_i a_i l_i \cdot s_i = \sum_i a_i \left[l_{iz} \cdot s_{iz} + \frac{1}{2}(l_i^+ s_i^- + l_i^- s_i^+) \right]$, where a is an operator that acts only on the radial part of the wave function. This results in the nonzero off-diagonal spin-orbit matrix elements, $A^{(2)} = \langle e^1\Pi | \hat{H}_{SO} | C^3\Pi \rangle$ between these two states. The energy matrix of the upper state is formed by the Hamiltonians of the $e^1\Pi$ and $C^3\Pi$ states as the diagonal and $A^{(2)}$ as the off-diagonal matrix elements in the PGOPHER software. The Hamiltonian for the lower $X^3\Delta$ state was taken from Ref. [22]. Approximately 260 peak positions of the rotational lines, mostly of R - and P -branches of the $C - X$ and $e - X$ subbands and few Q lines of the $e - X$ band were included in the fit. A few blended rotational lines of the ${}^3\Pi_{0^\pm} - X^3\Delta_1$ subband were given less weight in the fit. The rotational constants were determined by varying the spectroscopic constants for the $C^3\Pi \nu = 1$ and $e^1\Pi \nu = 1$ states and the interaction matrix element. The accurate rotational constants for the ground state were taken from the previous work [22] and held fixed in the fit. Initially the standard deviation of the fit was obtained as 0.11 cm^{-1} . However, this did not fit the rotational line positions of the $e^1\Pi - X^3\Delta_2$ band within the experimental accuracy. Adding higher-order terms in the diagonal matrix elements did not improve the fitting error. However, the inclusion of the centrifugal distortion spin-orbit interaction term, $A_D^{(2)}$, brought the average fitting error down to 0.05 cm^{-1} . Molecular constants for the $\nu = 1$ of the $C^3\Pi$ and $e^1\Pi$ states including the interaction terms are provided in Table 3.3. Figure 3.4 shows the observed

spectrum for the (1–0) $C^3\Pi_1 - X^3\Delta_2$ subband and the spectrum simulated with the molecular constants listed in Table 3.3.

Table 3.3 Rotational molecular constants for the deperturbed $C^3\Pi$ ($v = 1$) and $e^1\Pi$ ($v = 1$) states of NbN along with the interaction parameter. Values in cm^{-1} . T is the term energy, B , D , A and o are respectively rotational, rotational centrifugal distortion, spin-orbit and lambda doubling constants. $A^{(2)}$ and $A_D^{(2)}$ are respectively the second-order spin-orbit and its centrifugal distortion constants.

Parameter	$C^3\Pi$ ($v = 1$)	$e^1\Pi$ ($v = 1$)
T	18654.8278(70) ^a	18729.381(17)
B	0.492437(48)	0.48920(17)
$10^6 D$	0.296(60)	0.81(34)
A	206.2941(41)	
o	3.8083(53)	
	Interaction parameter	
$A^{(2)}$	685.36(1)	
$10^3 A_D^{(2)}$	-2.21(1)	

^a Numbers in parentheses denote one standard deviation in the last quoted digits.

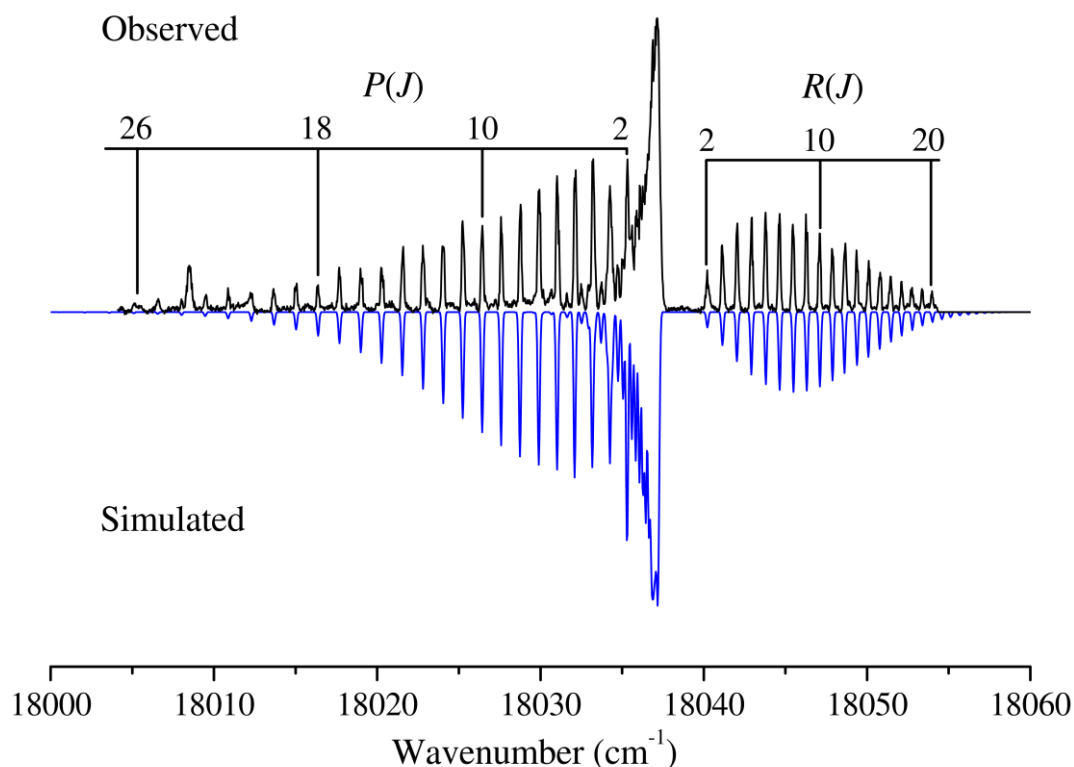


Figure 3.4 The experimental and simulated spectrum of the (1–0) $C^3\Pi_1 - X^3\Delta_2$ subband.

3.3.2.a(ii) Method of Calculation: Spin-orbit Interaction

There was one previous calculation by Langhoff and Bauschlicher [11] on the spectroscopy of the low lying electronic states of NbN, but to the best of our knowledge there

haven't been any *ab initio* calculations of the NbN spin-orbit levels. . In the present work, we focused on the $X^3\Delta$ and $C^3\Pi$ spin-orbit splittings. In all of our wavefunctions, the inner 28 electrons on Nb are described using the relativistic effective core potential (ECP28MDF) of Peterson et al. [45]. The remaining 13 electrons are represented explicitly using the cc-pVnZ-PP basis, n = T, Q and 5 [45]. The ECP that was used not only replaces the low-lying core electrons but also incorporates scalar and spin-orbit relativistic effects. The N atom is represented by the Dunning [46] all electron aVnZ basis. The $4s^2$ and the $4p^6$ orbitals on Nb and the $1s^2$ on N are kept doubly occupied in all calculations, leaving 10 valence electrons. The $^3\Delta$ state has a triple bond, a lone pair on N and two singly occupied orbitals. The valence electron configurations are $1\sigma^2$ (N2s) $2\sigma^2$ (bond) $1\pi_x^2$ (bond) $1\pi_y^2$ (bond) $3\sigma^1$ (5s) & either δ_+ or δ_- . Since we are interested in the spin-orbit levels, it is important to symmetrize the molecular orbitals so they were determined using the state averaged CASSCF procedure where we used the natural orbitals from the average of the four states $^3\Delta_{xy}$, $^3\Delta_{x^2-y^2}$, $^1\Delta_{xy}$, $^1\Delta_{x^2-y^2}$. Further correlation was added using the singles and doubles from the CASSCF wavefunction. The $^1\Pi_x$ and $^1\Pi_y$ states obtain from the $^3\Delta$ states by exciting the $3\sigma(5s)$ electron to a $2\pi_x$ ($\sim 5p_x$) and by exciting the δ_{\pm} electron to a $2\pi_x$ resulting in the configurations $1\sigma^2$ (N2s) $2\sigma^2$ (bond) $1\pi_x^2$ (bond) $1\pi_y^2$ (bond) $(2\pi_x\delta_+ - 2\pi_y\delta_-)$ and $1\sigma^2$ (N2s) $2\sigma^2$ (bond) $1\pi_x^2$ (bond) $1\pi_y^2$ (bond) $3\sigma(5s)2\pi_x(\sim 5p_x)$ with the corresponding configurations for the $^1\Pi_y$ and $^3\Pi_y$. As with the $^3\Delta$ calculations we determined the MO's for the $^3\Pi$ calculations by using a state averaged MCSCF over the $^1\Pi_x$, $^3\Pi_x$, $^1\Pi_y$ and $^3\Pi_y$ states. The subsequent MRCI included all singles and doubles with respect to this MCSCF function. The diagonal and off-diagonal spin-orbit matrix elements for both the $^3\Delta$ and $^3\Pi$ states were computed using the MRCI wavefunctions. All calculations used the MOLPRO [47] suite of programs.

3.3.2.b Bands Originating From the $v'' = 0$ of the $X^3\Delta$ State

In this section, observation of two new $^3\Pi$ states is presented. One of the $^3\Pi$ states is observed with all the three spin components, $^3\Pi_{0^\pm}$, $^3\Pi_1$ and $^3\Pi_2$, respectively at term energies 20,756.32, 20,900.1 and 21,240.3 cm^{-1} . The $^3\Pi_1$ spin-orbit component of this state is found to be mixed and was the reason for the observed asymmetric spin-orbit splitting of the $^3\Pi$ state. Another $^3\Pi$ state is observed with only two electronic transitions, 0–0 of $^3\Pi_{0^\pm} - X^3\Delta_1$ and $^3\Pi_1 - X^3\Delta_2$ with band origin at 19,841.5 and 19,716.1 cm^{-1} . These intense bands are located less than 100 cm^{-1} to the blue side of the respective subbands of the $^3\Pi - X^3\Delta$ transitions reported by Ram and Bernath [39], which are also observed in this work (see Figure 3.3). The $^3\Pi_2 - X^3\Delta_3$ 0–0 subband due to third spin component of this newly observed $^3\Pi$ state could not be detected, even though the relevant spectral region was searched carefully. These two $^3\Pi$ states are discussed in the following two sections.

3.3.2.b(i) $^3\Pi$ states with $^3\Pi_{0^\pm}$, $^3\Pi_1$ and $^3\Pi_2$ spin-orbit components, respectively, at term energies 20,756.32, 20,900.1 and 21,240.3 cm^{-1}

We report three new intense bands with *R* heads at 20,364.3, 20,508, and 20,771.8 cm^{-1} which have been respectively assigned as 0–0 bands of the $^3\Pi_2 - X^3\Delta_3$, $^3\Pi_1 - X^3\Delta_2$ and $^3\Pi_{0^\pm} - X^3\Delta_1$ transitions involving a new $^3\Pi$ state. The carrier of these bands was established both by the ground state combination differences of the rotational lines of the excitation spectra and the ground state vibrations observed in the wavelength dispersed fluorescence spectra.

The three newly observed bands showed *P*–, *Q*– and *R*– branches with the *Q*–branch being the most intense. The excitation spectrum for the 20,771.8 cm^{-1} band is shown in Figure 3.5. The *P*–branch was more intense than the *R*–branch indicating $\Delta\Lambda/\Delta\Omega = -1$ for these transitions. The 20,771.8 and 20,508 cm^{-1} bands showed double headed structure

indicating a large separation in the e and f parity rotational levels. The isolated R lines with low J showed broad structure, especially for the 20,364.3 and 20,771.8 cm^{-1} bands. This line broadening is due to the large hyperfine splitting, observed earlier in the NbN molecule [22,23,33,34,35], indicative of an a_β coupling case.

The matrix element used to fit the $^3\Pi - X^3\Delta$ transitions are given in equation (3.1–3.6). The observed band origins, their assignments and radiative lifetimes of the associated upper states are listed in Table 3.2. The assignment of the bands, discussed below in detail, was based on the observation of a number of branches and the first line, combination differences for the lower state, relative band intensity and radiative lifetime of the upper state. Rotational quantum number assignments of the P - and R -branches were doubling [35], thus the assignments of the Q branches were also based on the lower state combination differences of PQ and RQ transitions. Figure 3.5 shows the rotational quantum number assignments of the P -, Q -, and R -branches for the 20,771.8 cm^{-1} band. The 20,771.8 cm^{-1} band showed two R -, Q -, and P -branches viz., R_{ff} , Q_{fe} , P_{ff} and R_{ee} , Q_{ef} , P_{ee} . The two Q heads of the band were separated by 10.7 cm^{-1} .

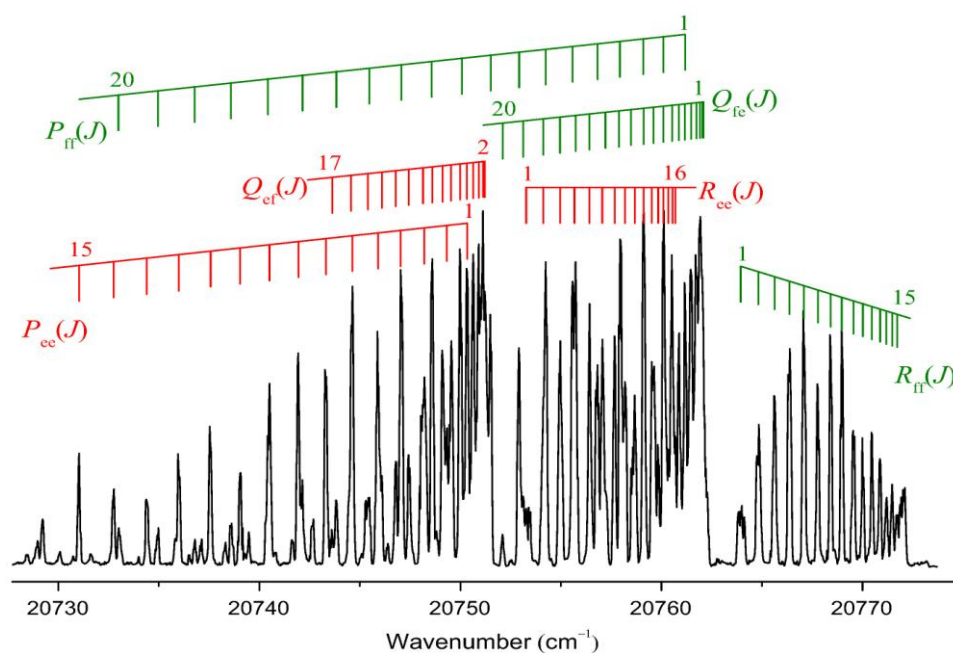


Figure 3.5 Rotational structure of the $^3\Pi_{0\pm} - X^3\Delta_1$ ($v',0$) band of the jet-cooled NbN molecule.

The lower state combination differences for both the P - and R -branches of this band coincided within the experimental precision with those of the $v = 0$ level of the $X^3\Delta_1$ state observed earlier [23,35,39]. The excitation spectrum (see Figure 3.5) showed appearance of the first lines, isolated $R_{ff}(1)$ and blended $P_{ff}(1)$ with $Q_{fe}(6)$ line and slightly blended $R_{ee}(1)$ with $Q_{fe}(19)$ and $P_{ee}(1)$ with $Q_{ef}(6)$. However, the low J members of the Q -branch were unresolved. This observation confirmed that the upper state has total angular momentum, $\Omega = 0$ with a large separation between the e and f parity levels and thus it is assigned as $^3\Pi_{0^\pm}$. The e and f labels for the two parities of the upper state were chosen arbitrarily. The f parity levels were chosen to lie at higher energy as observed in the $C^3\Pi_{0^\pm}$ by Azuma et al. [23]. The isolated R_{ff} lines with low J showed broadening due to the large hyperfine splitting in the $X^3\Delta_1$ state [22,23,34]. The $R_{ff}(1)$ line had a measured line width (FWHM) of $\sim 0.44\text{cm}^{-1}$. The broadening subsequently decreased with an increase in J . Since the hyperfine structure was not resolved in our spectra due to the limited resolution (0.1 cm^{-1}) of the laser, the center of the peak of each broadened rotational line was used for the rotational analysis. The DF spectra were also recorded in the 450–900 nm wavelength range by exciting a single rotational level of the upper state to support its identity (Section 3.3.3). The DF spectrum showed two vibrational progressions. After looking at the information on the low-energy states of NbN published earlier [23,38], we observed that, in addition to the fluorescence to $v = 0$ –4 of the $X^3\Delta_1$ state, the upper state also fluoresced with moderate intensity to $v = 0, 1$ and 3 of the $A^3\Sigma_1^-$. The fluorescence to the $A^3\Sigma_1^-$ state with the moderate intensity and the short radiative lifetime of 64 ns further confirmed the $^3\Pi_{0^\pm}$ assignment of the upper state.

The $20,508\text{ cm}^{-1}$ band also showed six branches, viz. R_{ff} , Q_{fe} , P_{ff} and R_{ee} , Q_{ef} , P_{ee} . The two Q heads of the band were separated by 2.7 cm^{-1} . The lower state combination differences for both the R - and P -branches of this band coincided with in the experimental precision with those of the $v = 0$ level of the $X^3\Delta_2$ state. The appearance of the first $R_{ff}(2)$ line and $P_{ff}(2)$

blended with the $Q_{fe}(7)$ line confirmed the upper state assignment as ${}^3\Pi_1$ with an unusually large separation between the e and f parity levels. The low J rotational lines were considerably less broadened ($\sim 0.2 \text{ cm}^{-1}$) than those of the band at $20,771.8 \text{ cm}^{-1}$. This further confirms the assignment of the transition as ${}^3\Pi_1 - X^3\Delta_2$ since the middle spin-orbit (SO) components of the triplet state (${}^3\Pi_1$ and ${}^3\Delta_2$ respectively for the ${}^3\Pi$ and ${}^3\Delta$ states) has a Σ quantum number equal to 0 and thus has a minimum hyperfine splitting (see equation 3.8) among the triplet multiplets [22,23]. Nuclear magnetic hyperfine Hamiltonian is given by,

$$H_{mag.hfs} = \frac{\Omega[aA + (b+c)\Sigma]}{2J(J+1)} [F(F+1) - I(I+1) - J(J+1)] \quad (3.8)$$

where, a , b , c are the hyperfine parameters. The radiative lifetime of the ${}^3\Pi_1$ state was measured as 119 ns, which is much higher in comparison to that of the other two spin-orbit components, ${}^3\Pi_{0\pm}$ and ${}^3\Pi_2$. This suggests a mixing of singlet character in the ${}^3\Pi_1$ component, probably with a ${}^1\Pi$ state. The mixing in the ${}^3\Pi_1$ state is also evident from the marked departure of its rotational constant from the other two spin-orbit components (see Table 3.2). However, no local perturbations were observed in this band. The second-order spin-orbit interaction of the $C^3\Pi_1$ sub-state with the $e^1\Pi$ state and that of $X^3\Delta_2$ with the $a^1\Delta$ state, causing highly asymmetric spin structure, have been reported earlier in NbN by Merer's group [22,23] and also in our work presented in the earlier section of this thesis. The $20,364.3 \text{ cm}^{-1}$ band showed only three branches P , Q and R . The e and f parity levels of this sub-state were not resolved at the employed resolution because of the negligible lambda doubling which is characteristic of a ${}^3\Pi_2$ state. The appearance of the first $R(3)$ and $P(3)$ lines and the lower state combination differences for both the R - and P -branches confirmed the assignment of the band to a ${}^3\Pi_2 - {}^3\Delta_3$ transition. The low J members of the Q branch were unresolved. The first R line, $R(3)$, showed the largest magnitude of broadening ($\sim 0.74 \text{ cm}^{-1}$) due to the largest hyperfine splitting in the highest Ω components in the triplet multiplets (see equation 3.8) [22]. This further confirms the band assignment as ${}^3\Pi_2 - X^3\Delta_3$. The

radiative lifetime of 65 ns for the $^3\Pi_2$ state is very similar to that of the $^3\Pi_{0\pm}$ component. The $^3\Pi_2$ state also weakly fluoresced to the $A^3\Sigma_1^-$ state.

We have observed three spin-orbit components of the $^3\Pi$ state: the $^3\Pi_{0\pm}$ and $^3\Pi_1$ components have large and moderate e/f parity level splitting respectively and the $^3\Pi_2$ component has negligible e/f splitting. Energetically these three spin-orbit subbands showed regular ordering of the spin-orbit components but asymmetric spacing with the central component ($^3\Pi_1 - X^3\Delta_2$) red shifted by about 53 cm^{-1} from the midpoint of the pattern.

3.3.2.b(ii) (0–0) band of $^3\Pi_{0\pm} - X^3\Delta_1$ and $^3\Pi_1 - X^3\Delta_2$ transitions with band origin at 19,841.5 and 19,716.1 cm^{-1} .

Two strong bands with R heads at 19,724.2 and 19,865.5 cm^{-1} were observed. Rotational analysis indicated that these transitions fit in $\Delta Q = -1$ with the ground state of NbN as the lower state. These bands are assigned as 0–0 of $^3\Pi_1 - X^3\Delta_2$ and $^3\Pi_{0\pm} - X^3\Delta_1$ subbands of $^3\Pi - X^3\Delta$ transition. A compressed portion of the spectrum in this region is presented in Figure 3.6. The rotational structure in each subband consists of P –, Q – and R – branches with intensities $I_Q > I_P > I_R$, conforming $\Delta A = -1$ for these transitions. The first line in the P –, Q – and R –branches was used to assign these transitions. The ground-state vibrations $v'' = 0$ –2 were observed in the wavelength-resolved DF spectrum. This did not help in identifying the spin component of the lower state as no satellite transitions $\Delta\Sigma \neq 0$ were found. In the 19,724.2 cm^{-1} band, lines terminating to the e and f parity levels with same J of the upper electronic state are close to each with the two R heads separated by only 0.75 cm^{-1} . First line in the Q – and R –branches were observed isolated and identified as $Q(2)$ and $R(2)$ in both the e and f parity levels.

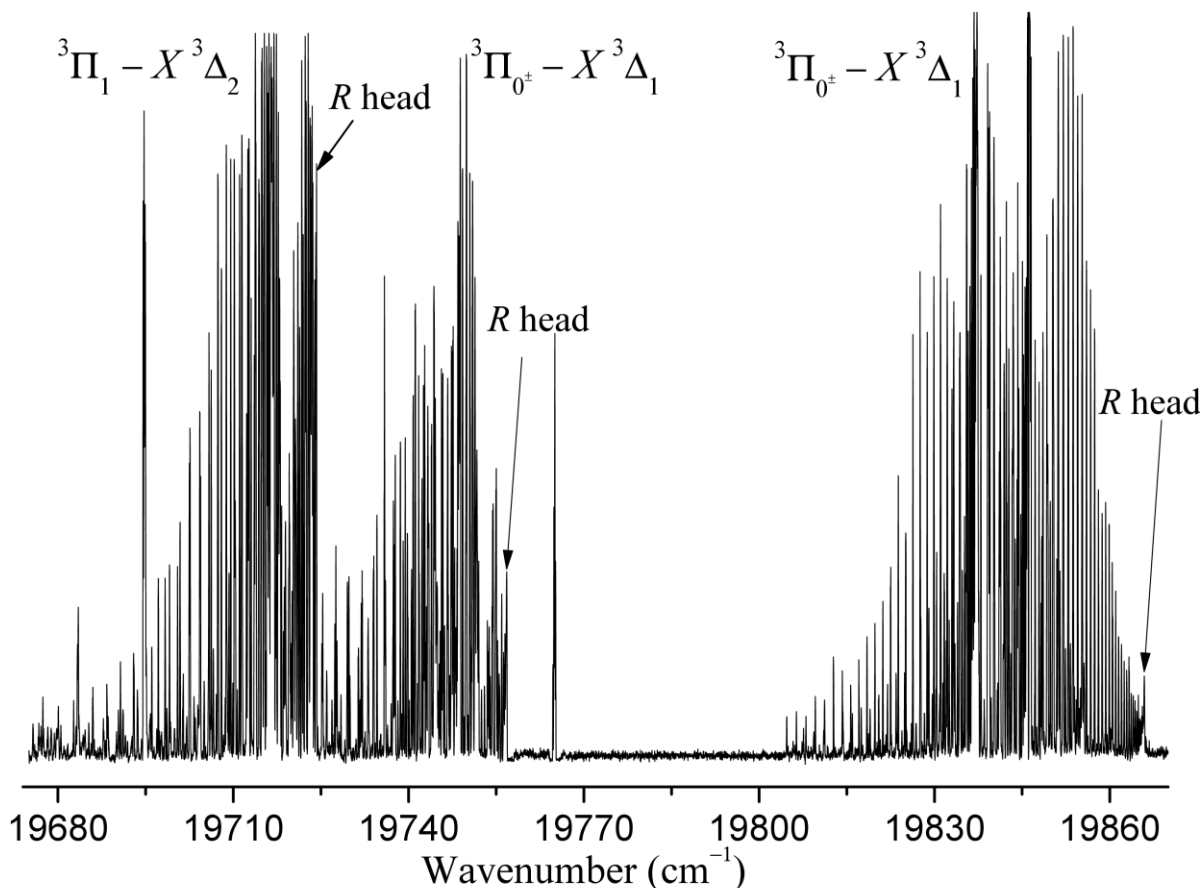


Figure 3.6 A compressed portion of the spectrum showing 0-0 bands of the two subbands of ${}^3\Pi - X^3\Delta$ transition and 0-0 of ${}^3\Pi_{0^\pm} - X^3\Delta_1$ subband at 19750 cm^{-1} reported in reference [39].

The ${}^3\Pi_{0^\pm} - X^3\Delta_1$ subband has two well separated R and Q heads with the R heads belonging to the e - and f -parity separated by 10.4 cm^{-1} . While the first R line, $R(1)$, could be identified isolated in both the e and f components, the first five lines in the Q branch were not resolved and piled up in a convoluted peak width of approximate 0.6 cm^{-1} . This is due to the B constant of the upper state being close to the lower state. Rotational lines up to $P_{ee}(24)$, $Q_{ef}(28)$, $R_{ee}(35)$, $P_{ff}(29)$, $Q_{fe}(21)$ and $R_{ff}(31)$ were observed in this band. The large e/f separation of 9.1 cm^{-1} and the energy spacing of 1.9 cm^{-1} between the $R(1)$ and the simulated position of $Q(1)$ line in the Q branch envelop confirmed the ${}^3\Pi_{0^\pm} - X^3\Delta_1$ assignment of this transition.

The e and f labels of the upper state of these bands were chosen arbitrarily. The f parity levels were chosen to lie at higher energy following the observation of Azuma *et al.* [23] in

the $C^3\Pi_{0^\pm}$ state. No rotational perturbation was observed in the bands and the e and f parity components of the upper state were fitted together to determine the rotational constants of the upper state. The matrix element used to fit the $^3\Pi_{0^\pm} - X^3\Delta_1$ and $^3\Pi_1 - X^3\Delta_2$ transitions are given in equation (3.1–3.6). The molecular parameter and radiative lifetimes of the associated upper states are listed in Table 3.2.

3.3.2.c Hot Bands: Bands Originating From the $\nu'' = 1$ of the $X^3\Delta$ State

Seven bands with considerable lower intensity, approximately one-fourth to one-fifth the intensity of the $^3\Pi - X^3\Delta$ bands reported in Section 3.3.2.b were observed. The DF spectra and the weak intensity of these bands indicated that they originated from the $\nu'' = 1$ of the ground state spin components. The radiative lifetime of three of the bands are measured to be in the range of 200–260 ns and the remaining in the range of 50–130 ns. The excited electronic states in these bands are defined by only Ω quantum number. The matrix element used to fit these transitions are given in equation (3.1–3.3, 3.7). The molecular parameters of the associated upper states are listed in Table 3.2. The details of individual bands are as follows:

3.3.2.c(i) Band origin $19,980.7\text{ cm}^{-1}$, $\tau = 207(8)\text{ ns}$, [0–1 of $\Omega = 2 - X^3\Delta_3$]

The R -branch is very weak with lines from $R(3)$ to $R(7)$ piled up in a single broad peak of width $\sim 0.4\text{ cm}^{-1}$. The branch forms a head at $R(5)$ and few returning lines from $R(8)$ to $R(12)$ could be identified. The intensity in the Q -branch is similar to the P -branch and isolated lines from $Q(3)$ to $Q(14)$ and $P(3)$ to $P(12)$ could be identified. The first few low J rotational lines have larger width of $\sim 0.5\text{ cm}^{-1}$, probably due to the large hyperfine splitting observed in case of the outer spin components of the ground state [22,23]. The appearance of the first P line, $P(3)$, is obvious from the higher intensity and larger width of the $Q(6)$ peak blended by $P(3)$. The DF spectra showed two peaks corresponding to the $\nu'' = 2$ and 3 of the lower state to the red side of the laser excitation peak ($\nu'' = 1$) and a very weak peak to the

blue side ($v'' = 0$). The fluorescence intensity was maximum at the $v'' = 3$ peak. A weak peak at 490 cm^{-1} blue side to this peak was also observed. This peak belonged to the satellite transition to the $X^3\Delta_2$ substate, which indicated the lower state of the band as $X^3\Delta_3$. Thus, the DF spectra confirmed the lower state as $v'' = 1$ of the $X^3\Delta_3$. The intensity pattern in the rotational branches, $I_Q > I_P > I_R$ indicated $\Delta\Omega = -1$, $\Delta A = -1$ in this transition.

3.3.2.c(ii) Band origin $20,006.2 \text{ cm}^{-1}$, $\tau = 225(10) \text{ ns}$, [0–1 of $\Omega = 0 - X^3\Delta_1$]

The P –, Q – and R –branches were observed with the P –branch intensity, a little higher than the R –branch. The first lines in the R – and Q –branches were observed isolated with an energy separation of 1.6 cm^{-1} . In case of $^{2S+1}\Phi_2 - X^3\Delta_1$ transition, this separation is $4B'' (= 1.99 \text{ cm}^{-1})$ whereas for $^{2S+1}\Pi_0 - X^3\Delta_1$ transition the same is $4B'$. This confirms the transition as $^3\Pi_0 - X^3\Delta_1$. We could identify rotational lines up to $P(10)$, $Q(20)$ and $R(12)$, wherein lines from $R(9)$ to $R(12)$ were collected into a single peak to form R head. DF did not show any peak to the blue side of the excitation peak to confirm the lower state as $v'' \neq 0$. However, the weak intensity of the band and the lower state combination differences indicate the lower state as $v'' = 1$ of $X^3\Delta_1$. No e/f splitting was observed in this band in contrast to the large e/f splitting observed in other transitions with $^{2S+1}\Pi_0$ as the upper state.

3.3.2.c(iii) Band origin $20,063.0 \text{ cm}^{-1}$, $\tau = 95(4) \text{ ns}$, [0–1 of $\Omega = 1 - X^3\Delta_2$]

This band consists of P –, Q – and R –branches with $I_Q > I_P \approx I_R$ and the rotational lines up to $P(17)$, $Q(15)$ and $R(14)$ were identified. The first lines in each of the rotational branches were observed isolated and identified as $P(2)$, $Q(2)$ and $R(2)$, which showed the Ω quantum numbers of the lower and upper states as 2 and 1, respectively. Rotational analysis and the DF, which showed a clear peak to the blue side of the laser excitation peak confirmed the lower state as $v'' = 1$ of $X^3\Delta_2$.

3.3.2.c(iv) Band origin 20,143.6 cm⁻¹, $\tau = 54(3)$ ns, [0–1 of $\Omega = 2 - X^3\Delta_3$]

This band consists of P –, Q – and R –branches with $I_Q > I_P > I_R$ indicating $\Delta\Omega = -1$, $\Delta A = -1$. First couple of lines in the R –branch were observed weak and broad with width >0.5 cm⁻¹, which indicated the transition originated from the outer spin components of the ground state, i.e. either $X^3\Delta_1$ or $X^3\Delta_3$. Since $R(1)$ peak was not observed, the lower state involved in the transition is $X^3\Delta_3$. First three lines in the Q –branch also were collected in the same peak with a combined width >0.7 cm⁻¹. The peak at $Q(10)$ is broad and of considerably higher intensity compared to the adjacent Q lines. This showed that the $Q(10)$ peak was blended with the first P line, which was $P(3)$. The rotational lines up to $P(16)$, $Q(29)$ and $R(14)$ were observed. A weak peak was observed at one ground-state vibrational quanta to the blue side of the laser excitation peak in the DF, which showed that the transition originated from the $\nu'' = 1$ of the lower state. Based on the above observations, the transition has been assigned as 0–1 of $\Omega = 2 - X^3\Delta_3$.

3.3.2.c(v) Band origin 20,243.3 cm⁻¹, $\tau = 130(4)$ ns, [0–1 of $\Omega = 1 - X^3\Delta_2$]

This band also consisted of PQR rotational branches with $I_P > I_R$. Only few rotational lines $J'' = 2-7$ in the R , 2–13 in the P and 2–19 in the Q branch could be identified. The DF showed a weak peak at one ground state vibrational quanta to the blue side of the laser excitation peak and also a few vibrations of the low-lying $a^1\Delta_2$, $b^1\Sigma^+$ and $A^3\Sigma_0^-$ states. The vibrational term values of the $a^1\Delta_2$, $b^1\Sigma^+$ and $A^3\Sigma_0^-$ states obtained from the DF spectra are discussed in Section 3.3.3. Rotational analysis and DF confirmed the transition as 0–1 of $\Omega = 1 - X^3\Delta_2$.

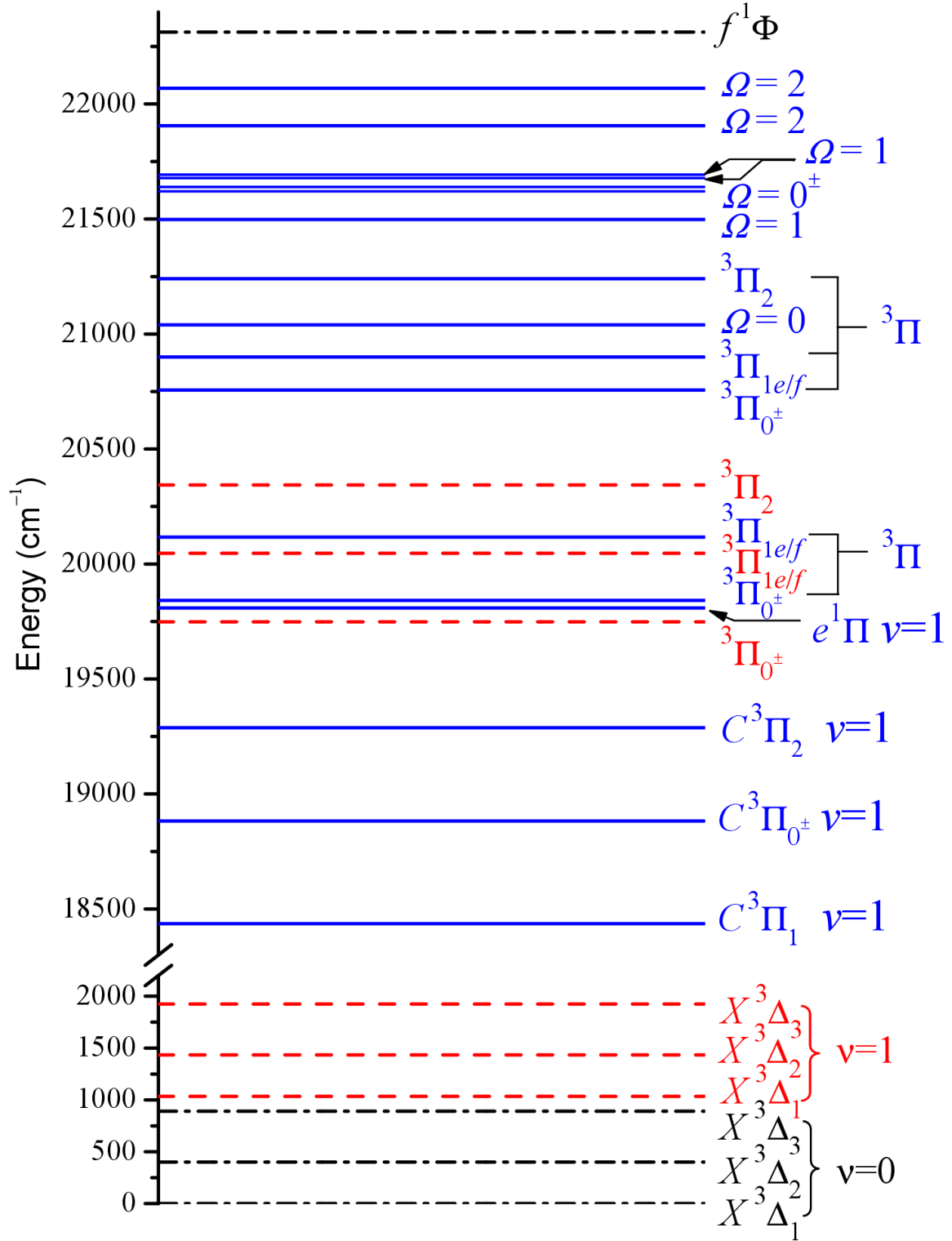


Figure 3.7 Schematic energy level diagram of the presently known observed electronic states of NbN in the energy region relevant to excitation study of this work. The dashed dotted lines (— · — ·) represent the states observed by Azuma *et al.* [23] and the states observed by Ram and Bernath [38] are marked by dashed lines (— — —). The solid lines (—) are the states from this work.

3.3.2.c(vi) Band origin 20,257.8 cm⁻¹, $\tau = 257(15)$ ns, [0–1 of $\Omega = 1 - X^3\Delta_2$]

This band is located only 14.5 cm⁻¹ to the blue side of the above mentioned 20,243.3 cm⁻¹ band and possesses similar rotational structure and DF pattern. However, the lifetime of this band is considerably higher 257 ns compared to 130 ns of the previous band. Only few rotational lines up to $P(9)$, $Q(10)$ and $R(9)$ were observed. Based on the identification of the first lines in the PQR branches and from the DF, this band was also assigned as 0–1 of $\Omega = 1 - X^3\Delta_2$.

3.3.2.c(vii) Band origins 20,586.7 and 20,605.3 cm⁻¹, $\tau = 80(4)$ ns, [0–1 of $\Omega = 0^\pm - X^3\Delta_1$]

This is a double R -headed band with $I_Q > I_P \approx I_R$ indicating $\Delta\Omega = \pm 1$. The two R heads corresponding to the e and f components are widely separated by 18.6 cm⁻¹. The first lines in the R - and Q -branches of the e and f components were identified clearly as $R(1)$ and $Q(1)$, which together with the large e/f separation in the rotational branches established the transition as $\Omega' = 0^\pm - \Omega'' = 1$. The DF did not show any peak to the blue side of the laser excitation peak to confirm the vibrational quantum number of the lower state. However, the weak intensity of the band suggests that it originates from a higher vibrational level of the ground state. The combination differences suggests the lower state as $v'' = 1$ of $X^3\Delta_1$.

Schematic energy level diagram of the presently known observed electronic states of NbN in the energy region relevant to excitation study of this work is given in Figure 3.7.

3.3.3 Dispersed Fluorescence Studies on NbN and Observation of Vibrational Progression in the Low-lying States

Dispersed Fluorescence spectra of NbN from $^3\Pi_{0^\pm}$, state at $T_0 = 20,756.32(1)$ cm⁻¹ and a $\Omega = 1$ state at 21677.89(1) cm⁻¹ carried a lot of information and are given respectively in Figure 3.8 and 3.9. These DF spectra gave information about the vibrational levels of the $X^3\Delta$, $A^3\Sigma_0^-$, $A^3\Sigma_1^-$, $a^1\Delta$ and $b^1\Sigma^+$ states. Equilibrium vibrational constants for the $X^3\Delta$ ground and low-lying $A^3\Sigma_0^-$, $A^3\Sigma_1^-$, $a^1\Delta$ and $b^1\Sigma^+$ states are obtained by combining the present data on

vibrational term values obtained from the DF spectra with more accurate band origin data of Ram and Bernath [38,39] and are listed in Table 3.4.

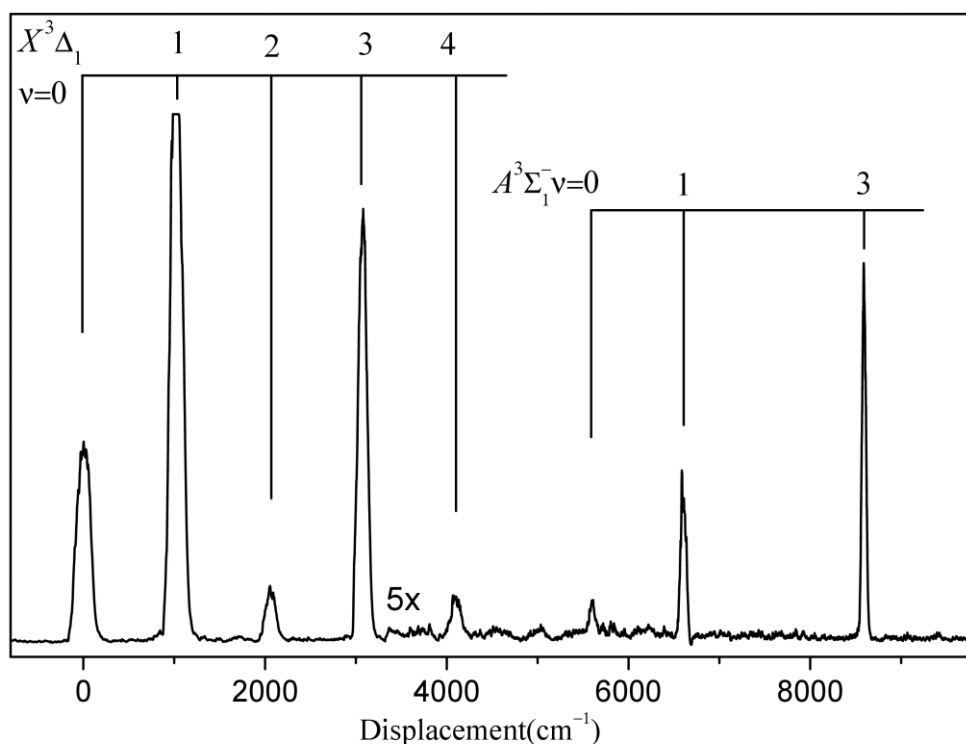


Figure 3.8 The DF spectrum obtained by exciting the isolated $P_{ff}(3)$ line of the ${}^3\Pi_{0^\pm} - X^3\Delta_1$ (0,0) band.

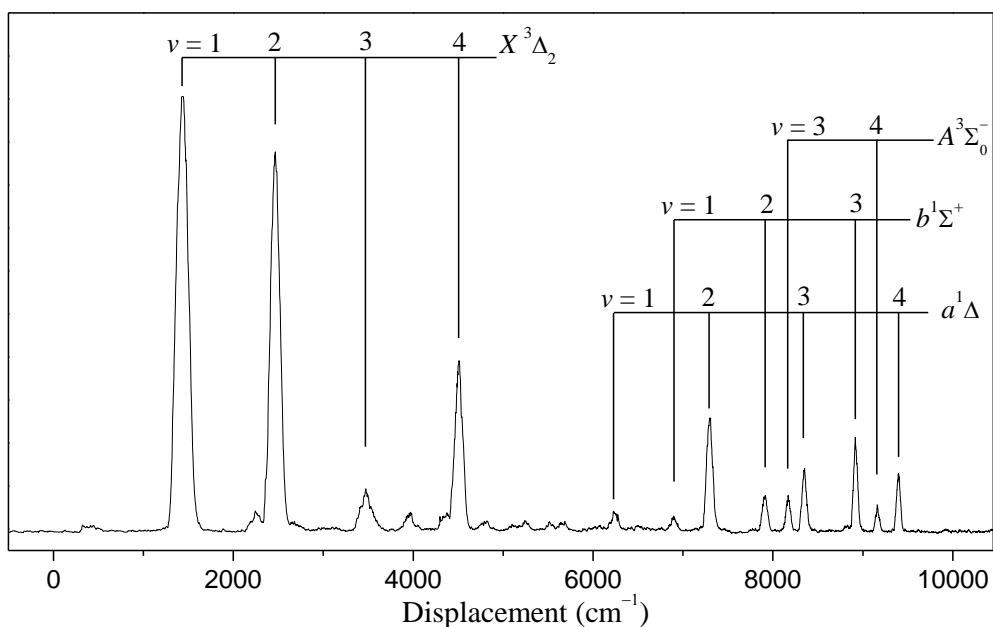


Figure 3.9 The DF spectrum obtained by exciting the isolated $Q(6)$ line of the $\Omega=1 - X^3\Delta_2$ (0,1) band.

Table 3.4 Vibrational term energies and equilibrium constants (in cm^{-1}) for the ground and low-lying states of NbN.

States	ν	T_v	T_e	ω_e	$\omega_e x_e$
$X^3\Delta_1$	0	0	0	1040.1(3) ^a	3.19(16)
	1	1033.7493(21) ^b			
		1036(7)			
	2	2063(5)			
	3	3079(4)			
	4	4098(4)			
$A^3\Sigma_0^-$	0	5111.8916(12) ^c	5122.8(2)		
	1	6128.4693(26) ^c		1016.578(3)	-
	2	7154(10) ^d			
	3	8168(10)			
	4	9161(10)			
$A^3\Sigma_1^-$	0	5604.53298(84) ^c	5625.8(2)	996.0(2)	-
		5600(5)			
	1	6600(4)			
	3	8593(5)			
$a^1\Delta$	0	5197.37374(93) ^c	5181.2(2)	1073.4(20)	5.06(99)
	1	6260.6461(19) ^c			
		6250(10)			
	2	7297(10)			
	3	8350(10)			
	4	9396(10)			
$b^1\Sigma^+$	0	5862.8389(15) ^c	5873.3(2)	1017.527(2)	-
	1	6880.3656(29) ^c			
		6890(10)			
	2	7908(10)			
	3	8916(10)			

^a Numbers in parentheses denote one standard deviation in the last quoted digits.

^b Term value from Ref. [39].

^c Term value from Ref. [38].

^d Calculated from Band origin value from Ref. [38] and our value of $\nu = 2$ of $b^1\Sigma^+$.

Prior to this work only $\Delta G_{1/2}$ value of the $X^3\Delta$ ground state [39] and few vibrational levels of the low-lying states were known. We see fairly good agreement between the term values measured directly in the present work from the DF spectra with those measured from the band origins for the ground and low-lying states. The vibrational constants at equilibrium for these states were determined by weighted least squares fitting of the vibration terms values to an anharmonic oscillator formula,

$$\Delta G = G(v) - G(0) = \omega_e v - \omega_e x_e v(v+1) \quad (3.9)$$

where v is a vibrational quantum number, $G(v)$ is the term value of the v^{th} vibrational level, ω_e is the harmonic and $\omega_e x_e$ is the anharmonic vibrational constants.

3.3.4 Results and Discussions

The spectra of $C^3\Pi - X^3\Delta$ (1–0) and $e^1\Pi - X^3\Delta_2$ (1–0) described in Section 3.3.2.a are found to be well behaved in the sense that no local rotational perturbations are found in any of the subbands. The sole irregularity is the depression of the central band, which is expected to lie halfway between the other two, in absence of the spin-spin and second-order spin-orbit interactions, lies 846.5 cm^{-1} below the $^3\Pi_{0^\pm} - X^3\Delta$ subband. The off-diagonal coupling between the $C^3\Pi_1$ and $e^1\Pi$ states, which causes this irregularity includes the spin-spin and second-order spin-orbit interactions. The separate contributions of these two effects could not be determined from the observed spectra. The magnitude of spin-spin interaction scales as $1/Z$, thus its importance for a heavy molecule like NbN is expected to be insignificant compared to the second order spin-orbit interaction. The second-order spin-orbit matrix element $\langle e^1\Pi | \hat{H}_{SO} | C^3\Pi \rangle = 685 \text{ cm}^{-1}$, which is larger than the A -constant ($= 206 \text{ cm}^{-1}$) of the $C^3\Pi$ state, pushed the central spin component 649 cm^{-1} from the halfway position of the other two. If the off-diagonal coupling is set to zero, the $C^3\Pi_1$ and $e^1\Pi$ states lie at $19,085.3$ and $19,161.4 \text{ cm}^{-1}$ respectively, i.e., the $e^1\Pi$ state occurring within the $^3\Pi$ manifold and just 76 cm^{-1} above the $^3\Pi_1$ component. These observations are similar in scale with the (0–0) band of this transition [23]. The $e - X$ system is a forbidden transition; it can only be observed owing to intensity borrowing from the nearby $C^3\Pi_1 - X^3\Delta_2$ subband through the mixing of the $e^1\Pi$ and $C^3\Pi_1$ states. We have estimated the composition of the $C^3\Pi_1$ and $e^1\Pi_1$ character in the eigenfunctions of the 2×2 system from the spectroscopic parameters, A and $A^{(2)}$ determined in the present work. We know that eigenfunctions of perturbed levels are described by [48]

$\psi_a = c\psi_1 - d\psi_2$ and $\psi_b = c\psi_1 + d\psi_2$; where the mixing coefficients are given by

$$c = \left(\frac{\sqrt{4|W_{12}|^2 + \delta^2} + \delta}{2\sqrt{4|W_{12}|^2 + \delta^2}} \right)^{1/2} \text{ and } d = \left(\frac{\sqrt{4|W_{12}|^2 + \delta^2} - \delta}{2\sqrt{4|W_{12}|^2 + \delta^2}} \right)^{1/2}.$$

Here W_{12} is the interaction matrix element and δ is the separation between the unperturbed levels. In the present case, $W_{12} = A = 206.3 \text{ cm}^{-1}$ and $\delta = 76 \text{ cm}^{-1}$. These values gives 40% mixing of $e^1\Pi$ character in $C^3\Pi_1$ state (3:2 ratio) and vice versa. Similarly, the composition of $a^1\Delta_2$ in $X^3\Delta_2$ was estimated and found to have negligible mixing because of the large separation between these states. It is reasonable to consider that the $e^1\Pi - a^1\Delta$ and $C^3\Pi_1 - X^3\Delta_2$ transitions have equal transition dipole matrix elements as both the upper and lower states are derived from the same electronic configuration. The comparison of fluorescence intensity of the triplet to triplet and triplet to singlet branch can be compared with the percentage mixing coefficient between these two states. The observed DF intensity from $v = 1$ of $C^3\Pi_1$ to $v = 1$ of $X^3\Delta_2$ and to $a^1\Delta_2$ is in 4:1 ratio and as expected it is in the reverse magnitude from the $e^1\Pi$ state to the same lower states. Thus the observed DF intensity ratio is in modest agreement with the calculated mixing ratio.

In our *ab initio* computation, the $X^3\Delta$ equilibrium bond length is calculated to be 1.649 \AA with the $^3\Delta - ^1\Delta$ splitting of 4805 cm^{-1} . At this bond length the first-order splitting is $\Delta E(\Omega_3 - \Omega_2) = \Delta E(\Omega_2 - \Omega_1) = 455 \text{ cm}^{-1}$ with $\Delta E(\Omega_3 - \Omega_1) = 910 \text{ cm}^{-1}$ in reasonable agreement with the experimental separation of 891.0 cm^{-1} . The second-order spin-orbit interaction mixes the Ω_2 levels of the $^3\Delta$ and $^1\Delta$ states via the calculated matrix element $\langle ^3\Delta_2 | \hat{H}_{SO} | ^1\Delta_2 \rangle = 465.3 \text{ cm}^{-1}$ (experimental = 467 cm^{-1} [22]) dropping the $^3\Delta_2$ level and increasing the $^1\Delta_2$ level by 45 cm^{-1} , in excellent agreement with the experimental value of 46 cm^{-1} [22] (see Figure 3.10(a)).

Figure 3.10 Comparison of experimental and theoretical study of the spin-orbit interaction between (a) the ground $X^3\Delta$ and $a^1\Delta$ states and (b) the $C^3\Pi$ and $e^1\Pi$ states of NbN at $v = 1$ vibrational level. Horizontal dashed lines (— —) are expected unperturbed positions and solid lines (—) are experimentally observed/calculated positions of the states. Experimental values in Figure 3.10(a) are taken from Ref. [22].

Now for the $^3\Pi$ states, the calculated equilibrium bond length is 1.65 Å with the $^3\Pi - ^1\Pi$ energy separation of 531.6 cm^{-1} . At this bond length, the first order splitting is $\Delta E(\Omega_2 - \Omega_1) = \Delta E(\Omega_1 - \Omega_0) = 206.8 \text{ cm}^{-1}$ with $\Delta E(\Omega_2 - \Omega_0) = 413.6 \text{ cm}^{-1}$ within reasonable agreement with the experiment value 400.4 cm^{-1} determined in the present work.. The second-order interaction mixes the Ω_1 levels of the $^3\Pi$ and $^1\Pi$ states via the calculated matrix element $\langle ^3\Pi_1 | \hat{H}_{SO} | ^1\Pi_1 \rangle = 641 \text{ cm}^{-1}$ (experimental = 685 cm^{-1}) dropping the $^3\Pi_1$ and lifting the $^1\Pi_1$ level by 428.3 cm^{-1} . This places the $^3\Pi_1$ level 221.5 cm^{-1} below the $^3\Pi_0$ in poor agreement with the experimental separation of 446 cm^{-1} (see Figure 3.10(b)). Most of this error can be traced to the calculated $^3\Pi - ^1\Pi$ energy separation of 531.6 cm^{-1} which is much larger than the experimental 76 cm^{-1} . Indeed, if we use the experimental energy difference and our calculated off diagonal matrix element, we calculate that the $^3\Pi_1$ level is 385 cm^{-1} below the $^3\Pi_0$, a substantial improvement. Increasing the basis to VQZ and V5Z has no effect on $\Delta E(\Omega_2 - \Omega_0)$ and as shown in Table 3.5 changes $\Delta E(\Omega_1 - \Omega_0)$ and the triplet-singlet separation $T_0 - S_0$ slightly. It's interesting to note that in contrast to VN [10], the $^3\Pi$ state of NbN has considerable multi configurational character. For example at $R = 1.65 \text{ Å}$ the $^3\Pi$ MCSCF function is $0.6216(2\pi_x\delta_+ - 2\pi_y\delta_-) + 0.3370(3\sigma 2\pi_x) + misc$, while at the MRCI level we have $0.540(2\pi_x\delta_+ - 2\pi_y\delta_-) + 0.530(3\sigma 2\pi_x) + misc$.

Table 3.5 Basis set dependence for energy separation in $^3\Pi/^1\Pi$ states; all entries are in cm^{-1} .

basis	$\Delta E(\Omega_2 - \Omega_0)$	$\Delta E(\Omega_1 - \Omega_0)$	$\Delta E(\Omega_1 - \Omega_2)$	$T_0 - S_0$	$\langle ^3\Pi_1 \hat{H}_{SO} ^1\Pi_1 \rangle$
VTZ	414	222	635	532	641
VQZ	414	232	646	505	644
V5Z	414	244	658	472	645

Further, from the rotationless term values of the $^3\Pi_Q$ substates as described in Section 3.3.2.b(i), it is evident that the upper state has regular spin-orbit ordering but with

asymmetric spin-orbit splitting. The spacing between $\Omega = 0-1$ and $1-2$ components are 143.8 and 340.2 cm^{-1} respectively. The radiative lifetimes of the $^3\Pi_0$ and $^3\Pi_2$ components are the same (65 ns), however that of $^3\Pi_1$ is substantially higher (119 ns) with respect to other two spin-orbit components. Also the values of rotational constants B for the $^3\Pi_0$ and $^3\Pi_2$ spin-orbit components are similar however; B is rather small for $^3\Pi_1$ substate (see Table 3.2). The effective rotational constant of the $^3\Pi_1$ substate departs significantly from Mulliken's formula [48], $B_{\text{eff};\Sigma} = B(1+(2B\Sigma/A\Lambda))$. These observations indicate that the $^3\Pi_1$ substate is mixed, most probably with a $^1\Pi$ state lying above it, which is not observed and characterized presently. The interaction of the observed $^3\Pi_1$ substate with that of the proposed $^1\Pi$ state would increase its radiative lifetime, lower the rotational constant and shift the $^3\Pi_1$ energetically down from its first-order position by about 98 cm^{-1} , resulting in the asymmetric spin-orbit splitting of the $^3\Pi$ state observed in the present work. We could not observe the spin-satellite branches to the ground state from the presently observed $^3\Pi$ state. This suggests that the presently observed $^3\Pi$ state follows the good Hund's coupling case (a).

In Section 3.3.2.b(ii), the rotational analysis places the $^3\Pi_{0\pm}$ and $^3\Pi_1$ levels respectively, at 19,841.5 and $20,116.6 \text{ cm}^{-1}$. The energy separation of 275.6 cm^{-1} between these two spin components is similar to the adjacent $^3\Pi$ states reported by Ram and Bernath [39]. Our effort to locate the $^3\Pi_2$ component did not succeed and thus, the spin splitting of this state could not be measured. Severe rotational perturbations were observed in the earlier reported [39] $^3\Pi_{0\pm}$ and $^3\Pi_{1\text{eff}}$ spin components located, respectively, at 19,750.3 and $20,047.5 \text{ cm}^{-1}$. The perturbations in these states were speculated possibly due to the interaction with some nearby state. Ram and Bernath [39] could not fit $^3\Pi_{0+}$, $^3\Pi_{0-}$ and $^3\Pi_{1e}$, $^3\Pi_{1f}$ substates together and also had to include higher order constants with non-physical values to minimize the least squares in the fit. Even though the presently observed $^3\Pi_{0\pm}$ and $^3\Pi_{1\text{eff}}$ states are only 91.2 and 69.1 cm^{-1} to the blue side of the corresponding states reported

in [39], no rotational perturbation was observed in the bands by the previously reported states. This indicates that the perturbing state (or states) which caused rotational perturbation to the previously reported bands remains still unidentified.

Seven weak 0–1 bands (Section 3.3.2.c) were observed, three of them having lifetime more than 200 ns and four of them having lifetime about 100 ns and less. The vibrational assignment of the upper states is based on our search scan extended to the lower wavenumber side up to $\sim 18,100 \text{ cm}^{-1}$, where no bands corresponding to these states were observed. The 0–0 bands are expected approximately 1000 cm^{-1} higher in energy. However, any of these bands were not observed while extending our survey scan up to $21,600 \text{ cm}^{-1}$. A possible reason for not observing these bands could be the low Franck-Condon factor associated with these vibrational transitions. This was evident in the DF spectra, where the blue side peak either observed extremely weak or not observed at all. The presence of the strong Q branches along with the P - and R -branches in all the transitions indicate $\Delta\Omega = \pm 1$. In general, $I_P > I_R$ observed in these bands suggest a Π symmetry of the upper states. Wherever a $\Omega = 2$ (or 0) spin component was identified, other spin components of the Π multiplet were expected. However, absence of regular energy spacing and different lifetimes of the upper states did not allow us to group them as the spin-orbit components of the Π state (or states) involved in these transitions.

Theoretical calculations together with the experimental evidence confirmed that the $X^3\Delta$ state of NbN has predominantly $4d\delta^1 5s\sigma^1$ character. This configuration also gives rise to a $^1\Delta$ state, which was experimentally detected as $a^1\Delta$. The promotion of $4d\delta^1$ or $5s\sigma^1$ electron results in other singlet and triplet states, namely, $5s\sigma^2$ ($^1\Sigma^+$), $4d\delta^2$ ($^1\Sigma^+$, $^3\Sigma^-$ and $^1\Gamma$) and $4d\delta^1 4d\pi^1$ ($^3\Phi$, $^3\Pi$, $^1\Pi$ and $^1\Phi$) states. All these states were predicted below $20,000 \text{ cm}^{-1}$ by Langhoff and Bauschlicher [11] and were experimentally observed by Azuma et al. [23] (see Figure 3.2). Ram and Bernath [39] proposed the $^3\Pi$ state, they observed in the $^3\Pi - X^3\Delta$

transition in the 18,000–20,000 cm^{-1} have $5s\sigma^1 4d\pi^1$ character, while the other $\Delta Q = 0$ bands in the 24,000–26,000 cm^{-1} originated from the $4d\delta^1 4d\sigma^1 {}^3\Delta - 4d\delta^1 5s\sigma^1 X^3\Delta$ transitions. The presently observed two ${}^3\Pi$ states were not predicted by theoretical studies. We have explored the possibilities of whether the presently observed states from the $v'' = 0$ and 1 of the $X^3\Delta$ state are the quintet states predicted by Langhoff and Bauschlicher [11] below 30,000 cm^{-1} . Theoretically, the ${}^5\Pi$ is the lowest quintet state to lie at 17,637 cm^{-1} following ${}^5\Sigma^-$, ${}^5\Delta$ and ${}^5\Phi$, respectively, at 19,015, 23,148 and 28,926 cm^{-1} . The ${}^5\Sigma^-$ state is not accessible from the $X^3\Delta$ ground state. The presence of strong Q branch in all of the presently observed transitions rules out the upper state being ${}^5\Delta$. Also the predicted ${}^5\Phi$ state is not expected to be observed in the presently studied range. The weaker bonds of these states resulted in a longer r_e value of 1.8–1.9 Å and smaller ω_e value of 689–879 cm^{-1} . Moreover, the transition probability for observing these quintet states from the ground state is extremely weak [11]. The r_0 of the upper states at 20,756.32, 20,900.1 and 21,240.3 cm^{-1} is 1.71, 1.74 and 1.69 Å, respectively. For another ${}^3\Pi$ state, the r_0 of the upper states associated with the two intense bands at 19,716.1 and 19,841.5 cm^{-1} is 1.72 and 1.68 Å, respectively. The r_0 value and the strong intensity observed in all these five bands rules out the possibility of the observed states having a quintet character. The upper states associated with some of the weak bands observed from $v'' = 1$ have bond length R value close to 1.8 Å. The absence of regular energy spacing among these bands and a widely varying lifetime did not permit us to group them in subbands. The potential energy curves (Figure 1) in [11] illustrate that only higher vibrational states of ${}^5\Pi$ are accessible from the ground state. Moreover, vibrational progression is expected in the presently studied range if higher vibrations of the ${}^5\Pi$ state were indeed accessed. However, as this was not the case, the possibility of having a quintet character for the presently observed states is rather weak.

3.4 Study of Electronic Structure of TaN

3.4.1 Literature Survey

There have been previous studies on TaN molecule in gas phase [49] identified several bands in electronic emission spectra, using a microwave discharge source. The bands were classified into singlet and triplet systems; however, symmetry of the ground state of TaN was not clear in their study. The studies in Ar matrix [50,51] determined the fundamental vibration. Ram et al. [12] investigated high-resolution emission spectra of TaN in the 3000–35,000 cm^{-1} region using a Fourier Transform Spectrometer. They also carried out *ab initio* calculations using internally contracted multireference configuration interaction (CMRCI) method and predicted the term energies (T_0), bond lengths (R_e), and vibrational constants (ω_e) of the excited electronic states up to energy 25,000 cm^{-1} . They predicted the ground state as $^1\Sigma^+$, arising from the electronic configuration $1\sigma^2 2\sigma^2 1\pi^4 3\sigma^2$ and the low-lying $^3\Delta$ and $^1\Delta$ states arising from the $1\sigma^2 2\sigma^2 1\pi^4 3\sigma^1 1\delta^1$ electronic configuration. As discussed in the introduction of this Chapter, the VN [52] and NbN [35] molecules are isovalent to TaN. While $^3\Delta$ state is the ground state for VN and NbN, the $^1\Sigma^+$ state is the ground state for TaN. This difference results from the net relativistic stabilization of the $(n + 1)s$ orbital compared to the nd orbital in Ta [13]. Recently, Skripnikov et al. [53] and Fleig et al. [54] carried out Dirac-Coulomb Hartree-Fock (DCHF) calculations on the first excited electronic state $^3\Delta$, relevant to EDM measurement and predicted its molecular constants. The prime motive of these calculations is to predict the parameters relevant to EDM measurements which are sensitive to the accuracy of the electronic wavefunction in the region of nucleus. The calculations of Fleig et al. [54] also accounted the spin-orbit effects.

Ram et al. [12], in addition to the previously reported bands [49], observed a number of new bands involving $^1\Sigma^+$ or $^3\Delta$ as a lower state. Their observation of an intercombination transition connecting the common upper state to the lower $^1\Sigma^+$ and $^3\Delta_1$ states confirmed the

$^1\Sigma^+$ as the ground state of TaN experimentally. The first excited state was identified as $a^3\Delta$, with its lowest spin component $\Omega = 1$ lying at 2827 cm^{-1} . Even though the transitions were observed from the $a^3\Delta_2$ spin component, they could not determine the term energy of this state. The $a^3\Delta_3$ component and the low-lying $A^1\Delta$ state remained unidentified. Thus the spin-orbit splitting in the $a^3\Delta$ state was not known. In absence of observation of the non-diagonal vibrational transitions, the gas phase vibration frequencies of these electronic states were also unknown. The experimental observation of the ground and low-lying electronic structure was in good agreement with the *ab initio* studies however, the electronic structure above $17,000\text{ cm}^{-1}$ was not well understood from the previous studies [12]. Almost parallel to our work, Bouchard et al. [55] determined the dipole moments of the earlier reported transitions [12] to the ground and $a^3\Delta_{1,2}$ states. They identified an efficient transition for populating the $a^3\Delta_1$ state for designing the experiments for eEDM measurements in TaN. Very recently Steimle et al. [56] determined the nuclear electric quadrupole coupling constants, eQq_0 and magnitude of the molecular frame electric dipole moments, $|\overrightarrow{\mu_{el}}|$ of the ground and $[18.42]0^+$ states.

The study of excited electronic states in the energy region above $17,000\text{ cm}^{-1}$ as well as in the low-lying $\Omega = 1$ and 2 spin components of the $a^3\Delta$ state and the $A^1\Delta$ state are carried out in this thesis. We report the observation of fifteen new bands of jet-cooled TaN using LIF study which led to the finding of thirteen new electronic states in the $23,500 - 30,000\text{ cm}^{-1}$ region. The Ω -quantum number and the rotational constants and radiative lifetimes of these states are determined. The term energies of the $a^3\Delta_{1,2}$ and $A^1\Delta$ states were measured from the DF spectra obtained from the excitation of the previously [12] as well as the newly observed excited electronic states. The equilibrium vibrational constants of the ground and $a^3\Delta$ states are also determined.

3.4.2 Excitation Spectra: High-Energy States

Figure 3.11 shows a survey spectrum of TaN, recorded over the 23,500–27,000 cm^{-1} range. Rotational analysis and assignments of the observed bands are discussed in the subsequent section.

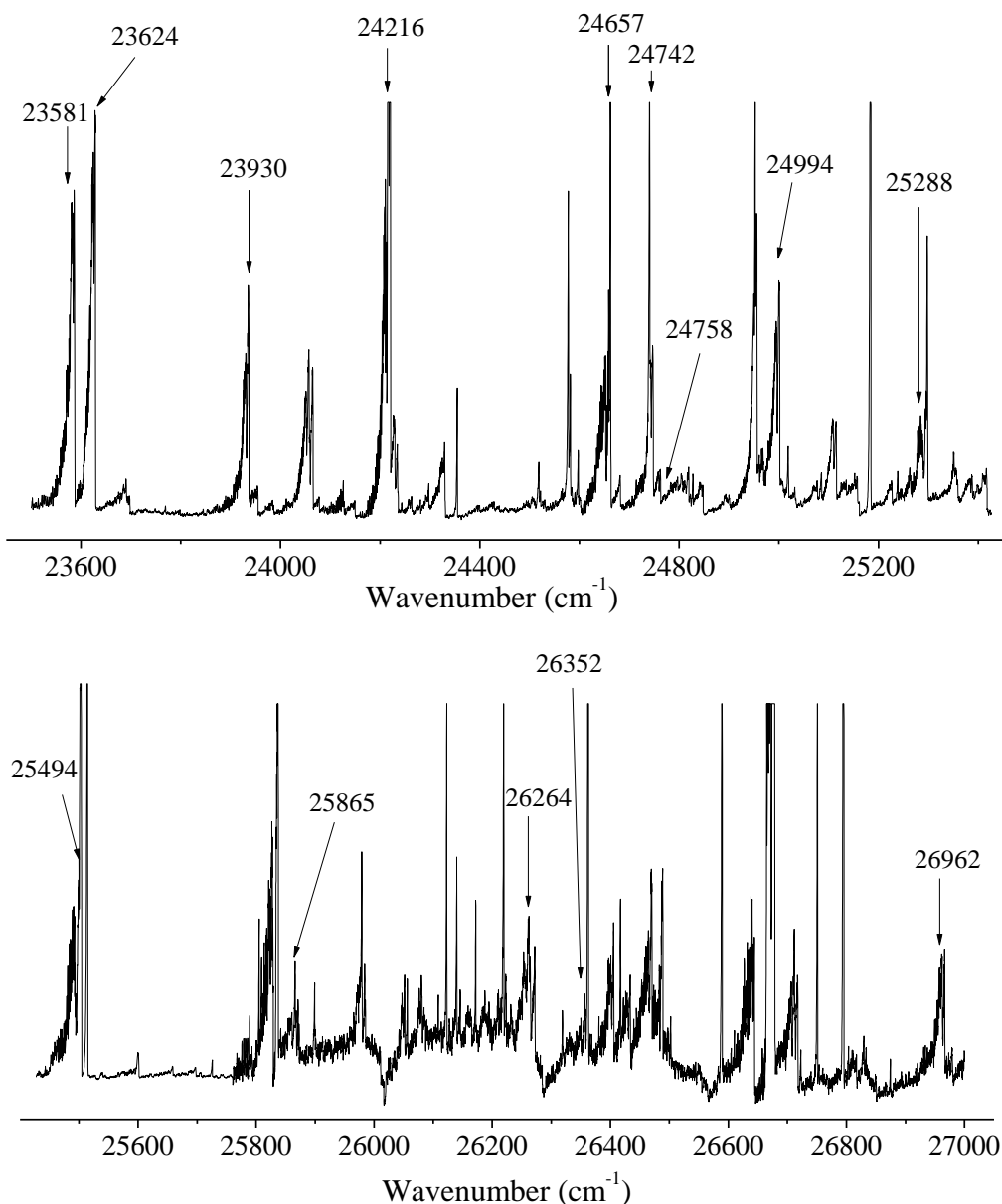


Figure 3.11 Laser-induced excitation survey spectrum of jet-cooled TaN is shown in two parts. Many atomic tantalum (Ta I) lines and TaO bands are also appeared in the spectrum.

3.4.2.a Rotational Analysis and Assignments of the Observed Bands

Ram et al. [12] have reported the emission spectra of TaN in the 3000–35,000 cm^{-1} region using a FTS. However in the present work, we have observed fifteen new bands in the

23,500–27,000 cm^{-1} region, in addition to the bands reported in Ref. [12] by recording the laser excitation spectra in the 365–710 nm region. The carrier of these bands was established both by ground and $a^3\Delta_1$ state combination differences in the excitation spectra and the ground and low-lying states vibrations observed in wavelength resolved DF spectra. The spectra of $^{181}\text{Ta}^{14}\text{N}$ isotopologue were investigated in our experiments.

The lower state vibrational assignments of the observed bands are based on the lower state combination differences and the DF spectra. The Ω -assignments of the upper states are determined from the first line in the R -, Q - and P -branches and by the appearance (for $\Delta\Omega = \pm 1$) or absence ($\Delta\Omega = 0$) of a Q -branch. The band assignments based on these observations are given in Table 3.6. The five bands marked with ‘b’ in Table 3.6, which were previously observed but unanalyzed [12], could now be analyzed because of the uncongested and intense nature of the jet-cooled spectra. A band observed at 21,497 cm^{-1} by Ram et al. [12] was assigned as (0,0) [24,325] $\Omega = 2 - a^3\Delta_1$ transition. The upper state of this band showed rotational perturbation at $J' = 6, 7$ and 8 with appearance of an extra line at 21502.77 cm^{-1} . The low J rotational lines were not observed in the earlier studies. A typical excitation band at 23,582 cm^{-1} with rotational quantum number assignment is shown in Figure 3.12. The Q -branch is the most intense and $I_R > I_P$, indicate $\Delta\Omega = +1$ for the transition. The 24,995 and 23,930 cm^{-1} bands are respectively assigned as (0,0) and (0,1) bands of the transition [24.99]1- $X^1\Sigma^+$ from the same upper state combination differences and lower state combination differences that of $\nu = 0$ and 1 of the $X^1\Sigma^+$ state. The DF from the 23,930 cm^{-1} band also showed a ground state vibrational quantum to the blue of excitation wavelength. The assignment is further validated by 44 (1) ns radiative lifetime of both the bands. Based on the similar arguments, the bands at 26,352 and 25,288 cm^{-1} are assigned as (0,0) and (0,1) bands of the [26.35]0 $^+$ - $X^1\Sigma^+$ system. The band (0,0) [26.35]0 $^+$ - $X^1\Sigma^+$ is shown in Figure 3.13.

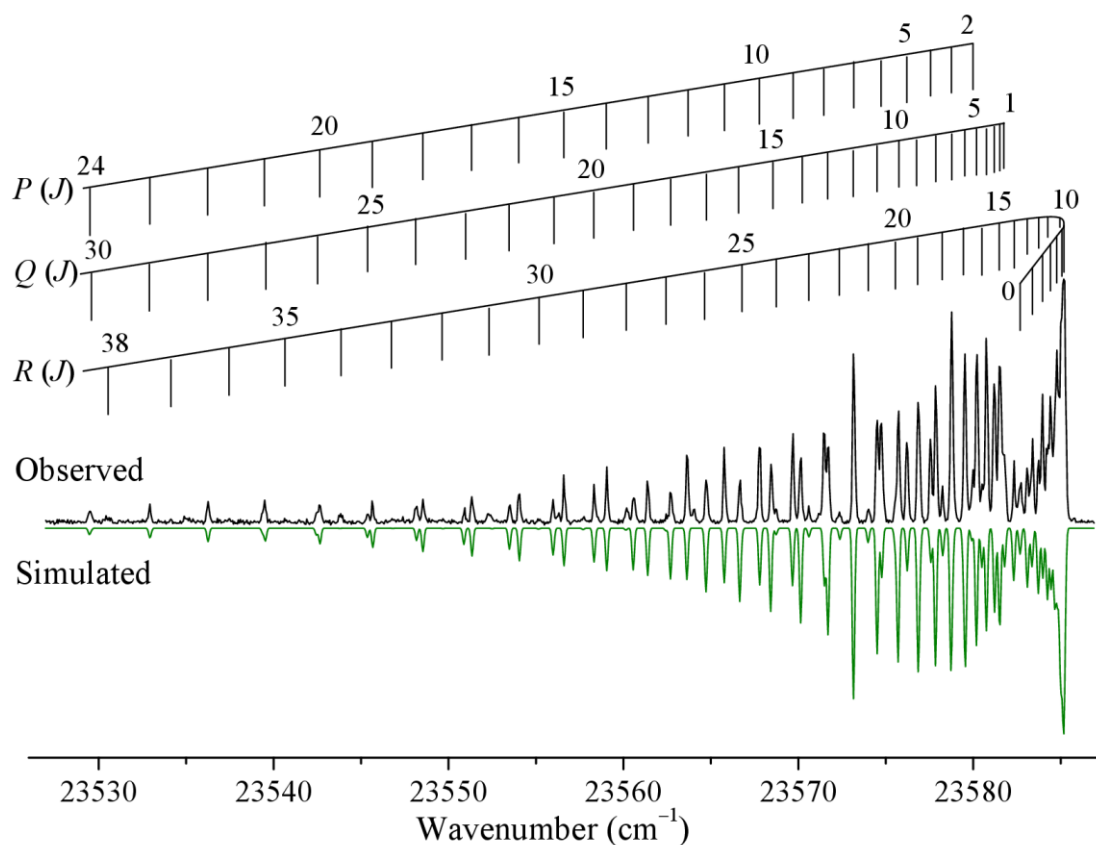


Figure 3.12 The observed jet-cooled and simulated spectrum of the $[23.58]1 - X^1\Sigma^+$ band of TaN.

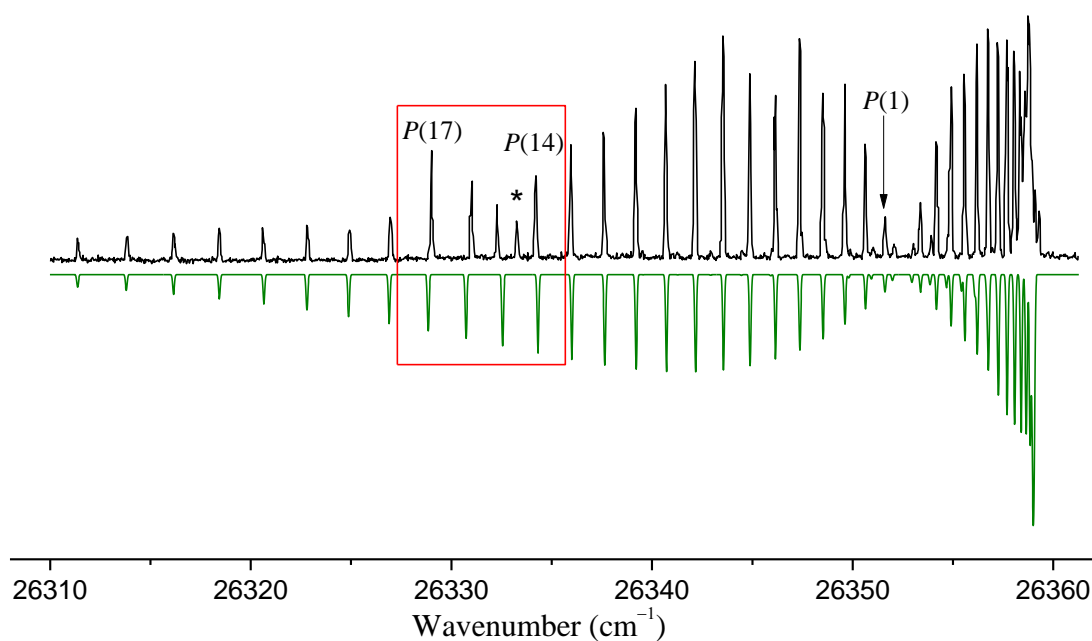


Figure 3.13 Rotational structure of the $(0,0)$ band of the $\Omega = 0^+ - X^1\Sigma^+$ transition of TaN. The line marked as * is the additional peak and perturbed region is shown inside box.

Table 3.6 Observed bands with their assignments, molecular constants (in cm^{-1}) and radiative lifetimes (in ns) of the excited electronic states of the TaN molecule.

T_v	Band Origin (cm^{-1})	Assignment	$v'-v''$	B	$D \times 10^7$	$H \times 10^9$	$q \times 10^4$	τ (ns)
23581.877 (6) ^a	23581.877 (6) ^b	[23.58]1 – $X^1\Sigma^+$	0-0	0.401255(26)	7.26 (21)		8.41 (15)	255(7)
23624.123 (8)	23624.123(8) ^b	[23.62]1 – $X^1\Sigma^+$	0-0	0.400489(44)	5.26(48)		9.68 (30)	275(7)
24216.668 (8)	24216.668 (8) ^b	[24.22]1 – $X^1\Sigma^+$	0-0	0.405617(73)	95.3(12)		2.98 (34)	71(4)
24657.483 (11)	24657.483(11)	[24.66]1 – $X^1\Sigma^+$	0-0	0.404365(78)	-9.29(92)		-4.94 (31)	210(22)
24742.115 (11)	24742.115(11)	[24.72]1 – $X^1\Sigma^+$	0-0	0.413057(99)	12.9(15)		4.90 (38)	77(1)
24758.023 (6)	24758.023 (6)	[24.76]1 – $X^1\Sigma^+$	0-0	0.404514(32)	-		9.57(48)	231(13)
24994.548(8)	24994.548(8) ^{b,c}	[24.99]1 – $X^1\Sigma^+$	0-0					
	23930.187(10) ^c		0-1	0.41950(12)	38.36(413)	-9.17(39)	3.50(26)	44(1)
25224.3(1)	21379.301(9) ^b	[21.38]2 – $a^3\Delta_1$	0-1	0.435722(74)	78.2(11)		-	37(1)
25494.109 (9)	25494.109(9)	[25.49]0 ⁺ – $X^1\Sigma^+$	0-0	0.433682(36)	17.11(23)		-	156(10)
25865.377(11)	25865.377(11)	[25.86]0 ⁺ – $X^1\Sigma^+$	0-0	0.40717(10)	11.3(15)		-	540(32)
26352.462(7)	26352.463(7) ^c	[26.35]0 ⁺ – $X^1\Sigma^+$	0/1-0				-	181(9)
	25288.101(9) ^c		0/1-1	0.427385(43)	21.56(41)		-	
29091.836(6)	26264.544(5)	[29.09]2 – $a^3\Delta_1$	0-0	0.425605(18)	-		-	114(10)
29790.288(9)	26962.996(9)	[29.79]2 – $a^3\Delta_1$	0-0	0.402445(80)	-2.8(13)		-	70(6)

^a Numbers in parentheses denote one standard deviation in the last quoted digits.

^b The bands were previously observed and unanalysed by Ram *et al.* [12]

^c These bands were fitted together to determine the term value of $v=1$ of $X^1\Sigma^+$ as 1064.361(6) cm^{-1} .

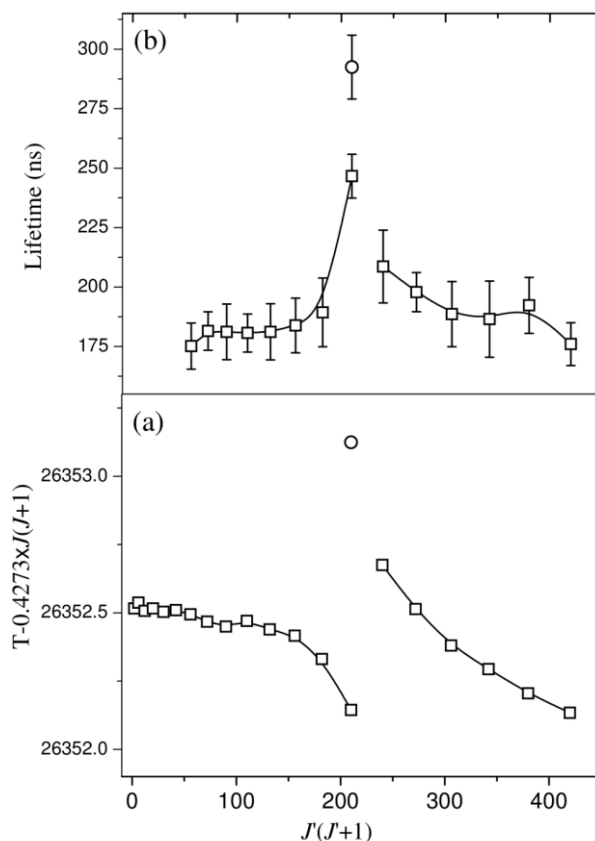


Figure 3.14 (a) Reduced term value plot for the $[26.35]0^+$ state of TaN. Square and circle symbols respectively represent rotational levels of $[26.35]0^+$ and perturber states. (b) The J -dependent radiative lifetime of $[26.35]0^+$ and a perturber state.

Both the 26,352 and 25,288 cm^{-1} bands showed a local perturbation at $J' = 13$ –16 and an extra line belonging to a perturber, as evident from the reduced term value plot shown in Figure 3.14 (a). The perturbation in the term values is also exhibited in the measured radiative lifetimes. The J -dependent radiative lifetime of the $[26.35]0^+$ upper state showed (Figure 3.14 (b)) an increase from 181 ns, a value for the unperturbed rotational levels, to a maximum 250 ns for $J' = 14$ and then steadily reached to the unperturbed value at $J' = 17$. The perturber showed a lifetime of 290 ns. Our observation of a moderate intensity (0,1) hot bands at 23,930 and 25,288 cm^{-1} is in contradiction with the assumption of the observation of only diagonal character vibrational bands by Ram et al. [12]. The vibrational assignment of the upper electronic state of the bands, originating from the $v = 1$ of the $X^1\Sigma^+$, was merely based on this assumption.

3.4.2.b Rotational Constants

We have observed excitation bands to the new excited electronic states having $\Omega' = 0^+$, 1 and 2 from the ground and $a^3\Delta_1$ states. The molecular constants of the excited electronic states were determined by simulating the observed rotationally resolved excitation spectra by PGOPHER program [44]. The ground $X^1\Sigma^+$ and the $\Omega = 0^+$ and higher Ω excited electronic states without Ω -doubling are described by the customary energy level expression

$$F_v(J) = T_v + B_v J(J+1) - D_v [J(J+1)]^2 \quad (3.10)$$

and the $\Omega = 1$ excited states with Ω -doubling are described by

$$F_v(J) \begin{pmatrix} e \\ f \end{pmatrix} = T_v + B_v J(J+1) - D_v [J(J+1)]^2 + H_v [J(J+1)]^3 \pm \frac{1}{2} q_v J(J+1) \quad (3.11)$$

Here T_v is the rotationless energy, B_v is the rotational and D_v is the centrifugal distortion constant and q_v is the Ω -doubling constant. The molecular constants of the $v = 0$ and 1 levels of the $X^1\Sigma^+$ ground and $a^3\Delta_1$ states were constrained in the fit at the values obtained by Ram et al. [12] from the analysis of their more precise (about $\pm 0.003 \text{ cm}^{-1}$) emission spectroscopy data obtained with FTS. The assignments in case (c), molecular constants and radiative lifetimes of the excited electronic states are listed in Table 3.6.

3.4.3 Dispersed Fluorescence Spectra: Ground and Low-energy States

The DF spectra were investigated in the 400–900 nm range by exciting the isolated rotational levels of the previously known excited electronic states [12] as well as the newly observed states, as discussed in the Section 3.4.2. The DF spectra were first recorded with a moderate resolution (FWHM ~ 50 – 100 cm^{-1}) to get coarse information about the ground and the low-lying states and their vibrational levels. The coarse spectra were then examined under relatively higher resolution (FWHM $\sim 5 \text{ cm}^{-1}$) wherever possible, to resolve the rotational structure in the lower states for determining their identities.

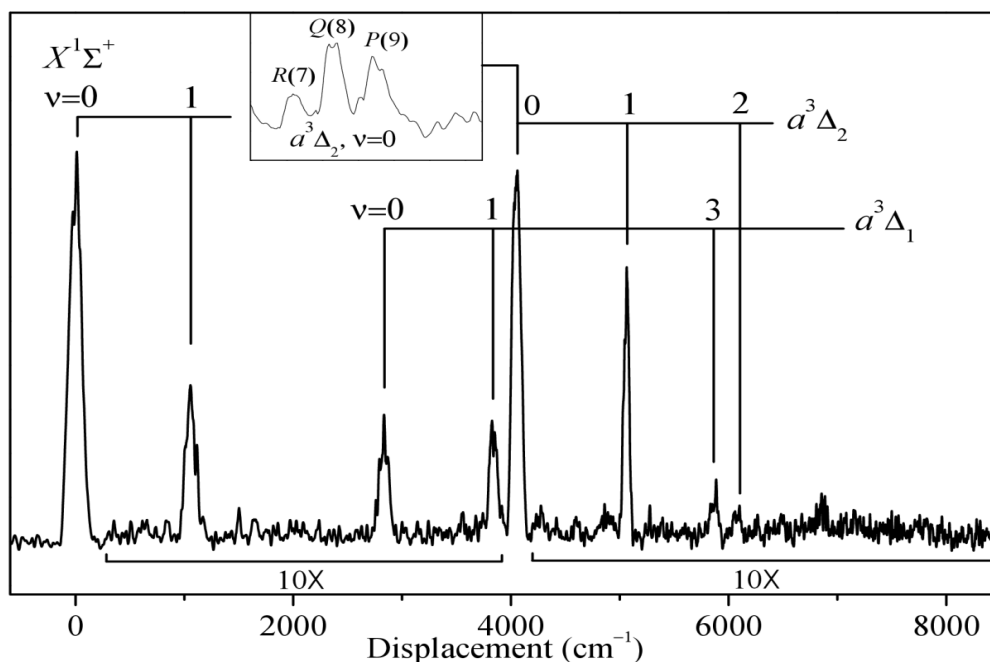


Figure 3.15 The dispersed fluorescence spectra of TaN following excitation of the $Q(8)$ line of the $\Omega' = 1 - X^1\Sigma^+ (0,0)$ band at 19217 cm^{-1} ; the x-axis shows the displacement in cm^{-1} from the excitation line. The inset shows the DF spectra at high-resolution where the R-, Q- and P-lines are well resolved.

A typical DF spectrum observed by exciting the $Q(8)$ line of the $\Omega' = 1 - X^1\Sigma^+ (0,0)$ band at $19,217\text{ cm}^{-1}$ is shown in Figure 3.15. In free-jet, we have also observed the bands reported in Ref. [12] which have originated from the $v = 1$ of the ground and $a^3\Delta_{1,2}$ states. These bands were observed to be weak due to the low population in the excited level. The DF was also studied from these bands. Most of the transitions arising from the $v = 0$ of the $a^3\Delta_1$ and $a^3\Delta_2$ states reported in Ref. [12] fluoresced back to the laser excitation line and did not give information about the low-lying states. The survey excitation scan showed two closely spaced new bands at $23,582$ and $23,624\text{ cm}^{-1}$. The rotational analysis confirmed both the transitions as $\Omega' = 1 - X^1\Sigma^+ (v',0)$. The DF spectra obtained from these two new excited states are very rich and is shown in Figure 3.16 for the $23,582\text{ cm}^{-1}$ state. The DF from this state showed transitions to the ground $X^1\Sigma^+ (v = 0-9, \text{ except } v = 2)$, $a^3\Delta_1 (v = 0)$, $a^3\Delta_2 (v = 0-6, \text{ except } v = 2)$ and to $A^1\Delta_2 (v = 0)$ states. A summary of the DF observed from different excited electronic states to the various vibrational levels of the lower states is given in Table 3.7.

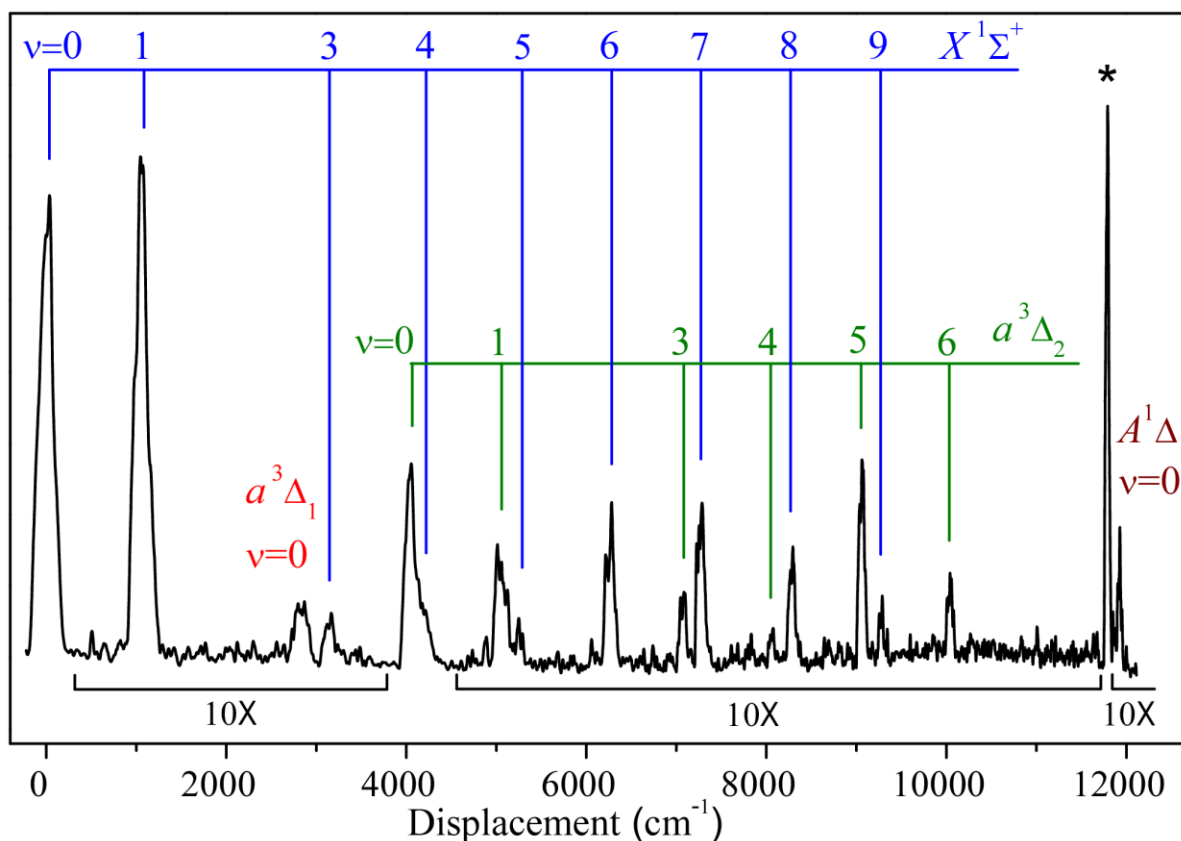


Figure 3.16 The dispersed fluorescence spectra of TaN, observed from the $J = 4$ level of the $\Omega = 1$ state at 23582 cm^{-1} . The observed vibrational progressions for the $X^1\Sigma^+$, $\Omega = 1-2$ spin components of the $a^3\Delta$ and the $A^1\Delta$ state are shown. The peak marked with ‘*’ is the laser excitation line in second order of the grating.

Table 3.7 Vibrational levels observed in the dispersed fluorescence spectra recorded by excitation of various relevant excited electronic states.

Excitation wavenumber	Excitation line	Upper state ^a	Observed lower state vibrational levels			
			$X^1\Sigma^+$	$a^3\Delta_1$	$a^3\Delta_2$	$A^1\Delta$
18429.63	<i>R</i> -head	[18422] $\Omega = 0^+$	0-2	0,1	-	-
19215.69	<i>Q</i> (8)	[19217] $\Omega = 1$	0,1	0,1,3	0-2	-
19395.44	<i>Q</i> (7)	[19397] $\Omega = 1$	0-2	0,2-4	0-2	-
18409.34	<i>R</i> -head	[<i>a</i> +18403] $\Omega = 0^+$	1-3	1,2	-	-
19180.38	<i>Q</i> (4)	[<i>a</i> +19181] $\Omega = 1$	0-2	-	1	-
23287.37	<i>R</i> -head	[<i>a</i> +23283] $\Omega = 1$	0-3	-	-	-
23953.13	<i>Q</i> (4)	[<i>a</i> +23955] $\Omega = 1$	0-3	1	1,2	-
23580.75	<i>Q</i> (4)	[23582] $\Omega = 1^*$	0,1,3-9	0	0,1,3-6	0
23622.42	<i>Q</i> (5)	[23624] $\Omega = 1^*$	0,1,3,5-9	0	0,1,3-6	0

^a All the excited electronic states were reported in ref. [12] except those marked with ‘*’ which have been observed in the present work.

3.4.3.a Equilibrium Vibrational Constants of the $X^1\Sigma^+$ Ground State

The vibrational term energies of the ground state ($\nu = 0-9$), obtained from the DF spectra from different excitations, were consolidated and the average term energies were determined and are listed in Table 3.8. The $\Delta G_{1/2} = 1064.3 \text{ cm}^{-1}$ was obtained from the (0,0) and (0,1) bands from the ground state to the newly observed $\Omega = 1$ excited state at 24994.5 cm^{-1} . The equilibrium vibrational constants of the $X^1\Sigma^+$ state were determined by fitting the observed vibrational term energies to the equation 3.9, and are listed in Table 3.9.

3.4.3.b Observation of the $a^3\Delta_{1,2}$ and $A^1\Delta$ Low-lying Excited Electronic States

Table 3.8 Vibrational term values^a T_ν (in cm^{-1}) of the ground & low-lying electronic states of TaN molecule

ν	$X^1\Sigma^+$	$a^3\Delta_1$	$a^3\Delta_2$	$A^1\Delta$
0	0	2830(4)	4051(3)	11925(5)
		2827.2917(24) ^b		
1	1064.3 (1) ^c	3844(7)	5072(5)	
		3845.0(1) ^d		
2	2127(5)	4856(5)	6078(8)	
3	3175(9)	5863(4)	7082(5)	
4	4213(5)	6855(10)	8078(5)	
5	5247(4)		9063(5)	
6	6269(3)		10044(3)	
7	7280(7)			
8	8285(3)			
9	9286(4)			

^a Values in parentheses are one standard deviation in the last digits quoted.

^b Ref. [12].

^c Value obtained from the origin of the ($\nu',0$) and ($\nu',1$) bands arising from the $X^1\Sigma^+$ to the $\Omega = 1$ state at 24994.5 cm^{-1} .

^d Value determined by combining the T_1 of the $X^1\Sigma^+$ state determined in the present work with the relative term value T_1 of the $a^3\Delta_1$ state reported in Ref. [12].

Other than the long vibrational progression ($\nu = 0-9$) to the ground state, the DF spectrum in Figure 3.16 shows a single line at 2830 cm^{-1} assigned as $\nu = 0$ of the $a^3\Delta_1$ substate. Ram et al. [12] have observed electronic transitions from the $\nu = 0$ and 1 of the $a^3\Delta_1$ substate. They reported the term energy $T_0 = 2827.3 \text{ cm}^{-1}$, however the $\Delta G_{1/2}$ was not known for the $a^3\Delta_1$ state. Thus, we assigned the vibrational progression starting at 2830 cm^{-1} to the $a^3\Delta_1$ substate. Ram et al. [12] have placed the $\nu = 1$ of $a^3\Delta_1$ substate 2780.7 cm^{-1} above the

$\nu = 1$ of $X^1\Sigma^+$ state. From the value of $\Delta G_{1/2} = 1064.3 \text{ cm}^{-1}$ for the $X^1\Sigma^+$ state, determined in the present work, the $\nu = 1$ of the $a^3\Delta_1$ substate is placed at $3845.0(1) \text{ cm}^{-1}$, which is in good agreement with the value $3844(7) \text{ cm}^{-1}$, obtained from the DF spectra (see Table 3.8).

Table 3.9 Equilibrium molecular constants^a (in cm^{-1}) for the ground and low-lying $a^3\Delta$ and $A^1\Delta$ states of TaN molecule and their comparison with the *ab initio* values.

State	T_e			ω_e			$\omega_e x_e$
	Present work		<i>ab initio</i>	Present work		<i>ab initio</i>	Present work
		DCHF ^b	MRCI ^c		DCHF ^b	MRCI ^c	
$X^1\Sigma^+$	0.0	0.0	0.0	1072.4(2)	1161	1049	4.0(1)
$a^3\Delta_1$	2851(4)	2526 ^d		1024.1(5)	1116 ^e		3.2(2)
$a^3\Delta_2$	4074(3)	3618	4301	1025.9(10)	1117	999	3.9(2)
$a^3\Delta_3$	-	5276		-	1119		-
$A^1\Delta$	11925 (5) ^f	11710 ^f	11727 ^f	-	1123	1053	-

^a Values in parentheses are one standard deviation in the last digits quoted.

^b Ref. [54]; With model MR₁₂-CISD(10).

^c Ref. [12].

^d $T_e = 2879 \text{ cm}^{-1}$ with model MR₁₂-CISD(18).

^e $\omega_e = 1088 \text{ cm}^{-1}$ with model M₁₂⁺⁺-CISD(10).

^f T_0 value.

The more accurate values of T_0 and T_1 , obtained from the rotational data, along with vibrational term energies for the $\nu = 2-4$, obtained from the DF data were used to evaluate the vibrational constants of the $a^3\Delta_1$ substate and are listed in Table 3.9. Though, the observation of the electronic bands from the $\nu = 0$ of the $a^3\Delta_2$ substate were reported in Ref. [12], the term energy of this state was not known. We have assigned the progression starting at 4051 cm^{-1} to the $\nu = 0-6$ levels of the $a^3\Delta_2$ substate. The confirmation of the $\Omega = 2$ assignment for this state was carried out with rotationally resolved DF. The rotationally resolved spectrum of DF line at displacement wavenumber 4051 obtained by exciting the $Q(8)$ line of the $\Omega' = 1 - X^1\Sigma^+$ (0,0) band at $19,217 \text{ cm}^{-1}$ is shown in the inset of Figure 3.15. It shows three R , Q , and P lines with the intensity pattern $I_R < I_P < I_Q$, indicating a $\Delta\Omega = -1$ transition and thus confirms the lower state as $\Omega = 2$. The *ab initio* calculations [12] predicted the first excited state as $a^3\Delta$ at

$T_0 = 4276 \text{ cm}^{-1}$ without spin-orbit interaction. In contrast, Fleig et al. [54] have included spin-orbit interaction in their DCHF calculations and predicted the three spin components $a^3\Delta_{1,2,3}$ respectively at $T_e = 2526, 3618, \text{ and } 5276 \text{ cm}^{-1}$ with 10 electron $\text{MR}_{12}\text{-CISD}(10)$ model. More refined $\text{MR}_{12}\text{-CISD}(18)$ model predicted the $a^3\Delta_1$ component at 2879 cm^{-1} , which agrees well with the experimental observation. Thus, the $\text{MR}_{12}\text{-CISD}(10)$ model underestimated the $a^3\Delta_1$ term energy by $\sim 300 \text{ cm}^{-1}$. Thus, our assignment of the observed states at 4051 cm^{-1} as $a^3\Delta_2$ is in concurrence with the prediction of this state at $T_e = 3618 \text{ cm}^{-1}$. This gives the spin-orbit (SO) separation of 1224 cm^{-1} between the $^3\Delta_1$ and $^3\Delta_2$ substates.

The observed SO separation in TaN corroborate with the large spin-orbit coupling constant of Ta atom (ζ_{5d} for Ta is 1699 cm^{-1} [24]). The observed vibrational term energies provided the $^3\Delta_2$ state vibrational constants which are shown in Table 3.9 and are similar to those of the $^3\Delta_1$ state. A weak but consistent, single DF line at $11,925(5) \text{ cm}^{-1}$ was observed from the two new bands at $23,582$ and $23,624 \text{ cm}^{-1}$. Very low intensity of this line did not permit us rotationally resolve the peak to confirm its identity, however Refs. [12] and [54] predicted a $A^1\Delta$ state respectively at $T_0 = 11,727$ and $11,710 \text{ cm}^{-1}$, which is very close to the observed position. As no other state is predicted in this region, the observed state at $11,925(5) \text{ cm}^{-1}$ is very likely to be the $v = 0$ of the $A^1\Delta$ state.

3.4.4 Results and Discussions

The ground state $X^1\Sigma^+$ of the TaN molecule is derived from the $1\sigma^2 2\sigma^2 1\pi^4 3\sigma^2$ electronic configuration and the excitation of a 3σ electron to the 1δ orbital results in low-lying $a^3\Delta$ and $A^1\Delta$ states. These states are characterized theoretically as well as experimentally by the previous [12,53,54,55,56] and present studies..

The term energies and vibrational constants at equilibrium of the ground $X^1\Sigma^+$ and $\Omega = 1$ and 2 spin-orbit components of the $a^3\Delta$ state determined in the present work using

laser-induced dispersed fluorescence from the excited electronic states. These states are compared with the *ab initio* values from Refs. [12,54] (see Table 3.9). The $\Omega = 3$ component of the $a^3\Delta$ state remained unobserved despite of our DF search from the $\Omega = 2$ and 3 excited states reported in Ref. [12]. This is probably because of the weak intensity associated with the corresponding bands. The experimentally determined molecular constants are in overall good agreement with the *ab initio* results. The $\omega_e = 1072.4$ (2) cm^{-1} , determined for the ground state in the present work is in good agreement with the MRCI value [12], while the DCHF value [54] is on the higher side. The estimated gas phase value of $\Delta G_{1/2} = 1070$ cm^{-1} , empirically corrected from an argon matrix studies [51], is also in excellent agreement with the value of 1064.3 cm^{-1} determined in this work (see Table 3.8). Fleig et al. [54] have employed different models for calculating the spectroscopic parameters for the EDM related $a^3\Delta_1$ substate. The $\text{MR}_{12}\text{-CISD}(18)$ model predicted $T_e = 2879$ cm^{-1} , closest to the experimental value of 2851 cm^{-1} , however the predicted $\omega_e = 1088$ cm^{-1} by $\text{M}_{12}^{+T} - \text{CISD}(10)$ model was closest to the experimental value of 1024 cm^{-1} . As seen from Table 3.9, the predicted T_e and ω_e for the $a^3\Delta_2$ spin-component are off by $\sim 10\%$, the predicted term energy on the lower side where as the vibrational frequency on the higher side of the observed value. Although, the spin-orbit coupling effects are not included in the studies reported by Ram et al. [12], the *ab initio* value of $T_e = 4301$ cm^{-1} for the $a^3\Delta$ state is in fairly good agreement with the experimental term energy of the central spin component of the $a^3\Delta$ state. The experimental and *ab initio* values of internuclear distances for the ground and the $a^3\Delta$ state reported in Refs. [12,54] also showed a good agreement. Thus, the *ab initio* results showed an overall good agreement with the reported experimental values. This gives confidence to our assignment of the $A^1\Delta$ state, which is solely based on the agreement of its T_0 value with the *ab initio* values [12,54].

The visible excitation spectra of TaN are very complex because of perturbations [49] and the assignment of higher-lying excited electronic states, and remained very difficult due to the lack of regular energy spacing among the states, even after the observation of many bands and their rotational analysis [12]. Tantalum is a heavy atoms and exhibit strong spin-orbit coupling ($\zeta_{5d} = 1699 \text{ cm}^{-1}$ [24]). Due to the strong spin-orbit effect, many of the high-lying terms get heavily mixed in TaN molecule and only Ω remain a good quantum number. Though, the Hund's case (*a*) is followed in low-lying electronic states, case (*c*) holds good for higher-energy electronic states in TaN. We have observed thirteen excited electronic states, out of which three, seven and three states have been assigned respectively to $\Omega = 0^+, 1$ and 2 quantum numbers. Table 3.10 lists the consolidated spectroscopic data like term energies, Ω -quantum number, molecular constants and radiative lifetime of the higher energy excited electronic states reported in the previous [12] and the present work. A total of 30 states are observed so far in the region $17,000\text{--}30,000 \text{ cm}^{-1}$. However, *ab initio* calculation predicted 11 terms comprising of 27 spin components between $\sim 18,000$ and $25,000 \text{ cm}^{-1}$ [12]. In the absence of regular energy spacing, systematic trend in Ω -quantum number, molecular constants and similar radiative lifetimes, it was not possible to group the observed individual states as the spin components of the multiplets. However, by using present radiative lifetimes and DF data (Section 3.4.3), we attempted to correlate the observed excited states with those calculated in Ref. [12]. The short lifetimes represent allowed transitions and longer ones, nominally forbidden. The DF spectra showing strong transitions to the $a^3\Delta_1$ indicate triplet excited states.

Table 3.10 The high-lying excited electronic states of TaN observed in the present and earlier work with their term energy, molecular constants (cm^{-1}) and radiative life-times (ns). The lower state from which the state is observed is also listed.

SN	Ω	v	T	Lower state	B	$D \times 10^7$	$q \times 10^4$	τ (ns)
1	2	0	17228.0784(32) ^a	$a^3\Delta_1, v=0$	0.3998242(57)	5.165(31)	-	788(51)
2	1	0	17266.0048(30) ^a	$a^3\Delta_1, v=0$	0.4262133(49)	3.980(25)	0.272(37)	792(36)
3	2	0	17363.5767(31) ^a	$a^3\Delta_1, v=0$	0.4077265(78)	16.543(69)	-	-
4	0 ⁺	0	17580.4995(21) ^a	$X^1\Sigma^+, v=0$	0.4369391(62)	-6.691(40)	-	454(32) ^b
5	2	0	17846.8085(27) ^a	$a^3\Delta_1, v=0$	0.4282961(39)	15.166(16)	-	352(7)
6	2	0	18083.2185(29) ^a	$a^3\Delta_1, v=0$	0.4271296(46)	16.674(24)	-	332(2)
7	2	0	18277.9667(29) ^a	$a^3\Delta_1, v=0$	0.4131802(49)	-5.868(30)	-	502(40)
8	0 ⁺	0	18422.4321(26) ^a	$X^1\Sigma^+, v=0$	0.4302930(44)	11.166(20)	-	460(2), 479(12) ^b
9	1	0	19217.4310(22) ^a	$X^1\Sigma^+, v=0$	0.434415(10)	25.34(12)	2.799(27)	336(28), 333(4) ^b
10	1	0	19397.3799(15) ^a	$X^1\Sigma^+, v=0$	0.4234865(82)	-12.01(11)	2.148(95)	461(30), 480(17) ^b
11	0 ⁺	1	19467.335(6) ^a	$X^1\Sigma^+, v=1$	0.4234715(85)	-15.676(55)	-	446(34)
12	3	0	19778.4(30) ^a	$a^3\Delta_2, v=0$	0.440386(15)	1.13(18)	-	-
13	1	1	20245.006(7) ^a	$X^1\Sigma^+, v=1$	0.442287(42)	32.7(17)	9.90(46)	301(11)
14	1	0	23581.877(6)	$X^1\Sigma^+, v=0$	0.401255(26)	7.26(21)	8.41(15)	255(7)
15	1	0	23624.123(8)	$X^1\Sigma^+, v=0$	0.400489(44)	5.26(48)	9.68(30)	275(7)
16	1	0	24216.668(9)	$X^1\Sigma^+, v=0$	0.405617(73)	95.3(12)	2.98(34)	71(4)
17	2	0	24324.524(25) ^a	$a^3\Delta_1, v=0$	0.44621(19)	34.8(47)	-	35(1)
18	1	1	24347.214(9) ^a	$X^1\Sigma^+, v=1$	0.412666(43)	-180.85(83)	6.12(16)	<10
19	1	0	24657.483(11)	$X^1\Sigma^+, v=0$	0.404365(78)	-9.29(92)	-4.94(31)	210(22)
20	1	0	24742.115(11)	$X^1\Sigma^+, v=0$	0.413057(99)	12.9(15)	4.90(38)	77(1)
21	1	0	24758.023(6)	$X^1\Sigma^+, v=0$	0.404514(32)	-	9.57(48)	231(13)
22	1	0	24994.548(8)	$X^1\Sigma^+, v=0$	0.41950(12)	38.36(413)	3.50(26)	44(1)
23	1	1	25019.27(14) ^a	$X^1\Sigma^+, v=1$	0.37264(57)	-435.2(87)	13.87(31)	236(20)
24	2	0	25224.3(1)	$a^3\Delta_1, v=1$	0.435722(74)	78.2(11)	-	37(1)
25	0 ⁺	0	25494.109(9)	$X^1\Sigma^+, v=0$	0.433682(36)	17.11(23)	-	156(10)
26	0 ⁺	0	25865.377(11)	$X^1\Sigma^+, v=0$	0.40717(10)	11.3(15)	-	540(32)
27	0 ⁺	0/1	26352.463(7)	$X^1\Sigma^+, v=0$	0.427385(43)	21.56(41)	-	181(9)
28	3	0	27442.9(30) ^a	$a^3\Delta_2, v=0$	0.447711(77)	37.7(27)	-	23(1)
29	2	0	29091.836(6)	$a^3\Delta_1, v=0$	0.425605(18)	-	-	114(10)
30	2	0	29790.288(9)	$a^3\Delta_1, v=0$	0.402445(80)	-2.8(13)	-	70(6)

^a Reported by Ram et al. [12].

^b Radiative lifetime values from ref. [55].

Two 0^+ states with $\nu = 0$ at 17580.5, 18422.4 cm^{-1} and a state at 19467.3 cm^{-1} with $\nu = 1$ are observed, all having long lifetime of about 450 ns, indicating a triplet character. Thus it is reasonable to assume that these states are mixtures of the 0^+ spin components of the $1^3\Pi$ and $1^3\Sigma^-$ terms predicted respectively at 18,732 and 19,298 cm^{-1} [12]. The 17,580 cm^{-1} state fluoresce back only to $\nu = 0$ $X^1\Sigma^+$ state and no fluorescence was observed to $a^3\Delta_1$ state. This indicates that the 17,580 cm^{-1} state could have leading character from the $1^3\Sigma^-$ state.

The DF from 18,422 and 19,467 cm^{-1} states are identical and fluoresce more strongly to the $a^3\Delta_1$ state than to the ground state. This indicate that the 18,422 cm^{-1} state is mainly a 0^+ spin-component of the $1^3\Pi$ state predicted at 18,732 cm^{-1} and the 19,467 cm^{-1} state could be $\nu = 1$ of this state; however a large α_e value of 0.0136 cm^{-1} puts $1^3\Pi$, $\nu = 1$ assignment in question. The assignment of the observed 18,422 cm^{-1} state to $1^3\Pi$ was also supported in Ref. [56], however with sizable contribution from $1\sigma^2 2\sigma^2 1\pi^3 3\sigma^1 1\delta^2$ configuration than predicted [12], in order to account for the observed value of nuclear electric quadrupole coupling constants, eQq_0 . The other spin-components of $1^3\Pi$ and $1^3\Sigma^-$ terms could not be assigned. The $[25.49]0^+$ and $[26.35]0^+$ states showed dispersed fluorescence only to the $X^1\Sigma^+$ ground state and exhibit similar short radiative lifetime respectively of 156 and 181 ns. This indicates that they most likely have $1^1\Sigma^+$ symmetry and could be the $\nu = 0$ and 1 levels of the predicted $2^1\Sigma^+$ state at 25,512 cm^{-1} .

The number of observed excited electronic states is significantly larger than currently predicted thus the configurations considered in Ref. [12] could not account for all the observed states. Some more configurations are considered in NbN and VN molecules which are isovalent to TaN. The ground electronic configuration of VN and NbN is $\pi^{4(n+1)}s\sigma^1nd\delta^1$ resulting in $X^3\Delta$ state ($n = 4$ for VN and $n = 5$ for NbN). The $^3\Phi$, $^1\Phi$, $^3\Pi$ and $^1\Pi$ states have been observed in VN [21,57,58] and NbN [22,23] in the 16,000–23,000 cm^{-1} region respectively from $\pi^4 3d\delta^1 3d\pi^1$ and $\pi^4 4d\delta^1 4d\pi^1$ configurations and the $^{3,1}\Pi$ and $^{3,1}\Delta$ states in

20,000–25,000 cm^{-1} region in NbN, speculated to arise respectively from the $5s\sigma^1 4d\pi^1$ and $4d\delta^1 4d\sigma^1$ configurations [39]. In view of this, the present observation of the excited electronic states warrants high level *ab initio* calculations emphasizing to consider more configurations.

3.5 Conclusion

This section concludes the chapter with a restatement of the important results obtained. LIF spectroscopy of the jet-cooled NbN and TaN molecules have been carried out. For NbN, new transitions in the 18,000–21,000 cm^{-1} spectral region have been observed. The LIF excitation spectra of the (1–0) bands of the $C - X$ and $e - X$ systems of NbN are recorded in the 18,000–19,500 cm^{-1} spectral region. Experimental and theoretical investigation of the spin-orbit interaction between the $C^3\Pi$ and $e^1\Pi$ states at $v = 1$ vibrational level has been presented. The spectra are found to be well behaved and free from local rotational perturbations. The only irregularity is the depression of the central subband of the $C - X$ system due to the strong second-order spin-orbit coupling between the $C^3\Pi_1$ and $e^1\Pi$ states. The rotational parameters of the $C^3\Pi/e^1\Pi$ complex are determined. The spectral features and the size of the off-diagonal spin-orbit interaction matrix elements are found to be similar to the 0–0 band of these transitions reported previously by Azuma et al. [23]. Our *ab initio* calculations are in reasonable agreement with the $\Delta E(\Omega_2 - \Omega_0)$ separation but underestimate the $\Delta E(\Omega_1 - \Omega_0)$ separation of the $^3\Pi$ state. This error is traced to our overestimate of the unperturbed singlet-triplet energy separation. Further, three bands in the energy region 20,300–20,800 cm^{-1} corresponding to a new triplet transitions $^3\Pi_{0^\pm} - X^3\Delta_1$, $^3\Pi_1 - X^3\Delta_2$, and $^3\Pi_2 - X^3\Delta_3$ have been identified. The three spin-orbit (SO) components of the newly observed $^3\Pi$ state have the term energies 20,756.32 cm^{-1} ($^3\Pi_{0^\pm}$), 20,900.1 cm^{-1} ($^3\Pi_1$), and 21,240.3 cm^{-1} ($^3\Pi_2$). The spin-orbit intervals of this $^3\Pi$ state have been observed to be asymmetric like those observed earlier in the $C^3\Pi$ and $X^3\Delta$ states of NbN, reported by Merer's group [22,23] and

$C^3\Pi$ at $\nu = 1$ vibrational level in the present work. The radiative lifetime and rotational constants for the $^3\Pi_1$ component markedly depart from those of the other two spin-orbit components of the $^3\Pi$ state. This suggests that the $^3\Pi_1$ substate is mixed, probably with the proposed $^1\Pi$ state lying higher in energy and the mixing is responsible for the asymmetry in the spin-orbit splitting of the $^3\Pi$ state. However, exact identity of the interacting state could not be determined. In addition, in the 19,000–21,000 cm^{-1} range, two new 0–0 of $^3\Pi_1 - X^3\Delta_2$ and $^3\Pi_{0^\pm} - X^3\Delta_1$ subbands at band origins respectively at 19,841.5 and 19,716.1 cm^{-1} of a $^3\Pi - X^3\Delta$ transition were identified. Seven weak bands were also observed in the same scan region. The rotational and DF studies together with the weak intensity suggested that the lower state of these bands is $\nu'' = 1$ of $X^3\Delta$ and the upper state probably have a Π character. It was not possible to understand the origin of these new excited $^3\Pi$ states as well as hot bands in the existing theory. Improved theoretical calculations, which take account of the states, observed by earlier workers [39] and the ones reported in this work are needed to better understand the electronic structure of this molecule.

TaN molecule is a promising candidate for search of permanent electron electric dipole moment and in view of this, spectroscopic information on the low-lying $a^3\Delta$ state is important. Laser-induced dispersed fluorescence investigations from the excited electronic states lead to the observation of the low-lying excited electronic states of TaN. The $\Omega = 1$ and 2 spin-orbit components of the $a^3\Delta$ state along with their vibrational structure and also the $A^1\Delta$ state have been observed. The harmonic and anharmonic vibrational constants at equilibrium for the ground $X^1\Sigma^+$ and low-lying $a^3\Delta_{1,2}$ states have also been determined. The experimentally determined term energies and vibrational constants of these electronic states are in good agreement with their *ab initio* values [12,54]. The present determination of the vibrational term energies of the lower states fixed the energies of several high-energy states reported by Ram et al. [12]. Further, the rotationally resolved LIF excitation spectra of the

jet-cooled TaN molecules have been investigated in the 365–710 nm region. Fifteen new bands were observed. The rotational analyses of these bands led to the observation of thirteen new states in the 23,500–30,000 cm⁻¹ region, labeled with their Ω -quantum numbers. The radiative lifetimes along with the Ω -quantum numbers, term energies and molecular constants of the observed states assisted in the correlating some of the observed states with those predicted by earlier *ab initio* studies [12]. However, in the absence of the regular energy spacing and expected trend in molecular constants it was not possible to group these observed states either as the spin components of the predicted terms or even the vibrational members with certainty. This is perhaps due to the strong spin-orbit interaction between the states which causes mixing and thus the individual state follow case (c) coupling. The observation of more number of spin-states, particularly of $\Omega = 1$ than expected from the earlier *ab initio* studies call for the inclusion of electronic configurations considered in isovalent VN and NbN molecules. Supplementary information for the rotational line positions and assignments of the observed bands associated with this chapter are listed at the end of the thesis.

3.6 References

-
- [1] P.F. McMillan, *Nat. Mater.* **1**, 19 (2002).
 - [2] E. Gregoryanz, C. Sanloup, M. Somayazulu, J. Badro, G. Fiquet, H.-K. Mao, R.J. Hemley, *Nat. Mater.* **3**, 294 (2004).
 - [3] S.T. Oyama, *The Chemistry of Transition Metal Carbides and Nitrides*, Blackie Academic & Professional, London (1996).
 - [4] H.O. Pierson, *Handbook of Refractory Carbides and Nitrides*, Noyes Publications, Westwood, New Jersey (1996).
 - [5] S. Yamanaka, K. Hotehama, H. Kawaji, *Nature* **392**, 580 (1998).

-
- [6] S. Yang, D.B. Lewis, I. Wadsworth, J. Cawley, J.S. Brooks, W.D. Munz, *Surf. Coat. Technol.* **131**, 228 (2000).
- [7] M. Grunze, Synthesis and decomposition of ammonia, in: D.A. King, D.P. Woodruff (Eds.), *The Chemical Physics of Solid Surfaces and Heterogeneous Catalysis*, vol. 4, Elsevier, New York (1982) p. 143.
- [8] F.A. Cotton, G. Wilkinson, C.A. Murillo, M. Bochmann, *Advanced Inorganic Chemistry, A Comprehensive Text*, sixth ed., Wiley, New York (1999).
- [9] A.J. Sauval, *Astron. Astrophys.* **62**, 295 (1978).
- [10] J. F. Harrison. *J. Phys. Chem.* **100**, 3513 (1996).
- [11] S.R. Langhoff and C.W. Bauschlicher Jr., *J. Mol. Spectrosc.* **143**, 169 (1990).
- [12] R.S. Ram, J. Liévin, P.F. Bernath, *J. Mol. Spectrosc.* **215**, 275 (2002).
- [13] O. Krechkivska, M.D. Morse, *J. Phys. Chem. A* **117**, 13284 (2013).
- [14] J. P. Desclaux, Relativistic Dirac–Fock Expectation Values for Atoms with $Z=1$ to 120. *At. Data Nucl. Data Tables*, **12**, 311 (1973).
- [15] A. Kalamos, T. H. Dunning, Jr., and A. Mavridis, *J. Chem. Phys.* **123**, 014301 (2005).
- [16] A. J. Merer, G. Huang, A. S-C. Cheung, A. W. Taylor, *J. Mol. Spectrosc.* **125**, 465 (1987).
- [17] B. Simard, P. I. Presunka, H. P. Loock, A. Bérces, and O. Launila, *J. Chem. Phys.* **107**, 307 (1997).
- [18] G. Cheval, J.-L. Femenias, *J. Mol. Spectrosc.* **131**, 113 (1988).
- [19] O. Krechkivska, M.D. Morse, *J. Phys. Chem.* **133**, 054309 (2010).
- [20] R.S. Ram, P.F. Bernath, *J. Mol. Spectrosc.* **191**, 125 (1998).
- [21] W.J. Balfour, A.J. Merer, H. Niki, B. Simard, P.A. Hackett, *J. Chem. Phys.* **99**, 3288 (1993).

-
- [22] Y. Azuma, J.A. Barry, M.P.J. Lyne, A.J. Merer, J.O. Schröder, J.L. Féménias, *J. Chem. Phys.* **91**, 1 (1989).
- [23] Y. Azuma, G. Huang, M.P.J. Lyne, A.J. Merer, V.I. Srdanov, *J. Chem. Phys.* **100**, 4133 (1994).
- [24] H. Lefebvre-Brion, R.W. Field, *Perturbations in the spectra of diatomic molecules*, Academic Press, San Diego (1986).
- [25] V.V. Flambaum, D. DeMille, M.G. Kozlov, *Phys. Rev. Lett.* **113**, 103003 (2014).
- [26] B.J. Barker, I.O. Antonov, V.E. Bondybey, M.C. Heaven, *J. Chem. Phys.* **144**, 201102 (2011).
- [27] J. Baron, W.C. Campbell, D. DeMille, J.M. Doyle, G. Gabrielse, Y.V. Gurevich, P.W. Hess, N.R. Hutzler, E. Kirilov, I. Kozyryev, B.R. O’Leary, C.D. Panda, M.F. Parsons, E.S. Petrik, B. Spaun, A.C. Vutha, A.D. West, *Science* **343**, 269 (2014).
- [28] V.V. Flambaum, *Phys. Lett. B* **320**, 211 (1994).
- [29] W. Zickendraht, *Phys. Rev. Lett.* **54**, 1906 (1985).
- [30] A.E. Leanhardt, J.L. Bohn, H. Loh, P. Maletinsky, E.R. Meyer, L.C. Sinclair, R.P. Stutz, E.A. Cornell, *J. Mol. Spectrosc.* **270**, 1 (2016).
- [31] D.N. Gresh, K.C. Cossel, Y. Zhou, J. Ye, E.A. Cornell, *J. Mol. Spectrosc.* **319**, 1 (2016).
- [32] Meggers WF, Corliss CH, Scribner BF. *Tables of spectral line intensities, Part I- arranged by elements*, NBS Monograph no.145. Washington, DC (1975).
- [33] T.M. Dunn and K.M. Rao, *Nature* **222**, 266 (1969).
- [34] J.L. Féménias, C. Athenour, and T.M. Dunn, *J. Chem. Phys.* **63**, 2861 (1975).
- [35] J.L. Féménias, C. Athenour, K.M. Rao, and T.M. Dunn, *J. Mol. Spectrosc.* **130**, 269 (1988).
- [36] D.W. Green, W. Kofmacher, and D.W. Gruen, *J. Chem. Phys.* **58**, 404 (1973).
- [37] E.A. Pazyuk, E.N. Moskvitina, and Yu.Ya. Kuzyakov, *Spectrosc. Lett.* **19**, 627 (1986).

-
- [38] R.S. Ram and P.F. Bernath, *J. Mol. Spectrosc.* **201**, 267 (2000).
- [39] R.S. Ram and P.F. Bernath, *J. Mol. Spectrosc.* **243**, 62 (2007).
- [40] H. Sellers, *J. Phys. Chem.* **94**, 1338 (1990).
- [41] A. Bérces, S.A. Mitchell, and M.Z. Zgierski, *J. Phys. Chem. A* **102**, 6340 (1998).
- [42] D.A. Fletcher, D. Dai, T.C. Steimle, K. Balasubramanian, *J. Chem. Phys.* **99**, 9324 (1993).
- [43] M. Sbata and J. Schamps, *J. Chem. Phys.* **113**, 2687 (2000).
- [44] C.M. Western, PGOPHER, a program for simulating rotational structure, University of Bristol, Bristol (2010). (<http://pgopher.chm.bris.ac.uk>).
- [45] K.A. Peterson, D. Figgen, M. Dolg, H. Stoll, *J. Chem. Phys.* **126**, 124101 (2007).
- [46] T.H. Dunning Jr., *J. Chem. Phys.* **90**, 1007 (1989).
- [47] H.J. Werner, P.J. Knowles, J. Almof, R.D. Amos, M.J.O. Deegan, S.T. Elbert, C. Hampel, W. Meyer, K. Peterson, R. Pitzer, A.J. Stone, P.R. Taylor, R. Lindh, M.E. Mura, T. Thorsteinsson, Molpro, A package of ab-initio programs, see (<http://www.molpro.net>).
- [48] G. Herzberg, *Molecular spectra and molecular structure I*, second ed., Van Nostrand, New York (1950).
- [49] J.K. Bates, *Optical Emission Spectra of Diatomic Metal Nitrides* Ph.D. thesis, University of Michigan (1975).
- [50] J.K. Bates, D.M. Gruen, *J. Chem. Phys.* **70**, 4428 (1979).
- [51] M. Zhou, L. Andrews, *J. Phys. Chem. A* **102**, 9061 (1998).
- [52] B. Simard, C. Masoni, P.A. Hackett, *J. Mol. Spectrosc.* **136**, 44 (1989).
- [53] L.V. Skripnikov, A.N. Petrov, N.S. Mosyagin, A.V. Titov, V.V. Flambaum, *Phys. Rev. A* **92**, 012521 (2015).
- [54] T. Fleig, M.K. Nayak, M.G. Kozlov, *Phys. Rev. A* **93**, 012505 (2016).

-
- [55] J.L. Bouchard, T. Steimle, D.L. Kokkin, D.J. Sharfi, R.J. Mawhorter, *J. Mol. Spectrosc.* **325**, 1 (2016).
- [56] T. Steimle, D.L. Kokkin, Y. Kim, R.J. Mawhorter, C. Linton, *Chem. Phys. Lett.* **664**, 138 (2016).
- [57] S.L. Peter, T.M. Dunn, *J. Chem. Phys.* **90**, 5333 (1989).
- [58] R.S. Ram, P.F. Bernath, S.P. Davis, *J. Mol. Spectrosc.* **215**, 163 (2002).

Study of Electronic Structure of Scandium Monohydride (ScH), Scandium Mononitride (ScN) and Scandium Monoxide (ScO) Molecules

4.1 Introduction

This chapter presents laser-induced fluorescence (LIF) spectroscopic study on ScH, ScN and ScO molecules in the free-jet. The scandium, the first transition element, exhibit simplest electronic structure among rather complex *d*-block elements. The ScH and ScO molecules are studied extensively both theoretically as well as experimentally. However, no transitions among triplet manifold were observed in ScH molecule, which otherwise are well characterized among its isovalant YH and LaH molecules. We observed this transition in the present work. In ScO molecule, which is a well-known stellar constituent [1,2], our spectroscopic study extended the electronic spectra to the higher vibrational levels in the visible region and improved molecular constants at equilibrium. Apart from this, spectroscopic data on ScN was very scanty. Transition metal nitrides are important for fixation of nitrogen in industrial, inorganic, and biological systems [3,4]. Many transition-metal-containing diatomic molecules have a special place in astrophysics. Transition metal atoms have relatively high abundances in many stars [5] and several transition metal hydrides (CrH, CuH, TiH, ZnH, FeH and NiH) and oxides (CrO, ScO, VO, TiO, YO, ZrO and LaO) [2] have been detected so far. However, transition metal nitrides have not been identified in the stellar atmospheres and may because of lack of precise spectroscopic data for a meaningful search in the complex stellar spectra. We carried out spectroscopic investigation on the electronic structure of ScN. The $^1\Sigma^+$ ground state symmetry of ScN molecule, predicted theoretically [6,7] and also observed in earlier experiment [8] is unequivocally established in

our present study. In addition, observations of low- and high-energy states of ScN are also discussed.

4.2 Experiment

The ScH, ScN and ScO molecules are produced under different experimental conditions in the free-jet of the supersonic molecular beam apparatus, details of which are discussed in Chapter 2. In brief, a rotating and translating scandium metal rod is ablated with the third harmonic beam of a Nd:YAG laser. To produce ScH and ScN molecules, laser produced scandium metal plasma reacted with 2% ammonia seeded in helium gas emerging from a pulse valve under a backing pressure of 275 kPa. Due to surface oxidation of scandium metal rod, strong molecular spectra of ScO are always present. However, optimum signal of ScO is obtained with the use of 2% of molecular oxygen seeded in helium. We have used naturally abundant ammonia and molecular oxygen in our experiments, and scandium has naturally occurring single isotope. Thus, the spectra of only ^{45}ScH , $^{45}\text{Sc}^{14}\text{N}$ and $^{45}\text{Sc}^{16}\text{O}$ isotopomer are observed. The laser-induced fluorescence excitation spectra and low-, high-resolution dispersed fluorescence (DF) spectra are recorded as described as earlier. Lifetimes of the excited electronic states are recorded by acquiring the fluorescence decay curve on a digital storage oscilloscope.

To confirm the carrier of the band in case of ScH molecules, the mass-selected resonance two-photon ionization (R2PI) spectroscopy technique is employed in the experiment. The free-jet is skimmed by a 5 mm diameter skimmer placed at a distance 200 mm from the pulsed valve nozzle. A resulting molecular beam entered the second vacuum chamber which is differentially pumped by a turbo molecular pump. The molecular beam is then crossed with the counter propagating resonant excitation tunable dye laser and XeCl excimer as ionizing laser. The photoions generated are mass analyzed by a Wiley-McLaren type time-of-flight mass spectrometer equipped with a microchannel plate

detector. The resonant photoionization spectrum is recorded by integrating the signal corresponding to the ScH^+ ion mass peak on a gated boxcar integrator and stored on a computer.

4.3 Laser-Induced Fluorescence (LIF) Study of ScH

The spectra of ScH and ScD molecule were known since 1973, when Smith [9] recorded a few complex bands in absorption, mainly in the visible region. Bernard et al. [10] also observed ScH and ScD emission spectra in the near infrared and visible region. All these observed bands remained largely unassigned because of limited resolution, poor signal-to-noise ratios and the complexity of the bands. Later, Ram and Bernath [11,12] studied the emission spectra of ScH and ScD in the $3500\text{--}26,000\text{ cm}^{-1}$ range by Fourier transform spectroscopy and observed several transitions involving only singlet manifolds. They assigned the ground state as $^1\Sigma^+$ based on *ab initio* predictions [13] and the experimental results for isovalent YH [14], LaH [15] and also ScF [16]. The observed bands were classified into electronic transitions between the ground $X^1\Sigma^+$, low-energy $A^1\Delta$ and $B^1\Pi$ and high-energy $C^1\Sigma^+$, $D^1\Pi$, $E^1\Delta$, $F^1\Sigma^-$, and $G^1\Pi$ states.

ScH is the simplest among transition-metal-containing molecules. So, there have been large numbers of theoretical studies on its electronic structure and spectroscopic properties [13,17,18,19,20,21,22,23]. The *ab initio* calculations [13,18,19,20,22] predict the ground state of ScH as a $^1\Sigma^+$ state with a close lying $^3\Delta$ as first excited state. Chong et al. [21], in addition to the spectroscopic constants calculated dipole moments of the ground and low-lying states of first-row transition metal hydrides. Recently, Koseki et al. [22] calculated potential energy curves of the low-lying spin-mixed states for the group 3 and 5 hydrides and also reported transition energies and transition moments for few selected transitions and compared them with experiments.

Ram and Bernath [11,12] assigned the observed emission spectra to various transitions involving only the singlet manifold. They as well as Bernard et al. [10], also reported the observation of complex bands at 11,620 and 11,630 cm^{-1} assigned respectively to ScH and ScD. Although the bands could not be rotationally analyzed due to the complex structure or assigned to a particular transition, they speculated it to be analogous with the $d^3\Phi - a^3\Delta$ transitions observed in isovalent YH [14] and LaH [15] in the same energy region. Bernard et al. [10] also observed a Q -form branch at 17,900 cm^{-1} which also could not be analyzed. The origin of this structure was speculated due to analogous $^3\Phi - a^3\Delta$ transition observed in YH [24] and LaH [25] in the same energy region. The missing observation and assignment of transitions in the triplet manifold of ScH, which otherwise are well characterized in isovalent YH and LaH, motivated us to take up the present study.

4.3.1 Appearance of the Spectra

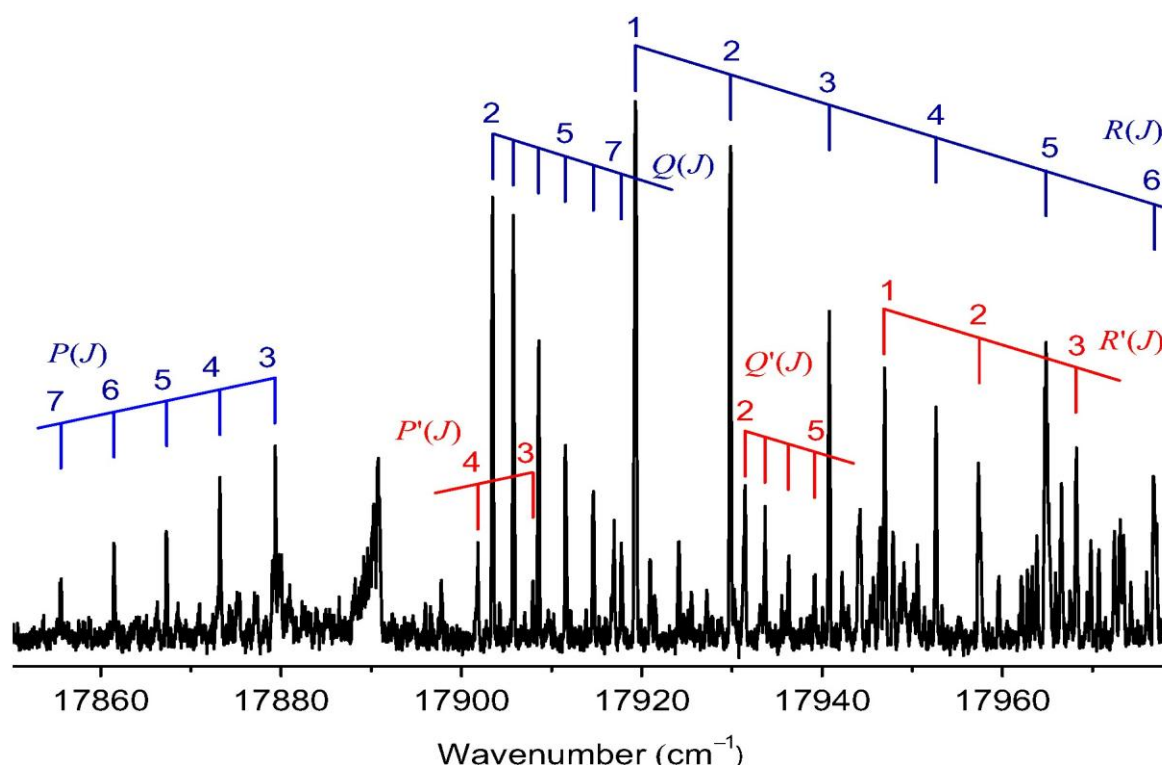


Figure 4.1 Rotational structure of the $g^3\Phi_2 - a^3\Delta_1$ band of jet-cooled ScH molecule. The PQR and $P'Q'R'$ represent (0,0) and (1,1) ScH bands respectively.

The excitation spectra of only the ^{45}ScH isotopologue are observed in our experiments. Two new violet degraded LIF excitation bands with neighboring origins at 17,914.5 and 17,942.3 cm^{-1} with rotational line spacing typical to ScH are observed (Figure 4.1). The dispersed fluorescence (DF) from ScH lines showed fluorescence only to the excitation wavelength and not to any of the vibrational levels of the lower state involved in the transition for further confirmation of the carrier of the band to ScH. The carrier of these bands was confirmed by obtaining the mass-selected resonance photo-ionization excitation spectra of ScH which is identical to that of the LIF excitation spectra. Both the bands at 17,914.5 and 17,942.3 cm^{-1} showed intense single R - and Q - and a weak single P -branch indicating a $\Delta I = +1$ transition. The band at 17,942.3 cm^{-1} was 5 times weaker than the band at 17,914.5 cm^{-1} . The later band was observed up to $J = 7$ for P - and Q - and $J = 6$ for R -branch however, P -, Q -, and R -branches for 17,942.3 cm^{-1} band ran up to $J = 4, 5$, and 3 respectively. The broad spectral feature at about 17,890 cm^{-1} does not belong to ScH. The dispersed fluorescence obtained from this broad feature showed three lines with successive wavenumber separation of about 870. The carrier of this spectral feature could not be identified.

4.3.2 Assignments of Bands and Molecular Constants

The assignments of bands are based on the observation of the number of branches and their first line, combination differences for the lower state, relative intensities of the branches within the band and overall band intensity. Rotational quantum number assignments of the P - and R -branches were carried out using the combination differences method. Distinctly different lower state combination differences for the 17,914.5 and 17,942.3 cm^{-1} bands from those of the ground $X^1\Sigma^+$ state [11] indicated that these transitions originate from the low-lying excited states. Our past experiments on LaH showed that the $a^3\Delta_1$ state at 1260 cm^{-1} was populated in the jet-cooled beam [26,27]. The *ab initio* calculations of ScH [13]

predict a $^3\Delta$ state as the first excited state at 2581 cm^{-1} . No Ω -splitting is observed in rotational lines observed up to maximum of $J'' = 7$ in P - and Q -, and $J'' = 6$ for R -branch. This is expected in the spectra obtained at a laser linewidth of 0.1 cm^{-1} and for a small Ω -doubling constant q_v of the order of $1\text{--}2 \times 10^{-3}$ typical for the $a^3\Delta_1$ state in YH [14] and LaH [15]. With no Ω -splitting seen at the employed experimental resolution, we have assigned rotational quantum number to the Q -branch by comparing the separation $\Delta_1 F(J)$ of the successive rotational levels obtained from corresponding PQ and RQ pair of lines with that of $\Delta_2 F(J)$ obtained from corresponding RP pair of lines [28]. Figure 4.1 shows the rotational quantum number assignment of the P -, Q - and R -branches for both the bands. The unassigned lines in the excitation spectra also fluoresce 1600 cm^{-1} to the red of the excitation wavelength. The excitation spectra recorded while parking the monochromator at 1600 cm^{-1} to the red of excitation wavelength showed mostly unassigned lines. As it is evident from Figure 4.1, the first line in P -, Q - and R -branches for both the bands are $R(1)$, $Q(2)$, and $P(3)$ which indicate that the transitions are $\Omega' = 2 - \Omega'' = 1$. The *ab initio* calculations [13] predict a $^3\Delta$ state as the first excited state at 2581 cm^{-1} . Bernard and Basis [24,25] reported the violet degraded $^3\Phi - a^3\Delta$ transitions respectively at $17,899$ and $16,007\text{ cm}^{-1}$ for isovalent YD and LaH. As mentioned earlier, Bernard et al. [10] also observed only a Q -form branch at $17,900\text{ cm}^{-1}$ belonging to ScH which could not be analyzed. At $17,903\text{ cm}^{-1}$, we also observed a Q -branch. The above observations indicate that the neighbouring bands at $17,914.5$ and $17,942.3\text{ cm}^{-1}$ can be plausibly assigned as (0,0) and (1,1) band of the $g^3\Phi_2 - a^3\Delta_1$ transition in ScH. The nomenclature for the newly observed $^3\Phi$ state as the 'g' state is taken from the equivalent $^3\Phi$ state assigned by Ram and Bernath in YH [14]. Due to the unavailability of deuterated ammonia (ND_3) in our laboratory, isotope shift studies for vibrational quantum number assignments of the electronic states could not be carried out. However, our assignment of the $v=0$ levels for the upper and lower electronic state was based on the

observation of bands on the lowest wavenumber side. Despite our best efforts we were unable to observe sub-bands corresponding to the other spin-orbit $g^3\Phi_3 - a^3\Delta_2$ and $g^3\Phi_4 - a^3\Delta_3$ transitions.

In the absence of the observation of transitions among other spin-orbit components of the $a^3\Delta$ and $g^3\Phi$ states, the observed wavenumbers of the (0,0) and (1,1) $g^3\Phi_2 - a^3\Delta_1$ sub-bands were fitted by treating each spin-orbit component as a separate Hund's case(c) state. The term energy expression for Hund's case (c) is given by

$$F_v(J) \left(\begin{smallmatrix} e \\ f \end{smallmatrix} \right) = T_v + B_v[J(J+1) - \Omega^2] - D_v[J(J+1) - \Omega^2]^2 + H_v[J(J+1) - \Omega^2]^3 \pm \frac{1}{2}q_v J(J+1) \quad (4.1)$$

Here B_v , D_v , and H_v are the rotational constant and its higher-order corrections and q_v is a Ω -doubling constant. In the absence of observation of Ω -splitting, the value of q_v was taken as zero. The molecular constants for the $v = 0$ and 1 level of the $a^3\Delta_1$ and $g^3\Phi_2$ states were determined in the fit and are given in Table 4.1. Equilibrium rotational constants, B_e , α_e and r_e respectively of 3.977(11), 0.076(11) cm^{-1} and 2.0737(14) Å for the $a^3\Delta_1$ state and 4.406(11), 0.078(11) cm^{-1} and 1.9701(12) Å for the $g^3\Phi_2$ state were determined.

Table 4.1 Molecular constants (cm^{-1}) for the $g^3\Phi_2 - a^3\Delta_1$ system and radiative lifetimes (ns) of ScH.

Constants	$a^3\Delta_1$		$g^3\Phi_2$	
	$v = 0$	$v = 1$	$v = 0$	$v = 1$
T_v	a	b	$a + 17914.50(4)$	$b + 17942.29(4)$
B_v	3.9391(69)	3.863(9)	4.3669(71)	4.289(9)
$D_v \times 10^3$	-4.33(27)	-4.11(36)	-1.62(30)	-1.15(44)
$H_v \times 10^5$	-1.90(30)	-	-1.15(36)	-
τ	-	-	42(2)	

4.3.3 Discussion

The observation of two new bands led to the assignment of two new electronic states of ScH with $\Omega = 2$ and 1 in $v = 0$ and 1 levels. Based on the nature of the experiment where only ground and low-energy states are populated, similarities in transition energies and rotational structure of the observed bands with those observed in isovalent YH and LaH

molecules and also *ab initio* calculations [13], the newly observed states are assigned as $a^3\Delta_1$ and $g^3\Phi_2$. The term energies of these triplet electronic states with respect to the ground state could not be determined due to the absence of observation of the inter combination transition. However, *ab initio* calculations of Anglada et al. [13] predict the $a^3\Delta$ state at 2581 cm^{-1} . These calculations predict transition energies with an uncertainty of about $\pm 2000\text{ cm}^{-1}$ and transition moments form any electric dipole allowed transitions. The observed $g^3\Phi_2 - a^3\Delta_1$ transition at $17,914.5\text{ cm}^{-1}$ in the present work is in good agreement with their calculated $2^3\Phi - 1^3\Delta$ transition at $19,200\text{ cm}^{-1}$ with a substantial transition moment of 0.99 a. u. While $g^3\Phi_2 - a^3\Delta_1$ (0,0) and (1,1) bands were observed with considerable intensity, transitions to the other spin-orbit $g^3\Phi_3 - a^3\Delta_2$ and $g^3\Phi_4 - a^3\Delta_3$ components were not observed. One of the reasons for lack of observation of other spin components of $g^3\Phi$ state could be predissociation. This hypothesis may be likely as it does not contradict the experimentally estimated dissociation energy D_0 of $16,615 \pm 725\text{ cm}^{-1}$ [29] and also *ab initio* D_e value of $18,850\text{ cm}^{-1}$ [13]. The observation of only one $g^3\Phi_4 - a^3\Delta_3$ out of the three possible sub-bands in YH by Bernard and Bacis [24] was conjectured on the basis of predissociation of $g^3\Phi_2$ and $g^3\Phi_3$ spin components. The negative sign of the centrifugal distortion constant D for both the states, especially in the lower $a^3\Delta_1$ state (Table 4.1) is quite unusual and indicates perturbation. Taher et al. [30] and Xia et al. [31] observed perturbations respectively in $v = 1$ and 2 of the ground $X^1\Sigma^+$ state in ScI. They explained this perturbation due to L-uncoupling and spin-orbit interaction between $X^1\Sigma^+$ and $a^3\Delta_1$ states via $^1\Pi$ and $^3\Pi$ states. The $\Delta G_{1/2}$ of the $X^1\Sigma^+$ state is 1547 cm^{-1} and thus energy-wise $v = 2$ of this state can perturb the $a^3\Delta_1$ state through above interaction via predicted $b^3\Pi$ [13] and observed $B^1\Pi$ states [12]. Following Taher et al., we attempted a deperturbation analysis by adding a $\mathbf{H}_{12}[J(J+1)]^{1/2}$ interaction term in a 2×2 matrix model to fit the lower state term energies, determined by combination differences. However, we did not get meaningful parameters which reproduce lower state

term energies. The parameters indicated *e/f* parity level separations of few cm^{-1} which was not observed experimentally. The fact that Ram and Bernath [11] did not observe any perturbations in $B^1\Pi$ ($v = 0-2$) indicates that this state does not interact with $a^3\Delta_1$ state. The direct interaction of the $b^3\Pi$ with the $a^3\Delta_1$ state were not considered as no extra lines originating from the $b^3\Pi$ state were observed. A better perturbation analysis could be possible with the observation of high J lines, which may help to obtain true rotational constants for $a^3\Delta_1$ state from the unperturbed portion of the spectra. The narrow energy window offered by jet-cooled spectra restricts the observation only to a few low J lines, which makes analysis difficult.

4.4 Spectroscopic Investigation of the Electronic Structure of ScN

Transition metal mononitrides, including ScN, which is the subject of this study, have received relatively little attention as compared to other transition-metal-containing diatomics, for example hydrides and oxides. The electronic states among singlet manifold of ScH are thoroughly studied while first observation of triplet-triplet transition by us is discussed in the previous section. Similarly, ScO molecule is also well studied however, we extended the vibrational levels in the $B - X$ transition and presented in Section 4.5 of this chapter. Prior to this experimental work on ScN, one paper on the gas-phase [8] and other on the matrix isolation [32] spectroscopy of ScN are the only experimental studies reported in the literature. A few *ab initio* studies [6,7,33,34] on the electronic structure of ScN have been also reported.

Ram and Bernath [8] have reported the first spectroscopic investigation of ScN in the gas-phase. They studied $\Delta v = 0$ sequence ($v = 0-2$) of the $A^1\Sigma^+ - X^1\Sigma^+$ system of ScN in the near-infrared region using Fourier transform emission spectroscopy. Rotational analysis resulted in accurate rotational constants for the three lowest vibrational levels of the $A^1\Sigma^+$ and $X^1\Sigma^+$ states and also indicated perturbations in the excited state vibrational levels $v' = 1, 2$; but the perturbations were not identified. Vibrational frequencies could not be determined due to the

lack of observation of off-diagonal bands. The lowest electronic state observed by Ram and Bernath [8] was assigned as the $X^1\Sigma^+$ ground state. However, this assignment was rather indirect and based on the comparison with the analogous transition in the isoelectronic CaO molecule [35] and the *ab initio* predictions of Kunze and Harrison [6]. The support of assignment of the observed bands to the $A^1\Sigma^+ - X^1\Sigma^+$ system of ScN attributed to the *ab initio* results was questionable, as no other low-energy $^1\Sigma^+$ state than the ground state was predicted for ScN at the time of experiment. Later Daoudi et al. [7] calculated a low-energy excited $^1\Sigma^+$ electronic state of ScN that correlated with $\text{Sc}(\text{ds}^2 \text{ } ^2\text{D}) + \text{N}(^2\text{D})$ excited asymptote, using Configuration Interaction by Perturbation of a multiconfiguration wavefunction Selected Iteratively (CIPSI) method. Most of the calculated spectroscopic constants of the $A^1\Sigma^+$ and $X^1\Sigma^+$ states agreed very well with the experiment. However, disagreement exist particularly for the equilibrium internuclear distance r_e of the $A^1\Sigma^+$ state which was attributed to possible misassignment and perturbation of this state with higher vibrational levels of $X^1\Sigma^+$ and close lying $^1\Pi$ state. They suspected the assignment of the $A^1\Sigma^+$ state involved in the transition. Several other electronic states correlating with that asymptote were also expected but not investigated. Along with the $X^1\Sigma^+$ and $A^1\Sigma^+$ states, Daoudi et al. [7] calculated potential energy curves and spectroscopic constants for three other low-energy excited states ($^3\Sigma^+$, $^3\Pi$ and $^1\Pi$). Recently Bai et al. [34] have recalculated potential energy curves and molecular constants of the $X^1\Sigma^+$ and $A^1\Sigma^+$ states using Multi-Reference Configuration Interaction (MRCI) method. Their results are in perfect agreement with the experiment [8].

Indirect experimental determination of the ground state symmetry, a doubt about the assignment of the $A^1\Sigma^+$ state raised by Daoudi et al. [7] and the electronic structure of ScN in the low-energy region where few states, predicted by *ab initio* studies [6,7] but unobserved experimentally, interaction of these low-lying states that causes perturbations, as well as

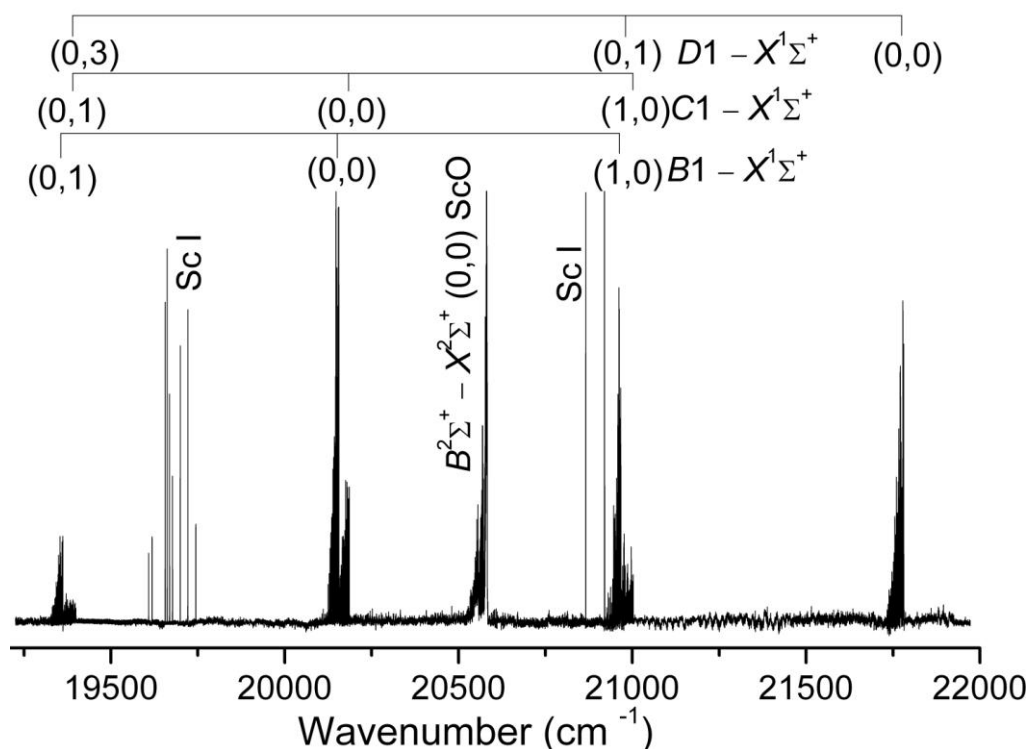
nonavailability of vibrational frequency data on the ground and low-energy states motivated us to conduct the present spectroscopic investigation of ScN in a jet-cooled molecular beam. In addition, *ab initio* studies [6,7] predict few strongly bound low-energy excited electronic states correlate to excited atomic asymptote and also shallow high-energy excited electronic states correlate to the lowest atomic asymptote which are still unobserved experimentally. Recent observation of the low- and high-energy excited electronic states in YN [36,37], isovalent to ScN also motivated us to take up the present study to shed some light on the electronic structure of ScN and compare the electronic structures of these two isovalent molecules.

Recently, to shed light on the character of the metal-nitrogen bond in ScN, Ziurys's group [38] recorded the Fourier transform microwave/millimeter-wave spectra in its $^1\Sigma^+$ ground electronic state. Hyperfine structure arising primarily from the nitrogen nucleus was resolved and electric quadrupole and nuclear spin-rotation parameters have been determined in their work. Their study supports the covalent, diradical bonding in the ScN ground state as suggested by Daoudi et al. [7].

4.4.1 Study of High-Energy States

4.4.1.a Description of the Observed Bands

Figure 4.2 shows a survey spectrum of ScN. Though total region explored was 18,200–23,600 cm^{-1} , the spectra attributed to ScN were observed in the range 19,300–21,800 cm^{-1} . Total nine excitation bands clustered in four groups with band origins at 19,356, 19,390, 19,391, 20,150, 20,184, 20,963, 20,981, 21,001, and 21,775 cm^{-1} were observed and are marked in the Figure 4.2. Along with the ScN bands we have observed (0,0) band of $B^2\Sigma^+ - X^2\Sigma^+$ system of ScO and many Sc I atomic lines which were used for wavelength calibration of ScN bands. The appearance of ScO band is due to the presence of sufficient oxide layer on scandium metal rod. Dispersed fluorescence spectra following excitation



All the nine bands were red degraded and each of them had P -, Q -, and R -branches. The intensities of bands with band origin at 20,150, 20,184, 20,963, 21,001, and 21,775 cm^{-1} were several times stronger than that of the bands at 19,356, 19,390, 19,391, 20,981 cm^{-1} among which 19,391 cm^{-1} band was the weakest. The intensity of 20,150 cm^{-1} band was stronger by approximately three times than the 20,184 cm^{-1} band. In 20,150 cm^{-1} band P -, Q - and R -branches stretched up to $J = 13$, 14 and 15, respectively, however, the 20,184 cm^{-1} band ran up to $J = 12$ for P and Q and $J = 13$ for R branch. The 21,775 cm^{-1} band showed a

rotational structure of long branches with Q branch running up to $J = 21$ however, the branches of the band at $19,390\text{ cm}^{-1}$ were shortest, extending up to $J = 11$.

4.4.1.b Quantum Number Assignment and Molecular Constants

All the observed nine bands were rotationally analyzed. The attribution of spectra to ScN is mainly due to the agreement of the rotational constant and harmonic wavenumber of the lower state observed in the present work with the $X^1\Sigma^+$ state observed previously by Ram and Bernath [8]. The attribution of spectra to ScN is also due to the agreement of term energy, harmonic wavenumber and symmetry of the $A^1\Sigma^+$ state observed in the disperse fluorescence spectra (Section 4.4.2.), with those reported in Ref. [8]. Rotational analysis also provided vibrational assignments which allowed the bands to classify into three systems. Rotational quantum number assignments of the P - and R -branches for all the observed bands except the $19,391\text{ cm}^{-1}$ band were established using combination differences of the $\nu = 0$ and 1 levels of the $X^1\Sigma^+$ ground state of ScN [8]. However, the assignments of the Q branches were based on the observation of the first line since no corresponding branches terminating on the levels with same symmetry of the upper states were present in the spectra.

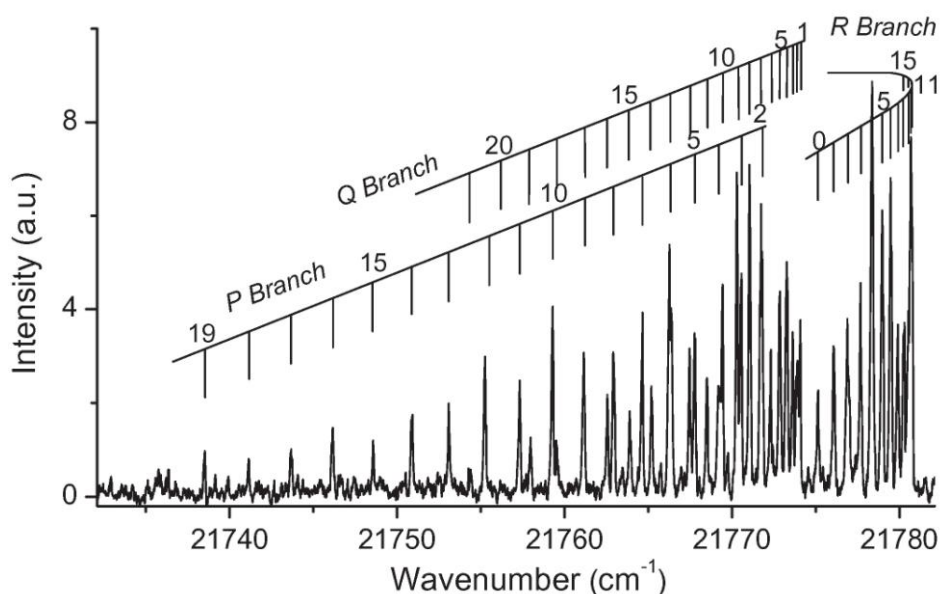


Figure 4.3 Rotational structure of the $(0,0)$ $D1 - X^1\Sigma^+$ excitation band of jet-cooled ScN molecule.

Figure 4.3 shows the rotational quantum number assignment for P -, Q -, and R -branches of the $21,775\text{ cm}^{-1}$ band. The combination differences and thus the rotational constant B for the lower state of the bands $20,150$, $20,184$, $20,963$, $21,001$, and $21,775\text{ cm}^{-1}$ coincided within the experimental precision with those of the $\nu = 0$ level of the $X^1\Sigma^+$ state observed by Ram and Bernath [8]. Similarly the combination differences for the lower state of the bands $19,356$, $19,390$, and $20,981\text{ cm}^{-1}$ coincided with those of $\nu = 1$ level of the $X^1\Sigma^+$ state. Since the spectra observed in the present work were in the free-jet molecular beam, where population is concentrated in the ground state, the present work further support and confirms that the $X^1\Sigma^+$ state, first observed by Ram and Bernath [8] as the lower electronic state of their infrared bands, is indeed the ground state of the ScN molecule. Due to unavailability of isotopically enriched ammonia ($^{15}\text{NH}_3$) in our laboratory, isotope shift studies for vibrational quantum number assignments of the excited states could not be carried out. However, our assignment of the $\nu' = 0$ levels was based on the observation of bands on the lowest wavenumber side and also with distinctly different B' value, originating from $\nu = 0$ level of the $X^1\Sigma^+$ state. Since no bands originating from $\nu = 0$ of the $X^1\Sigma^+$ state could be observed to the red of the bands at $20,150$, $20,184$, and $21,775\text{ cm}^{-1}$, these bands were assigned the $\nu' = 0$ vibrational quantum number in the upper electronic states. Similarly, the bands $19,356$, $19,390$, and $20,981\text{ cm}^{-1}$ were also assigned $\nu' = 0$ quantum number based on the similarity of their upper state combination differences with those of the bands with band origin, respectively, at $20,150$, $20,184$, and $21,775\text{ cm}^{-1}$. The $19,391\text{ cm}^{-1}$ band was also assigned $\nu' = 0$ quantum number based on the similarity of their upper state combination differences with $21,775\text{ cm}^{-1}$ band. The remaining two bands, $20,963$, and $21,001\text{ cm}^{-1}$, were assigned the $\nu' = 1$ vibrational quantum number. No obvious rotational perturbations were observed in any of the analyzed bands. The presence of P -, Q -, and R -branch structure in all the nine bands indicated that the observed transitions were $\Delta Q = \pm 1$ and thus the upper states

were assigned $\Omega = 1$. This established the assignments of the excitation bands and is given in Table 4.2 along with the radiative lifetimes of the *B1* and *C1* excited states in $v = 0$ and 1 levels and *D1* in $v = 0$ level. The radiative lifetimes of the excited states were determined by fitting the observed fluorescence decay curve with a convolution between a Gaussian function, closely represented excitation laser pulse and an exponential function with adjustable parameters.

Table 4.2 Band origins, vibronic assignments and excited state radiative lifetimes of ScN molecule.

Band Origin (cm ⁻¹)	$v' - v''$	Lifetime (ns)
<i>B1</i> – $X^1\Sigma^+$ system		
19356.284(18)	0 - 1	-
20150.330(18)	0 - 0	58(6)
20963.438(13)	1 - 0	59(3)
<i>C1</i> – $X^1\Sigma^+$ system		
19390.210(16)	0 - 1	-
20184.447(16)	0 - 0	205(16)
21000.838(11)	1 - 0	182(13)
<i>D1</i> – $X^1\Sigma^+$ system		
19391.3766(85)	0 - 3	-
20980.5226(65)	0 - 1	-
21774.6478(66)	0 - 0	48(4)

In conclusion, we have observed three excited electronic states, *B1* and *C1* with fundamental vibrations' wavenumbers of 813.1 and 816.4 cm⁻¹, respectively, and *D1* only in $v = 0$. The band origin, 21,774.6 cm⁻¹ for (0, 0) *D1* – $X^1\Sigma^+$ band is lie close to the likely band origin position of (2, 0) *B1* – $X^1\Sigma^+$ band. Also the measured lifetime value for this vibrational level was little lower but close to that of the *B1* state. The increase in the rotational constant value by 0.017 cm⁻¹ for the 21,774.6 cm⁻¹ level compared to that of the *B1* ($v = 1$) level (see Table 4.3) and the absence of any obvious perturbation in the band associated with *B1* ($v = 0$ and 1) and 21774.6 cm⁻¹ state prompted us to assign this state as *D1* ($v = 0$) rather than *B1* ($v = 2$). However, an alternate assignment as *B1* ($v = 2$) is also possible for this level given the prevalence of perturbations in transition-metal-containing diatomics. The isotope shift value upon $^{14}\text{N} \rightarrow ^{15}\text{N}$ substitution for this band may resolve the uncertainty in this

assignment. The wavenumber position of the band origin and the combination differences of the lower state indicated that the weak band at $19,391 \text{ cm}^{-1}$ was (0,3) band of $D1 - X^1\Sigma^+$ system. We did not observe (0, 2) but observed (0,3) band of the $D1 - X^1\Sigma^+$ system because of the much higher Frank-Condon overlap for the (0,3) than the (0,2) band as evident from the dispersed fluorescence spectra (Section 4.4.2).

Table 4.3 Molecular constants (in cm^{-1}) of the $X^1\Sigma^+$ ground state and B1, C1, D1 excited states.

	$v = 0$		$v = 1$		$v = 3$	
T_X	0.0		794.136	(81) ^{a,b}	2383.271	(11) ^{a,b}
B_X	[0.5527631] ^c		[0.5491456] ^c		0.54214	(10)
$D_X \times 10^7$	[10.508] ^c		[10.121] ^c		[9.411] ^{c,d}	
T_{B1}	20150.330	(18) ^a	20963.438	(13) ^a		
B_{B1}	0.50922	(36)	0.49292	(31)		
$D_{B1} \times 10^5$	6.28	(15)	8.92	(13)		
$q_{B1} \times 10^4$	8.1	(15)	3.3	(12)		
T_{C1}	20184.447	(16) ^a	21000.838	(11) ^a		
B_{C1}	0.42629	(44)	0.42335	(42)		
$D_{C1} \times 10^5$	- 4.21	(27)	- 6.22	(32)		
$q_{C1} \times 10^4$	5.2	(22)	8.8	(26)		
T_{D1}	21774.6478	(66) ^a				
B_{D1}	0.510129	(77)				
$D_{D1} \times 10^5$	0.151	(18)				
$q_{D1} \times 10^4$	-2.51	(33)				

^a This value represents a statistical error. In addition, there is a systematic error equal to $\sim 0.1 \text{ cm}^{-1}$.

^b Numbers in parentheses are one standard deviation in last two digits.

^c Parameters (from Ref. [8]) constrained in the fit.

^d Calculated using D_e and β_e values given Ref. [8].

The band origins, v_0 and molecular constants were determined by a nonlinear least squares fitting of the observed set of transition wavenumbers of the excitation bands to the expression, $v = v_0 + F'_v(J') - F''_v(J'')$

$$\text{where, } F'_v(J) \binom{e}{f} = B'_v[J(J+1) - 1] - D'_v[J(J+1) - 1]^2 \pm \frac{1}{2}q_v J(J+1) \quad (4.3)$$

$$\text{and } F''_v(J) = B''_v J(J+1) - D''_v [J(J+1)]^2 \quad (4.4)$$

are the rotational energy level expressions, respectively, for the excited B1, C1, and D1 with $\Omega = 1$ and the $X^1\Sigma^+$ ground states. Here B'_v and B''_v are the rotational and D'_v and D''_v are the

centrifugal distortion constants, respectively, for the excited and the ground states and q_v is a A -doubling constant for the excited state. Each rotational line was given an appropriate weight depending on the signal-to-noise ratio and the extent of blending. The molecular constants for the $v = 0$ and $v = 1$ levels of the $X^1\Sigma^+$ ground state were constrained in the fit at values obtained by Ram and Bernath [8] from the analysis of their more precise (about $\pm 0.002 \text{ cm}^{-1}$) near-infrared data on $A^1\Sigma^+ - X^1\Sigma^+$ bands and the molecular constants for the $B1$, $C1$, and $D1$ states were treated as adjustable parameters. All the nine bands belonging to three systems were initially fitted separately. However in the final fit, different bands those have vibrational level of the excited state in common, were combined and a fit was obtained to determine a single set of molecular constants for each vibrational levels of the $B1$, $C1$, and $D1$ states.

The 19391 cm^{-1} band was assigned as (0,3) band of $D1 - X^1\Sigma^+$ system. Ram and Bernath [8] did not observe $v = 3$ level of the $X^1\Sigma^+$ state. The rotational constant B for $v = 3$ level of the $X^1\Sigma^+$ state was determined in this work. The molecular constants for the $v = 0$ of the $D1$ state were constrained in the fit at the values previously determined from the combined fit of the (0,0) and (0,1) bands of the $D1 - X^1\Sigma^+$ system. Since our spectra are jet-cooled, where rotational structure did not extend to high enough J values, the determination of the centrifugal distortion constant D is not very accurate. So the value of D for $v = 3$ level of $X^1\Sigma^+$ state was also fixed at $9.411 \times 10^{-7} \text{ cm}^{-1}$ during fit. This value was determined by using usual expression $D_v = D_e + \beta_e(v + 1/2)$ and the D_e and β_e values reported in Ref. [8]. The obtained molecular constants for ScN are listed in Table 4.3. This work determined a value of $\omega_e'' = 793.8 \text{ cm}^{-1}$ for $X^1\Sigma^+$ state from the observed term values 794.1 and 2383.3 cm^{-1} , respectively, for $v = 1$ and 3 levels. Our value is in close agreement with the value of 795 cm^{-1} estimated using Kratzer relationship by Ram and Bernath [8], and also in fairly good agreement with the values of reported by various *ab initio* calculations. Kunze

and Harisson [6] calculated a value of 726 cm^{-1} using MCSCF calculations however; Daoudi et al. [7] have reported 765.5 cm^{-1} using CIPSI method. Recently, Bai et al. [34] have estimated a value of 806.6 cm^{-1} for ω_e'' using MRCI method. However, there is a large discrepancy for ω_e'' between our value and a value reported in Ref. [32] which utilized matrix isolation technique. Chertihin et al. [32] have attributed a band at 913 cm^{-1} to fundamental vibration of ScN in Ar matrix on the basis of $^{14}\text{N}/^{15}\text{N}$ isotope shift which was also in good agreement with their prediction from a density functional theory (DFT) calculation. The blue shift of about 119 cm^{-1} for fundamental vibration of ScN reported by Chertihin et al. [32] in Ar matrix is hard to account by just simple matrix effect. The ScN molecule has low ionicity with + 0.22 charge on Sc [7]. Ionic molecules usually experiences significant red shift in Ar matrix. However, large blue shift of 53 cm^{-1} for MgO in N_2 matrix [40] and 62 cm^{-1} for BeO in Ar matrix [41] have been observed earlier. MgO and BeO molecules are isoelectronic with ScN. The blue shift was explained on the basis of the mechanical coupling of Be with another atom in an ‘antisymmetric’ Ar-Be-O vibrational mode [41]. The major Ar interaction is with Be and not with BeO molecule as a whole. In fact, the observed bands show excellent agreement with *ab initio* calculations [42] that predict a strong infrared absorption for Ar-BeO blue shifted substantially from the BeO diatomic fundamental vibration frequency. Similar blue shift of 148 cm^{-1} for fundamental vibration in YN, isovalent with ScN, in N_2 matrix [43] compared to the gas-phase value [37] has been observed. Thus the possible reason for positive blue shift for fundamental vibration frequency of ScN in Ar matrix compared to presently measured gas-phase value could be due to the formation of Ar-Sc-N complex in Ar matrix.

4.4.2 Study of Low-lying States

4.4.2.a Dispersed Fluorescence Spectra and Assignments of the States

Dispersed fluorescence (DF) spectra were recorded in the wavelength region 450–850 nm. The DF spectra were obtained mainly by pumping a single rotation level of both e - and f -symmetry of $B1$, $C1$, and $D1$ states in the range $J = 4$ – 16 via (0,0) and (1,0) bands of the $B1 - X^1\Sigma^+$ and $C1 - X^1\Sigma^+$ transitions and (0,0) of $D1 - X^1\Sigma^+$ transition. Figure 4.4 shows the DF spectra wherein the displacement from the excitation laser wavenumber is indicated. The DF spectra showed three progressions with distinctly different vibrational spacing which revealed the presence of three low-lying electronic states, including the ground state and are marked in Figure 4.4. By combining the DF spectra originating from different vibrational levels in the excited states (Section 4.4.1), we have measured seven members of the progression terminating on the lowest energy electronic state (blue-end progression), only two members of the progression terminating on the middle state, and five members of the progression terminating on the highest energy state (red end progression). The middle progression was observed only from the $C1$ state. Due to unavailability of isotopically enriched ammonia ($^{15}\text{NH}_3$) in our laboratory, the assignments of vibrational quantum numbers to the members of the three progressions could not be established using an isotope shift observed upon $^{14}\text{N} \rightarrow ^{15}\text{N}$ substitution. However, our assignment of the $v = 0$ levels was based on the observation of the fluorescence peak on the lowest displaced wavenumber side in a particular progression. The term values of the vibrational levels of three progressions are listed in Table 4.4. Wavenumber separation between DF peak corresponding to $v = 0$ of the red-end progression to that of the $v = 0$ of the blue-end progression coincided within the experimental measurement precision with the origin of the (0–0) $A^1\Sigma^+ - X^1\Sigma^+$ band observed by Ram and Bernath [8]. Similarly, separation between 1–1 and 2–2 of the red- and the blue-end progressions coincided with the band origins of the (1–1) and (2–2) $A^1\Sigma^+ - X^1\Sigma^+$ bands.

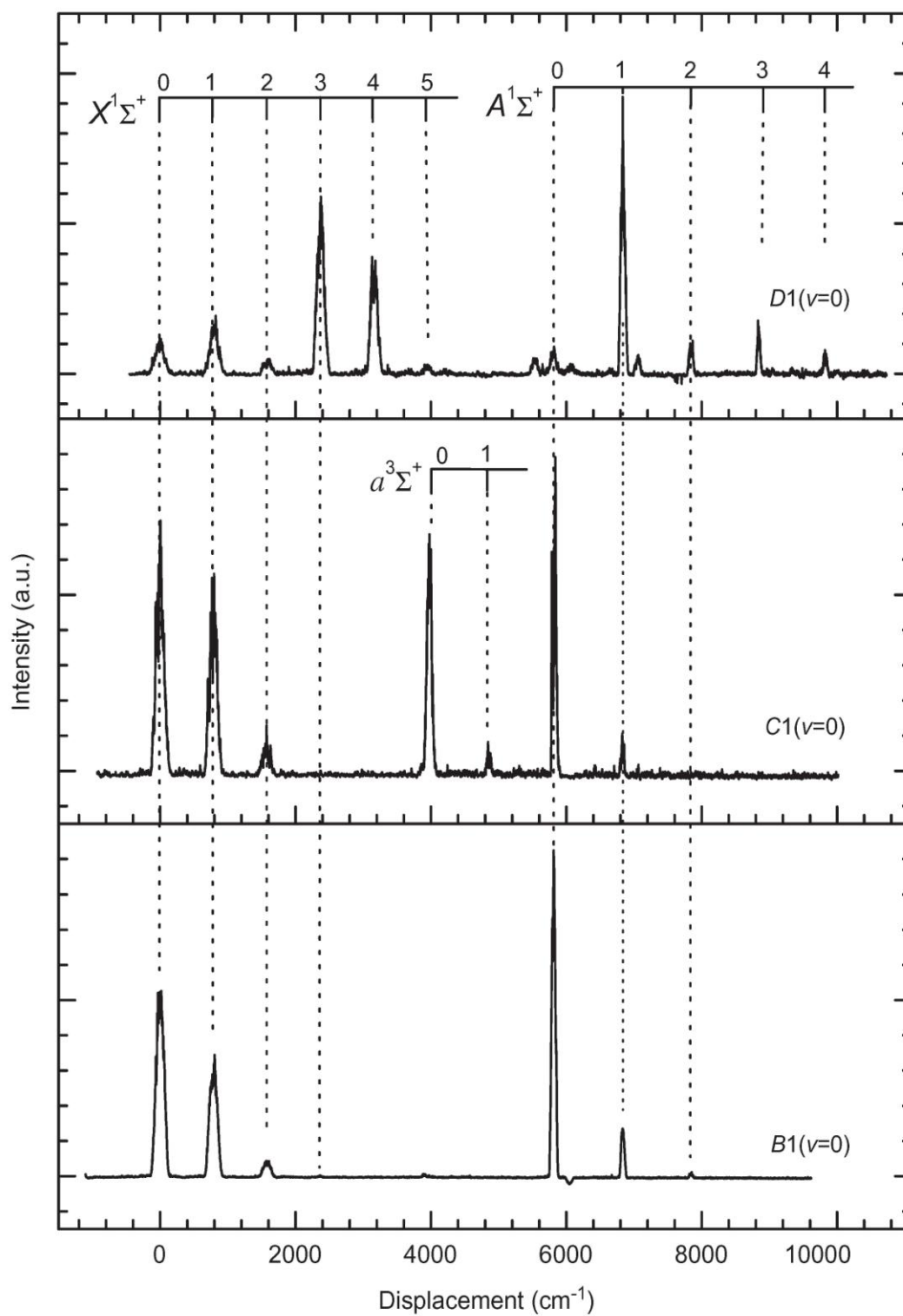


Figure 4.4 Laser-induced dispersed fluorescence spectra of ScN observed from $v = 0$ level of $B1$, $C1$, and $D1$ states; the x-axis shows the displacement in cm^{-1} from the excitation line.

Table 4.4 Term values (cm^{-1}) of the vibrational levels of the $X^1\Sigma^+$, $a^3\Sigma^+$, and $A^1\Sigma^+$ states of ScN.

v	$X^1\Sigma^+$		$a^3\Sigma^+$	$A^1\Sigma^+$		Ref. [8] ^a
				This work		
	T_v	$\Delta G_{v+1/2}$		T_v	$\Delta G_{v+1/2}$	
0	0.0	794.1	4009 (8) ^b	5818 (6)	1020	5820.1
1	794.1 (1) ^c	793.9	4897 (7)	6838 (6)	1015	6845.4
2	1588 (8)	795.3		7853 (6)	995	7854.1
3	2383.3 (1) ^c	787.7		8848 (3)	983	
4	3171 (4)	771.0		9831 (4)		
5	3942 (4)	826.0				
6	4768 (15) ^d					

^a Term values of $v = 0-2$ levels of $A^1\Sigma^+$ state determined by combining the $\Delta v = 0$ $A^1\Sigma^+ - X^1\Sigma^+$ band origins from Ram and Bernath [8] with the term values of the vibrational levels of the $X^1\Sigma^+$ state determined in the present work.

^b Numbers in parentheses indicate one standard deviation in the last quoted digits.

^c From Table 4.3.

^d Level not included in a fit for calculating vibrational constants.

In order to get information on the symmetries of the three low-energy electronic states on which DF terminated, the sufficiently intense DF lines of the three progressions were studied under higher resolution by reducing the monochromator slit width to 0.1 mm. Single line observed under low-resolution (1.0 mm slit) split into two-line pattern under high-resolution while pumping e -symmetry levels via either a P - or R -lines of any bands for all the three progressions. When f -symmetry levels were pumped via Q -lines, we have observed three-line fluorescence pattern under high-resolution for the middle progression and single-line pattern for the other two progressions (see Figure 4.5). Transitions with $\Delta J = 0, \pm 1$ can be observed in DF spectra. The Q -line emission ($\Delta J = 0$) follows the $e \leftrightarrow f$ and $f \leftrightarrow e$ selection rules, while the P - and R -line emissions ($\Delta J = \pm 1$) follow the $e \leftrightarrow e$ and $f \leftrightarrow f$ selection rules. All the three upper states $B1$, $C1$, and $D1$ involved in the transitions have $\Omega = 1$. With the upper state having $\Omega = 1$, the single-line emission from f -symmetry levels observed for DF lines terminating to the lowest- and the highest energy electronic states is consistent only with the lower states involved in these transitions being $^1\Sigma^+$ state. $A^1\Sigma^+$ state has only e -symmetry levels, thus only Q -line emission from the f -level and two lines, P - and

$R-$, from e -symmetry level are possible (see Figure 4.5a). Thus, from the wavenumber separation between the blue- and the red-end progressions in the low resolution DF spectra and also from the DF pattern under high-resolution, we conclude that the lower electronic states involved in the blue and the red-end progressions are $X^1\Sigma^+$ ground and $A^1\Sigma^+$ states, respectively. The present observation concerning the symmetry of the ground and the A states is consistent with the earlier works of Ram and Bernath [8] and of high-energy states (Section 4.4.1.). The observation of three-line pattern from f -level and two-line pattern from e -level under high-resolution for the middle progression is consistent only with the lower state being a $^3\Sigma^+$ state.

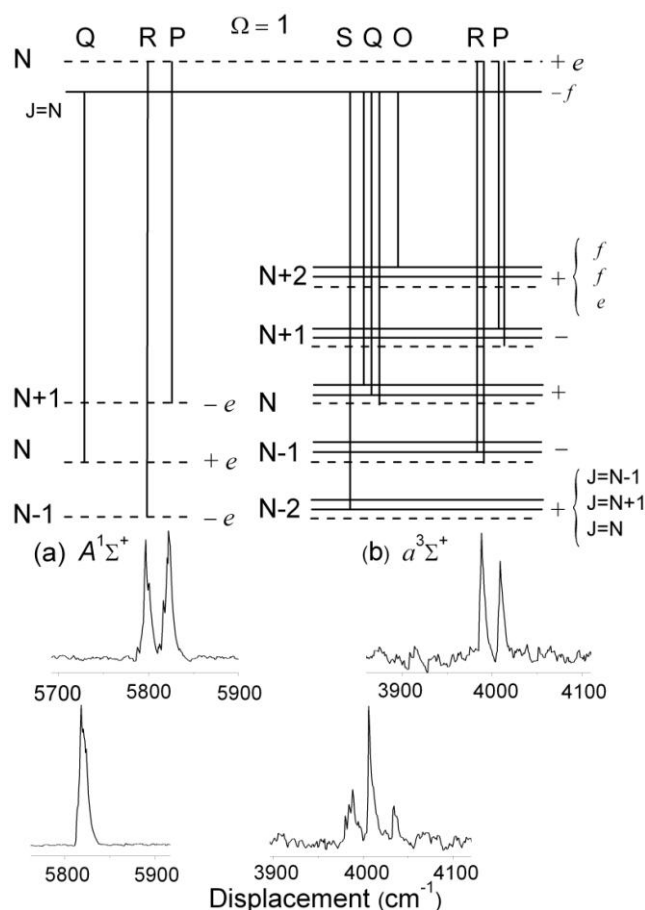


Figure 4.5 High-resolution dispersed fluorescence patterns from e - and f - symmetry levels of an $\Omega = 1$ state to (a) $^1\Sigma^+$ and (b) $a^3\Sigma^+$ state. The relevant energy levels of the upper and the lower states involved in the transitions are also shown.

As shown in energy level diagram of the Figure 4.5b, the middle line of the triplet consists of three unresolved Q -form ($\Delta N = 0$) lines, oR , oP , and Q and the two-lines on either side are oP ($\Delta N = -2$) and sR ($\Delta N = +2$) lines. Thus in the present study we have observed the first excited state of $^3\Sigma^+$ symmetry at $T_0 = 4009(8) \text{ cm}^{-1}$ and is consistent with the *ab initio* results of Kunze and Harrison [6] and Daoudi et al. [7] which predicted $^3\Sigma^+$ to be the first excited state with T_0 respectively equal to, 2687.6 and 2275.5 cm^{-1} . In addition to $A^1\Sigma^+$ and $^3\Sigma^+$, *ab initio* studies [6,7] predicted two more low-energy excited electronic states, $^1\Pi$ and $^3\Pi$. However, the high resolution pattern of the DF would have been different if the lower state of the middle progression be either a $^1\Pi$ or a $^3\Pi$. We would have observed three-line pattern from either e - or f -levels for the $^1\Pi$ state as well as for each spin-orbit component of the $^3\Pi$ state. Thus we labeled the new state observed at $T_0 = 4009(8) \text{ cm}^{-1}$ as $a^3\Sigma^+$.

We estimated rotational constants of the lower states to which the DF was terminated from the high-resolution DF spectra. Initially, rovibrational term values of the lower state were determined by subtracting the wavenumbers of the DF lines from the term energy of the pumped rotational levels of upper electronic state. The rovibrational term values, E_{Nv} , of the lower states obtained from the DF spectra were least squares fitted to the well known formula, $E_{Nv} = T_v + B_v N(N + 1) - D_v [N(N + 1)]^2$, where T_v is the rotationless term value of vibrational level v , B_v and D_v are rotational and centrifugal distortion constants and N is the quantum number of total angular momentum without spin. Rovibrational term values of $v = 0$ and 3 levels of $X^1\Sigma^+$ state obtained from different excitations were fitted to and obtained $B_0 = 0.550(24) \text{ cm}^{-1}$, $B_3 = 0.574(73) \text{ cm}^{-1}$, and $T_3 = 2384(6) \text{ cm}^{-1}$ which are in agreement with the value of $0.5527631 \text{ cm}^{-1}$ for B_0 reported by Ram and Bernath [8] and 0.54214 cm^{-1} for B_3 and 2383.3 cm^{-1} for T_3 values reported in Section 4.4.1. Similarly, the rotational constant $B_0 = 0.567(8) \text{ cm}^{-1}$ and $T_0 = 5819(1) \text{ cm}^{-1}$ for $A^1\Sigma^+$ state obtained in this work are in good

agreement with the values reported by Ram and Bernath [8]. Rovibrational term values of $v = 0$ level of $a^3\Sigma^+$ state obtained from different excitations were fitted to same equation and obtained $T_0 = 4012(1) \text{ cm}^{-1}$ and $B_0 = 0.515(5) \text{ cm}^{-1}$. D_0 was set at zero.

In addition to the members of three main DF progressions we have also observed few weak fluorescence features mainly at 5535 and 7056 cm^{-1} which may correspond to fluorescence terminating on vibrational levels of the $^1\Pi$ or the $^3\Pi$ states, but definite assignment in relation to this was not possible.

4.4.2.b Vibrational Constants and Potential Energy Curves

Vibrational constants and subsequently RKR potential curves for the three low-energy states, $X^1\Sigma^+$, $a^3\Sigma^+$, and $A^1\Sigma^+$ were obtained by combining the present data on vibrational term values with more accurate band origin data of Ram and Bernath [8] for $A - X$ transition and also data from our work on high-energy states of ScN (Table 4.4).

Ram and Bernath [8] observed only $A - X$ diagonal transitions up to $v = 2$, hence could not determine relative energies of the vibrational levels of the X and A state. In addition to the direct measurement of vibrational term values of X , a , and A states, we have determined vibrational term values of the A state up to $v = 2$ by combining vibrational term values of the X state determined in this work with accurate band origin determined by Ram and Bernath [8]. We see fairly good agreement between these term values with those measured directly in the present work from DF spectra (Table 4.4).

The vibrational term values for X and A states were fitted using weighted least squares method to an anharmonic oscillator formula,

$$\Delta G = G(v) - G(0) = \omega_e v - \omega_e x_e v(v+1) + \omega_e y_e [v(v^2+1.5v+0.75)] \quad (4.5)$$

where, v is a vibrational quantum number, $G(v)$ is term value of the v^{th} vibrational level, ω_e is harmonic and $\omega_e x_e$, $\omega_e y_e$ are anharmonic vibrational constants. The experimental error in the vibrational term value was used as a weight in the fit. For $X^1\Sigma^+$ state, term values of six

vibrational levels ($v = 0-5$) were included in the fit out of which term values for $v = 1$ and 3 were taken from more accurate band origin values. The $v = 6$ level was not included in the fit due to relatively large measurement uncertainty in its value. However for $A^1\Sigma^+$ state, the vibrational term values obtained by combining the $X^1\Sigma^+$ term values with band origins reported by Ram and Bernath [8] were used for $v = 0-2$ and for $v = 3$ and 4 the vibrational term values obtained from the present DF work were used. We could determine the value of fundamental vibration only for $a^3\Sigma^+$ state since we have observed only two members in the progression. The vibrational constants obtained in the fits are listed in Table 4.5 and compared with the experimental [8] and *ab initio* [6,7] values from the earlier works.

Table 4.5 Spectroscopic constants^a of the $X^1\Sigma^+$, $a^3\Sigma^+$, and $A^1\Sigma^+$ states of ScN.

State		T_e	r_e	ω_e	$\omega_e x_e$	$\omega_e y_e$
$X^1\Sigma^+$	Present work	0.0	-	787.7(3) ^b	-4.4(2)	-0.78(3)
	Ref. [8]	0.0	1.68 723	795.0	-	-
	Ref. [6]	0.0	1.768	726.0	0.30	-
	Ref. [7]	0.0	1.714	765.5	4.36	-
$a^3\Sigma^+$	Present work	3961(8) ^c	1.747(8)	888(11) ^d	-	-
	Ref. [8]	-	-	-	-	-
	Ref. [6]	2621.3	1.769	861.0	5.00	-
	Ref. [7]	2266.4	1.686	783.7	4.32	-
$A^1\Sigma^+$	Present work	5695(2)	-	1044.8(1)	10.5(1)	0.46(1)
	Ref. [8]	5694.2	1.69 540	1045.0	-	-
	Ref. [6]	-	-	-	-	-
	Ref. [7]	5702.3	1.584	1025.2	6.48	-

^a r_e in Å and other constants in cm^{-1} .

^b Numbers in parentheses indicate one standard deviation in the last quoted digits.

^c Value calculated using $\Delta G_{1/2}$ of $a^3\Sigma^+$ state and $\omega_e x_e$ value from Ref. [6].

^d $G_{1/2}$ value.

The RKR potential energy curves for $X^1\Sigma^+$, $a^3\Sigma^+$, and $A^1\Sigma^+$ states have been constructed by employing RKR1 program of LeRoy [44] and are shown in Figure 4.6. Vibrational constants from the present work and rotational constants (B_e and α_e) from the earlier work [8] were used to generate RKR potential energy curves for $X^1\Sigma^+$ and $A^1\Sigma^+$ states.

However for $a^3\Sigma^+$, fundamental vibration as an approximate value of ω_e and the equilibrium internuclear distance, $r_e = 1.747(8)$ Å from the present work and the *ab initio* value of $\omega_e x_e$ from Kunze and Harrison [6], were used to generate Morse potential for $a^3\Sigma^+$ state. The B_e value which was used to determine r_e was determined iteratively using the Pekeris relationship [28] from rotational constant $B_0 = 0.515(5)$ cm⁻¹. Using the RKR potential energy curves Frank-Condon factors for the $A^1\Sigma^+ - X^1\Sigma^+$ system have been calculated. The Frank-Condon factor values were found to be significant only for diagonal vibrational transitions, which is in agreement with Ram and Bernath's [8] observation of only diagonal bands with no signature for off-diagonal vibrational transition in $A^1\Sigma^+ - X^1\Sigma^+$ system.

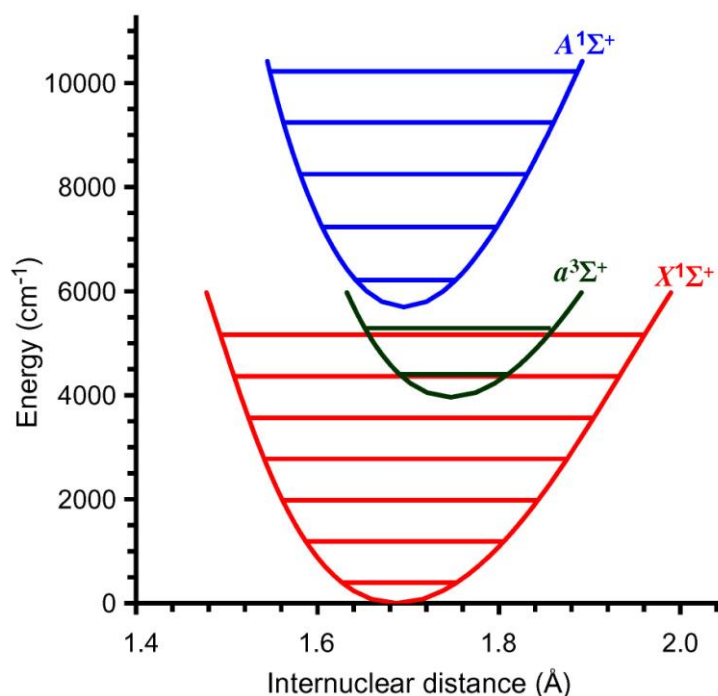


Figure 4.6 RKR potential energy curves for the $X^1\Sigma^+$, $a^3\Sigma^+$, and $A^1\Sigma^+$ states of ScN. Observed vibrational levels are shown by solid lines.

4.4.3 Discussion

The $X^1\Sigma^+$ ground state and two low-energy excited electronic states, $a^3\Sigma^+$ and $A^1\Sigma^+$ were observed and characterized in this work using laser-induced dispersed fluorescence from the excited electronic states. The $^1\Sigma^+$ ground state symmetry was confirmed

unequivocally. The first excited $a^3\Sigma^+$ state, predicted earlier by *ab initio* studies [6,7] was observed for the first time. We have directly measured the term energies of the vibrational levels of $X^1\Sigma^+$ and $A^1\Sigma^+$ states, not determined previously by Ram and Bernath [8]. The comparison of spectroscopic constants determined in the present work for the low-lying states with the earlier experimental and *ab initio* values are given in Table 4.5. There are five low-lying states, $A^1\Sigma^+$, $^1\Pi$, $^3\Pi$, $^3\Sigma^+$, and $X^1\Sigma^+$ predicted by *ab initio* studies. The $X^1\Sigma^+$, $^1\Pi$, and $^3\Sigma^+$ states correlate with excited, $\text{Sc}(3d^24s^1^4F) + \text{N}(^4S)$ however; $^3\Pi$ state with lowest atomic asymptote, $\text{Sc}(3d^14s^2^2D) + \text{N}(^4S)$. The $A^1\Sigma^+$ state, calculated by Daoudi et al. [7] and observed by Ram and Bernath [8], correlate with excited atomic asymptote $\text{Sc}(3d^14s^2^2D) + \text{N}(^2D)$.

The harmonic vibration wavenumber for the $X^1\Sigma^+$ state determined in the present work is in good agreement with the earlier experimental and *ab initio* values. Present work provided the value of $-4.4(2) \text{ cm}^{-1}$ for anharmonic vibrational constant for the X state. The negative value for $\omega_e x_e$, a consequence of abnormal vibrational spacing, is irrational for any physical potential. Of course it has to become positive at some vibration level. The $X^1\Sigma^+$ ground state showed unusual vibrational spacing i.e. $\Delta G_{v+1/2} = G(v+1) - G(v)$, which increased for certain v 's as shown in Table 4.4. For any physical potential the $\Delta G_{v+1/2}$ should decrease with increasing v . According to *ab initio* results of Daoudi et al. [7] the $X^1\Sigma^+$ ground state has 92% of $1\sigma^2 1\pi^4 2\sigma^1 3\sigma^1$ and 3% of $1\sigma^2 1\pi^4 2\sigma^2$ orbital configuration at internuclear distance, r_e . The 1π electrons form a double bond along with a weak σ dative bond in the former configuration and a triple bond with strong σ bond in the later configuration. However, $A^1\Sigma^+$ state has leading contribution of 67% from $1\sigma^2 1\pi^4 2\sigma^2$ configuration to form triple bond and 5% from $1\sigma^2 1\pi^4 2\sigma^1 3\sigma^1$ at r_e . Thus above two configurations are mixed in $X^1\Sigma^+$ and $A^1\Sigma^+$ states. We presume that the abnormal vibrational spacing, $\Delta G_{v+1/2}$ of $X^1\Sigma^+$

state could be due to the variation of the composition weights of the two orbital configurations with internuclear distance. Moreover, $v = 5$ and 6 levels of the $X^1\Sigma^+$ state fall within close proximity respectively with, $v = 0$ and 1 levels of $a^3\Sigma^+$ state (see Figure 4.6). However, only heterogeneous perturbation is possible between $^1\Sigma^+$ and $^3\Sigma^+$ states which would be small and would not distort the vibrational structure of the $X^1\Sigma^+$ state.

The term energy, T_e and ω_e value for the $A^1\Sigma^+$ state are also in good agreement with the earlier experimental [8] and *ab initio* [7] values. The $A^1\Sigma^+$ state showed a regular behavior as the $\Delta G_{v+1/2}$ decreased with v (see Table 4.5). However, the anharmonic constant determined in the present work is higher than the *ab initio* value [7]. Also, discrepancy exists between the observed and the calculated values for the equilibrium internuclear distances r_e , especially for $A^1\Sigma^+$ state. The experimental values of r_e for the $A^1\Sigma^+$ and $X^1\Sigma^+$ state [8] are about 7% more and 1.5% less than the respective *ab initio* values [7]. This again indicates stronger mixing of the doubly and triply bonded orbital configurations than predicted by *ab initio* results of Daoudi et al. [7] for X and A states. The equilibrium internuclear distance of $1.747(8)$ Å for $a^3\Sigma^+$ state, determined experimentally for the first time, is 3.6% more than the calculated value of Daoudi et al. [7] but close to the value of Kunze and Harrison [6]. However, the value of r_e determined in the present work for the $a^3\Sigma^+$ state was derived from the less precise dispersed fluorescence data ($\sim 4\text{--}8$ cm $^{-1}$) which resulted in its large standard deviation. The term energy and harmonic wavenumber for $a^3\Sigma^+$ state determined in the present work are also on the higher side than the *ab initio* values [6,7].

The three new $B1$, $C1$, and $D1$ with $\Omega = 1$ excited electronic states were observed respectively at $20,150.3(1)$, $20,184.4(1)$, and $21,774.6(1)$ cm $^{-1}$. The $B1$ and $C1$ states were observed in the $v = 0$ and 1 level, however $D1$ state was observed only in $v = 0$ level despite of our best efforts to observe transitions to higher vibrational levels of the excited states. The possible reason for lack of observation of higher vibrational levels could be predissociation,

as the predicted dissociation energy of $21,934 \text{ cm}^{-1}$ [6] is just above the highest vibrational level observed in our experiment.

In order to better understand the nature of these states we attempted to compare our results with *ab initio* calculations of electronic states by Kunze and Harrison [6] and Daoudi et al. [7]. Daoudi et al. [7] predicted bound states $^5\Delta$, $^3\Delta$, $^5\Pi$, $^3\Sigma^-$, and $^5\Sigma^-$ with potential minima in the range $15,900\text{--}21,200 \text{ cm}^{-1}$ above the ground state. All these states have equilibrium internuclear distances $\sim 0.36\text{--}0.48 \text{ \AA}$ longer than the ground state and relatively shallow ($D_e \approx 3000\text{--}9000 \text{ cm}^{-1}$) and strongly asymmetric potentials, adiabatically correlate with the lowest atomic asymptote, $\text{Sc } (3d^1 4s^2 \text{ } ^2D) + \text{N}(^4S)$. The calculated vibration wavenumbers were about 500 cm^{-1} . In addition to above, Kunze and Harrison [6] also calculated $^3\Delta$, $^1\Delta$, and $^5\Sigma^+$ states in the $18,000\text{--}21,000 \text{ cm}^{-1}$ region. Among these, $^5\Sigma^+$ state has shallow asymmetric potential with longer equilibrium internuclear distance (2.1 \AA) and vibration wavenumber of 530 cm^{-1} however, $^3\Delta$ and $^1\Delta$ states were bound relative to the ground-state atoms but correlate with pure $3d^3 \text{ } ^4F$ state of Sc atom.

The equilibrium internuclear distances (r_e) in the $B1$ and $C1$ states are estimated to be $1.7469 (7)$ and $1.9212 (10) \text{ \AA}$, respectively, and internuclear distance in $v = 0$ (r_0) in $D1$ state is $1.75925 (13) \text{ \AA}$. They are only slightly longer in $B1$ and $D1$ states than in the ground state ($1.68723(3) \text{ \AA}$ [8]) however; it is considerably longer ($\sim 0.234 \text{ \AA}$) in $C1$ state. The small difference between the B_0 and B_1 values ($\sim 0.016 \text{ cm}^{-1}$ for $B1$ and 0.003 cm^{-1} for $C1$ state) suggest fairly symmetric potentials for $C1$ and little asymmetric for $B1$ state. Also the fundamental vibrations' wavenumbers of 813.1 and 816.4 cm^{-1} , respectively, for $B1$ and $C1$, both larger than the fundamental vibration wavenumber of the ground state, equal to 794.1 cm^{-1} , indicate stronger bonding in the $B1$ and $C1$ state as compared with the ground state. Above mentioned facts about $B1$, $C1$, and $D1$ states makes them unlikely candidates for theoretical counterparts, $^5\Pi$, $^3\Sigma^-$, $^5\Sigma^-$, and $^5\Sigma^+$ states predicted by *ab initio* calculations with

potential minima in the range 15,900–21,200 cm^{-1} above the ground state. It is also difficult to imagine that the transitions to these states from $X^1\Sigma^+$ state would have sufficiently large intensity as observed in our experiments.

Including the $A^1\Sigma^+$ low-lying state, the $\text{Sc}(3d^14s^2\ ^2D) + \text{N}(^2D)$ asymptote gives rise to 30 electronic states [7] viz. two each of $^{1,3}\Sigma^+$, three each of $^{1,3}\Sigma^-$, four each of $^{1,3}\Pi$, three each of $^{1,3}\Delta$, two each of $^{1,3}\Phi$, and one each of $^{1,3}\Gamma$ symmetry. Daoudi et al. [7] have calculated no other potential energy curve than that of the $A^1\Sigma^+$ state. We speculate that some of the other states which correlate to atomic asymptote $\text{Sc}(3d^14s^2\ ^2D) + \text{N}(^2D)$, may be sufficiently bound to have the potential minimum in the range of presently observed $B1$, $C1$, and $D1$ states and thus to have potential depths and vibration wavenumbers comparable with the ground state. If this is true then the $B1$ and $D1$ states could correspond to two of the four $^1\Pi$ states and possibly, $C1$ state be one of the four $^3\Pi$ states. These assignments also support the presence of strong Q -branch in the observed bands. The possible reasons for speculation that the $C1$ state could be $^3\Pi_1$ are following: excited state lifetime for $C1$ state was higher, around 200 ns than that of $B1$ and $D1$ states which were in the range 50–60 ns; relative intensities of the bands arising from $X^1\Sigma^+$ state to $C1$ state were three to four times smaller than those to $B1$ and $D1$ states; and the dispersed fluorescence spectra from $C1$ state showed a group of extra lines, than that from $B1$ and $D1$ states, terminating to the lower state, assigned as $a^3\Sigma^+$ (See Figure 4.4). Thus if $C1$ state is assumed to be $^3\Pi_1$, then most of the intensity of the nominally forbidden $^3\Pi - X^1\Sigma^+$ transition would be due to the interaction between $C1(^3\Pi)$ state and neighboring $B1$ and $D1$ states ($^1\Pi_1$). As would be expected in this case, the intensity of $^3\Pi_1 - X^1\Sigma^+$ sub-band would be stronger than that of the other two and thus it would be also easy to explain why only $^3\Pi_1 - X^1\Sigma^+$ component was observed in our spectra.

Comparison of present data of ScN with isovalent YN [36,37] showed remarkable similarity. The ground state with $^1\Sigma^+$ symmetry and two low-energy excited states viz. $a^3\Sigma^+$

and $A^1\Sigma^+$ have also been observed in YN. Three excited states with $\Omega = 1$ were observed for YN in 18,900–20,000 cm^{-1} region. The exact identity of these states also could not be determined. Thus in order to elucidate the observation of excited electronic states in the region around 20,000 cm^{-1} for isovalent ScN and YN molecules, more extensive *ab initio* studies are required which take into account the involvement of higher excited atomic asymptotes.

4.5 LIF Spectroscopy of ScO in the Visible Region

The spectra of ScO molecule are of considerable astrophysical interest. Especially, the bands due to $B^2\Sigma^+ - X^2\Sigma^+$ system, which falls in the blue-green region, were identified in the stellar spectra [45,46]. The lines from $A^2\Pi_{3/2} - X^2\Sigma^+ (0,0)$, $A^2\Pi_{1/2} - X^2\Sigma^+ (0,0)$ and $B^2\Sigma^+ - X^2\Sigma^+ (0,0)$ were also found to be present in the sun spot umbral spectra [47]. The intensity distribution in the spectra of many astrophysical important diatomic molecules play crucial role in understanding the physicochemical state of the stellar object. Franck-Condon (FC) factors are directly proportional to the transition probabilities. A precise knowledge of equilibrium rotation, vibration constants and FC factors are thus essential for understanding many aspects of the molecule like rotational, vibrational temperature etc., which are related to the state of the emitting source. The present laser-induced fluorescence spectroscopic investigations on jet-cooled ScO molecule has been undertaken to improve the molecular constants at equilibrium for both, the $B^2\Sigma^+$ excited and the $X^2\Sigma^+$ ground electronic states. Spectroscopy of rotationally resolved $B - X$ system of ScO was previously carried out by Akerlind [48], who observed (0,1), (0,0),(2,1),and(1,0) bands and assigned the transition as $^2\Sigma^+ - ^4\Sigma^+$. Later, Adams et al. [49] reanalyzed the (0,0) band at higher resolution and corrected its assignment as $^2\Sigma - ^2\Sigma$ transition. The wrong assignment of the ground state of ScO was due to the applicability of different angular momentum coupling scheme, which was not recognized initially because of the presence of strong coupling of the nuclear spin with

electron spin. The ground state electronic configuration of ScO is $8\sigma^2 3\pi^4 9\sigma^1$, where, 9σ orbital is $4s\sigma$ of Sc. This configuration results in the ground state as $X^2\Sigma^+$. The ground state belongs to the unusual hyperfine coupling case ($b_{\beta S}$), where the Fermi contact operator $b\mathbf{I}\cdot\mathbf{S}$, couples the electron spin \mathbf{S} with the nuclear spin \mathbf{I} (see Figure 4.7 (a)).

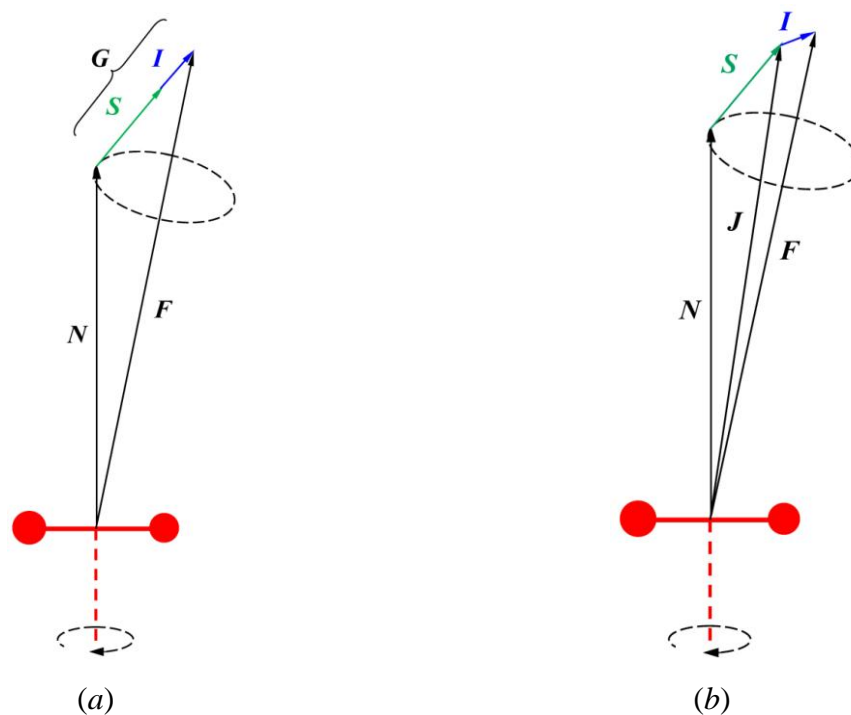


Figure 4.7 Vector diagram of (a) Case ($b_{\beta S}$) and (b) Case ($b_{\beta I}$) coupling scheme for the Σ states.

The only stable isotope, ^{45}Sc , has a nuclear spin $I = 7/2$ and a very large magnetic moment such that the Fermi contact interaction for an unpaired electron in the 9σ ($4s\sigma$ of Sc) molecular orbital of the ground state $X^2\Sigma^+$ in ScO is large. Thus the fine doubling of $4b \sim 0.25 \text{ cm}^{-1}$ observed in the spectrum was attributed to nuclear hyperfine structure. Due to the presence of fine doubling, there appear to be twice of the electron spin components in the excitation spectrum as there actually are, and therefore, the first rotational analyses [48] assigned the ground state of ScO as $^4\Sigma^+$. The excited electronic state $B^2\Sigma^+$ arises by promotion of 9σ electron to the 10σ ($3d\sigma$ of Sc), results in $8\sigma^2 3\pi^4 10\sigma^1$ configuration. The 10σ electron does not couple with the nuclear spin of the Sc. Thus, the excited state $B^2\Sigma^+$ follows the usual

coupling case ($b_{\beta I}$), where the electron spin \mathbf{S} is more strongly coupled to rotation \mathbf{N} than to \mathbf{I} (see Figure 4.7(b)).

Chalek and Gole [50] carried out vibrational analysis of band heads in the chemiluminescence spectra of $B - X$ and $A^2\Pi - X^2\Sigma^+$ systems resulting from the reaction of scandium atom with NO_2 and estimated equilibrium vibrational and rotational constants. Also of relevance is the work done on the other band system, $A^2\Pi - X^2\Sigma^+$ [51,52,53]. In the present study, a total of six rotationally resolved excitation bands viz. (0,0), (1,0), (2,0), (3,0), (4,0) and (1,2) of the $B^2\Sigma^+ - X^2\Sigma^+$ system were observed. We have also observed vibrational progression up to $v'' = 8$ in the ground electronic state from the dispersed fluorescence (DF) spectra obtained by populating well defined rotational levels of the $B^2\Sigma^+$ state. Analyses of these excitation and DF spectra resulted in the determination of improved molecular constants at equilibrium for the B and X states. These constants were used to construct the RKR potential energy curves for both the electronic states. Franck-Condon factors for the $B^2\Sigma^+ - X^2\Sigma^+$ system were also calculated. Very Recently, Ziurys's group has investigated the pure rotational spectrum of ScO [54] in their ground state which shows the current interest in this molecule.

4.5.1 Excitation and Dispersed Fluorescence Spectra of $B^2\Sigma^+ - X^2\Sigma^+$ System and Equilibrium Molecular Constants

In the present work, we have investigated (0,0), (1,0), (2,0), (3,0), (4,0) and (1,2) bands of the $B^2\Sigma^+ - X^2\Sigma^+$ system in the 19,400–23,800 cm^{-1} range and determined rotational constants. We have observed rotational lines up to $N = 40$ since the spectra were recorded in the free-jet. A portion of the (4,0) band is shown in Figure 4.8.

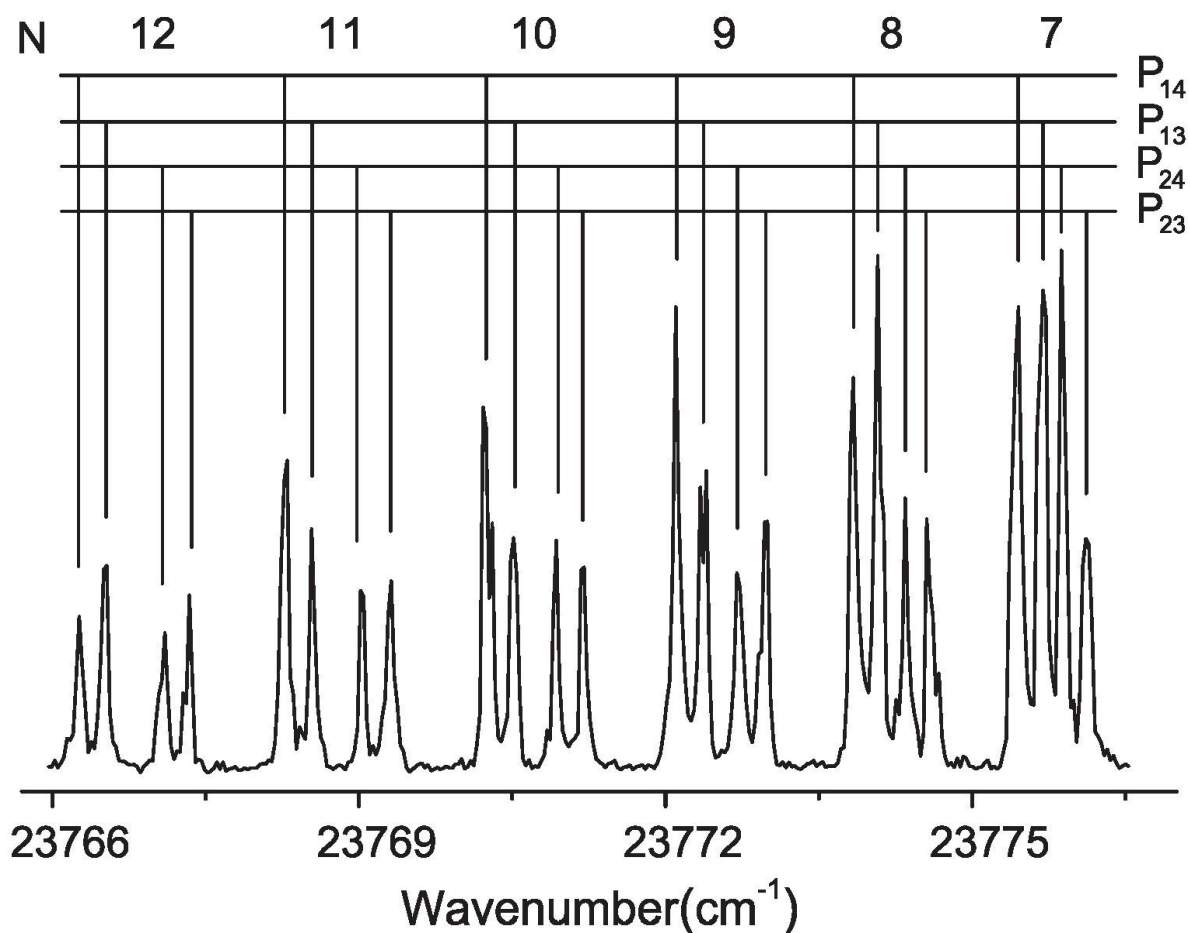


Figure 4.8 Rotational structure in the $(4,0) B^2\Sigma^+ - X^2\Sigma^+$ excitation band of jet-cooled ScO molecule.

The main feature of the spectrum is the appearance of quartets, in which one type of doublets has spacing of $\sim 0.25 \text{ cm}^{-1}$, which remained constant with rotational quantum number N , whereas for the other type of doublets, the spacing between the successive members increased monotonically with N . The doublets with constant spacing are attributed to the nuclear hyperfine structure in the ground state. The ground state belongs to the unusual hyperfine coupling case $b_{\beta S}$ where the Fermi contact operator, $b\mathbf{I}\cdot\mathbf{S}$, couples the electron spin \mathbf{S} to the nuclear spin \mathbf{I} . Since $I = 7/2$ for ^{45}Sc and $S = 1/2$ for a doublet state, the total spin momentum $\mathbf{G} = \mathbf{I} + \mathbf{S}$ can take the values 3 and 4. Thus the rotational levels are split into two components corresponding to $G = 3$ and 4, separated by $4b$, where b is the Fermi contact parameter (see Figure 4.9).

The term values for the two sublevels of a given vibrational level can expressed as

$$T_{3v}(N) = T_v + B_v[N(N + 1)] - D_v[N(N + 1)]^2 - \frac{9}{4}b \quad (4.6)$$

and

$$T_{4v}(N) = T_v + B_v[N(N + 1)] - D_v[N(N + 1)]^2 - \frac{7}{4}b \quad (4.7)$$

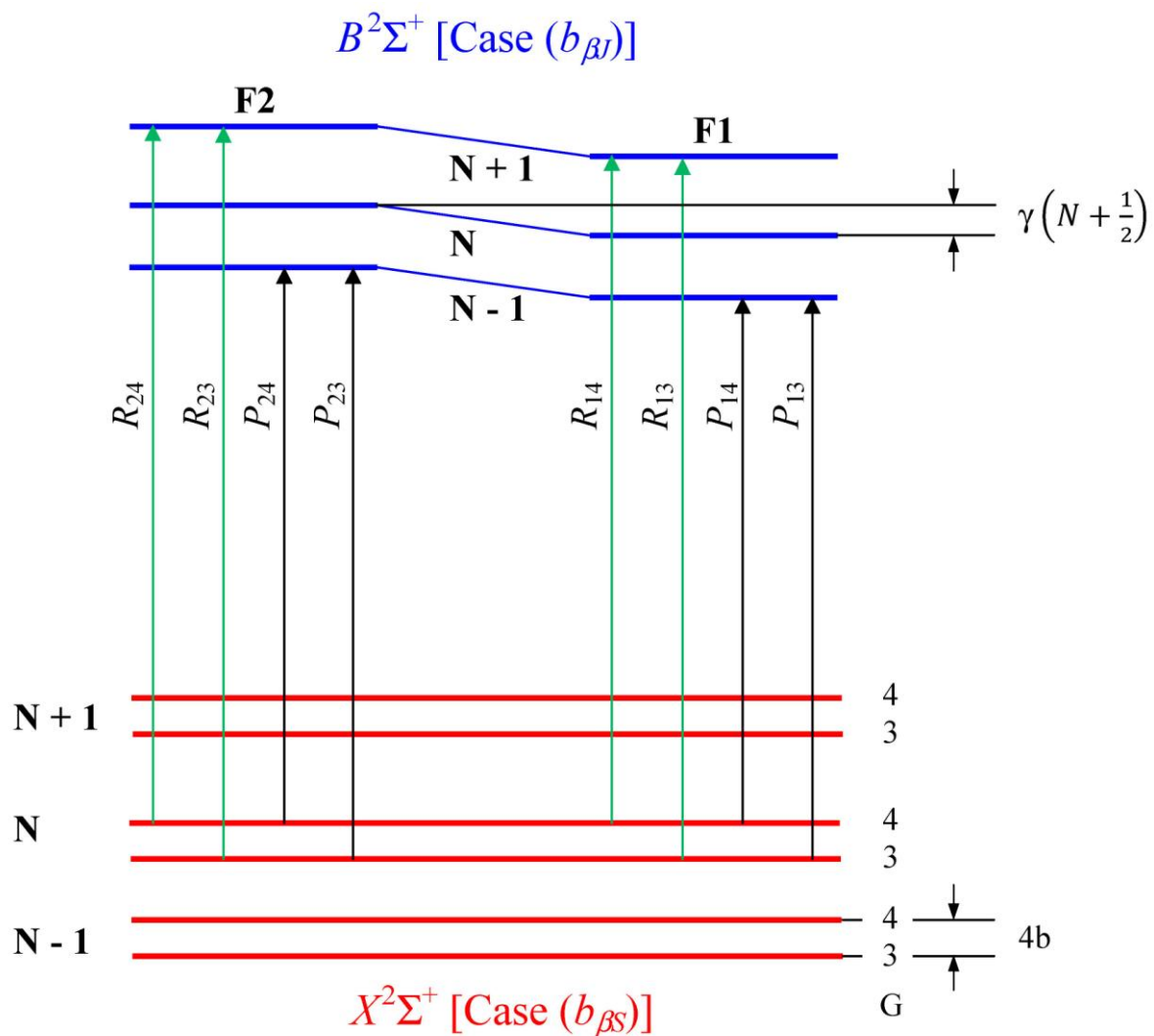


Figure 4.9 Energy level diagram of the $X^2\Sigma^+ - X^2\Sigma^+$ transition of ScO

The excited $B^2\Sigma^+$ state follows the more usual coupling case $b_{\beta J}$ where the electron spin \mathbf{S} is more strongly coupled to rotation \mathbf{N} than to \mathbf{I} . The vector coupling is then $\mathbf{J} = \mathbf{N} + \mathbf{S}$ and the F_1 and F_2 rotational sublevels correspond to $N = J - 1/2$ and $N = J + 1/2$, respectively.

The term value for the two sublevels of $B^2\Sigma^+$ state can be expressed as

$$T_{1v}(N) = T_v + B_v[N(N + 1)] - D_v[N(N + 1)]^2 + \frac{\gamma_v}{2}N \quad (4.8)$$

and

$$T_{2v}(N) = T_v + B_v[N(N + 1)] - D_v[N(N + 1)]^2 - \frac{\gamma_v}{2}(N + 1) \quad (4.9)$$

Figure 4.8 shows the constant hyperfine splitting of $\sim 0.25 \text{ cm}^{-1}$ in the P -branch of the $X^2\Sigma^+$ state as $P_{13}(N)$ and $P_{14}(N)$ and spin-rotation splitting in the $B^2\Sigma^+$ state as $P_{13}(N)$ and $P_{23}(N)$ which increases with N (see Figure 4.9). The molecular constants for the $v' = 2-4$ vibrational levels of the $B^2\Sigma^+$ state were determined by fitting the wavenumbers of the (2,0), (3,0) and (4,0) bands by weighted least squares fit program. The equations (4.6), (4.7) and (4.8), (4.9) were used respectively for describing the term values of the $X^2\Sigma^+$ and $B^2\Sigma^+$ states. The molecular constants for the $v'' = 0$ level of $X^2\Sigma^+$ state were fixed in the fit to the more accurate values from Rice et al. [53]. The values of centrifugal distortion constant D_v could not be determined accurately in the present work, because limited number of the rotational levels, N up to ~ 40 in this case, observed in the jet-cooled source. Hence, the D_v was fixed to the values from Akerlind [48] which was evaluated from the large number of rotational levels observed in their arc spectra. The molecular constants for $v' = 1$ and $v'' = 2$ were determined by fitting the (1,0) and (1,2) band together. These constants for the B and X states are listed in Table 4.6. The more accurate values for $v' = 0$ for the B state [49] and $v'' = 0, 1$ for the X state [53] are also listed in the Table 4.6 for the completeness since these values are used for determining the equilibrium molecular constants.

The DF spectra were recorded in the wavelength region 400–800 nm mainly by pumping a single rotational level within the vibrational levels $v' = 0-4$ of the B state via various excitation bands of the $B - X$ system observed in the present work. Fig. 2 shows the typical DF spectra where in the displacement from the excitation laser wavenumber is indicated. Single line observed under low-resolution split into two-line pattern, P and R , under high-resolution (see inset of Figure 4.10) as both the electronic states have $^2\Sigma$ symmetry.

Table 4.6 Molecular constants (in cm^{-1}) for the $X^2\Sigma^+$ and $B^2\Sigma^+$ states of ScO. The T_v values are accurate to 0.1 cm^{-1} .

$X^2\Sigma^+$ State					
Parameters	$v = 0^a$	$v = 1^b$		$v = 2$	
T_v	0	964.8739(20)		1922.44(4) ^c	
B_v	0.5134335(80)	0.5107618(85)		0.50808(23)	
$D_v (\times 10^6)$	0.5737(26)	0.5761(27)		0.5785(53) ^d	
b_v	0.06487(10)	-		0.06487 ^a	
$B^2\Sigma^+$ State					
	$v = 0^e$	$v = 1$	$v = 2$	$v = 3$	$v = 4$
T_v	20571.15(2)	21388.519(13)	22197.075(22)	22995.008(30)	23784.613(13)
B_v	0.48308(5)	0.47989(2)	0.47751(6)	0.47404(6)	0.47107(6)
$D_v (\times 10^6)$	0.674(5)	0.71 ^f	0.69 ^f	0.69 ^g	0.69 ^g
γ_v	-0.0670(2)	-0.0674(7)	-0.0676(17)	-0.0698(18)	-0.0698(12)

^a Parameters (from Ref. [53]) constrained in the fit.

^b Parameters from Ref. [53] tabulated for completeness of the table.

^c Number in parentheses denotes one standard deviation in the last quoted digits.

^d Parameter estimated from D_0 and D_1 from Ref. [53] by using relation $D_v = D_e + \alpha_D (v + \frac{1}{2})$ and constrained in the fit.

^e Parameters from Ref. [49] tabulated for the completeness of the table.

^f Parameter (from Ref [48]) constrained in the fit.

^g Parameter constrained in the fit.

By combining the DF spectra originating from different vibrational and rotational levels in the B state, we have measured nine members of the progression to the X state. For determining the vibrational quanta in the ground state from the DF spectra, we proceeded as follows: the combination differences between either P - or R - dispersed fluorescence lines, originating from the same upper state v' and terminating to successive vibrational levels v_1'' and v_2'' of the lower state have to satisfy [28],

$$R_{v'v_1''}(N) - R_{v'v_2''}(N) = P_{v'v_1''}(N) - P_{v'v_2''}(N) = \Delta G_{v''+\frac{1}{2}} - \alpha_e N(N+1) \quad (4.10)$$

where $\Delta G_{v''+\frac{1}{2}} = G''(v_2'') - G''(v_1'')$ and $\alpha_e = B_{v_1''} - B_{v_2''}$.

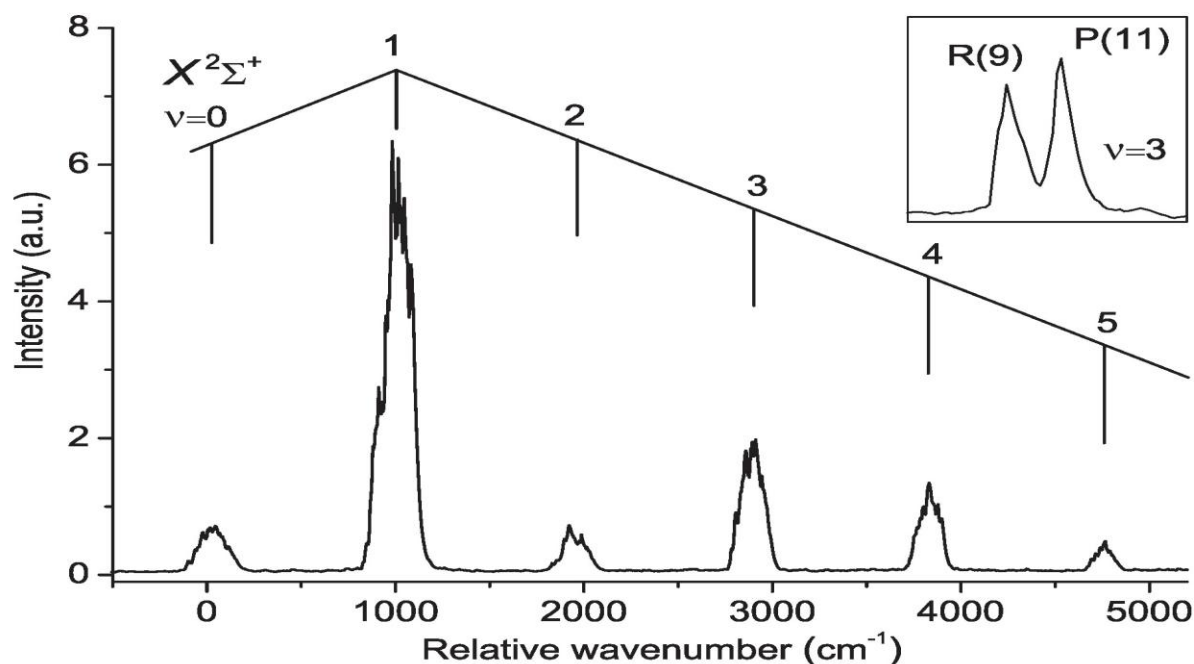


Figure 4.10 Dispersed fluorescence (DF) spectra of ScO observed from $v' = 2, N' = 10$ of $B^2\Sigma^+$ state; the x-axis shows the displacement (in cm^{-1}) from the excitation line. The inset shows the DF spectra at high-resolution where the $P(11)$ and $R(9)$ lines are well resolved.

Considering the accuracy of the DF data and observation of relatively low rotational levels N in the present work, the constant D_v can be disregarded. The DF spectra from $N' = 7-15$ were recorded so that the P - and R -lines terminating to a particular v'' were resolved with good fluorescence intensity. The $\Delta G_{v''+1/2}$ was determined from a least square fit of the wavenumber interval for P - (and R -) lines terminating to successive v'' s as a function of $N(N+1)$. The meaningful value of α_e could not be determined from fit due to low precision of the DF data. So $\alpha_e = 0.00267 \text{ cm}^{-1}$, determined from B_0, B_1 and B_2 values of X state (see Table 1) was fixed in the fit. The $\Delta G_{v''+1/2}$ and rotationless vibrational term T_v values are listed in Table 4.7. The term values for $v'' = 1$ and 2 are in good agreement with the more accurate values obtained from band origin which are listed in Table 4.6.

Table 4.7 $\Delta G_{v+1/2}$ values and vibrational term values T_v for the ground $X^2\Sigma^+$ state. Experimental error in $\Delta G_{v+1/2}$ is $\sim 4 \text{ cm}^{-1}$.

v	$\Delta G_{v+1/2}$	T_v	O-C ^a
0	965	0	-
1	956	965	1
2	948	1921	2
3	937	2869	2
4	930	3806	-1
5	924	4736	-2
6	915	5660	-1
7	911	6575	-2
8		7486	2

^a observed minus calculated wavenumbers generated from equilibrium vibrational constants listed in Table 3.

Equilibrium vibrational constants for the X and B states were obtained by combining the present vibrational term values with more accurate band origin at a from the present and the earlier work [49,53] listed in Table 4.8. These term values were fitted using least squares method to an anharmonic oscillator formula given in equation (4.5).

Table 4.8 Equilibrium molecular constants^a for the $X^2\Sigma^+$ and $B^2\Sigma^+$ states of ScO.

State	T_e	ω_e	$\omega_e x_e$	B_e	α_e	R_e (Å)
$X^2\Sigma^+$	0	972.2(6) ^b	4.06(8)	0.51477(12)	0.00267(8)	1.66608(19)
		975.74 ^c	4.2 ^c	0.5152 ^c	0.0033 ^c	-
$B^2\Sigma^+$	20643.96(30) ^b	826.91(3)	4.710(6)	0.48436(20)	0.00294(9)	1.71759(35)

^a Constants are in cm^{-1} , except r_e in Å.

^b Number in parentheses denotes one standard deviation in the last quoted digits.

^c The values for $X^2\Sigma^+$ state are from Ref. [50].

The accurate term values determined from band origins for $v'' = 1$ and 2 of X state were taken respectively from Rice et al. [53] and our present work, and for rest; the values were taken from the DF spectra. However, for the B state, vibrational term values were from band origins, the value For $v' = 0$ was taken from Adams et al. [49] and $v' = 1-4$ were from the present work. The molecular constants at equilibrium for X and B states are listed in Table 4.8 along with the values obtained by Chalek and Gole [50] for the X state. Chalek and Gole calculated the equilibrium molecular constants by fitting rotationally unresolved band heads involving v'' up to 11 of $A^2\Pi - X^2\Sigma^+$ system. Considering the resolution of $\sim 1\text{Å}$ at which

band heads were determined, the iterative process used to determine the equilibrium constants using a limited set of rotational data and the large difference ($\leq 10 \text{ cm}^{-1}$) between the calculated and observed values obtained by Chalek and Gole, suggests that the present values for the X state are better determined.

4.5.2 Potential Energy Curves and Franck-Condon Factors for $B^2\Sigma^+ - X^2\Sigma^+$ Transition

The RKR potential energy curves for B and X states were constructed earlier by Murthy and Murthy [55]. The Franck-Condon factors for $B - X$ transition were also estimated previously by Rao et al. [56] and later by Suárez [57]. They have used the molecular constants for $v'' = 0$ and 1 of the X state and $v' = 0-2$ of the B state reported in Refs. [48,49,51] to estimate equilibrium constants required for construction of RKR potential and FC factors. However, in the present work, the RKR potential energy curves for $X^2\Sigma^+$ and $B^2\Sigma^+$ states were constructed using the equilibrium molecular constants (Table 4.8) determined from the larger set of vibrational levels of X and B states. RKR1 program of LeRoy [44] was used to generate the potential curve and are shown in Table 4.9 and Figure 4.11.

Table 4.9 The classical turning points (in Å) and corresponding calculated term values (in cm^{-1}) of RKR potential energy curves of the $X^2\Sigma^+$ and $B^2\Sigma^+$ states of ScO.

v	$X^2\Sigma^+$			$B^2\Sigma^+$		
	$G(v)$	r_{\min}	r_{\max}	$T_e + G(v)$	r_{\min}	r_{\max}
0	485.0	1.6141	1.7227	21056.0	1.6614	1.7792
1	1449.0	1.5787	1.7675	21873.5	1.6233	1.8284
2	2405.0	1.5555	1.8001	22681.6	1.5984	1.8645
3	3352.8	1.5373	1.8278	23480.2	1.5789	1.8953
4	4292.6	1.5221	1.8526	24269.4	1.5626	1.9231
5	5224.2	1.5088	1.8755			
6	6147.6	1.4969	1.8971			
7	7063.0	1.4862	1.9176			
8	7970.2	1.4763	1.9373			

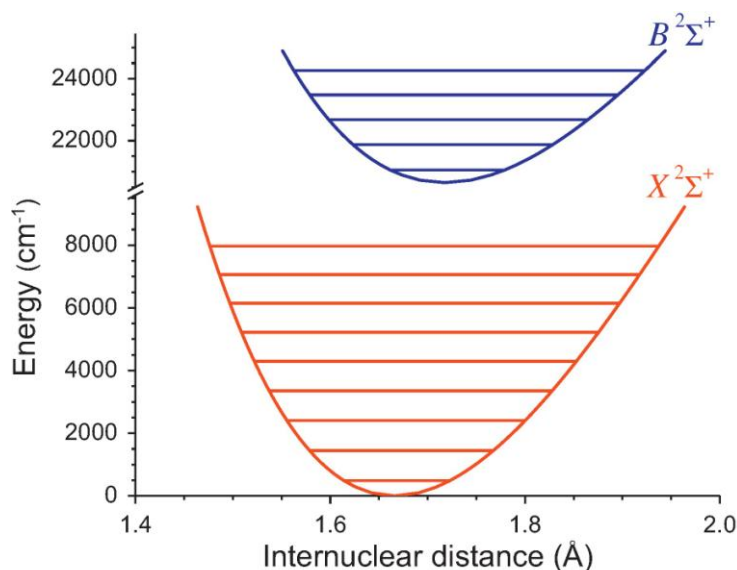


Figure 4.11 RKR potential energy curves for the $X^2\Sigma^+$ and $B^2\Sigma^+$ states of ScO.

Also considerable FC factor of 0.343 for the (1,2) band explains the observation of this hot band in the present work (Table 4.10). For (2,2) band, Rao et al. [56] calculated the FC factor equal to 0.28. However, the sum of FC factors calculated by them is ~ 1.2 for the $B - X$ band originating from $v' = 2$, which clearly indicates error in their calculation. We determined FC for (2,2) band as 0.033, which is in good agreement with the value of 0.044 reported by Suárez [57].

Table 4.10 Franck-Condon factors for the $B^2\Sigma^+ - X^2\Sigma^+$ transition of ScO.

$v' \backslash v''$	0	1	2	3	4	5	6	7	8
0	0.655	0.276	0.060	0.008	0.001	0	0	0	0
1	0.276	0.213	0.343	0.136	0.028	0.004	0	0	0
2	0.060	0.342	0.033	0.295	0.200	0.058	0.010	0.001	0
3	0.009	0.136	0.294	0.001	0.203	0.238	0.095	0.021	0.003
4	0.001	0.029	0.198	0.202	0.039	0.109	0.244	0.133	0.037

4.6 Conclusion

ScH, ScN and ScO molecules are produced in a pulsed free-jet apparatus and laser-induced fluorescence spectroscopy is employed to explore the electronic structure of these molecules. This section concludes the chapter with restatement of the results obtained in this study. The first observation of an electronic transition among the triplet manifolds in ScH is reported. Laser-induced-fluorescence and mass-selected resonance photoionization

spectroscopy of jet-cooled ScH molecules led to the observation of a (0,0) and (1,1) bands of $\Omega' = 2 - \Omega'' = 1$ transition, assigned as $g^3\Phi_2 - a^3\Delta_1$ transition. Rotational constants determined from the fit indicated perturbations in both states.

Laser-induced fluorescence excitation spectra of jet-cooled ScN molecules have been unequivocally established $^1\Sigma^+$ symmetry for the ground state. The vibrational progressions to the $X^1\Sigma^+$ ground and two low-energy excited electronic states have been observed. Out of the two excited states, the lower one is $a^3\Sigma^+$ state, observed for the first time and the higher one, $A^1\Sigma^+$ state observed earlier by Ram and Bernath [8]. The dispersed fluorescence pattern confirmed the symmetry of the ground and low-energy excited electronic states. The equilibrium internuclear distance equal to 1.747(8) Å determined for the $a^3\Sigma^+$ state in the present work is significantly longer than those of 1.68723(3) and 1.69540(3) Å, respectively for the $X^1\Sigma^+$ and $A^1\Sigma^+$ states [8]. The harmonic wavenumber of 787.7(3) and 1044.8(1) cm^{-1} are determined respectively for the $X^1\Sigma^+$ and $A^1\Sigma^+$ states, however the fundamental vibration of 888(11) cm^{-1} is observed for the $a^3\Sigma^+$ state. The RKR potential energy curves for these states are also constructed. Three new electronic states with $\Omega = 1$ have been observed at 20,150.3(1), 20,184.4(1), and 21,774.6(1) cm^{-1} . Also the fundamental vibrations and equilibrium internuclear distances are found to be 813.1(1) cm^{-1} and 1.7469(7) Å for the $B1$ state and 816.4(1) cm^{-1} and 1.9212(10) Å for the $C1$ state, respectively. The exact identity of these newly observed states could not be determined. The present observation of new excited states cannot be explained with the existing *ab initio* results [5,6] and thus the electronic structure of ScN molecule turns out to be more complex than it has been suggested by *ab initio* results.

The investigations on $B^2\Sigma^+ - X^2\Sigma^+$ system of ScO molecule is extended to higher vibrational levels using laser-induced fluorescence spectroscopy. The analyses of rotationally resolved excitation bands yielded molecular constants for $v' = 1-4$ of the B state and $v'' = 2$ of

the X state. The dispersed fluorescence spectra have given information about harmonic and anharmonic vibrational wavenumbers of the X state. The equilibrium molecular constants derived from these data are used to construct the RKR potential energy curves and subsequently the Franck-Condon factors for the $B^2\Sigma^+ - X^2\Sigma^+$ transition. The spectroscopic data obtained in the present work is expected to be useful in the extensive search of ScO molecule in stellar as well as solar spectra. Supplementary information for the rotational line positions and assignments of the observed bands associated with this chapter are listed at the end of the thesis.

4.7 References

-
- [1] W. Weltner, Jr., *Science* **155**, 155 (1967).
 - [2] J. Tennyson, Molecules in Space, Volume 3, Part 3, Chapter 14, pp 356–369 in Handbook of Molecular Physics and Quantum Chemistry, Edited by Stephen Wilson, John Wiley & Sons, Ltd, Chichester, 2003.
 - [3] G.J. Leigh, *Science* **279**, 506 (1998).
 - [4] Y. Nishibayashi, S. Iwai, M. Hidai, *Science* **279**, 540 (1998).
 - [5] C. Jaschek, M. Jaschek, The Behavior of Chemical Elements in Stars, Cambridge University Press, Cambridge (1995).
 - [6] K.L. Kunze, J.F. Harrison, *J. Am. Chem. Soc.* **112**, 3812 (1990).
 - [7] A. Daoudi, S. Elkhatabi, G. Berthier, J.P. Flament, *Chem. Phys.* **230**, 31 (1998).
 - [8] R.S. Ram, P.F. Bernath, *J. Chem. Phys.* **96**, 6344 (1992).
 - [9] R.E. Smith, *Proc. R. Soc. London A* **332**, 113 (1973).
 - [10] A. Bernard, C. Effantin, R. Bacis, *Can. J. Phys.* **55**, 1654 (1977).
 - [11] R.S. Ram, P.F. Bernath, *J. Chem. Phys.* **105**, 2668 (1996).
 - [12] R.S. Ram, P.F. Bernath, *J. Mol. Spectrosc.* **183**, 263 (1997).
 - [13] J. Anglada, P.J. Bruna, S.D. Peyerimhoff, *Mol. Phys.* **66**, 541 (1989).

-
- [14] R.S. Ram, P.F. Bernath, *J. Chem. Phys.* **101**, 9283 (1994).
- [15] R.S. Ram, P.F. Bernath, *J. Chem. Phys.* **104**, 6444 (1996).
- [16] D. McLeod Jr, W. Weltner Jr., *J. Phys. Chem.* **70**, 3293 (1966).
- [17] P.R. Scott, W.G. Richards, *J. Phys. B* **7**, 1679 (1974).
- [18] C.W. Bauschlicher Jr, S.P. Walch, *J. Chem. Phys.* **76**, 4560 (1982).
- [19] J. Anglada, P.J. Bruna, S.D. Peyerimhoff, R.J. Buenker, *J. Mol. Struct.* **93**, 299 (1983).
- [20] P.J. Bruna, J. Anglada, In: Veillard A, editor. Quantum chemistry: the challenge of transitions metals and coordination chemistry. Dordrecht: D. Reidel Publishing Company, pp. 67 (1986).
- [21] D.P. Chong, S.R. Langhoff, C.W. Bauschlicher Jr., S.P. Walch, H. Partridge, *J. Chem. Phys.* **85**, 2850 (1986).
- [22] S. Koseki, Y. Ishihara, D.G. Fedorov, H. Umeda, M.W. Schmidt, M.S. Gordon, *J. Phys. Chem. A* **108**, 4707 (2004).
- [23] L. Lodi, S.N. Yurchenko and J. Tennyson, *Mol. Phys.* **113**, 1998 (2015).
- [24] A. Bernard, R. Bacis, *Can. J. Phys.* **55**, 1322 (1977).
- [25] A. Bernard, R. Bacis, *Can. J. Phys.* **54**, 1509 (1976).
- [26] S. Yarlagadda, S. Mukund, S.G. Nakhate, *Chem. Phys. Lett.* **537**, 1 (2012).
- [27] S. Mukund, S. Yarlagadda, S. Bhattacharyya, S.G. Nakhate, *J. Chem. Phys.* **137** (234309), 1 (2012).
- [28] G. Herzberg Molecular spectra and molecular structure I. In: Spectra of diatomic molecules. Second edition, New York: Van Nostrand (1950).
- [29] R.R. Squires, *J. Am. Chem. Soc.* **107**, 4385 (1985).
- [30] F. Taher, C. Effantin, A. Bernard, J. d'Incan, J. Vergès, *J. Mol. Spectrosc.* **189**, 220 (1998).
- [31] Z.H. Xia, Y. Xia, Man-Chor Chan, A.S.-C. Cheung, *J. Mol. Spectrosc.* **268**, 3 (2011).

-
- [32] G.V. Chertihin, L. Andrews, C.W. Bauschlicher, *J. Am. Chem. Soc.* **120**, 3205 (1998).
- [33] G.H. Jeung, J. Koutecky, *J. Chem. Phys.* **88**, 3747 (1988).
- [34] F.J. Bai, C.L. Yang, Q. Qian, L. Zhang, *Chin. Phys. B* **18**, 549 (2009).
- [35] J.B. Norman, K.J. Cross, H.S. Schweda, M. Polak, R.W. Field, *Mol. Phys.* **66**, 235 (1989).
- [36] Z.J. Jakubek, S.G. Nakhate, B. Simard, *J. Mol. Spectrosc.* **211**, 86 (2002).
- [37] Z.J. Jakubek, S.G. Nakhate, B. Simard, *J. Mol. Spectrosc.* **219**, 145 (2003).
- [38] L.N. Zack, M.P. Bucchino, M.K.L. Binns, J.P. Young, P.M. Sheridan, L.M. Ziurys, *J. of Mol. Spectrosc.* **317**, 10 (2015).
- [39] S.G. Fougère, W.J. Balfour, J. Cao, C.X.W. Qian, *J. Mol. Spectrosc.* **199**, 18 (2000).
- [40] L. Andrews, E.S. Prochaska, B.S. Ault, *J. Chem. Phys.* **69**, 556 (1978).
- [41] C.A. Thompson, L. Andrews, *J. Am. Chem. Soc.* **116**, 423 (1994).
- [42] G. Frenking, W. Koch, J. Gauss, D. Cremer, *J. Am. Chem. Soc.* **110**, 8007 (1988).
- [43] G. Chertihin, W.D. Bare, L. Andrews, *J. Phys. Chem. A* **102**, 3697 (1998).
- [44] LeRoy R.J. RKR12.0, A computer program implementing the first-order RKR method for determining diatomic molecule potential energy curves. University of Waterloo, Chemical Physics Research Report CP-657R (2004). <http://scienide2.uwaterloo.ca/_rleroy/rkr/>.
- [45] D.N. Davis. *Publ. Astron. Soc. Pac.* **52**, 207 (1940).
- [46] P.W. Merrill, A.J. Deutsch, P.C. Keenan, *Astrophys. J.* **136**, 21 (1962).
- [47] P. Sriramachandran, S.P. Bagare, N. Rajamanickam, K. Balachandrakumar, *Sol. Phys.* **252**, 267 (2008).
- [48] L. Akerlind, *Ark. Fys.* **22**, 41 (1962).
- [49] A. Adams, W. Klemperer, T.M. Dunn, *Can. J. Phys.* **46**, 2213 (1968).
- [50] C.L. Chalek, J.L. Gole, *Chem. Phys.* **19**, 59 (1977).
- [51] R. Stringat, C. Athénour, J.L. Féménias, *Can. J. Phys.* **50**, 395 (1972).

-
- [52] W.J. Childs, T.C. Steimle, *J. Chem. Phys.* **88**, 6168 (1988).
- [53] S.F. Rice, W.J. Childs, R.W. Field, *J. Mol. Spectrosc.* **133**, 22 (1989).
- [54] D.T. Halfen, J. Min, L.M. Ziurys, *J. Mol. Spectrosc.* **331**, 1 (2017).
- [55] B.N. Murthy, N.S. Murthy, *Pramana* **2**, 269 (1974).
- [56] M.L.P. Rao, D.V.K. Rao, P.T. Rao, *Physica C* **81**, 392 (1976).
- [57] C.B. Suárez, *Physica C* **121**, 295 (1983).

Chapter 5

Wavelength-Resolved Laser-Induced Fluorescence Spectroscopy of the Jet-cooled Nickel Monocarbide (NiC) Molecule

5.1 Introduction

The transition metal carbides are of considerable current interest due to their importance in catalysis, organometallic chemistry, and biological processes. The diatomic transition metal carbides provide simple model systems for understanding the bonding of a carbon atom to transition metals and helps in understanding larger transition-metal-containing systems like organometallics. The metal-carbon interaction is the most basic aspect of organometallic chemistry and in view of this, study of low-lying states in such molecules is important. The experimental spectroscopic parameters also provide rigorous benchmarks for the validation of theoretical calculations of the electronic structure in systems with open *d*-subshells that result in large numbers of low-lying states [1]. Transition metal carbides, particularly those of the 3*d* period, are also of astrophysical importance and are likely to be detected in circumstellar environments of carbon-rich stars [2,3]. The gas phase spectroscopic investigations in the 3*d* transition metal monocarbides ScC[4], TiC[5,6], VC [7], CrC [8], FeC [9,10,11,12,13,14,15], CoC [3,16,17], and NiC [3,18] have been studied. However, spectroscopic investigations of ScC, TiC and VC impeded till recently due to atypical experimental conditions needed for their formation than those of metal monocarbides of later groups, as pointed out by Krechkivska and Morse [4]. In this Chapter, spectroscopic investigations of the NiC molecule in its ground and low-lying states are presented.

5.1.1 Motivation

The first spectroscopic observation of NiC molecule in the gas phase was reported by Brewster and Ziurys [3] in the millimetre region, providing the ground $X^1\Sigma^+$ state rotational constants to high accuracy. Later, Brugh and Morse [18] studied the jet-cooled NiC molecule

by mass-selected resonance two-photon ionization (R2PI) spectroscopy in the optical region and observed numerous transitions originating from ground $X^1\Sigma^+$ state to excited electronic states, all having $\Omega = 0^+$. In contrast to experimental studies, NiC has been theoretically studied extensively. The first, rather primitive, theoretical calculations was reported in 1982 by Kitaura et al. [19] using the generalized valence bond approach. They calculated the bond length, $r_0 = 1.80 \text{ \AA}$ and dissociation energy, $D_e = 23 \text{ kcal mol}^{-1}$, deviated strongly from the experimental values [18] estimated as $D_0 \geq 77 \text{ kcal mol}^{-1}$. A few years later, Shim and Gingerich [20] calculated low-lying singlet, triplet and quintet states of Σ^+ , Π , Δ , and Φ symmetries, including the $X^1\Sigma^+$ ground state, derived from $3d^8 4s^1$, $^4F \text{ Ni}^+$ and a $2s^2 2p^3$, $^4S \text{ C}^-$ ionic states based on all electron *ab initio* calculations. The first excited state was found to be a $^1\Pi$ state at 1532 cm^{-1} . The NiC bond was found to be quite polar, with substantial electron transfer from the Ni atom to the C ligand. Shim and Gingerich later revisited the NiC molecule at the complete active space self-consistent-field (CASSCF) level and found that the ground state $X^1\Sigma^+$ is separated from a dense manifold of excited states, with the first excited $^1\Pi$ state lying at 6465 cm^{-1} [21]. In 2001, Borin [22] examined the $X^1\Sigma^+$ and $A^1\Pi$ states of NiC using the multi-reference configuration interaction (MRCI) approach based on the CASSCF wavefunctions and reported potential energy curves, spectroscopic constants, radiative lifetimes and dipole moments of the $A^1\Pi - X^1\Sigma^+$ transition. Using same approach, a few years later Borin and Macedo [23] calculated six more low-lying states and revised the energy ordering of the lowest-lying singlet and triplet electronic states. They found $^3\Pi$ to be the lowest state, in contrast to the $^1\Pi$ state calculated by Shim and Gingerich [21]. Recently, Tzeli and Mavridis [24] investigated the electronic structure of the ground and low-lying excited states through multiconfiguration self-consistent field (MCSCF) calculations coupled with large basis sets and with inclusion of core-valence correlation and scalar relativistic effects. They found that the $X^1\Sigma^+$, $a^3\Pi$ and $A^1\Pi$ states are well separated from rest of the

states and $a^3\Pi$ is indeed the first excited state. The experimental observation of the energy ordering and character of the low-energy states can provide a validation of the level of theoretical calculations. However, to the best of our knowledge, experimental detection of the low-lying states in NiC molecule has not been reported. The confusion among theoretical investigations over the energy ordering of the $a^3\Pi$ and $A^1\Pi$ states motivated us to undertake dispersed fluorescence (DF) studies on NiC.

5.2 Experiment

The NiC molecules are produced in a pulsed free-jet apparatus. The details of the apparatus and method of production of molecules in the free-jet are already discussed in the Chapter 2. In brief, a rotating and translating nickel metal rod is ablated by a focused ~ 10 mJ/pulse, 355 nm radiation from a Q-switched Nd:YAG laser. The resulting nickel plasma is reacted with 3% methane seeded in He emerging from a pulsed valve under a backing pressure of 275 kPa. Approximately 50 mm downstream of the nozzle, the free-jet is probed by a tunable dye laser at right angle to the beam expansion axis. The resulting laser-induced fluorescence (LIF) is collected orthogonal to both free-jet and dye laser beam axes, dispersed by a monochromator and subsequently detected by a Peltier cooled photomultiplier tube. An output signal from the photomultiplier tube is integrated by a gated boxcar integrator, and stored on a computer. The dispersed fluorescence (DF) spectra are obtained from the excited electronic states of NiC reported by Brugh and Morse [18] by exciting isolated rotational lines. Typical DF spectral line widths (FWHM) ~ 5 cm^{-1} is obtained at the best resolution.

5.3 Observations and Analysis

Nickel atom has five naturally occurring isotopes; viz. ^{58}Ni (68.1%), ^{60}Ni (26.2%), ^{61}Ni (1.1%), ^{62}Ni (3.6%) and ^{64}Ni (0.9%) and we have used natural methane in these experiments. The DF spectra of NiC molecule are investigated in the 400–900 nm

wavelength range by exciting a single rotational level belonging to $^{58}\text{Ni}^{12}\text{C}$ isotopomer of the several excited states with $\Omega = 0^+$ observed by Brugh and Morse [18]. The DF spectra are first recorded with moderate resolution ($\text{FWHM} \sim 50 \text{ cm}^{-1}$) to get the coarse information about the low-energy and ground states and their vibrational levels. The coarse spectra are then examined under relatively higher resolution ($\text{FWHM} \sim 5 \text{ cm}^{-1}$) to resolve the rotational structure in the lower states for determining the identity of the observed states.

5.3.1 Vibrational Constants of the $X^1\Sigma^+$ Ground State

Figure 5.1 shows a typical DF spectrum of $^{58}\text{Ni}^{12}\text{C}$ isotopomer, where the $P(8)$ line of the $[24.6]0^+ - X^1\Sigma^+ (0,0)$ transition [18] is excited. The vibrational progression from $v'' = 0-10$ of the $X^1\Sigma^+$ ground state is observed and is marked in Figure 5.1.

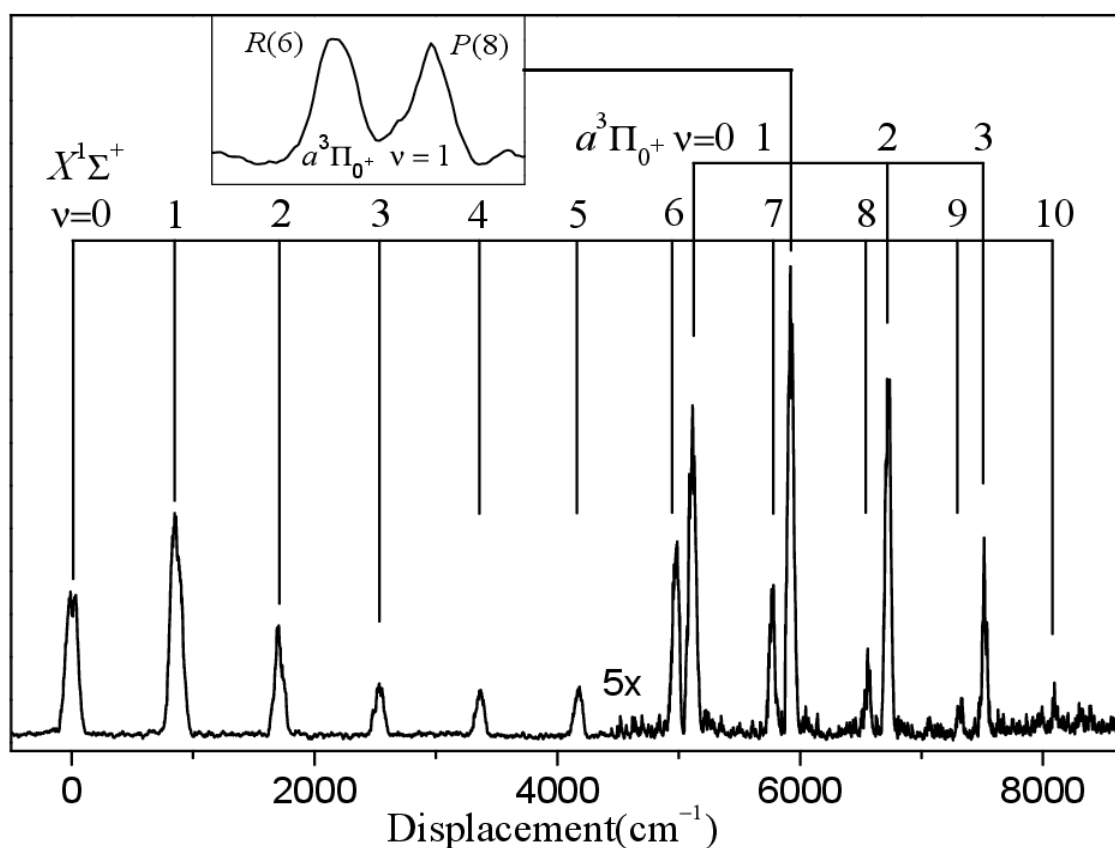


Figure 5.1 Dispersed fluorescence (DF) spectrum of $^{58}\text{Ni}^{12}\text{C}$ observed from $v' = 0, J' = 7$ of $[24.6] \Omega=0^+$ state; the x-axis shows the displacement in cm^{-1} from the excitation line. The inset shows the DF spectra at high-resolution where the $P(8)$ and $R(6)$ lines are well resolved.

The DF lines terminating to the ground state split into PR -doublets at higher resolution when either P - or R -lines of the upper electronic rovibrational levels are excited. Since the upper state has $\Omega = 0$ and the transitions are typical of $\Delta\Omega = 0$, the lower levels are confirmed as the vibrations of the ground electronic state. The term energies of the vibrational levels of the $X^1\Sigma^+$ state are listed in Table 5.1. The term energies of the $v'' = 1$ and 2 observed in the present study are in good agreement with the tabulated values reported by Brugh and Morse [18] derived from band origin data. The equilibrium vibrational constants $\omega_e = 874.6$ (17) cm^{-1} and $\omega_e x_e = 5.9$ (2) cm^{-1} of the $X^1\Sigma^+$ state is determined by fitting the observed vibrational term energies to the equation,

$$\Delta G = G(v) - G(0) = \omega_e v - \omega_e x_e v(v+1) \quad (5.1)$$

Table 5.1 Term values (in cm^{-1}) of the vibrational levels of the $X^1\Sigma^+$ and $\Omega = 0^+$ states of $^{58}\text{Ni}^{12}\text{C}$.

v	T_v		$\Omega = 0^+$
	$X^1\Sigma^+$		
	This work	Ref. [18]	
0	0	0.0	5157(5)
1	864(3)	864.3919	5976(9)
2	1720(5)	1718.0208	6783(14)
3	2555(7)		7574(14)
4	3388(8)		
5	4206(3)		
6	4978(3)		
7	5770(7)		
8	6557(6)		
9	7324(7)		
10	8101(10)		

5.3.2 Observation of the Low-lying $\Omega = 0^+$ Excited Electronic State

In addition to the vibrational progression to the ground state, the DF spectrum shows a vibrational progression beginning at 5157 cm^{-1} as marked in Figure 5.1. Theoretical calculations predict low-lying states $^3\Pi$, $^3\Sigma^+$, and $^1\Pi$ in the energy region 6000–8000 cm^{-1} [21,23,24]. However, the energy ordering between the $a^3\Pi$ and $A^1\Pi$ states was in question. Shim and Gingerich [21] predict $A^1\Pi$ as the first excited state 6465 cm^{-1} above the ground

state, however recent calculations of Borin and Macedo [23] and Tzeli and Mavridis [24] predict $a^3\Pi$ as the first excited state at $\sim 8000\text{ cm}^{-1}$. In order to confirm the identity of the low-lying state observed in the present experiment, the DF spectral line was studied at higher resolution to probe the rotational structure. The rotational structure of line terminating to the progression beginning at 5157 cm^{-1} split into PR -doublets, when either P - or R -lines of the $(0,0)$ band of the $[24.6]0^+ - X^1\Sigma^+$ transition were excited (see inset of Figure 5.1). This is in accordance with $\Delta\Omega = 0$ transition, confirming $\Omega = 0^+$ of the lower electronic state. This is the lowest excited state observed in the present work. The separation between the PR -doublets was used to estimate the rotational constant of the $\Omega = 0^+$ state and was found to be 0.59 (3) cm^{-1} . The evaluated rotational constant B value is accurate only to the first decimal place and no meaningful values of centrifugal distortion constants D could be determined. The α_e value also could not be determined from the set of evaluated B_v 's due to the low precision of the DF data, which was limited by the resolution of the monochromator. The term energies of up to $v = 3$ were used to evaluate the equilibrium vibrational constants $\omega_e = 833\text{ (4) cm}^{-1}$, $\omega_e x_e = 6.7\text{ (13) cm}^{-1}$ and the equilibrium term energy, $T_e = 5178\text{ (6) cm}^{-1}$ of the $\Omega = 0^+$ state.

The B_e value of $0.593\text{ (28) cm}^{-1}$ and thus $r_e = 1.69\text{ (4) \AA}$ was estimated iteratively using the Pekeris relationship (Equation 1.21). In addition to the members of the two main DF progressions we have also observed few weak fluorescence features mainly at 9371 , 9876 , 10588 , and 11342 cm^{-1} which may correspond to fluorescence terminating on vibrational levels of the $^1\Pi$, $^3\Pi$ or the $^3\Sigma^+$ states, but definite assignments were not possible. The RKR potential energy curves for the $X^1\Sigma^+$ and $\Omega = 0^+$ states assigned as $^3\Pi_{0^+}$ (Section 5.4) were constructed using the RKR1 program of LeRoy [25] and are shown in Figure 5.2. The vibrational constants from the present work and rotational constants

(B_e and α_e) from the earlier work [18] for the $X^1\Sigma^+$ and vibrational and rotational constants for the $^3\Pi_{0+}$ from this work were used to generate the RKR potential energy curves.

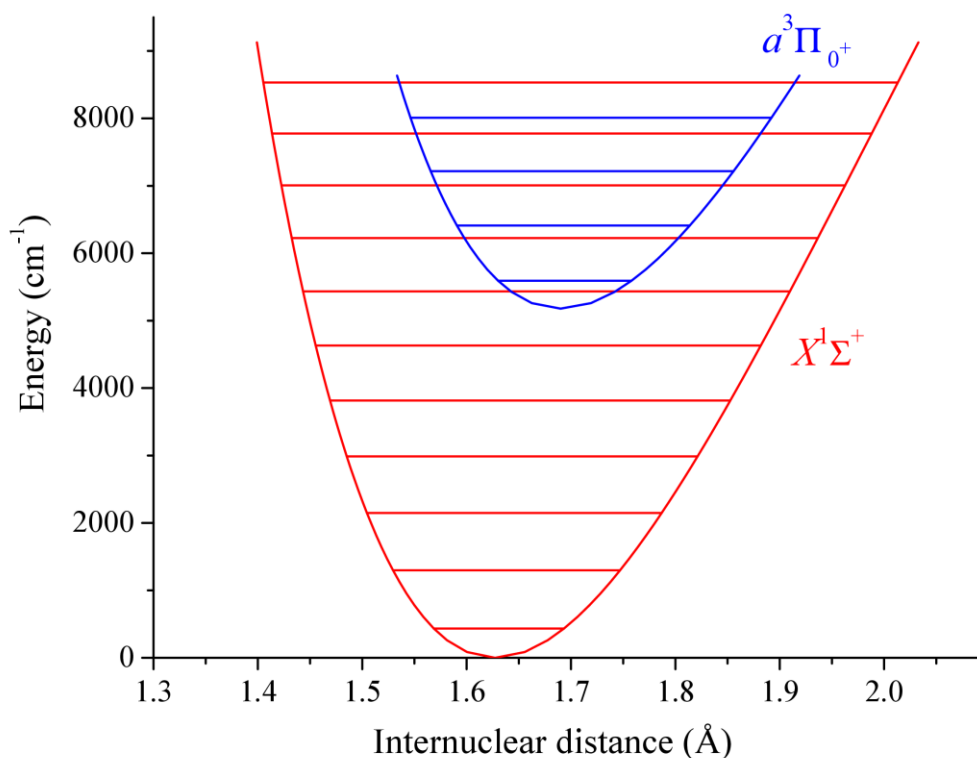


Figure 5.2 RKR potential energy curves for the $X^1\Sigma^+$, and $a^3\Pi_{0+}$ states of $^{58}\text{Ni}^{12}\text{C}$. Observed vibrational levels are shown by solid lines.

5.4 Discussion

In the present work, we have observed a vibration progression up to $v = 10$ for the ground $X^1\Sigma^+$ state and evaluated vibrational equilibrium constants ω_e and $\omega_e x_e$ which are in good agreement with the values in Ref. [18], evaluated from the band origin data up to $v = 2$ (see Table 5.2). In addition to this, we have observed a vibrational progression up to $v = 3$ terminating on a new electronic state at $T_e = 5178$ (6) cm^{-1} with $\Omega = 0^+$, $r_e = 1.69$ (4) Å and $\omega_e = 833$ (4) cm^{-1} . The relevant electronic states and their spectroscopic constants calculated by the *ab initio* studies [21,23,24], listed in Table 5.2, can be used to assign the newly observed electronic state. As can be seen from Table 5.2, Shim and Gingerich [21] predicted $^1\Pi$, $^3\Sigma^+$ and $^3\Pi$ states respectively at 6465, 6772 and 7451 cm^{-1} using CASSCF calculations. However, on the basis of MRCI calculations, Borin and Macedo [23] placed the $^3\Pi$ state

energetically lower at 7882 cm⁻¹ compared to the ¹Π and ³Σ⁺ states respectively at 9427 and 10835 cm⁻¹. Recent MCSCF/CISD calculations of Tzeli and Mavridis [24] had also shown that the ³Π state is energetically lower at 8746 cm⁻¹ compared to the ¹Π and ³Σ⁺ states respectively at 12419 and 13504 cm⁻¹. It is known that the CASSCF method alone is not sufficient to describe the multitude and correct energy ordering of the excited states in transition metal carbides. The inclusion of both nondynamical and dynamical correlation effects are very important in describing the excited electronic states.

Table 5.2 Spectroscopic constants^a of the experimentally observed $X^1\Sigma^+$ and $\Omega = 0^+$ states of ⁵⁸Ni¹²C and their comparison with *ab initio* values.

State		T_e	r_e	ω_e	$\omega_e x_e$
$X^1\Sigma^+$	Present work	0.0	-	874.6 (17) ^b	5.9 (2)
	Ref. [18] ^c	0.0	1.62729(17)	875.155	5.382
	Ref. [21] ^d	0.0	1.655	809	-
	Ref. [21] ^e	0.0	1.621	874	-
	Ref. [23] ^f	0.0	1.627	937	-
	Ref. [24] ^g	0.0	1.621	916.1	-
$\Omega = 0^+$	Present work	5178 (6)	1.69(4)	833 (4)	6.7 (13)
	Ref. [21] ^d	7451	1.957	564	-
	Ref. [23] ^f	7882	1.620	937	-
³ Π	Ref. [24] ^g	8746	1.606	981	-
	Ref. [21] ^d	6465	1.942	524	-
	Ref. [23] ^f	9427	1.773	539	-
¹ Π	Ref. [24] ^g	12419	1.622	940	-
	Ref. [21] ^d	6772	1.960	557	-
	Ref. [23] ^f	10835	1.843	561	-
³ Σ ⁺	Ref. [24] ^h	13504	1.669	874	-

^a r_e in Å and other constants in cm⁻¹.

^b Numbers in parentheses indicate one standard deviation in the last quoted digits.

^c Experimental.

^d CASSCF including relativistic corrections.

^e MRCI.

^f MRCI.

^g C-MRCI+DKH2/C5Z.

^h MRC

The computational work has shown that the lowest-lying excited states of NiC are of ³Π, ³Σ⁺, and ¹Π symmetry. When spin-orbit interaction is considered, these split into substates with $\Omega = 0^+$, 0^- , 1, and 2 from ³Π; $\Omega = 0^-$, 1 from ³Σ⁺ and $\Omega = 1$ only from ¹Π state. Because $\Omega = 0^+ \leftrightarrow \Omega = 0^-$ transitions are rigorously forbidden under electric dipole selection rules, the $\Omega = 0^+$ state that is initially excited can only radiate to states of $\Omega = 0^+$ or $\Omega = 1$

symmetry. The observation of pairs of P , R lines demonstrates that the new state is of $\Omega = 0^+$ symmetry.

If we accept the computational result that the low-lying states are $^3\Pi$, $^3\Sigma^+$, and $^1\Pi$, then the only possibility for the newly-discovered low-lying state is $^3\Pi_{0+}$, which is the lowest excited state observed so far. However, it is likely that other spin-orbit component of the $^3\Pi$ state will lie lower in energy. If the $^3\Pi$ state is regular, resulting from $1\sigma^2 2\sigma^2 3\sigma^1 1\pi^4 2\pi^1 1\delta^4$ configuration [21], it should have spin-orbit levels in the order $(\Omega = 0^+, 0^-) < \Omega = 1 < \Omega = 2$. However, in that case the $\Omega = 0^+$ component of $^3\Pi$ will interact with the $^1\Sigma^+$ ground state by off-diagonal spin-orbit coupling, causing it to be pushed above the $\Omega = 0^-$ component. This effect was observed in a DF study of PdC [29]. On the other hand, if the $^3\Pi$ state is irregular, resulting from configuration $1\sigma^2 2\sigma^2 3\sigma^2 1\pi^4 2\pi^1 1\delta^3$ [21], the spin-orbit levels will lie in the reversed order: $\Omega = 2 < \Omega = 1 < (\Omega = 0^+, 0^-)$. In either case, there will be an excited Ω -level lying below the $^3\Pi_{0+}$ state. The observation of emissions to the $^1\Sigma^+$ ground and $^3\Pi_{0+}$ states and not to the other $^3\Pi_{\Omega}$ levels also suggests that the $^3\Pi_{0+}$ state borrows much of its intensity in these emissions from the $^1\Sigma^+$ ground state. The comparison of observed spectroscopic constants for $^3\Pi_{0+}$ state with theory shows that the energy order of $^3\Pi$ with respect to the $^1\Pi$ and $^3\Sigma^+$ states, its internuclear distance and vibrational energy predicted by the CASSCF and MRCI calculations differ significantly, with MRCI values closer to the observation (see Table 5.2). The present work supports the MRCI prediction of $^3\Pi$ to be the first excited state; however the term energy is overestimated by about 40%. The CASSCF calculations overestimated r_e by $\sim 16\%$ and underestimated ω_e by $\sim 48\%$. However, MRCI values for r_e are about 4–5% lower and ω_e values are higher by about 10–15% than the observed. This is also valid for the ground state. Shim and Gingerich [21] calculated spectroscopic constants

for $X^1\Sigma^+$ ground state of NiC, both at the CASSCF and MRCI level. As evident from Table 5.2, r_e and ω_e values predicted by them at MRCI level are closer to the observed ones.

5.4.1 Comparison of NiC with Isovalent Monocarbides in their Ground and Low-lying Electronic States

The ground and first low-lying electronic states of NiC is compared with that of the isovalent PdC and PtC molecules. According to Shim & Gingerich [21], the $X^1\Sigma^+$ ground state of NiC have its primary/major electron configuration $1\sigma^2 2\sigma^2 3\sigma^2 1\pi^4 1\delta^4$, predicted by MRCI approach. Here, 1σ orbital is basically the C 2s orbital and is generally considered to be corelike in all of the transition metal monocarbides. The 2σ orbital is mainly the bonding combination of C $2p_\sigma$ with a hybrid orbital of Ni that is polarized away from the internuclear region. The 3σ and 1δ orbitals are nonbonding, arising from atomic orbitals of the nickel atom respectively from $3d_\sigma$ and $3d_\delta$. The 1π orbital is the bonding combination of Ni $3d_\pi$ and the C $2p_\pi$. Therefore, NiC has essentially a triple bond between the carbon and nickel atoms in its ground state. The excited $a^3\Pi_0+$ state, observed in the present study have electronic configuration $1\sigma^2 2\sigma^2 3\sigma^1 1\pi^4 2\pi^1 1\delta^4$ arises from the promotion of one nonbonding 3σ electron to antibonding 2π level [21]. Similar ground and low-lying state electronic configurations of PdC [28] and PtC [30] molecules are reported and listed in Table 5.3.

The similar symmetry in the ground and first low-lying states in all the group 10 transition metal monocarbide molecules are observed as opposed to the group 5 transition metal nitrides, as discussed in the Chapter 3. In this context, it is useful to consider the electronic structure of the constituent transition metal atom to accurately describe transition metal diatomics. We have seen in the Chapter 3, the ground state symmetry in TaN among the group 5 transition metal nitride molecules was changed due to relativistic stabilization of 6s orbital in the tantalum atom. However, when one moves across the period, the stabilization of the nd orbital increases substantially, relative to the $(n+1)s$ orbital due to increasing

nuclear charge [1,18,29,26]. The reason for similar ground state symmetry among all the group 10 transition metal monocarbides may be attributed to the increased stabilization of the nd orbital across the group, relative to the $(n+1)s$ orbital.

Table 5.3 Comparison of symmetry, term energy and vibrational frequency (in cm^{-1}) of the ground and first low-lying state of group 10 transition-metal-containing monocarbides

Molecules	Symmetry	Electron configuration from major contribution	T_0	ω_e	$\Delta G_{1/2}$
$^{58}\text{Ni}^{12}\text{C}$	$X^1\Sigma^+$	$1\sigma^2 2\sigma^2 3\sigma^2 1\pi^4 1\delta^4$ ^a	0	874.6 (17) ^b	864.3919(21) ^c
	$a^3\Pi_{0+}$	$1\sigma^2 2\sigma^2 3\sigma^1 1\pi^4 2\pi^1 1\delta^4$ ^a	5157(5) ^b	833(4) ^b	819 (10) ^b
PdC	$X^1\Sigma^+$	$1\sigma^2 2\sigma^2 3\sigma^2 1\pi^4 1\delta^4$ ^d	0	847.6(1.6) ^e	833.6(22) ^e
	$a^3\Pi_{0-}$		2157.1(2.6) ^e		765.1(37) ^e
	$a^3\Pi_{0+}$	$1\sigma^2 2\sigma^2 3\sigma^1 1\pi^4 2\pi^1 1\delta^4$ ^d	2289.1(3.8) ^e	788.4(5.4) ^e	781.8(74) ^e
	$a^3\Pi_1$		2453.1(2.7) ^e		762.3(38) ^e
	$a^3\Pi_2$		2818.0(2.6) ^e		759.9(37) ^e
PtC	$X^1\Sigma^+$	$1\sigma^2 2\sigma^2 3\sigma^2 1\pi^4 1\delta^4$ ^f	0	1051.13(2) ^g	1041.43(1) ^g
	$a^3\Pi_{0+}(A''^1\Sigma^+)^f$	$1\sigma^2 2\sigma^2 3\sigma^1 1\pi^4 2\pi^1 1\delta^4$ ^f	12643.19(1) ^g	943.40(3) ^g	932.85(1) ^g
	$a^3\Pi_1(A'^3\Pi_1)^f$		13196.14(1) ^g		906.93(2) ^g

^a Ref.[21]

^b This work, Ref.[27]

^c Ref.[18]

^d Ref.[28]

^e Ref.[29]

^f Ref.[30]

^g Ref.[31]

5.5 Conclusion

Laser-induced dispersed fluorescence spectra from isolated rotational levels of the excited electronic states of $^{58}\text{Ni}^{12}\text{C}$ [18], lead to the observation of an excited electronic state plausibly assigned to $^3\Pi_{0+}$ with the support of earlier *ab initio* studies. The rotationally resolved vibrational progression up to $v = 3$ yielded equilibrium constants $\omega_e = 833$ (4) and $\omega_e x_e = 6.7$ (13) and $B_e = 0.593$ (28) cm^{-1} for this state. Also, the extended vibrational progression up to $v = 10$ to the ground state lead to the determination of $\omega_e = 874.6$ (17) and $\omega_e x_e = 5.9$ (2) cm^{-1} for the ground $X^1\Sigma^+$ state. The RKR potential energy curves for the $X^1\Sigma^+$ ground and $^3\Pi_{0+}$ states were constructed.

5.6 References

-
- [1] J.F. Harrison, *Chem. Rev.* **100**, 679 (2000).
- [2] G. von Helden, A.G. Tielens, D. van Heijnsbergen, M.A. Duncan, S. Hony, L.B. Waters, G. Meijer, *Science* **288**, 313 (2000).
- [3] M.A. Brewster, L.M. Ziurys, *Astrophys. J.* **559**, L163 (2001).
- [4] C-W Chen, A. Merer, Y-C Hsu, International symposium on molecular spectroscopy RI11 p.235 (2016).
- [5] Z. Luo, H. Huang, Y. C. Chang, Z. Zhang, Q. Z. Yin, C. Y. Ng, *J. Chem. Phys.* **141**, 144307 (2014).
- [6] S.G. Nakhate, S. Mukund, S. Bhattacharyya, in Press (2017).
- [7] O. Krechkivska, M.D. Morse, *J. Phys. Chem. A.* **117**, 13284 (2013).
- [8] D.J. Brugh, M.D. Morse, A. Kalemios, A. Mavridis, *J. Chem. Phys.* **133**, 034303 (2010).
- [9] W.J. Balfour, J. Cao, C.V.V. Prasad, C.X. Qian, *J. Chem. Phys.* **103**, 4046 (1995).
- [10] M.D. Allen, T.C. Pesch, L.M. Ziurys, *Astrophys. J.* **472**, L57 (1996).
- [11] D.J. Brugh, M.D. Morse, *J. Chem. Phys.* **107**, 9772 (1997).
- [12] K. Aiuchi, K. Tsuji, K. Shibuya, *Chem. Phys. Lett.* **309**, 229 (1999).
- [13] K. Aiuchi, K. Shibuya, *J. Mol. Spectrosc.* **209**, 92 (2001).
- [14] M. Fujitake, A. Toba, M. Mori, F. Miyazawa, N. Ohashi, K. Aiuchi, K. Shibuya, *J. Mol. Spectrosc.* **208**, 253 (2001).
- [15] J.W.H. Leung, W.S. Tam, Q. Ran, A.S.C. Cheung, *Chem. Phys. Lett.* **343**, 64 (2001).
- [16] M. Barnes, A.J. Merer, G.F. Metha, *J. Chem. Phys.* **103**, 8360 (1995).
- [17] A.G. Adams, J.R.D. Peers, *J. Mol. Spectrosc.* **181**, 24 (1997).
- [18] D.J. Brugh, M.D. Morse, *J. Chem. Phys.* **117**, 10703 (2002).
- [19] K. Kitaura, K. Morokuma, I.G. Csizmadia, *J. Mol. Struct.* **88**, 119 (1982).
- [20] I. Shim, K.A. Gingerich, *Z. Phys. D* **12**, 373 (1989).

-
- [21] I. Shim, K.A. Gingerich, *Chem. Phys. Lett.* **303**, 87 (1999).
- [22] A.C. Borin, *Chem. Phys.* **274**, 99 (2001).
- [23] A.C. Borin, L.G.M. de Macedo, *Chem. Phys. Lett.* **383**, 53 (2004).
- [24] D. Tzeli, A. Mavridis, *J. Chem. Phys.* **126**, 194304 (2007).
- [25] R.J. LeRoy, Chemical Physics Research Report, CP-425, University of Waterloo (1992).
- [26] A.J. Merer, *Annu. Rev. Phys. Chem.* **40**, 407 (1989).
- [27] S. Mukund, S. Yarlagadda, S. Bhattacharyya, S.G. Nakhate, *Chem. Phys. Lett.* **591**, 43 (2014).
- [28] H. Tan, D. Dai, K. Balasubramanian, *Chem. Phys. Lett.* **286**, 375 (1998).
- [29] R.S. DaBell, R.G. Meyer, M.D. Morse, *J. Chem. Phys.* **114**, 2938 (2001).
- [30] B.F. Minaev, *Phys. Chem. Chem. Phys.* **2**, 2851 (2000).
- [31] O. Appelblad, C. Nilsson, R. Scullman, *Physica Scripta* **7**, 65 (1973).

Appendix 1

Supplementary information for rotational line positions and assignments of observed bands of NbN

Table S1.1: Line positions (in cm^{-1}) in the 1-0 of the $C^3\Pi_{0e/f}-X^3\Delta_1$ of subband of NbN.

$^3\Pi_{0e}$							$^3\Pi_{0f}$					
J	$R_{ee}(J)$	O-C	$Q_{ef}(J)$	O-C	$P_{ee}(J)$	O-C	$R_{ff}(J)$	O-C	$Q_{fe}(J)$	O-C	$P_{ff}(J)$	O-C
1	-	-	18878.12	-0.19	18876.32	0.02	18887.93	0.04	18885.75	-0.17	18884.97	0.03
2	-	-	18878.12	-0.16	18875.26	-0.01	18888.83	-0.01	18885.75	-0.14	18884.02	0.10
3	-	-	18878.12	-0.11	18874.20	-0.03	18889.8	0.01	18885.75	-0.10	18882.81	-0.08
4	18883.15	0.06	18878.12	-0.05	18873.17	0.01	18890.74	0.02	18885.75	-0.04	18881.79	-0.05
5	18884.02	0.01	18878.12	0.02	18872.12	0.03	18891.61	-0.02	18885.75	0.03	18880.74	-0.05
6	18884.97	0.07	-	-	18871.02	0.01	18892.47	-0.05	-	-	18879.66	-0.05
7	18885.76	-0.03	-	-	18869.94	0.03	18893.36	-0.04	-	-	18878.52	-0.10
8	18886.69	0.04	-	-	18868.83	0.05	18894.23	-0.04	-	-	18877.45	-0.07
9	18887.57	0.07	-	-	18867.69	0.04	18895.11	-0.01	-	-	18876.32	-0.08
10	18888.40	0.06	-	-	18866.50	-0.01	18895.93	-0.03	-	-	18875.26	-0.01
11	18889.20	0.03	-	-	18865.40	0.06	18896.76	-0.02	-	-	18874.20	0.08
12	18889.99	0.01	-	-	18864.22	0.06	18897.56	-0.02	-	-	18872.91	-0.04
13	18890.74	-0.03	-	-	18863.06	0.09	18898.38	0.01	-	-	18871.76	-0.02
14	18891.61	0.06	-	-	18861.83	0.07	18899.14	-0.02	-	-	18870.55	-0.03
15	18892.33	0.02	-	-	18860.57	0.02	18899.90	-0.02	-	-	18869.38	0.00
16	18893.10	0.04	-	-	18859.34	0.03	18900.68	0.01	-	-	18868.20	0.04
17	18893.82	0.03	-	-	18858.06	0.00	18901.41	0.00	-	-	18866.95	0.03
18	18894.52	0.00	-	-	18856.84	0.04	18902.12	0.00	-	-	18865.73	0.06
19	18895.11	-0.10	-	-	18855.56	0.04	18902.90	0.07	-	-	18864.43	0.02
20	18895.93	0.02	-	-	18854.29	0.05	18903.55	0.03	-	-	18863.06	-0.07
21	18896.62	0.04	-	-	18852.97	0.05	18904.23	0.03	-	-	18861.83	-0.01
22	18897.25	0.01	-	-	18851.65	0.05	18904.88	0.02	-	-	18860.57	0.03
23	18897.88	-0.02	-	-	18850.28	0.00	18905.53	0.02	-	-	18859.26	0.04
24	18898.54	0.01	-	-	18848.86	-0.07	18906.20	0.06	-	-	18857.88	0.00
25	18899.16	0.01	-	-	18847.49	-0.08	18906.86	0.10	-	-	18856.56	0.03
26	18899.68	-0.08	-	-	18846.08	-0.11	18907.45	0.08	-	-	18855.29	0.11
27	18900.29	-0.06	-	-	18844.72	-0.09	18908.03	0.07	-	-	18853.92	0.11
28	-	-	-	-	18876.32	0.02	-	-	-	-	18852.51	0.09
29	-	-	-	-	18875.26	-0.01	-	-	-	-	18850.92	-0.09
30	-	-	-	-	18874.20	-0.03	-	-	-	-	18849.70	0.10
31	-	-	-	-	18873.17	0.01	-	-	-	-	18848.21	0.03
32	-	-	-	-	18872.12	0.03	-	-	-	-	18846.75	0.01
33	-	-	-	-	18871.02	0.01	-	-	-	-	18845.28	-0.01

Note: O-C are observed minus calculated line positions.

Table S1.2: Line positions (in cm^{-1}) in the 1-0 of the $C^3\Pi_1-X^3\Delta_2$ subband of NbN.

J	$R(J)$	O-C	$Q(J)$	O-C	$P(J)$	O-C
2	18040.22	0.02	18037.14	-0.10	18035.32	0.05
3	18041.14	0.01	18037.14	-0.05	-	-
4	18042.04	0.00	18037.14	0.02	18033.22	0.05
5	18042.93	-0.01	-	-	18032.13	0.03
6	18043.79	-0.02	-	-	18031.02	0.02
7	18044.63	-0.03	-	-	18029.91	0.02
8	18045.47	-0.03	-	-	18028.77	0.01
9	18046.29	-0.03	-	-	18027.60	0.00
10	18047.10	-0.01	-	-	18026.43	-0.01
11	18047.88	-0.01	18036.09	0.01	18025.25	0.00
12	18048.65	0.01	18035.88	0.03	18024.03	-0.01
13	18049.37	-0.01	18035.59	-0.02	18022.81	0.00
14	18050.11	0.01	18035.32	-0.01	18021.57	0.01
15	18050.80	0.01	18035.04	-0.01	18020.28	-0.01
16	18051.44	-0.02	18034.74	-0.01	18019.01	0.01
17	18052.11	0.00	18034.33	-0.08	18017.69	-0.01
18	18052.73	-0.02	18034.08	0.01	18016.36	-0.01
19	18053.38	0.01	18033.72	0.02	18015.02	0.01
20	-	-	18033.22	-0.10	18013.66	0.01
21	-	-	18032.95	0.03	18012.24	-0.03
22	-	-	18032.50	0.00	18010.88	0.01
23	-	-	18032.13	0.05	18009.50	0.05
24	-	-	18031.61	-0.03	18008.02	0.00
25	-	-	-	-	18006.58	-0.01
26	-	-	-	-	18005.14	0.00

Table S1.3: Line positions (in cm^{-1}) in the 1-0 of the $C^3\Pi_2-X^3\Delta_3$ subband of NbN.

J	$R(J)$	O-C	$Q(J)$	O-C	$P(J)$	O-C
3	18403.68	0.04	18399.50	-0.20	18396.79	0.04
4	18404.59	0.04	18399.50	-0.12	18395.82	0.14
5	18405.49	0.07	-	-	18394.69	0.09
6	18406.35	0.06	-	-	18393.54	0.05
7	18407.12	-0.01	-	-	18392.40	0.03
8	18407.94	-0.01	-	-	18391.26	0.05
9	18408.76	0.01	-	-	18390.06	0.01
10	18409.57	0.04	-	-	18388.89	0.03
11	18410.35	0.06	-	-	18387.67	0.02
12	18411.06	0.03	-	-	18386.45	0.02
13	18411.77	0.01	-	-	18385.22	0.05
14	18412.43	-0.02	-	-	18383.94	0.03
15	18413.21	0.08	-	-	18382.62	0.00
16	18413.80	0.01	-	-	18381.31	0.00
17	-	-	-	-	18380.01	0.03
18	18415.02	-0.03	-	-	18378.61	-0.02
19	18415.67	0.02	-	-	18377.23	-0.03
20	18416.19	-0.04	-	-	18375.83	-0.05
21	-	-	-	-	18374.35	-0.12
22	-	-	-	-	18372.87	-0.18
23	-	-	-	-	18371.38	-0.22

Table S1.4: Line positions (in cm^{-1}) in the 1-0 of the $e^1\Pi-X^3\Delta_2$ band of NbN.

J	$R(J)$	O-C	$Q(J)$	O-C	$P(J)$	O-C
2	-	-	19409.83	-0.09	19407.91	-0.05
3	19413.74	-0.02	19409.73	-0.11	19406.93	0.03
4	19414.67	0.04	19409.73	-0.02	19405.79	-0.04
5	19415.52	0.03	19409.64	0.02	19404.71	-0.02
6	19416.41	0.08	19409.50	0.02	19403.58	-0.03
7	19417.21	0.07	19409.33	0.03	19402.43	-0.02
8	19417.99	0.07	19409.10	-0.01	19401.25	-0.03
9	19418.74	0.08	19408.86	-0.03	19400.06	-0.02
10	19419.48	0.09	19408.62	-0.01	19398.84	-0.01
11	19420.14	0.05	19408.33	-0.02	19397.60	0.00
12	19420.77	0.00	-	-	19396.31	-0.01
13	19421.34	-0.06	19407.69	-0.03	19394.99	-0.02
14	-	-	-	-	19393.61	-0.07

Table S1.5: Line positions (in cm^{-1}) in the $[20756]^3\Pi_0^+-X^3\Delta_1$ subband of NbN.

$^3\Pi_0^+$							$^3\Pi_0^-$					
J	$R_{ee}(J)$	O-C	$Q_{ef}(J)$	O-C	$P_{ee}(J)$	O-C	$R_{ff}(J)$	O-C	$Q_{fe}(J)$	O-C	$P_{ff}(J)$	O-C
1	20753.28	0.04	-	-	20750.33	-0.06	20763.94	-0.11	20762.09	-0.06	20761.17	-0.02
2	20754.12	0.03	20751.21	-0.03	20749.32	-0.02	20764.82	-0.09	20762.03	-0.02	20760.10	-0.05
3	20754.95	0.06	20751.12	0.03	20748.21	-0.03	20765.63	-0.09	20761.92	0.01	20759.08	0.03
4	20755.67	0.03	20750.92	0.03	20747.05	-0.04	20766.36	-0.12	20761.74	0.02	20757.92	0.01
5	20756.42	0.08	20750.63	-0.01	20745.88	-0.01	20767.08	-0.11	20761.47	-0.01	20756.74	0.02
6	20757.06	0.07	20750.33	-0.01	20744.61	-0.03	20767.78	-0.08	20761.17	-0.02	20755.57	0.09
7	20757.67	0.09	20750.01	0.03	20743.30	-0.03	20768.41	-0.07	20760.86	0.00	20754.24	0.05
8	20758.19	0.06	20749.54	-0.04	20741.93	-0.05	20768.98	-0.07	20760.52	0.04	20752.91	0.05
9	20758.67	0.05	20749.11	-0.02	20740.49	-0.09	20769.55	-0.02	20760.10	0.05	20751.50	0.03
10	20759.11	0.04	20748.59	-0.03	20739.04	-0.09	20770.01	-0.03	20759.59	0.02	20750.06	0.02
11	20759.52	0.06	20748.15	0.08	20737.55	-0.07	20770.46	0.00	20759.11	0.07	20748.54	-0.03
12	20759.84	0.04	20747.43	-0.03	20735.99	-0.07	20770.87	0.03	20758.49	0.03	20747.05	0.01
13	20760.10	0.01	20746.78	-0.02	20734.40	-0.06	20771.18	0.01	20757.88	0.04	20745.45	-0.01
14	20760.33	0.00	20746.09	0.00	20732.74	-0.06	20771.48	0.04	20757.21	0.04	20743.83	-0.01
15	20760.55	0.04	20745.39	0.06	20731.03	-0.06	20771.72	0.05	20756.42	-0.02	20742.13	-0.04
16	20760.69	0.04	20744.56	0.04	-	-	-	-	20755.73	0.06	20740.42	-0.03
17	-	-	20743.60	-0.05	-	-	-	-	20754.95	0.10	20738.58	-0.10
18	-	-	-	-	-	-	-	-	20754.05	0.07	20736.78	-0.08
19	-	-	-	-	-	-	-	-	20753.12	0.06	20734.95	-0.04
20	-	-	-	-	-	-	-	-	20752.10	0.01	20732.99	-0.08

Table S1.6: Line positions (in cm^{-1}) in the $[20900]^3\Pi_1-X^3\Delta_2$ subband of NbN.

$^3\Pi_{1e}$							$^3\Pi_{1f}$					
J	$R_{ee}(J)$	O-C	$Q_{ef}(J)$	O-C	$P_{ee}(J)$	O-C	$R_{ff}(J)$	O-C	$Q_{fe}(J)$	O-C	$P_{ff}(J)$	O-C
2	-	-	20499.40	-0.14	20497.80	0.05	20504.88	0.07	20502.04	0.01	20500.13	-0.04
3	20502.82	0.04	20499.22	0.010	20496.48	-0.05	20505.48	-0.02	20501.79	0.00	20498.99	-0.03
4	20503.22	0.00	20498.73	-0.04	20495.18	-0.02	20506.12	0.01	20501.49	0.00	20497.80	0.02
5	20503.53	0.01	20498.17	-0.03	20493.72	-0.03	20506.64	-0.01	20501.09	-0.01	20496.48	0.01
6	20503.66	-0.02	20497.56	0.06	20492.16	-0.02	20507.08	-0.03	20500.60	-0.03	20495.14	0.06
7	20503.66	-0.03	20496.64	-0.02	20490.49	0.01	20507.46	-0.03	20500.04	-0.05	20493.62	0.01
8	20503.53	0.00	20495.76	0.10	20488.63	0.00	20507.76	-0.03	20499.40	-0.06	20492.16	0.10
9	20503.22	0.02	20494.53	0.03	20486.67	0.04	20508.03	0.03	20498.73	-0.03	20490.49	0.06
10	20502.72	0.05	20493.09	-0.08	20484.42	-0.05	20508.15	0.02	20497.87	-0.10	20488.74	0.02
11	-	-	20497.06	-0.04	20482.13	0.00	20508.18	-0.01	20497.06	-0.04	20486.95	0.02
12	-	-	20489.80	-0.09	-	-	20508.18	0.02	20496.15	0.00	20485.06	0.00
13	-	-	20487.98	0.07	-	-	-	-	20495.18	0.06	20483.10	-0.01

Table S1.7: Line positions (in cm^{-1}) in the $[21240]^3\Pi_2-X^3\Delta_3$ subband of NbN.

J	$R_{ee}/R_{ff}(J)$	O-C	$Q_{ef}/Q_{fe}(J)$	O-C	$P_{ee}/P_{ff}(J)$	O-C
3	20355.63	0.09	20351.66	-0.01	20348.88	0.11
4	20356.29	-0.06	20351.45	-0.07	20347.74	0.09
5	20357.11	-0.02	20351.31	-0.02	20346.49	0.00
6	20357.85	-0.02	20351.09	-0.01	20345.32	0.02
7	20358.52	-0.05	20350.87	0.04	20344.09	0.03
8	20359.13	-0.10	20350.53	0.00	20342.80	0.01
9	20359.78	-0.07	20350.20	0.02	20341.50	0.02
10	20360.40	-0.03	20349.80	0.00	20340.17	0.03
11	20360.96	-0.02	20349.35	-0.03	20338.77	0.02
12	20361.50	0.02	20348.88	-0.04	20337.34	0.02
13	20361.93	-0.01	20348.48	0.06	20335.85	-0.01
14	20362.38	0.01	20347.90	0.02	20334.35	0.00
15	20362.78	0.03	20347.33	0.03	20332.83	0.02
16	20363.14	0.05	20346.63	-0.04	20331.22	0.00
17	20363.44	0.05	20346.00	-0.01	20329.65	0.05
18	20363.67	0.03	20345.32	0.01	20327.95	0.02
19	20363.90	0.04	20344.56	0.00	20326.17	-0.05
20	20363.99	-0.04	-	-	20324.38	-0.09
21	20364.12	-0.04	20342.80	-0.14	20322.63	-0.05
22	20364.28	0.04	20342.07	0.01	-	-
23	20364.28	0.00	-	-	-	-
24	20364.28	0.01	-	-	-	-

Table S1.8: Line positions (in cm^{-1}) in the 0-0 of the $[20117]^3\Pi_{1e/f}-X^3\Delta_2$ subband of NbN.

$^3\Pi_{1e}$							$^3\Pi_{1f}$					
J	$R_{ee}(J)$	O-C	$Q_{ef}(J)$	O-C	$P_{ee}(J)$	O-C	$R_{ff}(J)$	O-C	$Q_{fe}(J)$	O-C	$P_{ff}(J)$	O-C
2	19719.59	-0.01	19716.66	-0.09	19714.88	0.03	19720.65	-0.08	19717.92	-0.04	19716.11	0.00
3	19720.35	-0.04	19716.55	-0.04	19713.78	0.04	19721.37	-0.05	19717.69	-0.03	19714.92	-0.03
4	19721.06	-0.06	19716.37	0.00	19712.66	0.09	19721.96	-0.05	19717.47	0.07	19713.79	0.08
5	19721.72	-0.06	19716.11	0.01	19711.42	0.06	19722.48	-0.04	19716.95	-0.05	19712.49	0.10
6	19722.32	-0.06	19715.74	-0.02	19710.17	0.09	19722.85	-0.09	19716.47	-0.03	19711.09	0.11
7	19722.83	-0.08	19715.33	-0.03	19708.81	0.07	19723.25	-0.01	19715.90	-0.01	19709.56	0.08
8	19723.38	0.02	19714.88	0.00	19707.39	0.06	19723.48	0.01	19715.23	0.00	19707.97	0.08
9	19723.66	-0.07	19714.37	0.04	19705.85	0.00	19723.50	-0.08	19714.48	0.04	19706.22	0.02
10	19723.93	-0.08	19713.78	0.08	19704.28	-0.02	19723.50	-0.06	19713.61	0.07	19704.38	-0.03
11	19724.13	-0.06	19713.06	0.09	19702.60	-0.06	19723.40	-0.03	19712.50	-0.03	19702.48	-0.03
12	19724.24	-0.02	19712.25	0.10	19700.89	-0.04	-	-	19711.48	0.09	19700.46	-0.03
13	19724.12	-0.10	19711.36	0.14	19699.10	-0.01	-	-	19710.19	0.07	19698.34	-0.01
14	-	-	-	-	19697.17	-0.01	-	-	19708.81	0.10	19696.07	-0.01
15	-	-	-	-	19695.10	-0.03	-	-	19707.10	-0.05	19693.62	-0.04
16	-	-	-	-	19692.97	0.01	-	-	-	-	19691.13	0.03
17	-	-	-	-	19690.70	0.04	-	-	19703.50	-0.03	19688.39	0.01
18	-	-	-	-	-	-	-	-	19701.44	-0.01	-	-

Table S1.9: Line positions (in cm^{-1}) in the 0-0 of the $[19842]^3\Pi_0^\pm - X^3\Delta_1$ subband of NbN.

${}^3\Pi_0^+$							${}^3\Pi_0^-$						
J	$R_{ee}(J)$	O-C	$Q_{ef}(J)$	O-C	$P_{ee}(J)$	O-C	$R_{ff}(J)$	O-C	$Q_{fe}(J)$	O-C	$P_{ff}(J)$	O-C	
1	19839.26	-0.10	-	-	-	-	19848.37	-0.12	-	-	-	-	
2	19840.19	-0.09	-	-	19835.35	-0.06	19849.40	-0.02	-	-	19844.45	-0.09	
3	19841.10	-0.08	-	-	19834.31	-0.05	19850.30	-0.03	-	-	19843.47	-0.02	
4	19841.96	-0.10	19837.20	0.02	19833.29	0.01	19851.19	-0.02	-	-	19842.37	-0.05	
5	-	-	19837.10	0.05	19832.19	0.01	19852.05	-0.02	-	-	19841.24	-0.08	
6	19843.82	0.09	19836.96	0.06	19831.04	-0.01	19852.90	0.00	19846.00	-0.07	19840.19	-0.02	
7	19844.45	-0.07	19836.77	0.05	19829.91	0.01	19853.73	0.02	19845.93	0.03	19839.11	0.05	
8	19845.30	0.01	19836.57	0.05	19828.75	0.03	19854.51	0.01	19845.71	0.00	19837.96	0.06	
9	19846.02	-0.02	19836.32	0.03	19827.55	0.03	19855.28	0.02	19845.52	0.02	19836.77	0.06	
10	19846.75	-0.01	19836.07	0.03	19826.32	0.03	19856.02	0.02	19845.25	-0.01	19835.55	0.05	
11	19847.41	-0.04	19835.79	0.03	19825.09	0.05	19856.73	0.02	19845.02	0.02	19834.28	0.02	
12	19848.11	-0.01	19835.48	0.03	19823.80	0.04	19857.41	0.01	19844.72	0.01	19832.99	-0.01	
13	19848.75	-0.01	19835.14	0.02	19822.49	0.04	19858.07	0.01	19844.34	-0.06	19831.68	-0.03	
14	19849.37	0.00	19834.78	0.02	19821.17	0.05	19858.70	0.00	19844.14	0.08	19830.37	-0.03	
15	19849.91	-0.05	19834.35	-0.03	19819.81	0.05	19859.30	-0.02	19843.82	0.12	19829.03	-0.04	
16	19850.50	-0.02	19833.95	-0.01	19818.36	-0.02	19859.90	0.00	19843.33	0.01	19827.66	-0.05	
17	19851.06	0.01	19833.50	-0.02	19817.00	0.03	19860.46	-0.01	19843.07	0.16	19826.32	0.00	
18	19851.56	0.00	19832.99	-0.07	19815.52	-0.01	19861.02	0.02	19842.38	-0.09	19824.89	-0.02	
19	19852.05	0.02	19832.52	-0.04	19814.04	-0.02	19861.52	0.01	19841.96	-0.05	19823.43	-0.05	
20	19852.43	-0.05	19832.02	-0.02	19812.56	-0.01	19862.01	0.01	-	-	19821.96	-0.06	
21	19852.90	0.00	19831.45	-0.04	19811.18	0.13	19862.47	0.02	19841.08	0.07	19820.47	-0.06	
22	19853.25	-0.04	19830.87	-0.05	19809.60	0.09	19862.91	0.03	-	-	19818.98	-0.04	
23	19853.62	-0.04	19830.27	-0.04	19808.01	0.08	19863.30	0.01	-	-	19817.47	-0.01	
24	19853.96	-0.03	19829.63	-0.05	19806.38	0.05	19863.67	0.01	-	-	19815.94	0.02	
25	19854.27	-0.02	19829.03	0.02	-	-	19864.01	0.00	-	-	19814.34	0.01	
26	19854.51	-0.06	19828.28	-0.04	-	-	19864.33	0.00	-	-	19812.72	0.01	
27	19854.79	-0.02	19827.62	0.02	-	-	19864.62	0.00	-	-	19811.06	0.00	
28	19855.01	-0.02	19826.85	0.00	-	-	19864.89	0.01	-	-	19809.35	-0.04	
29	19855.27	0.06	-	-	-	-	19865.12	0.01	-	-	19807.60	-0.09	
30	19855.33	-0.03	-	-	-	-	19865.33	0.02	-	-	-	-	
31	19855.51	0.03	-	-	-	-	19865.48	0.00	-	-	-	-	
32	19855.60	0.04	-	-	-	-	-	-	-	-	-	-	
33	19855.63	0.01	-	-	-	-	-	-	-	-	-	-	
34	19855.63	-0.01	-	-	-	-	-	-	-	-	-	-	
35	19855.63	0.00	-	-	-	-	-	-	-	-	-	-	

Table S1.10: Line positions (in cm^{-1}) in the 0-1 of the $[21906]\Omega=2-X^3\Delta_3$ subband of NbN.

$\Omega=2(e)$							$\Omega=2(f)$					
J	$R_{ee}(J)$	O-C	$Q_{ef}(J)$	O-C	$P_{ee}(J)$	O-C	$R_{ff}(J)$	O-C	$Q_{fe}(J)$	O-C	$P_{ff}(J)$	O-C
3	19985.59	0.12	19982.17	0.09	19979.42	-0.11	19985.59	0.10	19982.17	0.08	19979.42	-0.12
4	19985.72	0.01	19981.54	0.07	19978.13	0.05	19985.72	-0.02	19981.54	0.05	19978.13	0.04
5	19985.77	-0.04	19980.74	0.03	19976.45	-0.02	19985.77	-0.09	19980.74	0.00	19976.45	-0.04
6	19985.77	0.00	19979.78	-0.03	19974.67	-0.05	19985.77	-0.06	19979.78	-0.08	19974.67	-0.08
7	-	-	19978.77	0.00	19972.82	0.00	-	-	19978.77	-0.06	19972.82	-0.04
8	19985.33	0.06	19977.62	0.03	19970.83	0.06	19985.33	-0.04	19977.62	-0.05	19970.83	0.00
9	19984.82	-0.01	19976.37	0.09	19968.64	0.05	19984.97	0.03	19976.37	0.00	19968.64	-0.03
10	19984.31	0.05	19974.90	0.07	19966.31	0.03	19984.46	0.07	19974.90	-0.05	19966.31	-0.06
11	19983.62	0.05	19973.29	0.03	19963.90	0.07	19983.80	0.07	19973.43	0.03	19963.90	-0.05
12	19982.77	0.00	19971.60	0.03	19961.18	-0.09	19983.05	0.09	19971.76	0.02	19961.34	-0.06
13	-	-	19969.81	0.04	19958.48	-0.10	-	-	19970.06	0.10	19958.64	-0.10
14	-	-	19967.80	-0.06	19955.62	-0.16	-	-	19968.14	0.05	19955.90	-0.07
15	-	-	-	-	-	-	-	-	-	-	-	-
16	-	-	19963.76	0.00	-	-	-	-	-	-	-	-

Table S1.11: Line positions (in cm^{-1}) in the 0-1 of the $[21040]\Omega=0-X^3\Delta_1$ subband of NbN.

J	$R(J)$	O-C	$Q(J)$	O-C	$P(J)$	O-C
1	20007.80	-0.07	20006.08	0.01	20005.12	-0.04
2	20008.67	0.09	20005.88	0.00	20004.15	0.08
3	20009.28	0.08	20005.59	0.00	20002.78	-0.11
4	20009.83	0.10	20005.20	-0.02	20001.50	-0.11
5	20010.26	0.08	20004.73	-0.03	20000.18	-0.06
6	20010.63	0.09	20004.15	-0.06	19998.79	0.00
7	20010.92	0.10	20003.50	-0.07	19997.28	0.04
8	20011.14	0.11	20002.78	-0.08	19995.74	0.13
9	20011.27	0.10	20001.96	-0.12	19994.08	0.17
10	20011.27	0.02	20001.10	-0.12	19992.37	0.24
11	20011.27	0.00	20000.18	-0.13	-	-
12	20011.27	0.03	19999.22	-0.11	-	-
13	20011.27	0.10	19998.25	-0.06	-	-
14	-	-	19997.28	0.04	-	-
15	-	-	19996.17	0.03	-	-
16	-	-	19994.80	-0.21	-	-
17	-	-	19994.08	0.21	-	-
18	-	-	19992.71	-0.01	-	-
19	-	-	19991.50	-0.07	-	-
20	-	-	19990.48	0.04	-	-

Table S1.12: Line positions (in cm^{-1}) in the 0-1 of the $[21498]\Omega=1-X^3\Delta_2$ subband of NbN.

J	$R(J)$	O-C	$Q(J)$	O-C	$P(J)$	O-C
2	20066.32	0.00	20063.42	-0.02	20061.56	0.04
3	20067.16	0.00	20063.36	0.04	20060.45	0.01
4	20067.95	-0.01	20063.19	0.02	20059.33	0.00
5	20068.69	-0.02	20063.01	0.04	20058.16	-0.02
6	20069.38	-0.02	20062.71	-0.01	20056.94	-0.04
7	20070.04	0.00	20062.44	0.03	20055.67	-0.06
8	20070.59	-0.02	20062.06	0.01	20054.38	-0.05
9	20071.07	-0.05	20061.63	0.00	20053.05	-0.02
10	20071.57	0.03	20061.13	-0.01	20051.69	0.04
11	20071.93	0.05	20060.54	-0.02	20050.27	0.11
12	20072.21	0.08	20059.83	-0.08	-	-
13	20072.30	0.03	20059.10	-0.06	-	-
14	20072.30	0.00	20058.29	-0.01	-	-
15	-	-	20057.31	-0.02	-	-

Table S1.13: Line positions (in cm^{-1}) in the 0-1 of the $[22069]\Omega=2-X^3\Delta_3$ subband of NbN.

J	$R(J)$	O-C	$Q(J)$	O-C	$P(J)$	O-C
3	20149.06	-0.11	20145.30	-0.09	20142.63	0.07
4	20149.91	0.01	20145.06	-0.11	20141.42	0.03
5	20150.58	0.01	20144.93	0.03	20140.17	0.00
6	20151.17	-0.01	20144.59	0.02	20138.96	0.06
7	20151.67	-0.07	20144.17	-0.02	20137.59	0.02
8	20152.19	-0.06	20143.69	-0.06	20136.20	0.01
9	20152.65	-0.05	20143.22	-0.03	20134.78	0.03
10	20152.95	-0.14	20142.71	0.01	20133.32	0.06
11	20153.31	-0.11	20142.09	0.00	20131.78	0.08
12	20153.56	-0.14	20141.43	0.00	20130.17	0.07
13	20153.87	-0.05	20140.70	0.00	20128.51	0.08
14	20154.09	0.01	20139.98	0.06	20126.75	0.04
15	-	-	20139.01	-0.08	20125.05	0.12
16	-	-	20138.17	-0.02	20123.16	0.06
17	-	-	20137.22	-0.01	-	-
18	-	-	20136.20	-0.02	-	-
19	-	-	20135.11	-0.03	-	-
20	-	-	20134.06	0.06	-	-
21	-	-	20132.86	0.06	-	-
22	-	-	20131.51	-0.03	-	-
23	-	-	20130.17	-0.04	-	-
24	-	-	20128.84	0.02	-	-
25	-	-	20127.43	0.06	-	-
26	-	-	20125.86	0.01	-	-
27	-	-	20124.30	0.04	-	-
28	-	-	20122.51	-0.09	-	-
29	-	-	20120.88	0.00	-	-

Table S1.14: Line positions (in cm^{-1}) in the 0-1 of the $[21678]\Omega=1-X^3\Lambda_2$ subband of NbN.

J	$R(J)$	O-C	$Q(J)$	O-C	$P(J)$	O-C
2	20246.24	-0.03	20243.60	0.02	20241.76	-0.02
3	20246.87	0.01	20243.23	-0.04	20240.52	-0.06
4	20247.40	0.05	20242.84	-0.03	20239.25	-0.03
5	20247.76	0.01	20242.37	0.01	20237.87	-0.01
6	-	-	20241.76	0.00	20236.43	0.06
7	20248.21	-0.02	20241.08	0.03	20234.83	0.06
8	-	-	20240.28	0.04	20233.06	0.00
9	-	-	20239.33	-0.01	20231.25	-0.01
10	-	-	20238.32	-0.01	-	-
11	-	-	20237.23	0.01	20227.40	0.05
12	-	-	20236.01	-0.01	20225.23	-0.02
13	-	-	20234.81	0.09	20222.97	-0.08
14	-	-	20233.21	-0.11	-	-
15	-	-	20231.82	0.00	-	-
16	-	-	20230.25	0.03	-	-
17	-	-	20228.53	0.00	-	-
18	-	-	20226.71	-0.03	-	-
19	-	-	20224.89	0.03	-	-

Table S1.15: Line positions (in cm^{-1}) in the 0-1 of the $[21692]\Omega=1-X^3\Lambda_2$ subband of NbN.

J	$R(J)$	O-C	$Q(J)$	O-C	$P(J)$	O-C
2	20260.68	0.07	20258.04	0.04	20256.26	0.01
3	20261.14	0.03	20257.64	0.02	20254.94	-0.06
4	20261.50	0.02	20257.12	0.00	20253.59	-0.03
5	20261.80	0.07	20256.47	-0.02	20252.08	-0.04
6	20261.88	0.02	20255.73	-0.01	20250.42	-0.08
7	20261.88	0.00	20254.94	0.06	20248.70	-0.06
8	20261.80	0.03	20253.88	-0.01	20246.87	-0.02
9	20261.50	-0.06	20252.80	0.01	20244.88	-0.03
10	-	-	20251.62	0.04	-	-

Table S1.16: Line positions (in cm^{-1}) in the 0-1 of the $[21620]\Omega=0^+-X^3\Delta_1$ and $[21639]\Omega=0^--X^3\Delta_1$ subband of NbN.

0^+							0^-					
J	$R_{ee}(J)$	O-C	$Q_{ef}(J)$	O-C	$P_{ee}(J)$	O-C	$R_{ff}(J)$	O-C	$Q_{fe}(J)$	O-C	$P_{ff}(J)$	O-C
1	20588.30	-0.04	20586.50	-0.05	20585.60	-0.05	20607.04	-0.01	20605.15	-0.04	20604.22	-0.05
2	20589.05	0.00	20586.38	0.02	20584.54	-0.02	20607.79	-0.01	20605.05	-0.01	20603.16	-0.04
3	20589.65	-0.01	20586.08	0.01	20583.37	0.00	20608.47	-0.02	20604.86	0.05	20602.09	0.04
4	20590.17	-0.01	20585.72	0.03	20582.09	0.00	20609.07	-0.03	20604.52	0.01	20600.84	0.01
5	20590.60	0.00	20585.21	0.01	20580.69	-0.02	20609.58	-0.05	20604.16	0.04	20599.54	0.01
6	20590.93	0.01	20584.62	-0.01	20579.24	0.01	20610.00	-0.08	20603.67	0.01	20598.19	0.04
7	20591.12	-0.01	20583.97	0.02	20577.68	0.02	20610.37	-0.07	20603.12	0.01	20596.75	0.06
8	20591.25	0.00	20583.25	0.07	20576.07	0.08	20610.64	-0.07	20602.50	0.02	20595.22	0.07
9	20591.25	-0.02	20582.27	-0.03	20574.28	0.06	20610.93	0.03	20601.76	0.00	20593.58	0.06
10	20591.25	0.06	20581.29	-0.04	20572.39	0.04	20610.93	-0.06	20600.91	-0.04	20591.84	0.03
11	-	-	20580.24	-0.01	20570.45	0.06	20610.93	-0.05	20600.07	0.02	-	-
12	-	-	20579.05	-0.02	-	-	-	-	20599.14	0.10	-	-
13	-	-	20577.70	-0.09	-	-	-	-	-	-	-	-
14	-	-	20576.28	-0.13	-	-	-	-	-	-	-	-
15	-	-	-	-	-	-	-	-	-	-	-	-
16	-	-	-	-	-	-	-	-	-	-	-	-
17	-	-	20571.70	0.08	-	-	-	-	-	-	-	-

Supplementary information for rotational line positions and assignments of observed bands of TaN

Table S2.1: Line positions (in cm^{-1}) in the 0-0 of the $[23582]\Omega=1-X^1\Sigma^+$ band of TaN.

J	$P(J)$	O-C	$Q(J)$	O-C	$R(J)$	O-C
0	-	-	-	-	23582.70	0.02
1	-	-	23581.75	-0.02	23583.38	0.01
2	23579.99	0.05	23581.51	-0.03	23583.96	0.00
3	23578.76	-0.04	23581.21	0.00	23584.41	-0.02
4	23577.56	-0.01	23580.75	0.00	23584.78	-0.01
5	23576.20	-0.01	23580.19	-0.01	23585.06	0.01
6	23574.72	-0.02	23579.52	-0.01	23585.17	-0.01
7	23573.17	0.00	23578.76	0.02	23585.17	-0.05
8	23571.47	-0.01	23577.86	0.01	23585.17	0.03
9	23569.69	0.00	23576.86	0.01	23585.00	0.05
10	23567.78	0.00	23575.72	-0.01	-	-
11	23565.76	0.00	23574.51	0.01	23584.27	0.03
12	23563.64	0.00	23573.17	0.02	23583.74	0.02
13	23561.39	-0.02	23571.70	0.01	23583.08	0.00
14	23559.05	-0.01	23570.14	0.02	23582.34	0.00
15	23556.59	-0.01	23568.45	0.01	23581.52	0.03
16	23554.03	0.00	23566.66	0.02	23580.51	-0.01
17	23551.33	-0.02	23564.74	0.00	23579.52	0.08
18	23548.53	-0.02	23562.71	-0.01	23578.23	-0.01
19	23545.64	-0.01	23560.59	0.01	23576.84	-0.10
20	23542.63	-0.01	23558.31	-0.01	23575.51	-0.01
21	23539.48	-0.03	23555.97	0.00	23574.00	0.00
22	23536.25	-0.02	23553.50	0.00	23572.35	-0.01
23	23532.92	-0.01	23550.92	0.02	23570.59	-0.01
24	23529.50	0.04	23548.14	-0.05	23568.73	-0.01
25	23525.86	-0.02	23545.39	0.01	23566.79	0.03
26	-	-	23542.47	0.02	23564.74	0.07
27	-	-	23539.48	0.09	23562.44	-0.02
28	-	-	23536.25	0.03	23560.18	0.05
29	-	-	23532.92	-0.03	23557.74	0.04
30	-	-	23529.50	-0.05	23555.15	0.00
31	-	-	23526.00	-0.04	23552.40	-0.09
32	-	-	-	-	23549.63	-0.07
33	-	-	-	-	23546.80	-0.01
34	-	-	-	-	23543.82	0.03
35	-	-	-	-	23540.68	0.01
36	-	-	-	-	23537.46	0.04
37	-	-	-	-	23534.13	0.07
38	-	-	-	-	23530.52	-0.06

Table S2.2: Line positions (in cm^{-1}) in the 0-0 of the $[23624]\Omega=1-X^1\Sigma^+$ band of TaN.

J	$P(J)$	O-C	$Q(J)$	O-C	$R(J)$	O-C
0	-	-	-	-	23624.92	0.00
1	-	-	23624.00	-0.01	23625.64	0.03
2	23622.21	0.03	23623.79	0.00	23626.20	0.01
3	23620.98	-0.07	23623.48	0.03	23626.67	0.00
4	23619.81	0.01	23622.99	0.01	23627.04	0.02
5	23618.46	0.02	23622.42	0.00	23627.28	0.02
6	23616.97	0.00	23621.76	0.02	23627.34	-0.05
7	23615.36	-0.03	23620.97	0.02	23627.34	-0.07
8	23613.77	0.07	23620.05	0.01	23627.34	0.02
9	23611.88	0.00	23619.02	0.00	23627.04	-0.08
10	23609.97	0.00	23617.89	0.01	23626.72	-0.09
11	23607.94	0.00	23616.63	0.00	23626.37	-0.01
12	23605.81	0.01	23615.36	0.09	23625.82	-0.02
13	23603.56	0.01	23613.77	-0.02	23625.20	0.01
14	23601.19	0.00	23612.20	0.00	23624.43	0.00
15	23598.71	0.01	23610.52	0.02	23623.46	-0.09
16	23596.12	0.00	23608.68	0.00	23622.41	-0.15
17	23593.42	0.00	23606.76	0.01	23621.48	0.01
18	23590.61	0.00	23604.70	0.00	23620.24	-0.02
19	23587.70	0.02	23602.55	0.01	23619.02	0.09
20	-	-	23600.27	0.01	23617.53	0.04
21	-	-	23597.87	0.00	23615.95	0.01
22	-	-	23595.38	0.01	23614.32	0.04
23	-	-	23592.75	0.00	23612.52	0.02
24	-	-	23589.98	-0.04	23610.61	-0.01
25	-	-	23587.15	-0.02	23608.66	0.05
26	-	-	-	-	23606.50	0.00
27	-	-	-	-	23604.27	0.00
28	-	-	-	-	23601.86	-0.06
29	-	-	-	-	23599.47	0.00
30	-	-	-	-	23596.89	-0.01
31	-	-	-	-	23594.24	0.02
32	-	-	-	-	23591.40	-0.01
33	-	-	-	-	23588.51	0.01

Table S2.3: Line positions (in cm^{-1}) in the 0-0 of the $[24217]\Omega=1-X^1\Sigma^+$ band of TaN.

J	$P(J)$	O-C	$Q(J)$	O-C	$R(J)$	O-C
0	-	-	-	-	24217.44	-0.04
1	-	-	24216.49	-0.07	24218.24	0.06
2	24214.71	-0.02	24216.35	-0.01	24218.81	0.01
3	24213.67	0.04	24216.06	0.00	24219.32	0.02
4	24212.41	0.01	24215.65	0.02	24219.76	0.06
5	24211.04	-0.04	24215.11	-0.01	24220.02	0.03
6	24209.70	0.05	24214.52	0.02	24220.20	0.02
7	24208.16	0.05	24213.74	-0.03	24220.20	-0.06
8	24206.48	0.00	24212.93	0.00	24220.20	-0.03
9	24204.74	0.01	24211.95	-0.03	-	-
10	24202.87	0.00	24210.91	-0.01	24219.76	-0.07
11	24200.91	0.00	24209.70	-0.04	24219.39	-0.06
12	24198.83	0.01	24208.45	0.01	24218.88	-0.07
13	24196.65	0.03	24207.01	-0.02	24218.38	0.03
14	24194.33	0.02	24205.51	0.01	24217.64	0.03
15	24191.88	0.02	24203.83	0.00	24216.73	-0.01
16	24189.33	0.04	24202.04	0.00	24215.66	-0.07
17	24186.63	0.03	24200.12	0.00	24214.51	-0.08
18	24183.82	0.05	24198.07	0.01	24213.34	0.02
19	24180.86	0.04	24195.87	0.01	24211.94	0.05
20	24177.75	0.03	24193.55	0.04	24210.29	-0.04
21	24174.46	-0.01	24191.04	0.02	-	-
22	24171.04	-0.04	24188.39	0.02	-	-
23	24167.53	0.00	24185.58	0.01	-	-
24	24163.84	0.02	24182.54	-0.05	-	-
25	-	-	24179.45	-0.01	-	-
26	-	-	24176.14	0.00	-	-
27	-	-	24172.67	0.02	-	-

Table S2.4: Line positions (in cm^{-1}) in the 0-0 of the $[24657]\Omega=1-X^1\Sigma^+$ band of TaN.

J	$P(J)$	O-C	$Q(J)$	O-C	$R(J)$	O-C
0	-	-	-	-	24658.30	0.01
1	-	-	24657.45	0.07	24659.02	0.03
2	-	-	24657.20	0.03	24659.61	0.01
3	24654.50	0.07	24656.86	0.00	24660.11	0.02
4	24653.23	0.03	24656.41	-0.03	24660.48	0.01
5	24651.81	-0.06	24655.88	-0.04	24660.71	-0.05
6	24650.49	0.06	24655.24	-0.06	24660.99	0.05
7	24648.88	-0.01	24654.50	-0.07	24660.99	-0.02
8	24647.23	0.00	24653.72	-0.02	24660.99	0.01
9	24645.47	-0.01	24652.73	-0.07	-	-
10	24643.57	-0.05	24651.71	-0.06	24660.65	0.04
11	24641.65	-0.01	24650.58	-0.04	24660.27	0.00
12	24639.64	0.04	24649.33	-0.06	24659.91	0.09
13	24637.44	0.01	24647.96	-0.08	24659.29	0.02
14	24635.20	0.04	24646.54	-0.05	24658.68	0.05
15	24632.83	0.04	24644.97	-0.08	24657.94	0.07
16	24630.38	0.06	24643.32	-0.08	-	-
17	24627.82	0.08	24641.64	-0.01	-	-
18	24625.17	0.10	24639.77	-0.03	-	-
19	24622.29	0.00	24637.82	-0.04	-	-
20	24619.44	0.03	24635.77	-0.05	-	-
21	24616.44	0.00	24633.61	-0.06	-	-
22	24613.39	0.03	24631.42	-0.01	-	-
23	24610.23	0.04	24629.14	0.04	-	-
24	24606.95	0.03	24626.67	0.00	-	-
25	24603.59	0.04	24624.06	-0.08	-	-
26	24600.08	-0.01	24621.49	-0.03	-	-
27	24596.47	-0.06	24618.83	0.03	-	-
28	24592.87	-0.01	24616.02	0.03	-	-
29	24589.09	-0.04	24613.17	0.07	-	-
30	24585.30	0.00	24610.23	0.13	-	-
31	24581.21	-0.16	-	-	-	-

Table S2.5: Line positions (in cm^{-1}) in the 0-0 of the $[24742]\Omega=1-X^1\Sigma^+$ band of TaN.

J	$P(J)$	O-C	$Q(J)$	O-C	$R(J)$	O-C
0	-	-	-	-	-	-
1	-	-	24741.96	-0.07	24743.69	0.01
2	24740.27	0.07	24741.77	-0.08	24744.24	-0.09
3	24739.10	-0.01	24741.63	0.04	24744.95	0.05
4	24738.01	0.07	24741.30	0.06	24745.39	0.01
5	24736.72	0.04	24740.86	0.06	24745.74	-0.02
6	24735.34	0.01	24740.27	0.00	24746.07	-0.01
7	24733.92	0.02	24739.68	0.03	24746.29	0.00
8	24732.39	0.02	24738.92	-0.03	24746.36	-0.06
9	24730.78	0.02	24738.10	-0.06	24746.36	-0.10
10	24729.04	-0.02	24737.30	0.03	24746.36	-0.05
11	24727.20	-0.08	24736.31	0.01	-	-
12	24725.35	-0.05	24735.34	0.10	-	-
13	24723.47	0.03	24734.06	-0.03	-	-
14	24721.39	0.00	24732.90	0.06	-	-
15	24719.26	0.01	24731.53	0.01	-	-
16	24717.04	0.01	24730.11	0.01	-	-
17	24714.72	0.01	24728.55	-0.03	-	-
18	24712.32	0.02	24727.00	0.02	-	-
19	24709.73	-0.07	24725.33	0.04	-	-
20	24707.22	0.00	24723.47	-0.03	-	-
21	24704.51	-0.02	24721.69	0.07	-	-
22	24701.74	-0.03	24719.71	0.06	-	-
23	24698.92	0.02	24717.51	-0.07	-	-
24	24695.99	0.04	24715.43	0.01	-	-
25	24692.91	0.01	24713.12	-0.04	-	-
26	24689.75	-0.01	24710.76	-0.05	-	-
27	24686.56	0.04	-	-	-	-

Table S2.6: Line positions (in cm^{-1}) in the 0-0 of the $[24758]\Omega=1-X^1\Sigma^+$ band of TaN.

J	$P(J)$	O-C	$Q(J)$	O-C	$R(J)$	O-C
0	-	-	-	-	24758.75	-0.08
1	-	-	24757.90	-0.02	24759.54	0.00
2	24756.10	0.01	24757.67	-0.04	24760.15	0.01
3	24755.05	0.08	24757.39	0.00	24760.65	0.01
4	24753.76	0.02	24756.99	0.02	24761.00	-0.03
5	24752.40	-0.02	24756.47	0.03	24761.33	0.00
6	24750.99	0.00	24755.80	-0.01	24761.50	-0.02
7	24749.47	0.01	24755.05	-0.02	24761.56	-0.04
8	24747.82	0.00	24754.25	0.02	24761.56	-0.02
9	24746.10	0.02	24753.30	0.02	24761.50	0.03
10	24744.22	-0.01	24752.27	0.04	24761.25	0.01
11	24742.22	-0.07	24751.05	-0.02	24760.92	0.00
12	24740.21	-0.03	24749.82	0.01	24760.54	0.05
13	24738.08	-0.01	24748.44	0.00	24759.98	0.02
14	24735.88	0.05	24746.98	0.01	24759.35	0.02
15	24733.46	-0.02	24745.40	0.01	24758.58	0.00
16	24731.03	0.02	24743.74	0.02	24757.76	0.01
17	24728.41	-0.04	24741.94	0.01	24756.80	0.00
18	24725.78	-0.01	24739.98	-0.05	24755.81	0.05
19	24723.02	0.00	-	-	24754.61	0.01
20	24720.20	0.05	-	-	24753.30	-0.06
21	24717.16	-0.02	-	-	24752.01	0.00
22	-	-	-	-	24750.54	-0.01
23	-	-	-	-	24749.00	-0.01
24	-	-	-	-	24747.35	0.00

Table S2.7: Line positions (in cm^{-1}) in the 0-0 of the $[24995]\Omega=1-X^1\Sigma^+$ band of TaN.

J	$P(J)$	O-C	$Q(J)$	O-C	$R(J)$	O-C
0	-	-	-	-	24995.40	0.01
1	-	-	24994.48	0.01	24996.08	-0.07
2	-	-	24994.24	-0.08	24996.79	-0.05
3	24991.57	-0.01	24994.05	-0.05	24997.47	0.01
4	24990.40	-0.05	24993.81	0.01	24998.03	0.03
5	24989.21	-0.03	24993.44	0.02	24998.48	0.01
6	24987.93	-0.02	24992.94	-0.03	24998.86	0.01
7	24986.57	-0.02	24992.44	0.00	24999.16	-0.01
8	24985.16	0.01	24991.83	0.00	-	-
9	24983.63	-0.01	24991.17	0.02	24999.54	-0.01
10	24982.06	0.02	24990.40	0.02	24999.54	-0.08
11	24980.38	0.01	24989.51	-0.02	24999.54	-0.07
12	24978.57	-0.04	24988.60	0.01	24999.54	0.04
13	24976.74	-0.03	24987.52	-0.05	-	-
14	24974.82	-0.03	24986.47	0.02	24999.06	0.04
15	24972.80	-0.03	24985.16	-0.08	24998.56	-0.07
16	24970.66	-0.05	24983.87	-0.06	-	-
17	24968.45	-0.05	24982.46	-0.05	24997.46	-0.07
18	24966.12	-0.06	24980.96	-0.02	24996.81	0.01
19	24963.72	-0.03	24979.35	0.03	24995.93	-0.01
20	24961.17	-0.03	24977.49	-0.05	24994.91	-0.03
21	24958.45	-0.06	24975.59	-0.02	-	-
22	24955.66	-0.03	24973.62	0.09	-	-
23	24952.67	-0.05	-	-	-	-
24	24949.55	-0.03	-	-	-	-

Table S2.8: Line positions (in cm^{-1}) in the 0-1 of the $[24995]\Omega=1-X^1\Sigma^+$ band of TaN.

J	$P(J)$	O-C	$Q(J)$	O-C	$R(J)$	O-C
0	-	-	-	-	23931.01	-0.02
1	-	-	23930.11	-0.01	23931.80	0.00
2	23928.24	-0.06	23929.98	0.00	23932.49	-0.01
3	23927.26	0.01	23929.79	0.02	23933.15	0.02
4	23926.16	0.03	23929.51	0.03	23933.71	0.03
5	23924.95	0.00	23929.16	0.03	23934.20	0.03
6	23923.69	0.00	23928.74	0.04	23934.58	-0.01
7	23922.39	0.03	23928.25	0.04	23934.93	0.00
8	23920.98	0.03	23927.69	0.06	23935.21	0.01
9	23919.50	0.02	23927.01	0.02	23935.41	0.02
10	23917.94	0.01	23926.28	0.02	23935.52	0.01
11	23916.32	0.01	23925.52	0.06	23935.52	-0.02
12	23914.62	0.02	23924.58	0.00	23935.52	0.03
13	23912.84	0.02	23923.68	0.07	23935.41	0.05
14	23911.00	0.04	23922.57	0.01	23935.21	0.08
15	23909.01	0.01	23921.47	0.05	23934.90	0.09
16	23906.97	0.01	23920.20	0.02	23934.33	-0.06
17	23904.83	0.00	23918.87	0.04	23933.84	-0.01
18	23902.57	-0.02	23917.42	0.04	23933.15	-0.06
19	23900.26	0.02	23915.86	0.05	23932.49	0.06
20	23897.77	-0.01	23914.15	0.03	23931.57	0.05
21	23895.21	0.02	23912.28	0.00	23930.52	0.06
22	23892.45	-0.01	23910.31	0.01	-	-
23	23889.62	0.03	23908.16	0.00	-	-
24	23886.58	0.02	23905.83	-0.01	-	-
25	23883.39	0.04	23903.28	-0.04	-	-
26	23880.04	0.10	23900.58	-0.02	-	-
27	-	-	23897.63	0.00	-	-
28	-	-	23894.37	-0.03	-	-

Table S2.9: Line positions (in cm^{-1}) in the 0-1 of the $[25224]\Omega=2-a^3\Delta_1$ band of TaN.

J	$P(J)$	O-C	$Q(J)$	O-C	$R(J)$	O-C
1	-	-	-	-	21380.92	-0.09
2	-	-	-	-	21381.90	0.07
3	21376.50	-0.02	-	-	21382.70	0.09
4	21375.47	-0.06	-	-	21383.41	0.04
5	21374.49	-0.03	-	-	21384.12	0.03
6	21373.46	-0.01	-	-	21384.79	0.01
7	21372.39	-0.01	21378.54	0.05	21385.46	0.01
8	21371.31	0.02	21378.28	0.04	21386.07	0.01
9	21370.13	-0.02	21378.02	0.05	21386.64	-0.01
10	21369.00	0.03	21377.62	-0.04	21387.18	-0.02
11	21367.75	-0.01	21377.27	-0.03	21387.71	-0.01
12	21366.49	-0.03	21376.90	-0.02	21388.16	-0.02
13	21365.21	-0.02	21376.50	0.01	21388.63	0.03
14	21363.87	-0.02	21375.99	-0.02	21388.97	0.00
15	21362.53	0.02	21375.47	-0.02	21389.32	0.03
16	21361.09	-0.01	21374.88	-0.03	21389.56	-0.01
17	21359.58	-0.04	21374.31	0.03	21389.78	-0.01
18	21358.07	-0.03	21373.58	-0.03	-	-
19	21356.52	0.00	21372.84	-0.02	-	-
20	21354.89	0.01	21372.15	0.09	-	-
21	21352.85	-0.33	21371.19	0.00	-	-
22	21351.41	0.00	21370.31	0.07	-	-
23	21349.56	-0.01	21369.25	0.01	-	-
24	21347.67	0.01	21368.13	-0.01	-	-
25	21345.69	0.01	21367.00	0.03	-	-
26	21343.59	-0.02	21365.71	0.00	-	-
27	21341.37	-0.08	-	-	-	-
28	21339.22	0.02	-	-	-	-

Table S2.10: Line positions (in cm^{-1}) in the 0-0 of the $[25494]\Omega=0^+-X^1\Sigma^+$ band of TaN.

J	$P(J)$	O-C	$R(J)$	O-C
0	-	-	25495.01	0.03
1	25493.23	0.03	25495.84	0.04
2	25492.27	0.04	25496.60	0.02
3	25491.26	0.03	25497.34	0.04
4	25490.21	0.03	25498.01	0.03
5	25489.12	0.04	25498.64	0.02
6	25487.97	0.03	25499.22	0.01
7	25486.78	0.03	25499.75	0.00
8	25485.51	0.01	25500.22	-0.02
9	25484.22	0.00	25500.67	-0.02
10	25482.88	-0.01	25501.10	0.01
11	25481.50	-0.01	25501.38	-0.06
12	25480.07	-0.01	25501.70	-0.04
13	25478.60	-0.01	25501.93	-0.06
14	25477.07	-0.02	25502.19	-0.01
15	25475.50	-0.01	25502.32	-0.03
16	25473.86	-0.02	25502.39	-0.06
17	25472.18	-0.04	25502.45	-0.05
18	25470.45	-0.04	25502.45	-0.05
19	25468.68	-0.04	-	-
20	25466.86	-0.04	-	-
21	25464.98	-0.04	-	-
22	25463.05	-0.03	-	-
23	25461.06	-0.04	-	-
24	25459.06	0.00	-	-
25	25456.96	0.00	-	-
26	25454.85	0.03	-	-
27	25452.63	0.02	-	-
28	25450.37	0.02	-	-
29	25448.01	-0.02	-	-
30	25445.72	0.07	-	-
31	25443.26	0.06	-	-
32	25440.73	0.03	-	-
33	25438.23	0.10	-	-
34	25435.63	0.13	-	-
35	25432.78	-0.04	-	-
36	25430.01	-0.05	-	-
37	25427.15	-0.09	-	-
38	25424.31	-0.03	-	-
39	25421.44	0.06	-	-
40	25418.36	0.01	-	-
41	25415.26	0.02	-	-
42	25412.00	-0.07	-	-
43	25408.79	-0.02	-	-

Table S2.11: Line positions (in cm^{-1}) in the 0-0 of the $[25865]\Omega=0^+-X^1\Sigma^+$ band of TaN.

J	$P(J)$	O-C	$R(J)$	O-C
0	-	-	25866.19	0.00
1	25864.46	0.00	25866.92	0.02
2	25863.48	0.03	25867.54	0.02
3	25862.37	0.03	25868.05	0.01
4	25861.17	0.04	25868.48	0.02
5	25859.83	0.01	25868.81	0.04
6	25858.40	-0.01	25869.01	0.01
7	25856.87	-0.03	25869.15	0.04
8	25855.25	-0.04	25869.15	0.02
9	25853.54	-0.04	25869.07	0.02
10	25851.72	-0.06	25868.82	-0.05
11	25849.82	-0.05	25868.58	0.00
12	25847.80	-0.06	25868.22	0.01
13	25845.72	-0.03	25867.73	0.02
14	25843.47	-0.08	25867.14	0.01
15	25841.18	-0.06	25866.46	0.01
16	-	-	25865.65	0.00
17	-	-	25864.77	0.00
18	-	-	25863.83	0.06
19	-	-	25862.72	0.04
20	-	-	25861.58	0.10
21	-	-	25860.20	0.03
22	-	-	25858.75	-0.02
23	-	-	25857.25	0.00
24	-	-	25855.64	0.00
25	-	-	25853.80	-0.12
26	-	-	25852.14	0.05

Table S2.12: Line positions (in cm^{-1}) in the 0/1-0 of the $[26352]\Omega=0^+-X^1\Sigma^+$ band of TaN.

J	$P(J)$	O-C	$R(J)$	O-C
0	-	-	26353.39	0.07
1	26351.63	0.08	26354.17	0.06
2	26350.63	0.05	26354.93	0.08
3	26349.62	0.07	26355.56	0.03
4	26348.50	0.04	26356.19	0.04
5	26347.36	0.05	26356.75	0.04
6	26346.14	0.04	26357.22	0.01
7	26344.88	0.05	26357.69	0.04
8	26343.54	0.03	26358.04	0.01
9	26342.13	0.01	26358.32	-0.02
10	26340.67	0.00	26358.60	0.00
11	26339.19	0.02	26358.80	0.00
12	26337.60	0.00	-	-
13	26335.96	-0.01	-	-
14	26334.20	*	-	-
15	26332.28	*	-	-
15	26333.26	Perturber*		
16	26331.02	*	-	-
17	26329.01	*	-	-
18	26326.97	0.09	-	-
19	26324.92	0.05	-	-
20	26322.81	0.02	-	-
21	26320.66	0.02	-	-
22	26318.44	0.01	-	-
23	26316.15	0.00	-	-
24	26313.84	0.04	26355.47	0.04
25	26311.36	-0.02	26354.70	0.01
26	26308.89	0.00	26353.90	0.03
27	26306.34	0.02	26353.03	0.05
28	26303.70	0.01	26352.06	0.05
29	26300.98	0.01	26351.00	0.04
30	26298.19	0.01	26349.88	0.05
31	26295.33	0.01	-	-
32	26292.35	-0.02	-	-
33	26289.33	-0.01	-	-
34	26286.25	0.01	-	-
35	26283.02	-0.02	-	-
36	26279.73	-0.04	-	-

*Excluded from fit.

Table S2.13: Line positions (in cm^{-1}) in the 0/1-1 of the $[26352]\Omega=0^+-X^1\Sigma^+$ band of TaN.

J	$P(J)$	O-C	$R(J)$	O-C
0	-	-	25288.91	-0.05
1	25287.16	-0.03	25289.73	-0.03
2	25286.20	-0.03	25290.49	-0.01
3	25285.17	-0.04	25291.17	-0.02
4	25284.12	-0.02	25291.83	0.00
5	25282.99	-0.02	25292.36	-0.05
6	25281.79	-0.04	25292.92	-0.02
7	25280.56	-0.04	25293.40	-0.01
8	25279.26	-0.05	25293.80	-0.03
9	25277.90	-0.06	25294.12	-0.07
10	25276.50	-0.06	25294.45	-0.04
11	25275.06	-0.04	25294.69	-0.04
12	25273.52	-0.07	-	-
13	25271.92	-0.09	-	-
14	25270.21	*	-	-
15	25268.36	*	-	-
15	25269.35	Perturber*		
16	25267.18	*	-	-
17	25265.22	*	-	-
18	25263.31	0.03	-	-
19	25261.34	-0.01	-	-
20	25259.36	-0.01	-	-
21	25257.30	-0.02	-	-
22	25255.16	-0.04	-	-
23	25252.95	-0.07	-	-
24	25250.70	-0.08	-	-
25	-	-	-	-
26	-	-	-	-
27	-	-	-	-
28	-	-	25289.45	-0.01
29	-	-	25288.46	-0.08

*Excluded from fit.

Table S2.14: Line positions (in cm^{-1}) in the 0-0 of the $[29092]\Omega=2-a^3\Delta_1$ band of TaN.

J	$P(J)$	O-C	$Q(J)$	O-C	$R(J)$	O-C
1	-	-	-	-	-	-
2	-	-	-	-	26267.81	-0.03
3	-	-	26265.13	0.00	26268.51	-0.02
4	26261.48	-0.03	26264.93	0.01	26269.15	-0.02
5	26260.38	-0.01	26264.67	0.02	26269.75	0.00
6	26259.22	-0.01	26264.34	0.01	26270.27	-0.02
7	26258.02	0.01	26263.97	0.00	26270.76	-0.01
8	26256.77	0.04	26263.53	-0.01	26271.20	0.01
9	26255.39	-0.01	26263.05	-0.01	26271.57	0.00
10	26254.03	0.01	26262.54	0.00	26271.91	0.01
11	26252.60	0.02	26261.95	0.00	26272.16	0.00
12	26251.12	0.02	26261.35	0.04	26272.37	-0.01
13	26249.59	0.03	26260.57	-0.06	26272.60	0.05
14	26247.99	0.02	26259.86	-0.02	26272.65	-0.01
15	26246.34	0.01	26259.11	0.01	26272.73	0.02
16	26244.66	0.03	26258.23	-0.02	26272.73	0.01
17	26242.87	-0.02	26257.34	-0.02	-	-
18	26241.04	-0.04	26256.46	0.05	-	-
19	26239.22	-0.02	26255.39	-0.02	-	-
20	26237.29	-0.05	26254.37	0.01	-	-
21	-	-	26253.27	0.02	-	-
22	-	-	26252.08	-0.02	-	-
23	-	-	26250.88	-0.01	-	-
24	-	-	26249.65	0.01	-	-
25	-	-	26248.39	0.05	-	-
26	-	-	26247.00	0.02	-	-
27	-	-	26245.52	-0.05	-	-

Table S2.15: Line positions (in cm^{-1}) in the 0-0 of the $[29790]\Omega=2-a^3\Delta_1$ band of TaN.

J	$P(J)$	O-C	$Q(J)$	O-C	$R(J)$	O-C
1	-	-	-	-	26964.45	-0.05
2	-	-	26962.70	0.00	26965.12	0.01
3	26959.99	0.01	26962.37	-0.03	26965.61	-0.01
4	26958.76	-0.02	26962.02	0.02	26966.11	0.08
5	26957.51	0.03	26961.48	-0.02	26966.38	0.05
6	26956.07	-0.01	26960.94	0.03	26966.53	-0.01
7	26954.58	0.01	26960.23	0.01	26966.67	0.01
8	26952.94	-0.04	26959.43	0.01	26966.67	0.00
9	26951.27	-0.01	26958.54	0.01	26966.53	-0.04
10	26949.48	0.00	26957.51	-0.03	26966.42	0.03
11	26947.58	-0.01	26956.47	0.03	26966.13	0.02
12	26945.56	-0.04	26955.20	-0.06	26965.75	0.03
13	26943.45	-0.05	26953.95	-0.02	26965.27	0.03
14	26941.30	-0.01	26952.60	0.02	26964.74	0.08
15	26939.01	-0.02	26951.11	0.01	26964.03	0.05
16	26936.65	0.01	26949.48	-0.04	26963.24	0.03
17	26934.12	-0.03	26947.82	-0.02	-	-
18	26931.56	-0.01	26946.05	-0.01	-	-
19	26928.88	-0.02	26944.19	-0.01	-	-
20	-	-	26942.22	-0.01	-	-
21	-	-	26940.14	-0.03	-	-
22	-	-	26938.04	0.03	-	-
23	-	-	26935.80	0.05	-	-
24	-	-	26933.33	-0.06	-	-
25	-	-	26931.03	0.08	-	-
26	-	-	26928.35	-0.06	-	-

Supplementary information for rotational line positions and assignments of observed bands of ScH

Table S3.1 Line positions (cm^{-1}) of the $g^3\Phi_2-a^3\Delta_1$ system of ScH.

0-0 band							1-1 band						
J	$R(J)$	O-C	$Q(J)$	O-C	$P(J)$	O-C	$R(J)$	O-C	$Q(J)$	O-C	$P(J)$	O-C	
1	17919.30	0.00	-	-	-	-	17946.94	-0.06	-	-	-	-	
2	17929.78	0.05	17903.44	0.00	-	-	17957.37	0.11	17931.44	-0.01	-	-	
3	17940.77	-0.14	17905.77	0.07	17879.38	-0.03	17968.19	-0.02	17933.66	-0.02	17907.92	0.04	
4	17952.63	-0.03	17908.56	0.10	17873.21	-0.05	-	-	17936.28	-0.04	17901.79	0.00	
5	17964.80	0.06	17911.55	0.03	17867.31	-0.01	-	-	17939.11	0.02	-	-	
6	17976.86	-0.01	17914.61	-0.06	17861.46	0.01	-	-	-	-	-	-	
7	-	-	17917.75	0.01	17855.56	0.01	-	-	-	-	-	-	

Supplementary information for rotational line positions and assignments of observed bands of ScN

Table S4.1: Line positions (in cm^{-1}) in the 0-1 of the $B1-X^1\Sigma^+$ band of ScN.

J	$P(J)$	O-C	$Q(J)$	O-C	$R(J)$	O-C
0	-	-	-	-	19356.86	0.07
1	-	-	19355.74	0.04	19357.74	0.01
2	19353.56	0.06	19355.55	0.02	19358.58	-0.01
3	19352.30	0.06	19355.31	0.03	19359.34	-0.01
4	19350.93	0.03	19354.97	0.03	19359.99	-0.04
5	19349.49	0.02	19354.52	0.01	19360.57	-0.03
6	19347.90	-0.04	19353.98	0.00	19361.02	-0.04
7	19346.28	-0.05	19353.32	-0.01	19361.38	-0.02
8	19344.53	-0.06	19352.56	0.00	19361.58	-0.03
9	19342.68	-0.05	19351.66	0.01	19361.60	-0.07
10	19340.69	-0.06	19350.70	0.09	19361.60	0.03
11	19338.64	0.02	19349.49	0.10	19361.34	0.05
12	19336.42	0.09	19348.11	0.11	19360.74	-0.09
13	19333.95	0.09	19346.52	0.11	19360.02	-0.12
14	19331.27	0.08	19344.67	0.07	19359.04	-0.18
15	-	-	19342.57	0.00	-	-
16	-	-	19339.97	-0.30	-	-

Table S4.2: Line positions (in cm^{-1}) in the 0-0 of the $B1-X^1\Sigma^+$ band of ScN.

J	$P(J)$	O-C	$Q(J)$	O-C	$R(J)$	O-C
0	-	-	-	-	20150.89	0.05
1	-	-	20149.75	0.02	20151.77	0.00
2	20147.59	0.07	20149.59	0.03	20152.59	-0.02
3	20146.30	0.06	20149.29	0.00	20153.34	-0.02
4	20144.88	0.00	20148.93	0.01	20153.95	-0.06
5	20143.41	0.01	20148.45	0.00	20154.46	-0.07
6	20141.82	-0.02	20147.87	-0.01	20154.87	-0.09
7	20140.12	-0.05	20147.15	-0.02	20155.23	-0.02
8	20138.32	-0.06	20146.29	-0.06	20155.32	-0.08
9	20136.38	-0.08	20145.34	-0.03	20155.33	-0.06
10	20134.32	-0.08	20144.33	0.08	20155.14	-0.08
11	20132.20	0.01	20143.01	0.05	20154.88	0.01
12	20129.87	0.06	20141.60	0.12	20154.44	0.13
13	20127.28	0.04	20139.60	-0.20	20153.55	0.02
14	-	-	20137.96	0.06	20152.59	0.08
15	-	-	-	-	20151.42	0.20

Table S4.3: Line positions (in cm^{-1}) in the 1-0 of the $B1-X^1\Sigma^+$ band of ScN.

J	$P(J)$	O-C	$Q(J)$	O-C	$R(J)$	O-C
0	-	-	-	-	20963.96	0.03
1	-	-	20962.86	0.03	20964.84	0.04
2	20960.67	0.06	20962.61	0.03	20965.57	0.03
3	20959.29	0.02	20962.25	0.04	20966.15	0.00
4	20957.80	0.00	20961.73	0.01	20966.57	-0.04
5	20956.17	-0.03	20961.07	0.00	20966.93	0.01
6	20954.43	-0.02	20960.21	-0.07	20967.02	-0.05
7	20952.53	-0.02	20959.29	-0.03	20967.02	-0.03
8	20950.42	-0.07	20958.16	-0.02	20966.83	0.00
9	20948.19	-0.07	20956.85	0.00	20966.40	0.02
10	20945.77	-0.05	20955.30	0.01	20965.72	0.01
11	20943.10	-0.08	20953.58	0.07	20964.78	0.01
12	20940.26	-0.03	20951.54	0.07	20963.60	0.04
13	20937.18	0.02	20949.20	0.07	20962.01	-0.02
14	20933.81	0.08	20946.52	0.02	20960.13	-0.02
15	20930.05	0.06	20943.47	-0.03	-	-
16	-	-	20940.06	-0.09	-	-

Table S4.4: Line positions (in cm^{-1}) in the 0-1 of the $C1-X^1\Sigma^+$ band of ScN.

J	$P(J)$	O-C	$Q(J)$	O-C	$R(J)$	O-C
0	-	-	-	-	19390.64	0.00
1	-	-	19389.54	0.00	19391.27	0.03
2	19387.36	0.01	19388.99	-0.06	19391.61	-0.01
3	19385.81	0.05	19388.30	-0.01	19391.72	-0.02
4	19383.99	0.06	19387.36	0.02	19391.65	0.01
5	19381.93	0.08	19386.22	0.09	19391.23	-0.06
6	19379.63	0.08	19384.75	0.06	19390.70	-0.03
7	19377.00	-0.02	19383.09	0.07	19389.93	-0.03
8	19374.31	0.05	19381.22	0.08	19388.99	0.01
9	19371.26	-0.03	19379.13	0.08	19387.74	-0.04
10	19368.07	-0.04	19376.73	-0.03	19386.45	0.04
11	19364.68	-0.06	19373.99	-0.28	19384.76	-0.11

Table S4.5: Line positions (in cm^{-1}) in the 0-0 of the $C1-X^1\Sigma^+$ band of ScN.

J	$P(J)$	O-C	$Q(J)$	O-C	$R(J)$	O-C
0	-	-	-	-	20184.83	-0.04
1	-	-	20183.74	-0.02	20185.42	-0.06
2	20181.50	-0.06	20183.25	-0.01	20185.79	-0.04
3	20179.95	0.01	20182.49	-0.01	20185.90	-0.03
4	20178.07	-0.02	20181.50	0.00	20185.79	-0.01
5	20175.95	-0.04	20180.24	-0.02	20185.38	-0.05
6	20173.64	0.00	20178.74	-0.03	20184.83	0.01
7	20171.14	0.08	20177.04	-0.01	20183.99	-0.01
8	20168.32	0.07	20175.08	-0.03	20182.92	-0.03
9	20165.28	0.07	20172.96	0.00	20181.61	-0.09
10	20161.99	0.04	20170.65	0.06	20180.24	-0.02
11	20158.48	-0.01	20168.16	0.13	20178.63	0.00
12	20154.89	0.05	20165.28	-0.01	20176.94	0.12
13	-	-	-	-	20174.89	0.03

Table S4.6: Line positions (in cm^{-1}) in the 1-0 of the $C1-X^1\Sigma^+$ band of ScN.

J	$P(J)$	O-C	$Q(J)$	O-C	$R(J)$	O-C
0	-	-	-	-	21001.24	-0.02
1	-	-	21000.16	0.00	21001.86	0.01
2	20997.92	-0.03	20999.64	0.00	21002.17	-0.02
3	20996.35	0.03	20998.88	0.02	21002.27	-0.01
4	20994.44	-0.01	20997.85	0.01	21002.17	0.04
5	20992.32	-0.01	20996.60	0.02	21001.72	-0.02
6	20990.00	0.03	20995.07	0.00	21001.09	-0.03
7	20987.39	0.02	20993.32	-0.01	21000.26	-0.03
8	20984.46	-0.08	20991.38	0.00	20999.23	-0.03
9	20981.56	0.06	20989.23	0.00	20998.01	-0.02
10	20978.30	0.04	-	-	20996.60	-0.04
11	20974.88	0.06	-	-	20995.07	-0.01
12	20971.25	0.03	-	-	-	-

Table S4.7: Line positions (in cm^{-1}) in the 0-3 of the $D1-X^1\Sigma^+$ band of ScN.

J	$P(J)$	O-C	$Q(J)$	O-C	$R(J)$	O-C
0	-	-	-	-	19391.80	-0.09
1	-	-	19390.79	-0.02	19392.84	0.00
2	19388.61	-0.02	19390.72	0.04	19393.74	0.00
3	19387.39	-0.03	19390.47	-0.01	19394.54	-0.02
4	19386.21	0.07	19390.23	0.00	19395.30	-0.02
5	19384.79	-0.01	19389.89	-0.02	19395.98	-0.04
6	19383.44	0.05	19389.50	-0.02	19396.64	-0.02
7	19381.99	0.07	19389.06	-0.02	19397.19	-0.03
8	19380.47	0.07	19388.56	-0.01	19397.75	0.03
9	19378.81	0.01	19388.07	0.07	19398.11	-0.05
10	19377.14	0.01	19387.38	0.03	19398.54	0.00
11	19375.40	0.00	19386.68	0.03	19398.93	0.08
12	19373.62	0.01	19385.84	-0.04	19399.11	0.02
13	19371.71	-0.04	-	-	-	-
14	19369.81	-0.02	-	-	-	-
15	19367.79	-0.05	-	-	-	-

Table S4.8: Line positions (in cm^{-1}) in the 0-1 of the $D1-X^1\Sigma^+$ band of ScN.

J	$P(J)$	O-C	$Q(J)$	O-C	$R(J)$	O-C
0	-	-	-	-	20981.04	0.01
1	-	-	20979.93	-0.01	20981.98	0.01
2	20977.72	-0.02	20979.81	0.03	20982.84	0.00
3	20976.45	-0.04	20979.55	0.01	20983.62	0.00
4	20975.18	0.03	20979.22	-0.01	20984.32	-0.01
5	20973.84	0.10	20978.89	0.04	20984.91	-0.05
6	20972.30	0.05	20978.41	0.03	20985.47	-0.03
7	20970.69	0.01	20977.85	0.01	20985.95	-0.03
8	20969.08	0.04	20977.23	0.02	20986.32	-0.05
9	20967.30	-0.01	20976.52	0.01	20986.63	-0.05
10	20965.54	0.04	20975.77	0.04	20986.92	0.01
11	20963.60	-0.02	20974.91	0.03	20987.08	0.01
12	20961.67	0.00	20973.84	-0.09	20987.16	0.01
13	-	-	20972.94	0.02	20987.08	-0.06
14	20957.47	-0.04	20971.82	0.00	20987.08	0.03
15	20955.26	-0.05	20970.71	0.06	20986.86	-0.02
16	20953.02	-0.01	20969.41	0.01	20986.64	0.00
17	20950.65	-0.03	20968.01	-0.06	20986.31	-0.01
18	-	-	20966.61	-0.04	20985.93	0.02
19	20945.73	0.00	20965.20	0.03	20985.44	0.02
20	-	-	20963.60	0.01	-	-
21	-	-	20961.92	-0.02	20984.18	-0.02

Table S4.9: Line positions (in cm^{-1}) in the 0-0 of the $D1-X^1\Sigma^+$ band of ScN.

J	$P(J)$	O-C	$Q(J)$	O-C	$R(J)$	O-C
0	-	-	-	-	21775.13	-0.02
1	-	-	21774.08	0.03	21776.07	-0.02
2	21771.81	-0.03	21773.89	0.01	21776.89	-0.05
3	21770.54	-0.02	21773.62	-0.01	21777.66	-0.04
4	21769.21	0.01	21773.27	-0.02	21778.36	-0.02
5	21767.76	0.00	21772.85	-0.01	21778.96	-0.01
6	21766.26	0.04	21772.31	-0.04	21779.47	-0.01
7	21764.62	0.01	21771.74	-0.02	21779.91	0.01
8	21762.92	0.02	21771.05	-0.03	21780.26	0.03
9	21761.15	0.04	21770.28	-0.02	21780.53	0.05
10	21759.27	0.04	21769.43	-0.03	21780.62	-0.02
11	21757.33	0.05	21768.51	-0.01	21780.74	0.02
12	21755.25	0.03	21767.46	-0.04	21780.67	-0.03
13	21753.09	-0.01	21766.37	-0.02	21780.62	0.02
14	21750.88	0.01	21765.20	0.01	-	-
15	21748.57	0.00	21763.89	-0.02	21780.23	0.09
16	21746.15	-0.03	21762.57	0.03	-	-
17	21743.68	-0.02	21761.15	0.07	-	-
18	21741.14	0.00	21759.52	-0.03	-	-
19	21738.49	0.01	21757.96	0.04	-	-
20	-	-	21756.19	-0.02	-	-
21	-	-	21754.40	-0.01	-	-

Supplementary information for rotational line positions and assignments of observed bands of ScO

Table S5.1: Line positions (in cm^{-1}) in the 1-0 of the $B^2\Sigma^+-X^2\Sigma^+$ band of ScO.

J	$P_{13}(J)$	O-C	$P_{14}(J)$	O-C	$P_{23}(J)$	O-C	$P_{24}(J)$	O-C
1	21387.62	-0.02	21387.38	0.00	-	-	-	-
4	21384.12	0.07	21383.88	0.09	21384.36	0.07	21384.06	0.03
5	21382.83	0.10	21382.56	0.09	21383.10	0.07	21382.83	0.06
6	21381.43	0.10	21381.13	0.06	21381.76	0.06	21381.49	0.05
7	21379.85	-0.02	21379.64	0.03	21380.32	0.02	21380.03	-0.02
8	21378.32	-0.02	21378.08	0.00	21378.86	0.02	21378.59	0.01
9	21376.71	-0.03	21376.44	-0.04	21377.28	-0.03	21377.01	-0.04
10	21375.01	-0.07	21374.74	-0.08	21375.67	-0.05	21375.40	-0.06
11	21373.24	-0.10	21372.97	-0.11	21373.96	-0.09	21373.69	-0.10
12	21371.45	-0.10	21371.18	-0.11	21372.20	-0.12	21371.96	-0.10
13	21369.54	-0.14	21369.27	-0.15	21370.38	-0.14	21370.11	-0.15
14	21367.54	-0.21	21367.27	-0.22	21368.46	-0.20	21368.20	-0.20
15	21365.39	-0.36	21365.15	-0.34	21366.47	-0.26	21366.20	-0.27
16	21363.33	-0.35	21363.06	-0.36	21364.38	-0.35	21364.11	-0.36
17	21361.21	-0.34	21360.95	-0.34	21362.29	-0.37	21362.05	-0.35
18	21359.10	-0.24	21358.86	-0.22	21360.23	-0.29	21359.96	-0.30
21	21352.42	0.09	21352.18	0.10	21353.76	0.04	21353.49	0.03
22	21349.97	0.11	21349.70	0.10	21351.41	0.10	21351.17	0.12
23	21347.44	0.12	21347.17	0.10	21348.96	0.12	21348.69	0.11
24	21344.82	0.10	21344.55	0.09	21346.40	0.10	21346.13	0.09
25	21342.08	0.04	21341.81	0.03	21343.72	0.02	21343.48	0.04
26	21339.37	0.07	21339.11	0.07	21341.04	0.02	21340.77	0.01
27	21336.55	0.06	21336.28	0.05	21338.36	0.08	21338.09	0.07
28	21333.60	-0.02	21333.36	0.00	21335.50	0.03	21335.23	0.02
29	21330.68	0.01	21330.45	0.04	21332.58	-0.01	21332.32	-0.01
30	21327.77	0.11	21327.50	0.10	21329.70	0.05	21329.44	0.05
31	21324.70	0.13	21324.41	0.09	21326.67	0.04	21326.40	0.03
32	21321.49	0.07	21321.23	0.06	21323.63	0.08	21323.37	0.08
33	21318.20	-0.01	21317.93	-0.02	21320.46	0.06	21320.21	0.07
34	21314.87	-0.05	21314.60	-0.06	21317.16	-0.02	21316.86	-0.06
35	21311.45	-0.12	21311.19	-0.12	21313.80	-0.09	21313.53	-0.10
36	21307.92	-0.22	21307.66	-0.22	21310.36	-0.18	21310.12	-0.16

Table S5.2: Line positions (in cm^{-1}) in the 2-0 of the $B^2\Sigma^+ - X^2\Sigma^+$ band of ScO.

J	$P_{13}(J)$	O-C	$P_{14}(J)$	O-C	$P_{23}(J)$	O-C	$P_{24}(J)$	O-C
1	22196.31	0.12	22196.10	0.17	-	-	-	-
2	22195.20	0.14	22194.96	0.16	22195.29	0.13	22195.05	0.15
3	22193.91	0.05	22193.70	0.10	22194.15	0.12	22193.91	0.14
4	22192.68	0.10	22192.41	0.09	22192.92	0.10	22192.68	0.12
5	22191.27	0.04	22191.03	0.06	22191.60	0.06	22191.36	0.08
6	22189.72	-0.09	22189.48	-0.07	22190.20	0.01	22189.93	0.00
7	22188.19	-0.13	22187.92	-0.14	22188.67	-0.09	22188.40	-0.10
8	22186.52	-0.24	22186.25	-0.25	22187.02	-0.25	22186.78	-0.23
9	22184.78	-0.34	22184.54	-0.32	22185.38	-0.32	22185.14	-0.30
10	22183.04	-0.38	22182.78	-0.38	22183.70	-0.36	22183.43	-0.37
11	22181.34	-0.30	22181.10	-0.28	22182.03	-0.32	22181.79	-0.30
12	22179.63	-0.16	22179.40	-0.13	22180.35	-0.21	22180.11	-0.20
13	22177.84	-0.02	22177.60	-0.01	22178.62	-0.09	22178.38	-0.07
14	22175.99	0.12	22175.72	0.11	22176.82	0.04	22176.58	0.06
15	22173.98	0.18	22173.72	0.18	22174.94	0.16	22174.67	0.14
16	22171.89	0.22	22171.65	0.24	22172.94	0.23	22172.67	0.22
17	22169.65	0.19	22169.38	0.18	22170.79	0.22	22170.52	0.21
18	22167.26	0.09	22166.99	0.08	22168.49	0.13	22168.22	0.12
19	22164.81	-0.01	22164.57	0.01	22166.10	0.03	22165.86	0.05
20	22162.42	0.03	22162.15	0.02	22163.71	0.00	22163.44	-0.01
21	22159.88	-0.02	22159.65	0.01	22161.29	0.01	22161.05	0.03
22	22156.99	-0.33	22156.99	-0.08	22158.75	-0.03	22158.48	-0.04
23	22154.63	-0.05	22154.36	-0.06	22156.09	-0.11	22155.86	-0.08
24	22152.01	0.04	22151.77	0.06	22153.53	-0.03	22153.29	-0.01
25	22149.29	0.11	22149.05	0.13	22150.90	0.06	22150.66	0.08
26	22146.43	0.11	22146.19	0.13	22148.16	0.11	22147.92	0.13
27	22143.36	-0.03	22143.12	-0.01	22145.24	0.06	22144.97	0.05
28	22140.20	-0.18	22139.93	-0.20	22142.14	-0.10	22141.90	-0.09
29	22137.07	-0.24	22136.80	-0.25	22139.01	-0.23	22138.74	-0.24
30	22133.70	-0.46	22133.44	-0.46	22135.82	-0.33	22135.55	-0.34

Table S5.3: Line positions (in cm^{-1}) in the 3-0 of the $B^2\Sigma^+-X^2\Sigma^+$ band of ScO.

J	$P_{13}(J)$	O-C	$P_{14}(J)$	O-C	$P_{23}(J)$	O-C	$P_{24}(J)$	O-C
1	22994.01	-0.12	22993.79	-0.08	-	-	-	-
2	22992.87	-0.12	22992.65	-0.08	22993.00	-0.09	22992.71	-0.12
3	22991.60	-0.17	22991.34	-0.17	22991.82	-0.12	22991.53	-0.15
4	22990.23	-0.24	22989.98	-0.23	22990.52	-0.19	22990.23	-0.22
5	22988.87	-0.22	22988.58	-0.25	22989.15	-0.26	22988.87	-0.28
6	22987.35	-0.29	22987.09	-0.29	22987.73	-0.29	22987.50	-0.26
7	22985.82	-0.28	22985.60	-0.24	22986.27	-0.29	22986.05	-0.25
8	22984.27	-0.22	22983.98	-0.25	22984.78	-0.23	22984.52	-0.23
9	22982.68	-0.12	22982.43	-0.11	22983.25	-0.14	22983.00	-0.13
10	22981.00	-0.03	22980.75	-0.02	22981.64	-0.05	22981.38	-0.05
11	22979.29	0.11	22979.04	0.12	22979.96	0.05	22979.70	0.05
12	22977.42	0.17	22977.20	0.21	22978.18	0.13	22977.96	0.17
13	22975.52	0.28	22975.26	0.28	22976.34	0.22	22976.09	0.23
14	22973.42	0.26	22973.17	0.27	22974.38	0.28	22974.12	0.28
15	22971.24	0.25	22970.98	0.25	22972.25	0.25	22972.00	0.25
16	22968.96	0.21	22968.70	0.21	22970.03	0.20	22969.78	0.21
17	22966.58	0.15	22966.33	0.16	22967.72	0.14	22967.47	0.15
18	22964.17	0.14	22963.92	0.15	22965.38	0.13	22965.12	0.13
19	22961.67	0.12	22961.42	0.13	22962.97	0.13	22962.72	0.14
20	22959.08	0.09	22958.82	0.09	22960.44	0.09	22960.19	0.10
21	22956.45	0.10	22956.20	0.11	22957.84	0.06	22957.59	0.07
22	22953.76	0.13	22953.51	0.14	22955.22	0.09	22954.96	0.09
23	22951.07	0.24	22950.82	0.25	22952.56	0.16	22952.31	0.17
24	22948.19	0.23	22947.94	0.24	22949.81	0.21	22949.55	0.21
25	22945.16	0.16	22944.91	0.17	22946.90	0.19	22946.64	0.19
26	22942.03	0.06	22941.78	0.07	22943.83	0.08	22943.58	0.09
27	22938.84	-0.02	22938.59	-0.01	22940.70	0.00	22940.45	0.00
28	22935.55	-0.11	22935.27	-0.13	22937.48	-0.10	22937.23	-0.09
29	22932.08	-0.31	22931.83	-0.30	22934.13	-0.25	22933.88	-0.24
30	22928.57	-0.47	22928.32	-0.46	22930.69	-0.41	22930.40	-0.44

Table S5.4: Line positions (in cm^{-1}) in the 4-0 of the $B^2\Sigma^+ - X^2\Sigma^+$ band of ScO.

J	$P_{13}(J)$	O-C	$P_{14}(J)$	O-C	$P_{23}(J)$	O-C	$P_{24}(J)$	O-C
2	23782.47	-0.12	23782.23	-0.10	23782.47	-0.22	23782.38	-0.05
3	23781.15	-0.20	23780.97	-0.13	23781.39	-0.14	23781.15	-0.12
4	23779.95	-0.09	23779.71	-0.07	23780.22	-0.06	23779.95	-0.07
5	23778.60	-0.04	23778.36	-0.02	23778.93	-0.02	23778.66	-0.03
6	23777.19	0.04	23776.95	0.06	23777.58	0.04	23777.34	0.06
7	23775.66	0.08	23775.42	0.10	23776.11	0.07	23775.87	0.09
8	23774.08	0.15	23773.84	0.17	23774.59	0.14	23774.35	0.16
9	23772.37	0.18	23772.10	0.17	23772.97	0.19	23772.73	0.21
10	23770.51	0.15	23770.24	0.13	23771.20	0.17	23770.93	0.16
11	23768.54	0.08	23768.27	0.07	23769.32	0.13	23769.05	0.12
12	23766.50	0.04	23766.26	0.06	23767.34	0.07	23767.07	0.06
13	23764.41	0.03	23764.17	0.05	23765.31	0.05	23765.04	0.04
14	23762.25	0.03	23761.98	0.02	23763.18	0.02	23762.94	0.04
15	23760.01	0.04	23759.74	0.03	23761.00	0.01	23760.76	0.03
16	23757.59	-0.05	23757.35	-0.03	23758.69	-0.03	23758.45	-0.01
17	23755.16	-0.06	23754.90	-0.06	23756.30	-0.08	23756.06	-0.06
18	23752.68	-0.04	23752.44	-0.02	23753.88	-0.06	23753.61	-0.07
19	23750.14	0.01	23749.87	0.00	23751.40	-0.03	23751.13	-0.04
20	23747.48	0.02	23747.21	0.01	23748.80	-0.02	23748.56	0.00
21	23744.70	0.00	23744.43	-0.02	23746.14	0.00	23745.90	0.02

Table S5.5: Line positions (in cm^{-1}) in the 1-2 of the $B^2\Sigma^+ - X^2\Sigma^+$ band of ScO.

J	$P_{13}(J)$	O-C	$P_{14}(J)$	O-C	$P_{23}(J)$	O-C	$P_{24}(J)$	O-C
7	19457.78	0.09	19457.53	0.10	19458.24	0.11	19457.97	0.10
8	19456.30	0.05	19456.06	0.07	19456.81	0.05	19456.56	0.06
9	19454.78	0.02	19454.51	0.01	19455.33	0.00	19455.08	0.01
10	19453.14	-0.07	19452.88	-0.07	19453.81	-0.03	19453.55	-0.03
11	19451.51	-0.09	19451.22	-0.12	19452.21	-0.09	19451.95	-0.09
12	19449.81	-0.12	19449.58	-0.09	19450.58	-0.13	19450.31	-0.14
13	19448.14	-0.07	19446.26	0.08	19448.97	-0.09	19448.72	-0.08
14	19446.51	0.07	19444.51	0.16	19447.30	-0.05	19447.10	0.01
15	19444.74	0.13	19457.53	0.10	19445.70	0.12	19445.42	0.10